

AD-A239 132



2

PL-TR-91-2065

**A CHARACTERIZATION OF THE HOT INFRARED
BACKGROUND: THE INFRARED CIRRUS, ZODIACAL
DUST BANDS, AND SOLAR SYSTEM DUST TRAILS**

F. Low
M. Sykes
R. Cutri

University of Arizona
Steward Observatory
Tucson, AZ 85721

1 April 1991

Final Report
3 June 1987 - 31 December 1990

APPROVED FOR PUBLIC RELEASE; DISTRIBUTION UNLIMITED

DTIC
ELECTE
AUGO 1 1991
S B D



**PHILLIPS LABORATORY
AIR FORCE SYSTEMS COMMAND
HANSCOM AIR FORCE BASE, MASSACHUSETTS 01731-5000**

91-06563



"This technical report has been reviewed and
is approved for publication"

Paul D. LeVan

PAUL D. LEVAN
CONTRACT MANAGER

Stephan D. Price

STEPHAN D. PRICE
BRANCH CHIEF

FOR THE COMMANDER

R. Earl Good

R. EARL GOOD
DIVISION DIRECTOR

This report has been reviewed by the ESD Public Affairs Office (PA) and is releasable to the National Technical Information Service (NTIS).

Qualified requestors may obtain additional copies from the Defense Technical Information Center. All others should apply to the National Technical Information Service.

If your address has changed, or if you wish to be removed from the mailing list, or if the addressee is no longer employed by your organization, please notify OL-AA PL/IMA, Hanscom AFB, MA 01731. This will assist us in maintaining a current mailing list.

Do not return copies of this report unless contractual obligations or notices on a specific document requires that it be returned.

Unclassified

SECURITY CLASSIFICATION OF THIS PAGE

REPORT DOCUMENTATION PAGE				Form Approved OMB No 0704-0188	
1a REPORT SECURITY CLASSIFICATION Unclassified			1b RESTRICTIVE MARKINGS		
2a. SECURITY CLASSIFICATION AUTHORITY			3. DISTRIBUTION / AVAILABILITY OF REPORT Approved for public release; Distribution unlimited		
2b. DECLASSIFICATION / DOWNGRADING SCHEDULE					
4 PERFORMING ORGANIZATION REPORT NUMBER(S)			5 MONITORING ORGANIZATION REPORT NUMBER(S) PL-TR-91-2065		
6a. NAME OF PERFORMING ORGANIZATION Steward Observatory		6b OFFICE SYMBOL (If applicable)	7a. NAME OF MONITORING ORGANIZATION Phillips Laboratory		
6c. ADDRESS (City, State, and ZIP Code) University of Arizona Tucson, AZ 85721			7b ADDRESS (City, State, and ZIP Code) Hanscom AFB Massachusetts 01731-5000		
8a. NAME OF FUNDING / SPONSORING ORGANIZATION		8b OFFICE SYMBOL (If applicable)	9 PROCUREMENT INSTRUMENT IDENTIFICATION NUMBER F19628-87-K-0045		
8c ADDRESS (City, State, and ZIP Code)			10 SOURCE OF FUNDING NUMBERS		
			PROGRAM ELEMENT NO 63220C	PROJECT NO S321	TASK NO 18
			WORK UNIT ACCESSION NO AA		
11. TITLE (Include Security Classification) A Characterization of the Hot Infrared Background: The Infrared Cirrus, Zodiacal Dust Bands, and Solar System Dust Trails					
12 PERSONAL AUTHOR(S) F. Low, M. Sykes, R. Cutri					
13a. TYPE OF REPORT Final Report		13b TIME COVERED FROM 6/3/87 TO 12/31/90		14 DATE OF REPORT (Year, Month, Day) 1991 April 1	
				15 PAGE COUNT 238	
16. SUPPLEMENTARY NOTATION					
17. COSATI CODES			18. SUBJECT TERMS (Continue on reverse if necessary and identify by block number)		
FIELD	GROUP	SUB-GROUP			
			Infrared Interstellar dust Asteroids		
			Cirrus Zodiacal Dust Asteroid collisions		
			Dust Comets Asteroid families		
19. ABSTRACT (Continue on reverse if necessary and identify by block number)					
<p>Utilizing data from the Infrared Astronomical Satellite, we have completed an investigation into the nature and properties of the principal components of the hot thermal background. These include the warm infrared cirrus, zodiacal dust bands, and cometary dust trails.</p> <p>A large set of high galactic latitude IRAS Skyflux maps have been "cleaned" using an image-space processor which we have developed. Using these enhanced infrared maps, 44 fields have been identified which exhibit "hot" 12 μm cirrus emission. Cooler, 100 μm emission can be seen in all of the fields, and there is at least a qualitative correlation between the 12 μm cirrus and diffuse optical emission.</p> <p>The relationship between the 12 μm and 100 μm emission was examined in two prominent cirrus complexes. In one of those fields, the ratio of the 12/100 μm surface brightness</p>					
20 DISTRIBUTION / AVAILABILITY OF ABSTRACT <input type="checkbox"/> UNCLASSIFIED/UNLIMITED <input checked="" type="checkbox"/> SAME AS RPT <input type="checkbox"/> DTIC USERS			21 ABSTRACT SECURITY CLASSIFICATION Unclassified		
22a NAME OF RESPONSIBLE INDIVIDUAL Paul LeVan			22b TELEPHONE (Include Area Code) PL/OPC		22c OFFICE SYMBOL PL/OPC

varies coherently by nearly a factor of 50 across the face of the cloud. The variation is smaller in the second cloud. This implies that the 100 μm emission cannot be used reliably as a tracer of the fainter hot emission.

An investigation of a sample of compact 100 μm cirrus sources has shown that the infrared emission can be reproduced by a simple two-component dust model. A warm component, with $T \sim 22\text{K}$ produces the far infrared light, and a hot component, with $T \sim 160 - 170\text{K}$ is the source of the mid-infrared emission. There is essentially no variation seen in the temperature of the warm dust between all of the sources studied, and a small, but probably significant range of temperatures is observed in the hot components. Most of the cirrus sources also exhibit diffuse optical emission. Large variations in the relative amount of 100 μm and blue light suggest that a third, extremely cold, dust component may also be present.

Two-dimensional power spectra have been evaluated for a selection of 12 and 100 μm cirrus clouds. The spectra show that the spatial energy in most clouds is distributed homogeneously. In the few instances where coherent structure is present, it spans only a small range in spatial frequency. Below frequencies of $\sim .05 \text{ arc-minutes}^{-1}$, both the 12 and 100 μm spectra can be characterized by power laws with slopes of -2.9 to -3.0.

Principal conclusions concerning dust bands and dust trails include the following:

A number of faint dust band pairs have been discovered. Zodiacal dust bands arise from non-equilibrium dust production mechanisms in the asteroid belt, are globally associated with principal concentrations of asteroids (the major Hirayama families), but fail in detail to be associated with local asteroid concentrations (e.g. the Flora region). Dust band particles have greater dispersion in their orbital elements than the asteroids from which they ultimately derive, providing evidence for collisional diffusion of dust elements.

A survey of all cometary dust trails has been completed. Eight trails are found in association with known short-period comets. At least two comets have been discovered as a consequence of the detection of their associated dust trails. Trails are a general phenomena associated with all short-period comets and consisting of mm to cm-sized particles emitted at low velocities (m/sec). Trails represent the primary mass loss mechanism for comets. It is suggested that comets have a significantly larger refractory mass fraction than has been determined previously.



Accession For	
NTIS GRA&I	<input checked="checked" type="checkbox"/>
DTIC TAB	<input type="checkbox"/>
Unannounced	<input type="checkbox"/>
Justification	
By	
Distribution/	
Availability Codes	
Dist	Avail and/or Special
A-1	

TABLE OF CONTENTS

I. INTRODUCTION	1
II. INFRARED CIRRUS	1
A. Enhancement of the IRAS Skyflux Maps	2
B. Cirrus Distribution and Census of Hot Cirrus Emitting Clouds	3
C. Relationship Between the 12 and 100 μm Cirrus Emission	4
D. Analysis of Cirrus Emission in Selected Clouds	4
E. Fourier Spatial Analysis of Selected Cirrus Clouds	5
III. ZODIACAL DUST BANDS	8
A. The Dust Band Population	8
B. The Spatial Distribution of Dust Band Particles	8
C. The Origin of the Dust Bands	11
D. The Relationship Between Dust Bands and the Zodiacal Cloud	12
IV. COMETARY DUST TRAILS	12
V. COMETARY DUST	13
VI. PUBLICATIONS UNDER CONTRACT F19628-87-K-0045	15

VII. SCIENTIFIC REPORTS UNDER CONTRACT F19628-87-K-0045	16
Appendix I. Selected Cirrus Investigations.....	17
Appendix II. An Infrared/Optical Investigation of 100 μm "Cirrus"	44
Appendix III. Power Spectral Analysis of the Infrared Cirrus	66
Appendix IV. A Survey of Cometary Dust Trails.....	142
Appendix V. Thermal Properties of Dust Grains in Comets	199

I. INTRODUCTION

The Infrared Astronomical Satellite (IRAS) was launched early in 1983 and during its 10 month mission charted the celestial sphere with great precision and accuracy in four broad infrared wavelength bands centered at 12, 25, 60, and 100 μm . Among the various findings made as a result of a systematic survey of the sky was the discovery of several forms of diffuse, highly structured infrared emission. One of these, the infrared cirrus, is associated with clouds of interstellar material. A second, the zodiacal dust bands, are associated with asteroid collision debris in the main asteroid belt. A third source of emission, cometary dust trails, are large debris covering portions of the orbits of short-period comets. The solar system phenomena shift position in the sky as a consequence of intrinsic orbital motions and parallax (due to the motion of the Earth).

These phenomena are seen in all four IRAS bands and contribute significantly to the overall complexion of the cosmic background. They also provide a variable (in the case of dust bands and comet trails) background against which the detection, tracking and study of all discrete objects must be made. Consequently, we mounted a three year program to study these phenomena in an effort to characterize them, learn about their physical properties, as well as their origin and evolution.

II. INFRARED CIRRUS

We have carried out a program to characterize the spatial distribution and physical composition of the short wavelength emitting, or "hot" component of the infrared cirrus. The program had several goals: 1) to develop an enhanced image database based on the IRAS Skyflux maps; 2) to probe the distribution of cirrus and identify regions of "prominent" 12 μm infrared emission; 3) to examine the empirical relationship between the 12 and 100 μm cirrus in selected regions to determine the effectiveness of using the long wavelength emission as a tracer of the hot cirrus; 4) to model the infrared emission from selected cirrus regions; 5) and to carry out a Fourier analysis of the spatial distribution of the cirrus to determine the characteristic spatial frequencies of the cirrus clouds.

The results of each phase of this program are described in detail in Appendices I, II and III of this report. In this section we describe the development of the enhanced infrared image database and briefly summarize the major findings of the analysis portions of this investigation.

A. ENHANCEMENT OF THE IRAS SKYFLUX MAPS

The IRAS Skyflux maps were the primary data set employed in our study of the cirrus. However, the hot cirrus appears at very low contrast in the 12 and 25 μm Skyflux maps because of its intrinsic faintness and the relative intensity of the zodiacal background at these wavelengths. Therefore, in order to accurately assess both the large and small-scale distribution cirrus and to identify candidate 12 μm cirrus complexes for study, it was necessary to develop techniques to enhance the low surface brightness emission in the IRAS Skyflux maps.

The raw Skyflux plates are dominated by linear, fixed-pattern artifacts known as "stripes" which are the result of background offset and gain variations in individual IRAS detectors. These stripes are most prominent in the shorter wavelength images, but can be seen plainly in all four bands. We developed an image-based "destriping" procedure for the Skyflux maps which exploits the large linear coherence of the stripes to generate a pure "stripe map." This stripe map is simply subtracted from the raw Skyflux image to leave a destriped image. The steps involved in the procedure are as follows:

- Rotate the Skyflux image such that the stripes run horizontally.
- One-dimensionally median filter the image along the stripes. This eliminates the signatures of real celestial sources such as stars, galaxies and small-scale modulations in the cirrus.
- Run a one-dimensional "min-max" filter orthogonal to the stripe direction (along each column). This filter searches for subsequent minima and maxima associated with the stripe pattern, and evaluates the average between them. A spline fit is made to this average along each column, and the individual fits are combined to form a two-dimensional stripe map. This procedure filters out the true broad structure in the sky background, and leaves a stripe map with zero net intensity.
- Subtract the stripe map from the raw image to produce a destriped Skyflux map.

A detailed comparison between the original Skyflux maps and the destriped versions have shown that this processing preserves the radiometric properties of the IRAS maps to within 1% at 12, 25 and 60 μm , and to within 3% at 100 μm . Furthermore, the processing neither introduces nor suppresses structure to better than 3% in all bands. This performance evaluation was submitted as part of CBSD Annual Report No. 1, under Air Force contract

The broad zodiacal background is removed from the Skyflux maps using an empirical method rather than a global model of the zodiacal emission, thus avoiding the uncertainties in shape and zero points associated with the current models, as well as errors that can be introduced by real small scale deviations from the smooth distributions used to model the background. For 12, 25 and 60 μm Skyflux plates, a two-dimensional, third order Chebyshev polynomial was fit to the image; the fits are of sufficiently low order to model only the trends in the broad background, and to effectively ignore small scale brightness deviations. The background fits were then subtracted from the destriped Skyflux maps, yielding a "flat-fielded" image. The broad zodiacal emission was not removed from 100 μm images because bright cirrus complexes with scale sizes comparable to the image size tend to be integrated into the empirical fit and thus suppressed in the final product.

B. CIRRUS DISTRIBUTION AND CENSUS OF HOT CIRRUS EMITTING CLOUDS

In Appendix I of this final report, we describe how the database of enhanced IRAS Skyflux maps have been used to examine the global distribution of both the cold and hot cirrus emission. We have developed software which combines multiple Skyflux maps into large-scale mosaics, covering areas up to $\sim 5600 \text{ deg}^2$. Examination of these mosaics shows that cirrus complexes can extend over tens of degrees on the sky. Between the major complexes, low level filamentary cirrus emission is visible at 100 μm , indicating that it is unlikely that any region of the sky is completely free from cirrus. The level of faint ambient cirrus emission is typically 100-1000 times fainter than the peak 100 μm intensity within the brighter clouds. In both the bright cirrus complexes, and fainter cirrus "background," modulation in the surface brightness is apparent down to the 2 arc-minute resolution of the Skyflux maps.

The enhanced Skyflux maps were examined, and a census was made for fields containing detectable 12 μm cirrus emission, as well as diffuse optical emission associated with the cirrus. The results of this census are also described in Appendix I. While this survey was not intended to be complete, it provides a good overview of the distribution of hot cirrus in Galactic coordinates. Skyflux fields which exhibit 12 μm cirrus appear to be concentrated near the Galactic Plane, although selected regions of hot cirrus can be found even at high galactic latitudes. This distribution likely results from the scale height of the hot cirrus, or of the interstellar radiation field.

C. RELATIONSHIP BETWEEN THE 12 AND 100 μm CIRRUS EMISSION

From the list of cirrus complexes with detectable 12 μm emission, two fields with the most prominent examples of hot emission were identified. In Appendix I is described the investigation of the interrelationship between the short and long wavelength emission in these two clouds. The most significant result of this study is that in one complex, the ratio of 100 to 12 μm surface brightness of the cirrus varies coherently by up to a factor of 50 across the face of the cloud. In the second cloud, the variation is much smaller, only factors of 4-5. The primary implication of this is that, in general, the 100 μm cirrus cannot be used a reliable tracer of the hot cirrus emission. The significant variation in the relative strengths of the 12 and 100 μm cirrus brightness is also discussed in Appendix II, in the context of variations in the relative abundances of the populations of dust grains which emit the 12 and 100 μm emission.

D. ANALYSIS OF CIRRUS EMISSION IN SELECTED CLOUDS

As described in Appendix I, two fields with prominent 12 μm cirrus emission were studied in some detail. Color maps of these clouds showed that the long wavelength cirrus (60-100 μm) emission exhibits characteristic color temperatures in the range 20-30K. The short wavelength emission (12-25 μm) has a much warmer color temperature of 200-300K. This well-known discrepancy has been interpreted as evidence that the hot emission arises predominantly from very small grains which are transiently heated to these very high temperatures upon absorption of ultraviolet photons from the interstellar radiation field. The long wavelength emission arises from larger, "classical" dust grains which are in radiative equilibrium with the ambient radiation field. The large variation of the 100/12 μm brightness ratio discussed above strongly suggests that the two grain populations are not well mixed.

An in-depth analysis of the emission of a selection of bright, compact 100 μm cirrus sources is given in Appendix II. This work constituted the major portion of Liz Paley's Master's Thesis at the University of Arizona, and has now been accepted for publication in the July 1991 issue of the *Astrophysical Journal*. In this work, compact cirrus sources were identified from a list of the brightest 100 μm -only sources in the IRAS Point Source Catalog. Improved surface brightness measures at 12, 25, 60 and 100 μm were obtained for the sources using IRAS ADDSCAN and two-dimensional survey co-added data. The observed infrared spectral energy distributions of the cirrus require that the emission arise from at least two discrete components: a hot component, with physical temperatures in the range 160-170K, and a warm component, with a temperature of $\sim 22\text{K}$. The hot component, which presumably arises from transiently heated very small grains, accounts for between 15 and 42% of the total infrared luminosity. The temperature of the

warm dust component is essentially the same for all of the sources studied, suggesting that a single type of grain produces the warm component of the emission.

Discussion of the diffuse optical emission associated with the infrared cirrus is made in Appendices I and II. In Appendix I, we list Skyflux maps which contain cirrus which has been detected optically. There is at least a qualitative correlation between the presence of optical emission and $12\text{ }\mu\text{m}$ emission from the cirrus. As described in Appendix II, the optical emission from the cirrus is too red to be accounted for simply by the scattering of interstellar radiation field photons from dust grains in the cirrus clouds. Similarity between the red optical colors of the cirrus and those of reflection nebulae suggest that some part of the optical emission arises from luminescence from macro-molecules such as Polycyclic Aromatic Hydrocarbons (PAHs) or Hydrogenated Amorphous Carbon grains (HACs). This is in apparent agreement with the models which ascribe the $12\text{ }\mu\text{m}$ emission to transiently heated small grains and/or macro-molecules. However, the relationship between the infrared and optical emission is apparently complex. Appendix II describes a survey of the optical emission from the cirrus made from examination of the Palomar and ESO Sky Survey plates. No obvious correlations were found between the optical brightness or color of the cirrus and either the brightness at $100\text{ }\mu\text{m}$ or the ratio of hot to warm dust. Nevertheless, in two isolated cirrus complexes, the optical and $100\text{ }\mu\text{m}$ morphology is well correlated, except in certain specific areas. Clearly, a more detailed investigation of the optical emission is warranted in order to probe the relationship between the optically emitting material and the hot cirrus component. Such a study may reveal that, in fact, optical emission is a better tracer of the hot cirrus than the $100\text{ }\mu\text{m}$ light.

E. FOURIER SPATIAL ANALYSIS OF SELECTED CIRRUS CLOUDS

The results of a Fourier analysis of a number of prominent cirrus complexes is presented in Appendix III. This study has yielded a number of quantitative results concerning the characteristic spatial distribution of the infrared cirrus. Below is the summary of those results reprinted from Appendix III.

- The two-dimensional power spectra of $12\text{ }\mu\text{m}$ IRAS Skyflux maps are virtually dominated by the influence of stars in the maps. The power spectra of the $100\text{ }\mu\text{m}$ cirrus fields are also influenced by point sources, although to a much smaller degree. Two dimensional median filtering of the $12\text{ }\mu\text{m}$ maps can suppress the contribution of the point sources, but such filtering produces artifacts which must be taken into account.
- The two-dimensional power spectra of most 12 and $100\text{ }\mu\text{m}$ cirrus fields are az-

imutally symmetric, indicating that the spatial power is distributed homogeneously. That is, the spatial structure of the cirrus is generally not coherent over large spatial scales.

- In 20% of the fields studied, the two-dimensional power spectra exhibit some asymmetries. However, these asymmetries extend over relatively small ranges in spatial frequencies. This suggests that although certain coherent cirrus structures can be present, such as large linear features, the bulk of the cirrus structure is distributed with no preferred spatial orientation. At least some of the asymmetries observed in the power spectra may be caused by the presence of discrete, compact non-cirrus sources.
- At frequencies below ~ 0.05 arc-minutes $^{-1}$, both the 12 and 100 μm two dimensional power spectra typically have power law slopes, α , of -2.9 to -3.0. Above 0.05 arc-minutes $^{-1}$, the slopes of the 100 μm steepen to values of approximately -5.3 to -3.5. Although we cannot rule out the that steepening is indicative of the small-scale structure of the cirrus, analysis of the Pointed Observation data strongly suggest that the curvature is caused by the contribution of point sources in the images. Because of the compromising effects of median filtering, the high frequency behavior of the 12 μm spectra is unknown.
- Because only moderately bright cirrus was serendipitously scanned during the Pointed Observations of IRAS, the cirrus data and resulting power spectra are of relatively low signal-to-noise. The ability to verify that point sources are not present in the scan allows much higher confidence to be placed on the interpretation of the power spectral slopes at the highest frequencies. For the three brightest cirrus regions covered by Pointed Observations, the slopes of the 100 μm power spectra up to spatial frequencies of ~ 0.2 arc-minutes $^{-1}$ agree well with the lower frequency slopes observed in the Skyflux data ($\alpha \approx -2.9$). The hot cirrus emission is too faint in these areas to produce useful power spectral information.

These analyses point out the strengths and limitations of the IRAS Skyflux maps and Pointed Observations database for studies of the spatial power distribution of the cirrus. The Skyflux maps cover essentially the entire sky so regions of the brightest cirrus emission may be selected for study. The individual scans of Pointed Observations, although limited in spatial coverage, can be screened for point sources. It would be advantageous to develop a "smart" processor which is able to remove selectively non-cirrus sources from the Skyflux maps, including stars, galaxies and compact HII regions and molecular clouds. However, we suggest that better a data set to employ for future spatial power studies of the cirrus may be the IRAS Survey CRDD. Survey CRDD scans for selected regions covering

the brightest cirrus complexes can be selected. As with the Pointed Observation data, these individual scans can be selectively filtered for non-cirrus sources and then combined into two-dimensional images, thus alleviating many of the problems incurred in post-processing the existing Skyflux maps.

III. ZODIACAL DUST BANDS

Our work in the area of zodiacal dust band studies has focussed on several areas: 1) the identification and characterization of the zodiacal dust band population; 2) modeling the spatial distribution of particles comprising a dust band torus; 3) determine whether zodiacal dust bands represent an equilibrium or stochastic dust production process in the asteroid belt.

The results have been detailed in publications (Sykes 1988a; 1988b; Sykes *et al.* 1989; Sykes 1990) and in Scientific reports #1, #2, and #4 to AFGL under this contract. They are summarized in the following sections.

A. THE DUST BAND POPULATION

A set of special images of the sky within 30° of the ecliptic were constructed from high-pass filtered scans from the IRAS Zodiacal History File to look for high spatial frequency structures which correlated in ecliptic longitude. Such structures had been predicted by Sykes and Greenberg (1986) in their non-equilibrium model of zodiacal dust band formation. Apart from the original 3 bands reported by Low *et al.* (1984) a number of new bands were discovered (Sykes 1988b) which are listed in Table 1. Dust band morphology was found to vary between different pairs of bands, having typical apparent widths of a few degrees, but ranging from less than 0.5° (the β bands) to several degrees (the γ bands). The observed population was found to be in agreement with the predictions of Sykes and Greenberg (1986).

B. THE SPATIAL DISTRIBUTION OF DUST BAND PARTICLES

A mathematical model of the spatial distribution of orbitally evolved collisional debris was developed which reproduces the dust band phenomenon (Sykes 1990). The model was derived by considering what happens in detail to the debris from the catastrophic disruption of a single asteroid. It was found that three steps occur: distribution over the initial orbit, distribution of the ascending nodes of the particle orbits over 360° , and the distribution of the periapses over 360° . The result is a torus of material whose volume density can be separated into radial and azimuthal components:

$$P_{vol}(r, \beta) = R(r)\Theta(\beta)$$

Table 1.

Name	Geocentric Ecliptic Latitude (HCON 1 and 2)	Comments
α	$\pm(0 \text{ to } 2.5)$	Possible association with Themis asteroid family (Sykes, 1986).
β	$\pm(1 \text{ to } 3.5)$	Well defined in Skyflux Maps. Possible association with Koronis asteroid family (Sykes, 1986).
γ	$\pm(8.5 \text{ to } 11.5)$	Possible association with Eos asteroid family (Dermott <i>et al.</i> , 1984).
A	3.5 to 7	Partial band (Sykes, 1986). Probable trail (this paper). The western end (HCON 2) is observed at 60° geocentric ecliptic longitude (GEL) and (HCON 3) at $\sim 125^\circ$ (longitude of earth $\sim 156^\circ$ and $\sim 37^\circ$, respectively). The eastern end is observed at 160° longitude (HCON 2) (not observed in HCON 3 due to death of IRAS).
B	-3.5 to -7.5	Dust trail (HCON 1 and 2). GEL 111° to 155° .
C	4 to 7	Dust trail (HCON 3). GEL 99° to 157° .
D	-3.5 to -5.5	Dust trail (HCON 3). GEL 215° to 242° .
E	4 to 6	Possible pair with F.
F	-4 to -6.5	Possible pair with E. Best resolved over GEL 270° to 360° HCON 2.
G	6.5 to 8	Possible pair with H
H	-5.5 to -8.5	Possible pair with G. Best resolved over GEL 310° to 360° HCON 2.
J	12.5 to 15	Probable pair with Band K. Possible association with Io asteroid family (Sykes, 1988b).
K	-13 to -16	Probable pair with Band J. Possible association with Io asteroid family (Sykes, 1988b).
M	15 to 17.5	Probable pair with Band N. Seen to latitude 21 (HCON 3)
N	-17 to -20	Probable pair with Band M. Seen to latitude -22 (HCON 3)

noindent where, r is the heliocentric distance, and β is the azimuth angle relative to the plane of symmetry of the torus, and

$$R(r) = \frac{C}{a^2 r} \frac{1}{\left[e^2 - (r/a - 1)^2 \right]^{1/2}}$$

$$\Theta(\beta) = [2\pi^2]^{-1} [\cos^2 \beta - \cos^2 i]^{-1/2}$$

with the limits

$$a(1 - e) \leq r \leq a(1 + e)$$

$$-i \leq \beta \leq i$$

where C is a constant of normalization, a is semi-major axis, e is orbital eccentricity, and i is proper inclination. The torus thus described is squarish and sun-centered, with a radial extent bounded by the perihelion and aphelion distance of the particles, and whose latitudinal extent is bounded by the inclinations of the particle orbits. It is assumed in the above that all torus particles have identical orbital elements with the exception of having distributed nodes and mean anomalies. Maxima in volume density at perihelion and aphelion give rise to "perihelion" and "aphelion" band pairs which generally align when viewed from the Earth to give rise to the roughly parallel bands of dust observed by IRAS.

Particles distributed over a single orbit will be found preferentially near aphelion as a consequence of the lower orbital speeds there. However, randomization of periapses and nodes will dilute this radial probability distribution by $\sim 1/r^2$. As a result, the particle number density of the dust band torus is maximum near perihelion. Bolometric luminosity of these particles will also be higher because of their lower heliocentric distances (hence higher temperatures).

Of course, particles comprising a dust band torus do not have identical orbital elements. There will be some dispersion in a , e , and i . This significantly effects the spatial density of the dust band particles, hence the location from which their flux originates (Sykes 1990). In general, the volume of the torus increases with increasing dispersion in elements, but the peaks of emission decrease in latitudinal separation.

C. ORIGIN OF THE DUST BANDS

Utilizing the above model of the dust band torus, convolved with Gaussian dispersions in the orbital elements of various variances, detailed models were generated for 7 hypothetical asteroid family dust tori that were then mapped onto the IRAS data scan by scan and compared to the actual IRAS observations (Sykes 1990). The most prominent 2 tori (β and γ) were found to be associated with the Koronis and Eos families, respectively. With the Eos torus requiring a significantly greater dispersion in orbital elements in order to match the IRAS observations. This was explained by collisional diffusion of dust acting over a longer period of time in the Eos family. In other words, the Eos family is much older than the Koronis family, consistent with the conclusions derived from rotational studies of family members by Binzel (1986). A fainter pair (α) was found in association with the Themis family.

With the possible exception of the Io family, no other significant asteroid family was found to have an associated dust band torus. At the same time, other fainter bands were known (Table 1), not in association with any other family. Were erosional processes (such as cratering) the dominant source of dust in the asteroid belt, then dust bands would be expected to be found only in association with the largest asteroid families as they represent concentrations of asteroids in $a - \sin i$ space. This would also be the case if the size distributions of the asteroid population from the size of observed asteroids to dust-sized particles were in collisional equilibrium and could be approximated by a single power-law distribution (e.g. Dermott *et al.* 1984). While dust bands are found in association with the three largest families (Themis, Eos, Koronis), the breakdown of this hypothesis at other locations (Phocaea, Flora, Nysa, and Maria) and the existence of band pairs not associated with any large family suggests that stochastic large catastrophic disruptions play a major role in asteroid dust production, rather than a more continuous process such as cratering.

The equilibrium hypothesis of dust band origin does not account for the larger brightness of the β bands compared to the α bands. Dermott *et al.* (1984) used this theory to calculate that dust associated with the Koronis asteroid family would have a surface brightness an order of magnitude *less* than the dust associated with the much larger Themis family. The *opposite* is observed. The non-equilibrium model of Sykes and Greenberg (1986) offers an explanation for this discrepancy: the Themis family is much older than the Koronis family. Under this model, dust bands fade with time, and the ages of their associated families, in this case, have been calculated by Sykes (1986) and Sykes *et al.* (1989) to be 1.5×10^9 and 1.3×10^8 years, respectively. These model ages are very uncertain, given the large number of assumptions on which they are based. The relative ages, however, are reliable to the extent that collision probabilities and fragmentation mechanics are similar among the asteroid families considered.

D. THE RELATIONSHIP BETWEEN DUST BANDS AND THE ZODIACAL CLOUD

Dust being generated in the asteroid belt from the communiton of collisional disruption products does not simply disappear. While some may be lost due to radiation pressure, much of it will spiral in towards the Sun under the influence of Poynting-Robertson drag. Estimates of dust production rates in the principal families combined with estimates of their increased bolometric luminosity as they move in towards the Sun has resulted in the conclusion that the principal dust bands may be the principal source of the zodiacal thermal emission observed by IRAS (Reach 1991). This opens the possibility of constructing physical models of the cloud based on source region descriptions utlizing the description of the dust band tori above, coupled to a knowledge of the dynamical and collisional evolution of the dust band particles.

IV. COMETARY DUST TRAILS

One of the major discoveries of the IRAS mission was of narrow streams of debris in the orbits of short-period comets (Sykes *et al.* 1986). Our work on cometary dust trails has focussed on: 1) Surveying all trails in the IRAS database, and identify their sources; 2) Characterizing their physical and thermal properties; and 3) Explore new insights into the nature and evolution of comets as a consequence of our better understanding this new phenomenon.

Our results have been presented in publications (Sykes 1988a, 1988b, and Sykes *et al.* 1990), Scientific Reports #3 and #4 to AFGL, and Appendix IV in the present report.

This work involved an exhaustive survey of 1836 IRAS Skyflux Maps. Each image was individually processed and examined by eye in the search for cometary dust trails. The result was 104 detections of 17 trails, of which 8 were associated with known short-period comets (P/Churyumov-Gerasimenko, P/Encke, P/Gunn, P/Kopff, P/Pons-Winnecke, P/Schwassmann-Wachmann 1, P/Tempel 1, P/Tempel 2). Nine of these detections were of trails not associated with any known solar system object, though it is obvious in two cases that we have discovered previously undetected short-period comets. Trail comets tend to be among the more active short-period comets, however, the principal reason for their detection is that trails tended to be observed near perihelion in association with those comets having the smallest perihelion distances. In other words, these particles were the hottest at the time of the IRAS mission. This strongly suggests that the trail phenomenon is common to all short-period comets and is not peculiar to these comets. This also means that we may generalize from properties derived for trail comets to the rest

of the short-period comet population. The survey results are presented in Appendix IV.

There are several important conclusions to the survey of cometary dust trails. First is the generality of the phenomenon. Second, comets have a much greater mass fraction of refractory material than has been previously inferred. This suggests that comets may be more "icy mudballs" than "the dirty snowballs" of Whipple. The fact that the bulk of cometary mass appears to be lost in trail particles, which have a narrow size range, suggests that either some surface processing (e.g. welding together of particles into a mantle which is then fragmented) is going on, or that this particle size is representative of the granules which accreted to form the proto-cometary bodies early in solar system history. Thirdly, comets are losing mass at greater rates than previously thought, suggesting that they have a greater role in the resupply of the zodiacal dust complex, particularly in large particles.

V. COMETARY DUST

In order to more better understand the properties and observable behavior of cometary particles in general, work was also undertaken to investigate the optical and thermal properties of cometary dust. This has resulted in publications (Lien 1990 and 1991), scientific report #5 to AFGL, and Appendix V.

References

Binzel, R. 1986. *Collisional Evolution in the Asteroid Belt: An Observational and Numerical Study*. Ph.D. Thesis, University of Texas at Austin.

Dermott, S., P. Nicholson, J. Burns, and J. Houck 1984. Origin of the solar system dust bands discovered by IRAS. *Nature* **312**, 505.

Lien, D. 1990. Dust in comets. I. Thermal properties of homogeneous and heterogeneous grains. *Astrophys. J.* **335**, 680.

Lien, D. 1991. Thermal properties of cometary dust. In *Comets in the Post-Halley Era* (R. Newburn, Ed.), in press.

Low, F. *et al.* 1984. Infrared cirrus: New components of the extended infrared emission. *Astrophys. J. (Letters)* **278**, L19.

Reech, W. 1991. Asteroid dust and the zodiacal emission. In *Origin and Evolution of Interplanetary Dust* (Levasseur-Regourd, Ed.), in press.

Sykes, M. 1986. *IRAS Observations of Asteroid Dust Bands and Cometary Dust Trails*. Ph.D. Thesis, University of Arizona.

Sykes, M. 1988a. The albedo of large refractory particles from P/Tempel 2. In *Comets to Cosmology* (A. Lawrence, Ed.), Springer-Verlag, 66.

Sykes, M. 1988b. IRAS observations of extended zodiacal structures. *Astrophys. J. (Letters)* **334**, L55.

Sykes, M. 1990. Zodiacal dust bands: Their relation to asteroid families. *Icarus* **84**, 267.

Sykes, M. and R. Greenberg 1986. The formation and origin of the zodiacal dust bands as a consequence of single collisions between asteroids. *Icarus* **65**, 51.

Sykes, M., D. Lien, and R. Walker 1990. The Tempel 2 dust trail. *Icarus* **86**, 236.

Sykes, M. *et al.* 1989. Dust bands in the asteroid belt. In *Asteroids II* (R. Binzel, T. Gehrels, and M. Matthews, Eds.). University of Arizona Press (Tucson), 336.

VI. PUBLICATIONS UNDER CONTRACT F19628-87-K-0045

Sykes, M. 1988a. The albedo of large refractory particles from P/Tempel 2. In *Comets to Cosmology* (A. Lawrence, Ed.), Springer-Verlag, 66.

Sykes, M. 1988b. IRAS observations of extended zodiacal structures. *Astrophys. J. (Letters)* **334**, L55.

Sykes, M., R. Greenberg, S. Dermott, P. Nicholson, T.N. Gautier 1989. Dust bands in the asteroid belt. In *Asteroids II* (R. Binzel, T. Gehrels, and M. Matthews, Eds.). University of Arizona Press (Tucson), 336.

Spencer, J., L. Lebofsky, and M. Sykes 1989. Systematic biases in radiometric diameter determinations. *Icarus* **78**, 1989.

Lien, D. 1990. Dust in comets. I. Thermal properties of homogeneous and heterogeneous grains. *Astrophys. J.* **335**, 680.

Sykes, M. 1990. Zodiacal dust bands: Their relation to asteroid families. *Icarus* **84**, 267.

Sykes, M., D. Lien, and R. Walker 1990. The Tempel 2 dust trail. *Icarus* **86**, 236.

Lien, D. 1991. Optical properties of cometary dust. In *Comets in the Post-Halley Era* (R. Newburn, Ed.), in press.

Paley, E., F. Low, J. McGraw, R. Cutri, and H. Rix 1991. An infrared/optical investigation of 100 μ m cirrus. *Astrophys. J.* **377**, in press.

Sykes, M. and R. Walker 1991. Cometary dust trails. I. Survey. In preparation.

VII. SCIENTIFIC REPORTS UNDER CONTRACT F19628-87-K-0045

- (1) Dust bands in the asteroid belt.
- (2) Zodiacal dust bands: Their relation to asteroid families.
- (3) The Tempel 2 dust trail.
- (4) Detecting extended solar system structures with COBE.
- (5) Optical properties of cometary dust.

APPENDIX I

SELECTED CIRRUS INVESTIGATIONS

A. HOT CIRRUS EMISSION FIELD CENSUS

Despite nearly 7 years having passed since the discovery of the emission from the interstellar clouds known as infrared cirrus, details of the global distribution of the clouds have been surprisingly slow in forthcoming. Most cirrus studies have concentrated on prominent complexes of warm ($T_c \sim 20\text{--}30\text{K}$) emission which are visible in virtually every $100\mu\text{m}$ IRAS Skyflux map. Examination of apparently "cirrus-free" regions on our cleaned $100\mu\text{m}$ maps reveals low level emission and structure which suggests that the warm cirrus may blanket the entire sky visible from the terrestrial neighborhood, precluding the presence of any true viewing windows through the interstellar clouds. Because of its much lower surface brightness, the "hot" component of the cirrus clouds, as manifested by emission at 12 and $25\mu\text{m}$, is seen much less frequently on the Skyflux maps. As a consequence, relatively little is known about the large-scale distribution of the hot cirrus, and its relationship to the more prevalent warm clouds.

We have carried out a "census" of IRAS Skyflux fields to probe the frequency of occurrence and location of detectable $12\mu\text{m}$ and optical cirrus emission, to serve as a basis for more detailed investigations of the hot cirrus. The results of this census are summarized in Table 1 which lists those IRAS Skyflux fields which exhibit cirrus emission that is visible in the $12\mu\text{m}$ images or on POSS or ESO-SRC plates. Those with detectable $12\mu\text{m}$ emission are indicated with an "X" in the "Hot" Cirrus column. The column denoted "Optical" describes where the detection of optical nebulosity was first made: "L" denotes Plates on which there are Lynd's Bright Nebulae (hereafter LBN; see below) coincident with cirrus emission, "P" marks the fields with optical emission highlighted by Paley *et al.* (1991; and Appendix II), and those fields imaged optically by Guhathakurta and Tyson (1989) are denoted with "G." Prominent $100\mu\text{m}$ cirrus can be found on all of the Plates listed.

This list does not represent a complete survey for either $12\mu\text{m}$ or optical cirrus emission for the following reasons:

- The raw Skyflux photographs were examined to test for the presence of $12\mu\text{m}$ cirrus, in most cases. Windowing of these images was not necessarily optimized for the display of the faint $12\mu\text{m}$ structure. In addition, cirrus can be seen on many of these Plates only after stripe artifacts, and the broad zodiacal emission component are removed through processing. A more complete survey will be possible when we complete the processing of all high galactic latitude $12\mu\text{m}$ Skyflux images.
- The Lynd's Catalog of Bright Nebulae covers only the region of the POSS ($|\delta| > -24^\circ$), and there is no corresponding survey of diffuse optical emission in the southern sky. While Paley *et al.* (1990; and Appendix II) included southern Plates in their survey, they investigated only a selection of apparently compact, bright $100\mu\text{m}$ sources.

Southern optical cirrus which is not associated with compact 100 μm emission (or emission which was reported to be compact because of the processing) will not be included. Furthermore, the LBN represent the optically-brightest cirrus. Examination of the glass POSS plates reveals very low surface brightness emission in the region of many other bright cirrus clouds.

Cutri, Low and Lien (1991) report the discovery of the correlation between the 100 μm cirrus and the high galactic latitude Lynd's Bright Nebulae. Of the 77 LBN not associated with known HII regions and with $|b| > 30^\circ$, 76 are spatially coincident with 100 μm cirrus complexes. The one high latitude LBN which does not exhibit prominent infrared cirrus emission, is extremely faint on the POSS plates, and may in fact not be a true source. Frequently, the morphologies of both the infrared and optical emission are quite similar.

From Table 1, it can be seen that there is at least a qualitative correlation between the presence of 12 μm emission and detectable optical emission. 67% of the fields containing LBN also exhibit some 12 μm emission. It is likely that when more cleaned Skyflux fields are examined the percentage will become even larger. Consequently, it may prove that diffuse emission at visible wavelengths will be the optimum tracer of the hot cirrus. The relative strengths of the 100 and 12 μm and optical emission have currently been measured for only a few clouds (Cutri, Low and Lien 1991).

B. GLOBAL DISTRIBUTION OF CIRRUS

When viewed on a map of the sky, the Skyflux fields containing LBN are seen to roughly parallel the Galactic Plane, seldom extending above $|b| > 40^\circ$. This is also seen to some extent in the fields containing $12\mu\text{m}$ cirrus, although they do seem to range to higher latitudes. These distributions must be a result of the scale height of either the "warm" cirrus or of the interstellar radiation field.

This cursory examination of the distribution of warm cirrus illustrates how little is known about the global distribution of the cirrus, in general. For example, the characteristic "size" of cirrus complexes is uncertain. Since most studies have focused on individual Skyflux fields, it has been difficult to gauge whether the complexes extend beyond the 15° scale of the maps. Do the morphologies of cirrus clouds differ with galactic latitude; if clouds are observed to appear flatter towards the galactic plane, then this could be evidence that they are thick "pancake" structures rather than roughly spherical ones. To understand the origin and evolution of cirrus, it would also be extremely useful to know if cirrus clouds are physically isolated structures, or if the complexes we identify as prominent clouds are just condensations in a tenuous, uniform "sea" of interstellar dust, as is suggested by the homogeneous low level emission seen in the cleaned $100\mu\text{m}$ images. This distinction has considerable bearing on how the cirrus is related to, and influences the rest of the ISM. What is the scale-height of the cold cirrus and the warm cirrus? Are they different? Do the scale-heights differ from other ISM components?

All of these questions highlight the need to develop a general cirrus taxonomy. To address this, we have developed a procedure to combine several cleaned IRAS Skyflux images into large-scale mosaics. This process places a central image into the center of the mosaic and properly maps a number of other images into the projected coordinate system of primary image. The resulting large-scale gnomonic projection preserves the full resolution and radiometry of the original images. Several examples of $100\mu\text{m}$ mosaics of the north and south galactic polar regions, and the north celestial pole are shown in Figures 1-3. The galactic poles exhibit the low-level, but fairly uniform emission described above. Small, wispy condensations can be seen within the homogeneous background. The character of the north celestial pole field is quite different, however. This image, which contains 12 individual Skyflux maps, displays a remarkable cloud complex which extends across nearly 40° of the sky. The hook-like feature has a counterpart in the HI maps of Heiles (1976). From these mosaics it is possible to see the rather dramatic large-scale distribution and structure of the warm cirrus, and eventually the hot cirrus, as well. Using these maps, we are developing a catalog of bright cirrus complexes which can serve as the basis for further systematic studies of cirrus cloud properties.

C. STUDIES OF INDIVIDUAL CIRRUS COMPLEXES

To probe the characteristics of the short wavelength cirrus emission, and its interrelationship with the emission at longer wavelengths, we have examined in detail two smaller regions of the large mosaic shown in Figure 3.

a. Plate 1

IRAS Skyflux Plate 1 is the central field in Figure 3. Centered on the north celestial pole, it contains one of the most prominent examples of $12\mu\text{m}$ cirrus emission in the sky. Emission is clearly visible in all four bands, as is shown in Figure 4. The gross morphology is similar in each band, although close study shows some important differences between bands which imply that there are significant color variations across the cloud. To quantify this, color maps of the field were generated. This procedure involved binning the individual images 4×4 , subtracting the mean sky level, and identifying super-pixels which had intensities 3σ above the sky level. Binning improves signal-to-noise and reduces the influence of point sources. Color maps were constructed by dividing the resulting binned, sky-subtracted images in different bands by one another. Color values were recorded in a pixel only if there were detections in both bands, otherwise no value was assigned (i.e. no limit information is provided).

In Figure 5 is shown the ratio of $100\mu\text{m}/60\mu\text{m}$ emission for Plate 1. This color is essentially uniform over most of the cloud, having an intensity ratio corresponding to a color temperature near 25K. There is a suggestion of a cooler edge (green-red) where T_c is down to $\leq 20\text{K}$. Paley *et al.* (1991; and Appendix II) found that when corrected for the contribution of the short wavelength hot cirrus component, the physical temperature found for the warm dust component was remarkably constant between 11 different cirrus sources in quite different regions of the sky. This fact and the observed temperature uniformity in the Plate 1 cloud (and that in Plate 6 as discussed below) suggests that the physical composition of the warm dust is surprisingly similar both within individual clouds, and over a large region of the galaxy.

The $25\mu\text{m}/12\mu\text{m}$ color distribution is also roughly uniform over the cloud. However, the short wavelength emission has characteristic color temperatures of 200-300K, far warmer than the band 3 and 4 emission. This discrepancy is the well-known result indicating that the short and long wavelength emission must arise from different grain populations. The $12\text{-}25\mu\text{m}$ light likely originates from very small grains or macro-molecules which undergo transient thermal pulses upon absorption of ultraviolet radiation, while the long wavelength emission arises from larger silicate or graphite grains which are in thermal equilibrium with the ambient interstellar radiation field.

Of greater interest is the map of the $100\mu\text{m}/12\mu\text{m}$ color shown in Figure 6. From this image, it can be seen that there is a large gradient in the color across the cloud. The $100\mu\text{m}$ emission dominates on the right edge of the cloud, where the $100/12$ ratio is as large as 50, but the relative strength of the hotter emission increases towards the left and bottom, where the ratio drops to $\ll 10$. This coherent variation of the $100\mu\text{m}/12\mu\text{m}$ surface brightness ratio has a number of critical implications. From a practical standpoint, this means that it will not be possible, in general, to trace the faint $12\mu\text{m}$ emission with the brighter $100\mu\text{m}$ light. Physically, the color

gradients imply that there must be significant spatial variations in the relative populations of large and small grains. It is difficult to envision how the gradients could be due to local anisotropies in the radiation field or optical depth variations because both the 100/60 and 25/12 μ m colors are so uniform across the cloud.

A number of different mechanisms might result in the segregation of the grain populations. For instance, the passage of shocks could either destroy or help create the small grains, resulting in fairly abrupt transitions in the relative populations. Alternately, magnetic fields might more efficiently "herd" small charged grains because of their larger charge per unit mass. Another possibility is that the complex molecules which have been proposed as the source of the hot cirrus emission actually form as mantles on the larger "classical" silicate or graphite grains. Formation of such mantles is thought to occur in protected environments such as dense cores of dark clouds; evidence for mantle formation has been observed in the core of at least one isolated cirrus clouds by Laureijs *et al.* (1989). The color gradients observed in the Plate 1 cloud could indicate slight optical depth differences which produce just enough shielding in part of the cloud, allowing mantle formation, although it is not clear how efficiently mantles would form in such a tenuous medium as the cirrus. Alternately, sites of strong 12 μ m emission in cirrus complexes may identify dissipating cores in which the mantles producing the mid-infrared emission are beginning to be destroyed by the steadily intensifying interstellar radiation field. The relatively large number of clouds containing 12 μ m emission would indicate that the occurrence of dense cores is quite common.

b. Plate 6

A similar analysis has been carried out for the Skyflux field in Plate 6. This field, centered near 9^h36^m and +75°, is in the 8-o'clock position in the north celestial pole mosaic (Figure 3), and has cirrus emission visible in all four bands as is shown in Figure 7. This region of the sky also exhibits diffuse extended optical emission noted by Sandage (1976).

The 100/60 μ m color map, shown in Figure 8, displays colors which are roughly uniform throughout the cloud indicating color temperatures which are slightly higher than those of the warm emission in Plate 1. This is also the case for the distribution of 25/12 μ m colors. However, as is shown in Figure 9, this cloud does not show the large variation in 100/12 μ m color seen in Plate 1; in Plate 6 the ratio varies by a factor of 4-5, compared to as much as 50 in Plate 1. The one exception is a compact region of bright 100 μ m emission in which the surface brightness ratio drops to a minimum.

c. Color Distributions

The color properties of Plates 1 and 6 are compared in Figures 10-13. Figures 10 and 11 show the distribution of 100/60 μ m surface brightness ratios for pixels in the Plate 1 and 6 images, respectively. The average color temperature for the warm emission in Plate 1 appears to be 3-4 degrees below that in Plate 6. Slight uncertainties in the level of the sky subtraction could account for about 1-2 degrees difference, and the remainder is probably due to differing contributions by the hot cirrus component to the 60 μ m emission (see below). Also intriguing are

the profiles of the distributions. Galactic and extragalactic point sources contribute to the weak, broad wings towards the blue, but there are proportionately more "warm" pixels in Plate 6.

The histograms of the 25/12 μ m colors are shown in Figures 12 and 13. Again, the cloud in Plate 6 seems to exhibit a slightly higher characteristic color temperature than Plate 1.

Figures 14 and 15, which illustrate how the 100/12 μ m colors vary with 12 μ m surface brightness, help to shed some light on the differences between the portions of the north celestial pole cirrus cloud found in Plates 1 and 6. It can be seen that both fields exhibit comparably bright 12 μ m emission. However, portions of the Plate 1 cloud are nearly five times brighter at 100 μ m than that in Plate 6. Therefore, the different ranges of 100/12 color seen in the two regions result not from different levels of hot cirrus emission, but from different relative amounts of warm (100 μ m) emission. Because the mean level of emission from the hot cirrus component relative to the warm component is larger in Plate 6, a larger fraction of the 60 μ m light is contributed by the hot cirrus, thus elevating the observed 60-100 μ m color temperature. Most importantly, we see that even within a single large cloud complex such as that at the north celestial pole the 100 and 12 μ m cirrus emission can be distinctly non-correlated.

D. OPTICAL CIRRUS EMISSION

In an effort to probe the small-scale structure of the hot cirrus emission, single detector scans from IRAS Pointed Observations of bright cirrus regions have been analyzed (see Appendix III). Unfortunately, it has become increasingly apparent that Fourier analysis of the $12\mu\text{m}$ cirrus using these data will ultimately be limited because of the marginal signal-to-noise in the data. Co-addition of power spectra from parallel scans provides only marginal improvement, while compromising cross-scan resolution. We will continue to explore this data set, although we do not expect the results for which we once hoped.

What has developed into a very promising alternative study of the small-scale spatial signature of the hot cirrus component is imaging at visual wavelengths. It has been known since the discovery of the interstellar cirrus that selected regions are visible on the Palomar and ESO Sky Survey plates. As discussed above, our discovery that the Lynds Bright Nebulae are the optically bright manifestation of the cirrus allows for the development of an optically-selected sample of clouds for quantitative study. Frequently, the LBN correspond to prominent, compact condensations in the $100\mu\text{m}$ emission, and when several LBN are found in close proximity, they are usually associated with the same larger infrared complex. Study of these clouds can take advantage of the sensitivity and extremely high spatial resolution available with modern 2-dimensional optical detectors, yielding information on the spatial structure down to the scale of ~ 1 arc-second. Optical surface photometry will also help probe the composition of the cirrus clouds, particularly at the small end of the grain size distribution.

Several methods of optical imaging of cirrus are being pursued, including digitization of existing photographic media such as the POSS and ESO plates, as well as wide-field CCD direct imaging at a variety of telescopes. Use of the POSS and ESO plates has required the development of techniques to calibrate point source and surface photographic photometry. We have digitized regions from many plates using the NOAO PDS scanner, and have determined the general analytic form of the point source calibration by measuring large numbers of photometric standard stars drawn from several large catalogs. Description of this calibration procedure will be published in the P.A.S.P. (Cutri, Low and Marvel 1991). Calibrated point sources have been used in conjunction with measured instrumental surface brightness profiles to construct self-consistent calibrations for surface photometry for the POSS plates, which have no sensitometer spots. This technique, which is applicable to any plate material for which point source calibrations exist, is also being prepared for publication in the P.A.S.P. (Cutri 1991).

We have made experimental deep exposures of cirrus fields using a TI-CCD at the Steward Observatory 2.3m telescope. These observations made use of the deep imaging techniques described by Guhathakurta and Tyson (1989), and have provided firm R and B-band detections of extended emission associated with 10 cirrus clouds. Figure 16 illustrates the remarkable result of approximately ~ 1 hour of R-band exposures for a cirrus field centered at $10^{\text{h}}38^{\text{m}}+83^{\circ}00'$. Spatial structure can be discerned down to 1-2 arc-seconds, and the photometric quality of the data are very good, allowing colors to be measured. Preliminary results from these observations were presented to the American Astronomical Society at their Philadelphia meeting in January 1991 (Guhathakurta *et al.* 1990). Our general program to obtain deep, multicolor images of cirrus has been granted long-term status for the 1991 observing season at Steward Observatory.

and time has been awarded to use the CTIO Schmidt telescope with the Tek 1024x1024 CCD for observations of southern cirrus sources.

REFERENCES

Cutri, R.M. 1991, *in preparation*.

Cutri, R.M., Low, F.J. and Lien, D. 1991, *in preparation*.

Cutri, R.M., Low, F.J. and Marvel, K.B. 1991, *in preparation*.

Guhathakurta, P. and Tyson, J.A. 1989, *Ap.J.*, **356**, 773.

Guhathakurta, P., Cutri, R.M., van Gorkom, J.H. and Knapp, G.R. 1990, *Bull.A.A.S.*, *in press*.

Heiles, C. 1976, *As.Ap.*, **46**, 333.

Laureijs, R.J., Chlewicki, G., Clark, F.O. and Wesselius, P.R. 1989, *As.Ap.*, **220**, 226.

Lynds, B.T. 1965, *Ap.J.Suppl.*, **105**, 163.

Paley, E.S., Low, F.J., McGraw, J.T., Cutri, R.M. and Rix, H.W. 1991, *Ap.J.*, *in press*.

Sandage, A. 1976, *A.J.*, **81**, 954.

Table 1.

**CENSUS OF HIGH GALACTIC LATITUDE SKYFLUX FIELDS
WITH 12 μ m AND/OR OPTICAL CIRRUS EMISSION**

IRAS Plate	RA	DEC	"Hot" Cirrus	Optical
1	0:00	+90	X	L
6	9:36	+75	X	L
7	12:00	+75	X	P
17	8:00	+60		L
18	9:36	+60	X	L
19	11:12	+60	X	
22	16:00	+60		L
34	8:24	+45		L
35	9:36	+45	X	
39	14:24	+45	X	
40	15:36	+45	X	
42	18:00	+45		G
47	0:00	+30	X	P
48	1:00	+30	X	
51	4:00	+30	X	L
63	16:00	+30	X	
70	23:00	+30		L
71	0:00	+15	X	L
72	1:00	+15	X	L
73	2:00	+15	X	L
74	3:00	+15	X	L
75	4:00	+15	X	
83	12:00	+15	X	
84	13:00	+15		P
87	16:00	+15	X	L
93	22:00	+15		L
94	23:00	+15		L
95	0:00	+00		P
96	1:00	+00	X	
98	3:00	+00	X	L
99	4:00	+00	X	L
100	5:00	+00	X	L
105	10:00	+00		L,P
106	11:00	+00		P
109	14:00	+00	X	
110	15:00	+00	X	
111	16:00	+00	X	L
117	22:00	+00	X	L,P
118	23:00	+00		L
119	0:00	-15		P
120	1:00	-15	X	P
121	2:00	-15	X	
122	3:00	-15	X	L
123	4:00	-15	X	L
124	5:00	-15	X	L
129	10:00	-15		L
131	12:00	-15		P

Table 1. (continued)

IRAS Plate	RA	DEC	"Hot" Cirrus	Optical
132	13:00	-15	X	
133	14:00	-15		P
134	15:00	-15	X	
135	16:00	-15		L
140	21:00	-15		L
145	2:00	-30	X	
146	3:00	-30	X	P
147	4:00	-30	X	
169	2:24	-45	X	
170	3:36	-45	X	
185	21:36	-45	X	
188	1:36	-60	X	
189	3:12	-60	X	P
201	22:24	-60	X	
202	0:00	-75	X	P

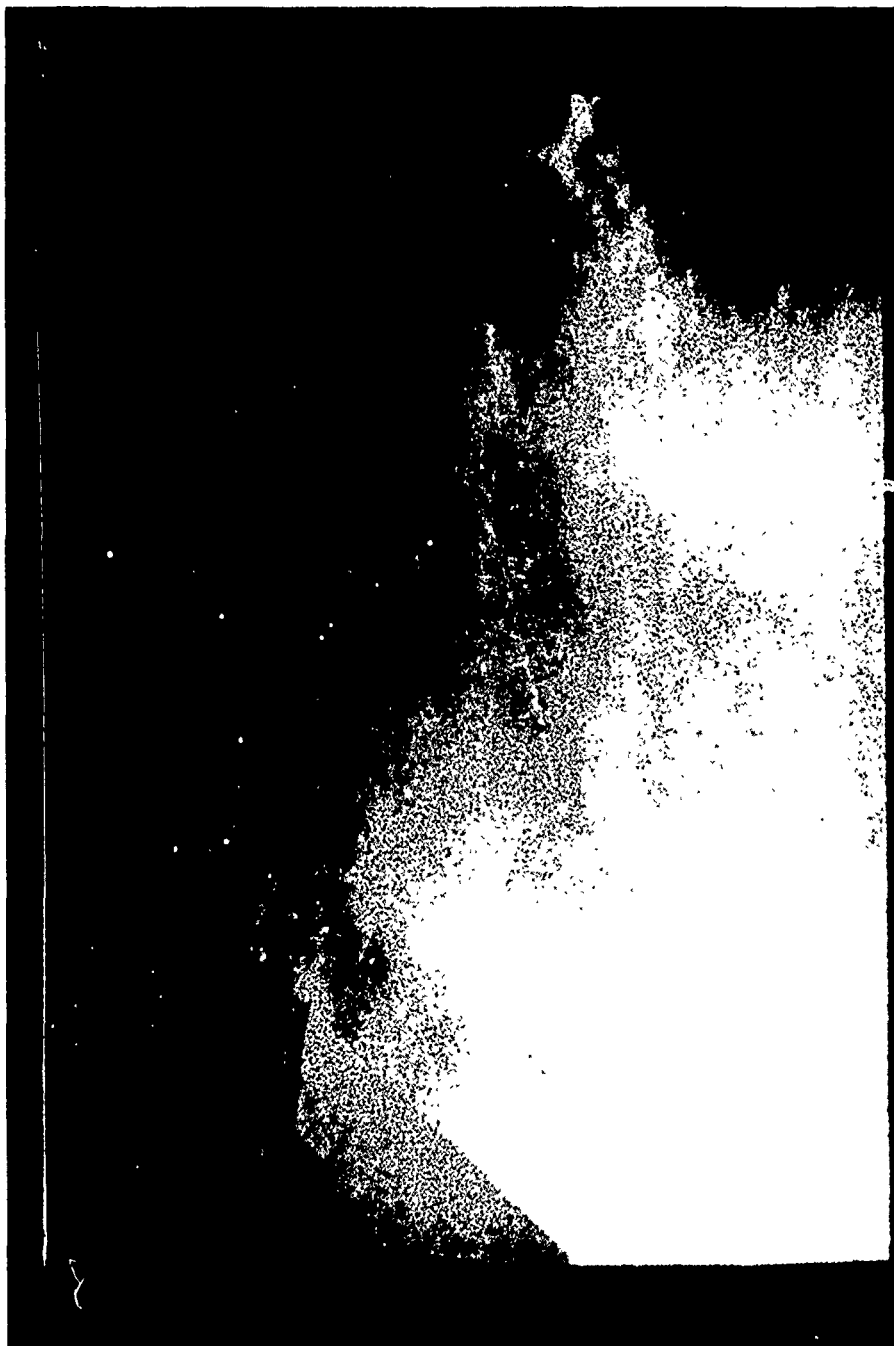


Figure 1. A mosaic of nine 100 μ m HCON 1 IRAS Skyflux maps centered on the north galactic polar region. The individual maps have been "cleaned" using the University of Arizona image-plane destriping and dewaving procedure. The mosaicing software maps each frame into the coordinate system of the central image, using a gnomonic projection and preserving radiometry of the individual frames. The background gradient is due to the broad zodiacal emission which has not been removed from this image. The diagonal cut in the upper left portion of the image corresponds to regions of bad scan overlap which were edited out of the original data.



Figure 2. A mosaic of nine 100μm HCON 1 IRAS Skyflux maps centered on the southern galactic polar region. The bright source complex at the bottom of the frame is the Large Magellanic Cloud. Again, regions of bad scan overlap in the upper right parts of the image have been edited out.



Figure 3. A mosaic of twelve 100 μ m HCON 1 IRAS Skyflux maps centered on the north celestial pole. The galactic plane is the bright feature running across the very top of the image. The cut in the upper portion of the image corresponds to regions of bad scan overlap which were edited out of the original data.

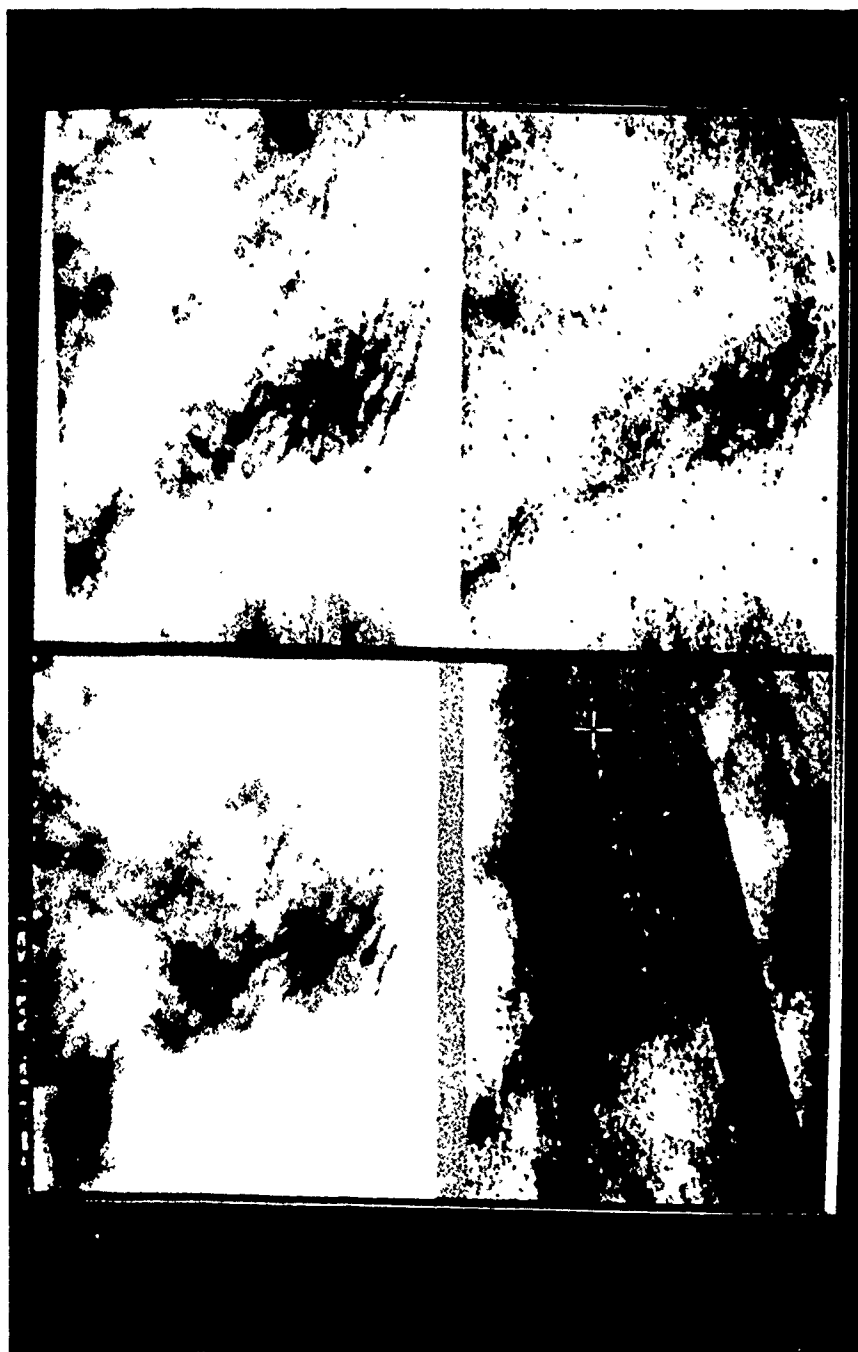


Figure 4. A montage showing the cleaned IRAS Skyflux maps of Plate 1 HCON 3, centered on the north celestial pole. Band 4 is in the upper left, band 3 in upper right, band 2 in lower left and band 1 is in the lower right. The Skyflux maps have been destriped, dewaved and have had the broad zodiacal emission removed. The diagonal cut in the 25 μ m image is a region of bad scan overlap in the raw data, and has been edited out.



Figure 5. 100μm/60μm color map for Plate 1. Full scale corresponds to a range of 0 to 50 in surface brightness ratio, blue representing smaller (warmer) values, and red the largest (coolest) values. The typical value in the blue regions is $S(100)/S(60) \sim 10-15$, corresponding to color temperatures of 23-25K.

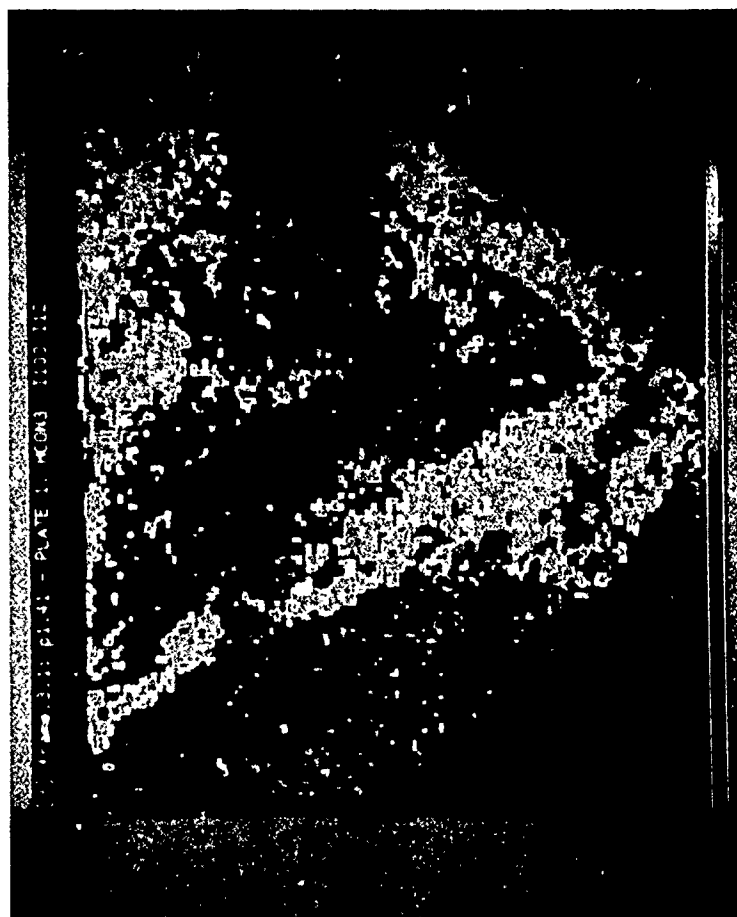


Figure 6. 100 μ m/12 μ m color map for Plate 1. Full scale in the S(100)/S(12) ratio ranges from <1 (black) to >50 (red). Notice the wide variation in the surface brightness ratio over the cloud.



Figure 7. A montage showing the cleaned IRAS Skyflux maps of Plate 6 HCON 1, centered at $9^{\text{h}}36^{\text{m}} + 75^{\circ}$. Band 4 is in the upper left, band 3 in upper right, band 2 in lower left and band 1 is in the lower right. These data have been processed as described for Figure 4. The two bright "point" sources in the upper central parts of the images are the galaxies M81 and M82. Regions of bad scan overlap have been edited out of the $12\mu\text{m}$ image.

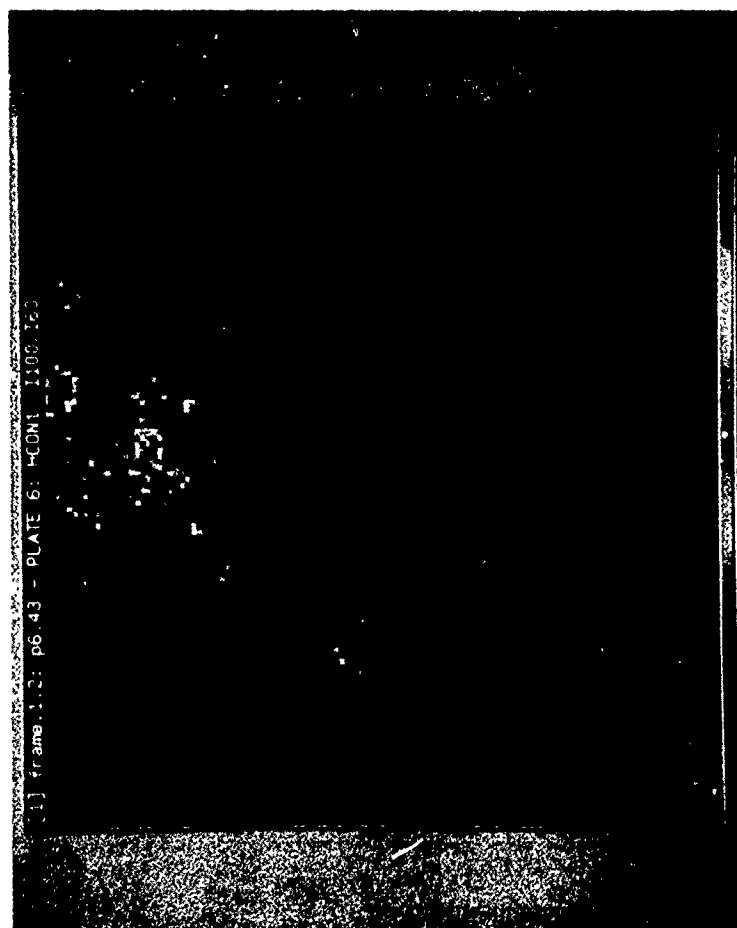


Figure 8. 100 μ m/60 μ m color map for Plate 6. The color scale is identical to that in Figure 5. The typical value in the blue regions is S(100)/S(60)~8-12, corresponding to a color temperature of 25-27K.

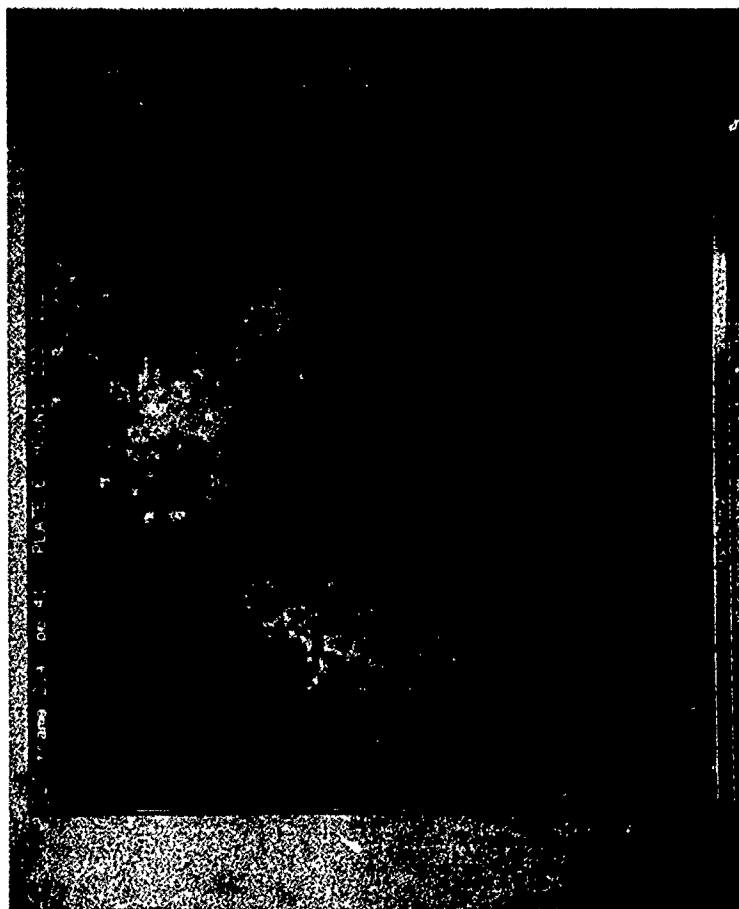


Figure 9. 100 μ m/12 μ m color map for Plate 6. The color scale is identical to that in Figure 6.

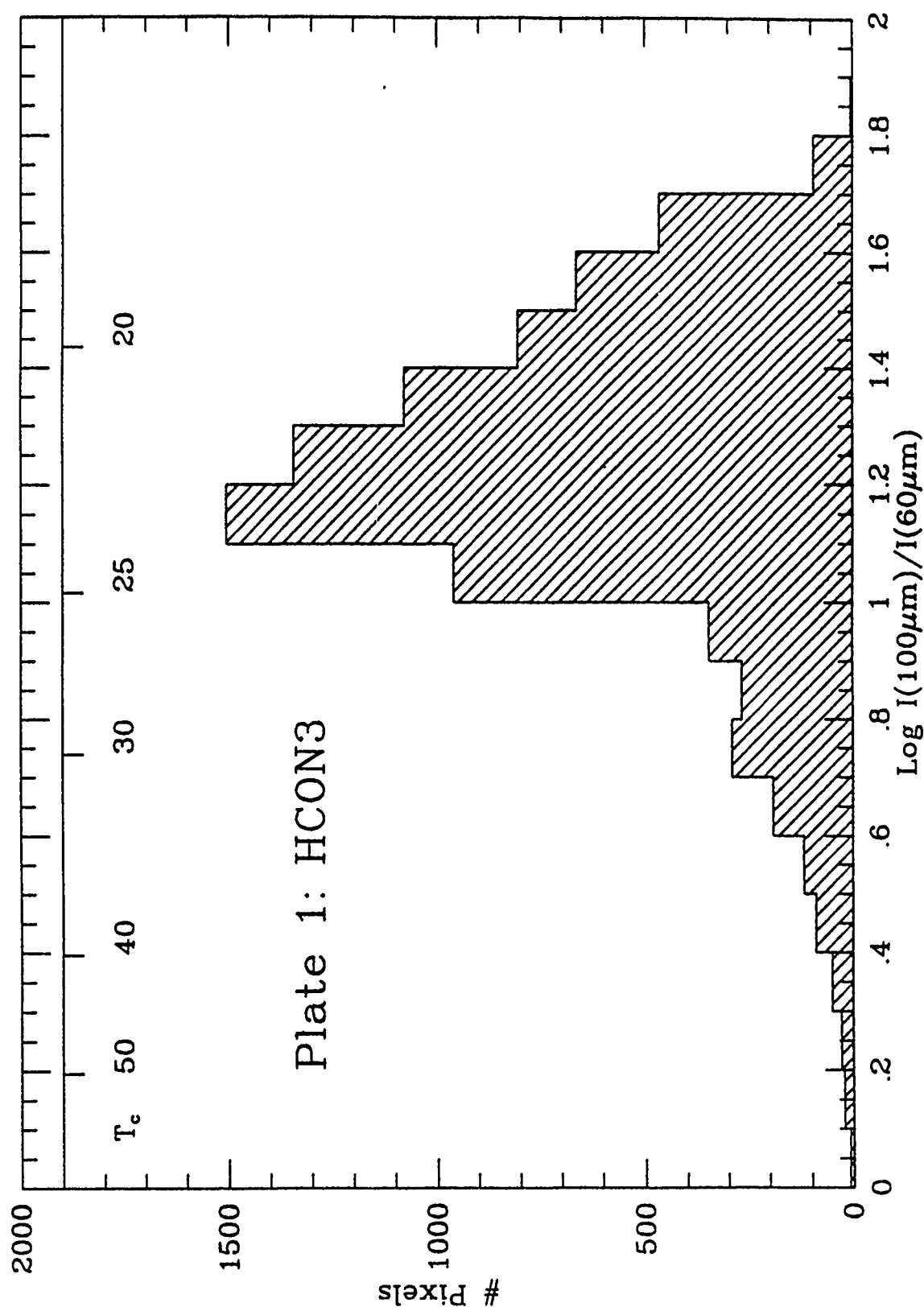


Figure 10. Histogram of the $S(100)/S(60)$ values for $8' \times 8'$ super-pixels in the cirrus cloud in Skyflux Plate 1.

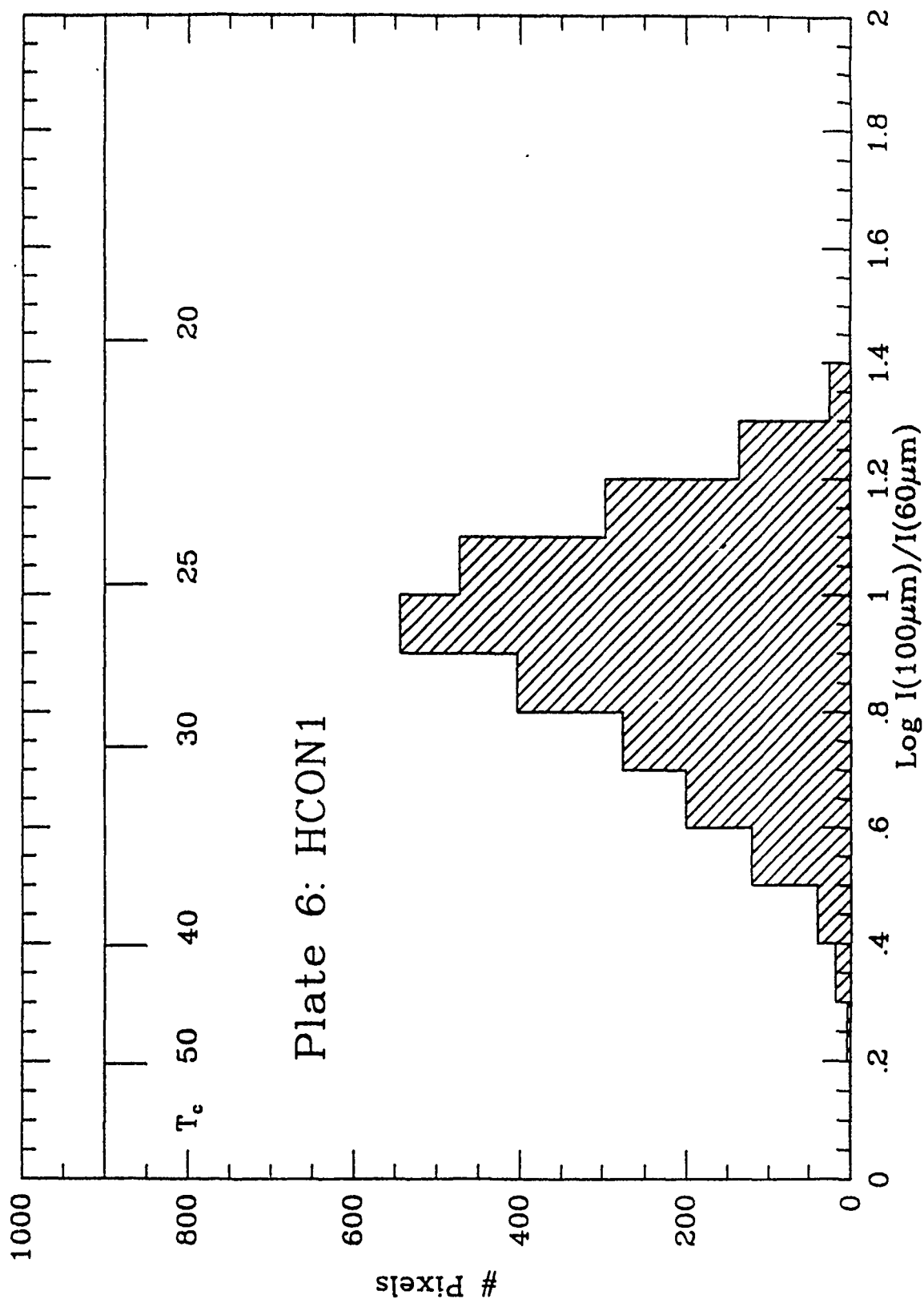


Figure 11. Histogram of the $S(100)/S(60)$ values for 8'x8' super-pixels in the cirrus cloud in Skyflux Plate 6.

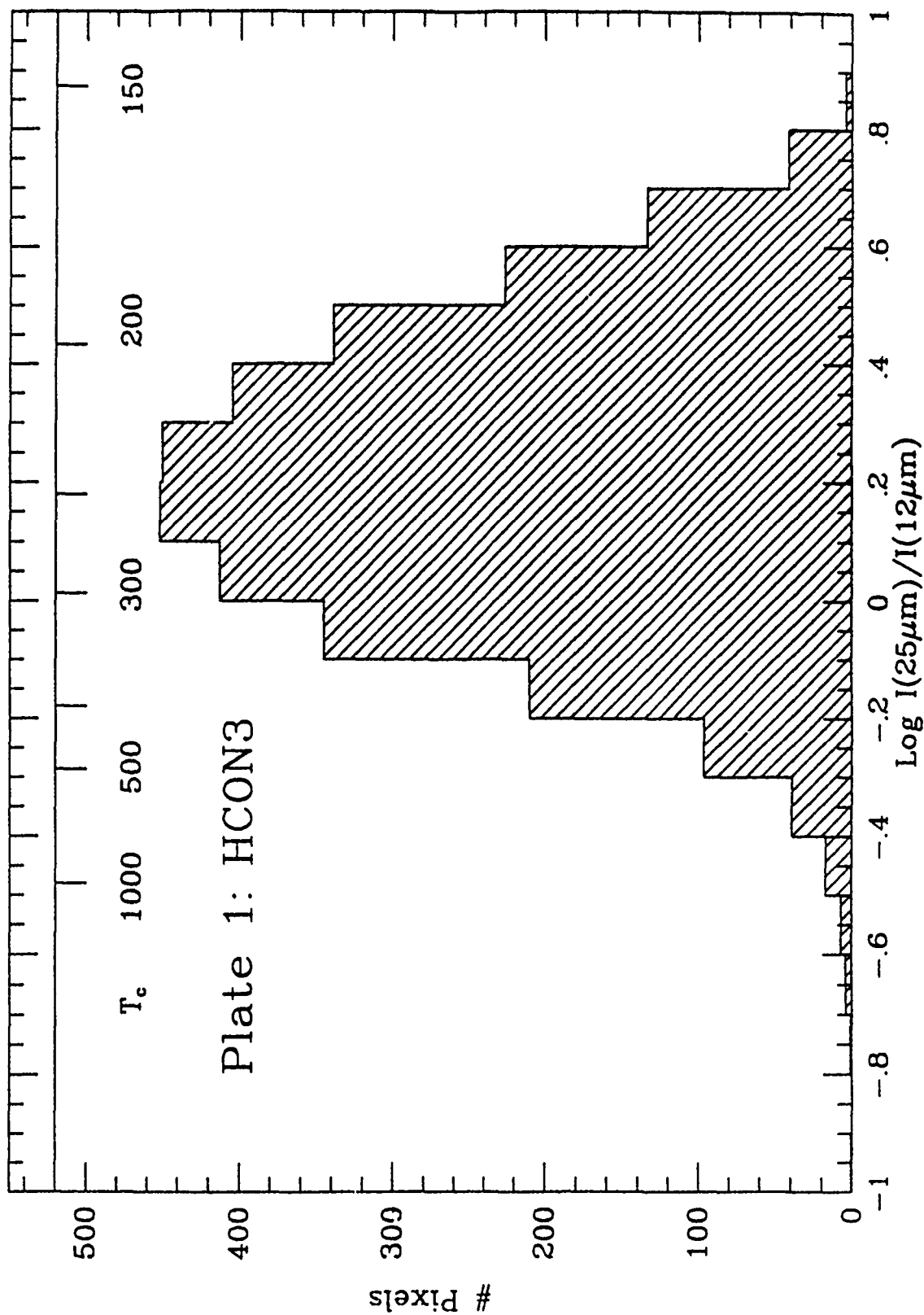


Figure 12. Histogram of the $S(25)/S(12)$ values for 8'x8' super-pixels in the cirrus cloud in Skyflux Plate 1.

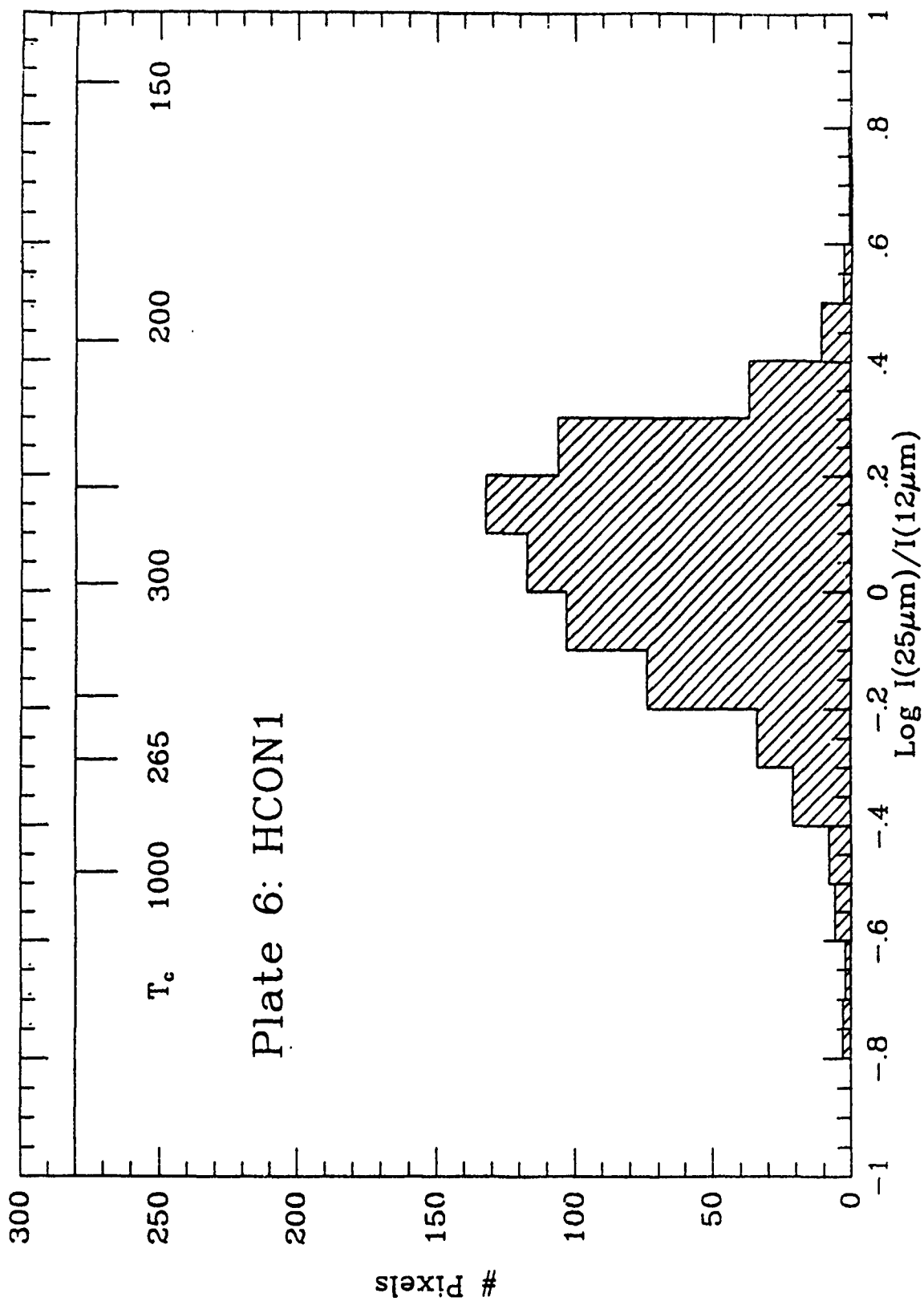


Figure 13. Histogram of the $S(25)/S(12)$ values for 8'x8' super-pixels in the cirrus cloud in Skyflap Plate 6.

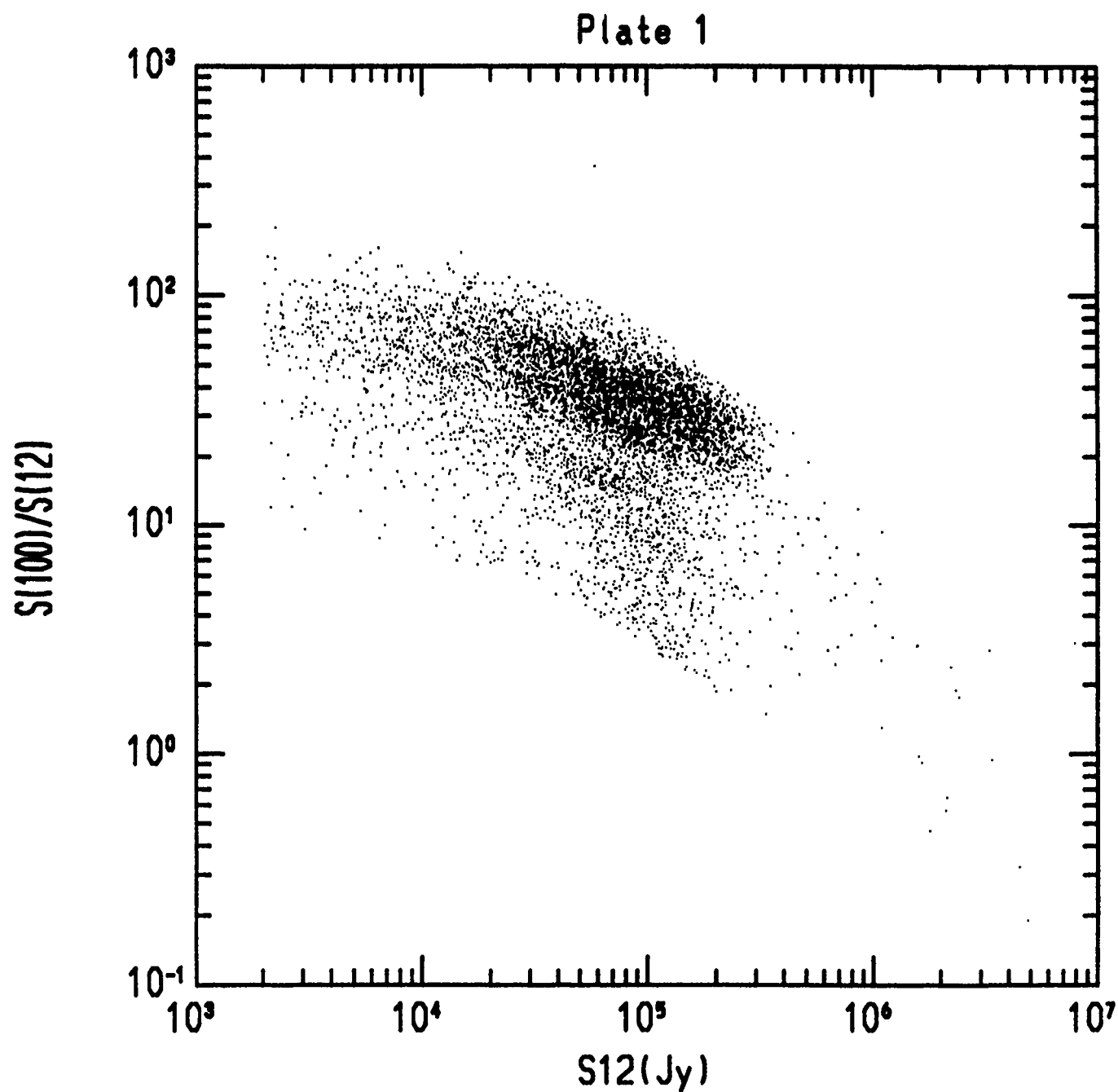


Figure 14. The ratio of the 12-to-100μm surface brightness plotted versus the 12μm surface brightness for Skyflux Plate 1.

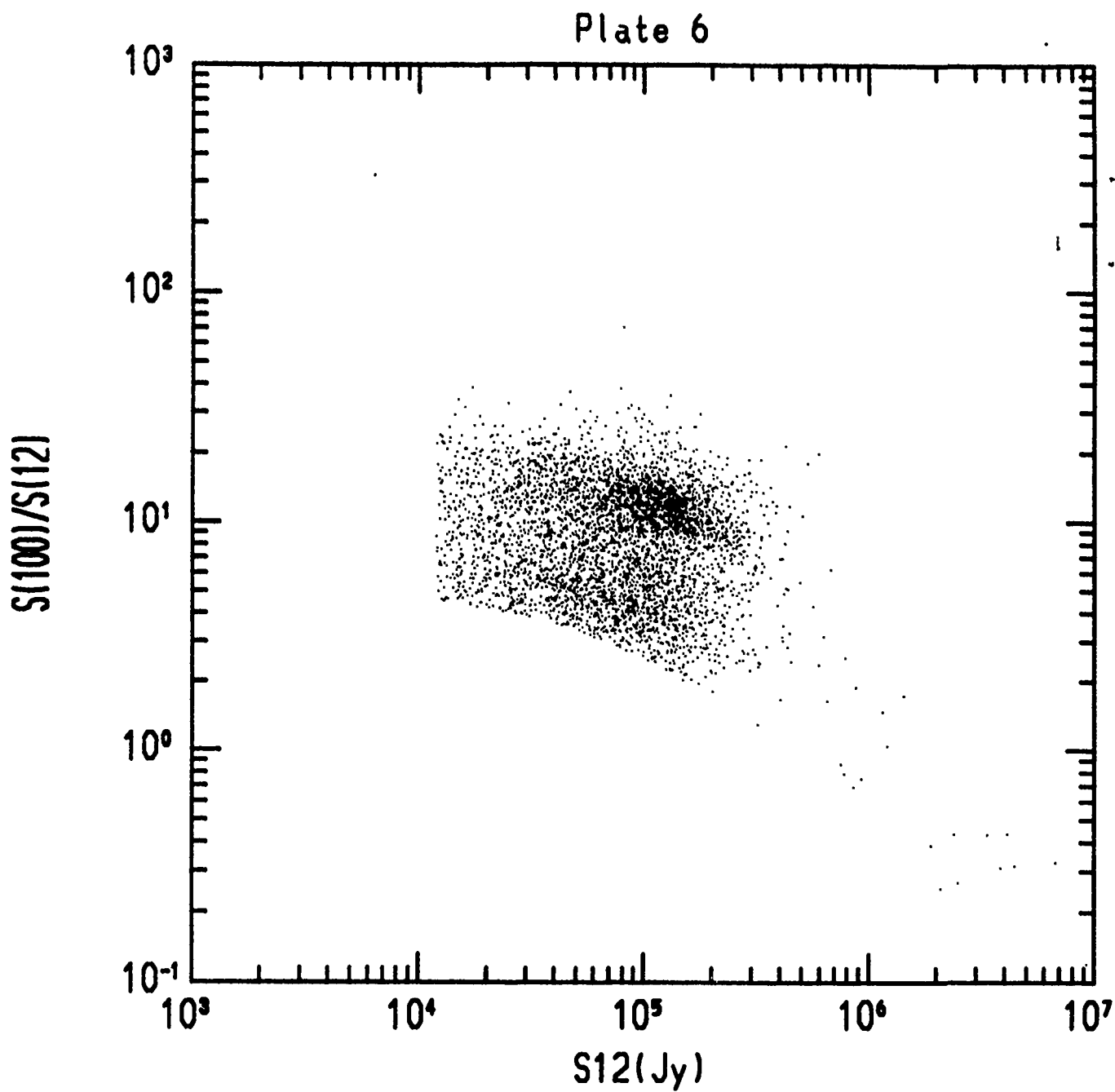


Figure 15. The ratio of the 12-to-100μm surface brightness plotted versus the 12μm surface brightness for Skyflux Plate 6.



Figure 16. A composite of 20 three-minute R-band images of an infrared cirrus complex at $10^{\text{h}}38^{\text{m}}+83^{\circ}$. This image was obtained at the Steward Observatory 90-inch telescope using a TI-CCD and focal reducer which provided a field of view of $\sim 7' \times 7'$. Structure is visible down to the scale of several arc-seconds. The faintest diffuse emission has a surface brightness of ~ 27 mag/sec².

APPENDIX II

AN INFRARED/OPTICAL INVESTIGATION OF 100 μ m "CIRRUS"

ELIZABETH S. PALEY, FRANK J. LOW, JOHN T. MCGRAW

ROC M. CUTRI AND HANS-WALTER RIX

Steward Observatory
University of Arizona

To be published in the July 2, 1991 issue of the *Astrophysical Journal*

ABSTRACT

A sample of 151 compact cirrus sources from the IRAS Point Source Catalog, having $l \geq 40^\circ$, $100 \mu\text{m}$ flux $\geq 2.5 \text{ Jy}$, and upper limit fluxes at 12, 25 and $60 \mu\text{m}$, was studied using IRAS SKYFLUX images, all available IRAS survey scans, and POSS and ESO/SRC photographic plates. Accurate infrared fluxes were obtained for 11 of the sources and 7 were detected in all four bands. Infrared colors require at least two dust components at significantly different temperatures. Ratios of $12 \mu\text{m}$ fluxes to corresponding $100 \mu\text{m}$ fluxes range from less than 0.01 to 0.07, suggesting a wide range in the amount of hot dust relative to warm dust. A simple two-temperature dust model yields a mean physical temperature of $22.5 \pm 0.3 \text{ K}$ for the warm dust and $173 \pm 8 \text{ K}$ for the hot dust. The hot dust accounts for 15 to 42% of the total IR luminosity. The narrow range of temperatures found for the warm dust suggests a single type of grain rather than a mixture. No correlations were found between the optical brightness or the optical color of the cirrus and either the brightness at $100 \mu\text{m}$ or the ratio of hot to warm dust. Nevertheless, in two isolated cloud complexes the optical and $100 \mu\text{m}$ morphology is well correlated, except in certain specific areas which are noted. This suggests a variable proportion of cold dust which, though not detected at $100 \mu\text{m}$, contributes heavily to the optical brightness in these sources.

A single compact cirrus source was studied using data from the CCD/Transit Instrument; this cloud is relatively bright and red optically but only weak emission occurs at 12 and $25 \mu\text{m}$, consistent with no apparent relationship between hot grains and either bright or red optical cirrus.

The sample of " $100 \mu\text{m}$ only" sources, from which our cirrus sample of 151 sources is drawn, contains 13 galaxies, a planetary nebula and no new types of sources.

SUBJECT HEADINGS: infrared: sources: interstellar: grains

I. INTRODUCTION

In November 1983, the Infrared Astronomical Satellite (IRAS) completed an unbiased survey of 96% of the sky at wavelength bands centered on 12, 25, 60 and 100 μm . The 100 μm emission is characterized by extended, wispy clouds denoted "infrared cirrus" for their similarity in appearance to the terrestrial clouds (Low et al., 1984). IRAS 100 μm SKYFLUX images show detail in the cirrus down to the arcminute resolution of IRAS, while arms and rings of cirrus are seen to extend over tens of degrees. The striking relationship between 100 μm images and optical images of such nebulosities (e.g. Sandage, 1976), were noted by ourselves and by others (see also de Vries, 1985 and de Vries, 1986).

Preliminary data at 100 and 12 μm indicated that many cirrus clouds are composed of mixtures of both warm ($\sim 25\text{-}30\text{ K}$) and hot ($\sim 100\text{-}1000\text{ K}$) material, with the warm component best explained as a mixture of graphite and silicate dust (Low et al., 1984); recent evidence points to extremely small grains of Quenched Carbonaceous Composite (QCC: Sakata et al., 1989), Polycyclic Aromatic Hydrocarbons (PAH: Puget et al., 1985) or Hydrogenated Amorphous Carbons (HAC: Witt and Schild, 1988) as possible candidates for the hot component.

The IRAS Point Source Catalog (PSC) contains many sources listed as detected only at 100 μm . The formal implication is that these sources are either undetected or resolved in the three shorter wavelength bands. Thus, these are nominally among the coldest objects seen by IRAS. In fact, the bulk of these sources are associated with regions of infrared cirrus, usually condensations within larger complexes.

We have begun a systematic study of the brightest high galactic latitude "100 μm only" point sources, expecting to find examples of compact, isolated regions of cirrus. If so, these sources would be ideal for study since they would not be confused with other interstellar clouds and their surrounding background levels should be more easily measured, leading to more reliable results on the intrinsic properties of individual clouds. In addition, we expected the brightest, most compact infrared sources to have the brightest optical counterparts, and we were interested in quantifying the optical to infrared properties as a means of constraining grain properties. We therefore selected a sample of the brightest "100 μm only" sources in the PSC for a systematic study of their infrared and optical properties. Our secondary objective was to explore the general properties of the sample using optical identification to locate galaxies or other types of sources that might be found.

We began our study using optical and infrared images to identify the sources and found 89% to be cirrus. We then used one and two-dimensional IRAS coadded data (ADDSCANS and COADDS, respectively), made available by the Infrared Processing and Analysis Center (IPAC), to obtain higher quality flux measurements for representative sub-samples at all four wavelength bands. The photographic appearance of these sources suggest a complex relationship between their IR and optical properties. Lastly, we used optical data made available from the CCD/Transit Instrument (CTI) on Kitt Peak to measure optical colors for one cirrus cloud identified on the IRAS SKYFLUX images.

II. THE 100 μ m SAMPLE

While cirrus clouds are generally not point sources, the IRAS Point Source Catalog contains many cirrus sources because tight condensations within clouds fit the IRAS 100 μ m point source template well enough to pass the rather lenient criteria used to reject extended sources. At 60, 25 and 12 μ m, these sources are generally resolved or undetected, thus the cirrus sources were passed into the catalog as "100 μ m only point sources", even though most are not true point sources and most are bright at 60 μ m.

Our sample was constructed by searching the IRAS PSC for all sources having high quality detections at 100 μ m, with $F_{100} \geq 2.5$ Jy, and only upper limit fluxes at 12, 25 and 60 μ m (see Explanatory Supplement, 1984). Because of our interest in isolated clouds, we limited our sample to sources having $|b| \geq 40^\circ$. The resulting sample contained 170 sources: 128 at southern Galactic latitudes, and 42 at northern latitudes. Optical identification with Palomar Observatory Sky Survey (POSS) and European Southern Observatory (ESO/SRC) red and blue photographic plates and infrared identification with IRAS SKYFLUX images yielded the census given in Table 1. First, we make note that, based on this census, there are three times more compact cirrus sources at southern galactic latitudes than at northern latitudes; we regard this as due to the "local" distribution of interstellar material. Second, a cursory examination of the 13 galaxies in this sample show them to be similar to the coolest members of a flux limited sample of galaxies studied by Smith et al. (1987). The colors of the planetary nebula (PK 318+41.1) are consistent with the colder colors in a sample of IRAS planetary nebulae studied by Pottasch et al. (1984). Thus, we conclude that, despite their nominally very cold temperatures, this poorly studied subset of the PSC contains few, if any, fundamentally new types of objects.

On the 100 μ m SKYFLUX images, all of the cirrus sources in our sample appear as tight knots within larger cirrus features; generally, these sources can be seen as fainter and more diffuse, but still distinct, condensations at 60 μ m. Rarely was a source found on the SKYFLUX images at 12 or 25 μ m. While the 100 μ m cirrus clouds range in size from roughly half a degree to tens of degrees in diameter, the 100 μ m "point sources" range from 4 to 10 arcminutes, barely consistent with the 3 x 5 arcmin size of the IRAS detectors. The SKYFLUX images showed only two of the cirrus sources to be within truly isolated clouds, (IRAS 02356-2959 and IRAS 23446-7202).

III. INFRARED MEASUREMENTS

a) INFRARED FLUXES FROM ADDSCANS

We examined 29 of the cirrus sources in greater detail using IRAS one-dimensional coadded data (ADDSCANS). These sources were selected on the basis of 100 μ m PSC flux (the ten brightest sources at northern and southern Galactic latitudes each) and for different representative combinations of optical vs. infrared appearance (based on relative surface brightnesses on the POSS and/or ESO/SRC photographic plates and the IRAS SKYFLUX images).

In order to justify our choice of background levels on the ADDSCANS, we compared the scans to in-scan direction slices through the sources on the SKYFLUX images, generally giving us longer baselines to examine than those covered by the ADDSCANS. All but one of the ADDSCAN sources were found to have adequate baselines for flux measurements. Measurements of 12, 25, 60 and 100 μm fluxes for the remaining 28 ADDSCAN sources along with qualitative assessments of the brightness of the optical component of the cirrus as it appears on the POSS and ESO/SRC plates are given in Table 2. Few of the sources have measurable ADDSCAN fluxes at 12 or 25 μm ; upper limits for those sources without 12 or 25 μm detections, derived from noise levels, are generally well below flux levels for sources having measurable fluxes in these bands.

b) INFRARED FLUXES FROM SURVEY COADDs

In addition to the PSC and ADDSCANS, flux information is available from two-dimensional coadded data, the survey COADDs. These data are more accurate than the ADDSCAN data because they retain 2-D information and permit a careful selection of "on source" pixels. Selecting 8 of the brightest and 2 of the faintest 100 μm ADDSCAN sources, we measured integrated fluxes directly from coadded images provided by IPAC; the integration region was the same in all four bands. In order to derive accurate spectral energy distributions from the raw COADD measurements, the fluxes must be color-corrected to account for the wide IRAS bandwidths (see Explanatory Supplement). There are potentially small systematic errors in the color corrections because the color-correction procedure assumes smooth spectra and this may not be valid, especially at 12 and 25 μm . Table 3 lists the resulting flux densities, after color correction; for comparison, the corresponding 100 μm PSC fluxes are included but without color-corrections.

COADD errors were calculated from "sky" variance, assuming a comparable error "on source." COADD measurements show the PSC to have systematically underestimated 100 μm fluxes by as much as 300%! This means that our source selection was based on highly imperfect fluxes. However, our sample does contain an appreciable number of discrete cirrus clouds for which useful measurements were obtained.

Comparison shows acceptable agreement between COADD and ADDSCAN measurements at 100 μm , but there are large differences at 12, 25 or 60 μm . Because the sources are so faint at the shorter wavelengths and because defining accurate baselines within extended clouds is difficult, the definition of baselines is expected to differ between ADDSCANS and COADDs. However, the 2-D COADDs produce more internally consistent results: the 12 and 25 μm COADD fluxes vary widely with respect to 100 μm COADD measurements, as is the case for ADDSCAN results. Fortunately, the 60/100 μm COADD ratios are remarkably consistent. We therefore conclude that the COADDs are considerably more reliable than either the PSC or ADDSCANS for flux measurements, at all wavelengths.

IV. AN OPTICAL STUDY OF CIRRUS

a) PHOTOGRAPHIC PLATES

In a visual inspection of the POSS and ESO/SRC photographic plates, 119 of the 151 cirrus clouds in our original sample were visible on either one or both of the red or blue plates. Our sources appear on these photographs as diffuse, faint nebulosities that are generally visible over diameters 10-20 arcminutes. According to their visual appearance on the plates, the 29 ADDSCAN sources have been characterized in Table 2 as follows: cirrus not apparent (--), faint cirrus (F), moderate cirrus (M), or bright cirrus (B). To characterize the optical colors we noted (::) the level of contrast between the red and blue plates for the brighter sources.

Two of the COADD sources are especially well isolated and optically bright and are, therefore, good candidates for optical study, IRAS 02356-2959 and IRAS 23446-7202. 100 μ m contour plots (COADD image) and enhanced digitized images of the blue ESO/SRC photographic plates are shown for each source in Figures 1 and 2. As can be seen, these two fields contain pairs of isolated clouds whose optical morphologies correspond very well to the infrared. IRAS 02356-2959, the lower right lobe in Figure 1, is located in Fornax. It is associated with a molecular cloud studied by Keto and Myers (1986), who place it at a distance on the order of 100 pc. The entire cloud extends over a $\sim 1^\circ \times 1^\circ$ region in Figure 1, yielding a value of about 1 pc for the cloud radius. The upper left lobe in Figure 1 is IRAS 02365-2950. The morphology is similar to that of IRAS 02356-2959, but it fails to meet our minimum flux criterion. The upper right lobe in Figure 2 is IRAS 23446-7202. The lower left lobe, at $\alpha = 23^h 48^m 58^s$, $\delta = -72^\circ 20' 34''$, does not correspond to any source listed in the PSC.

The four bright regions in Figures 1 and 2 are prime examples of cirrus where the scattered interstellar light appears to be produced by the same grains that reradiate the absorbed component at 100 μ m. It must be noted, however, that there are weaker 100 μ m features in both fields which are not so well associated with optical features. To the south of the left lobe in Figure 1, there are two well defined 100 μ m maxima lacking optical counterparts. In Figure 2, we note the prominent ridge of 100 μ m emission protruding to the south of the northwestern source, which falls just to the east of the similar optical feature. We believe that these apparent variations in the optical to infrared brightness are real and represent localized variations in the composition of the clouds.

Despite the fact that many cirrus clouds have nearly identical optical and infrared morphologies, we found no apparent correlation between optical brightness on the photographic plates and infrared flux densities as measured from the survey COADD data. Cases in which multiple infrared sources lay on the same photographic plate demonstrated a wide variation in the optical to infrared surface brightness of the cirrus. Unable to satisfactorily calibrate the photographic plates and thus unable to quantify this statement, we turned to the CCD/Transit Instrument (CTI) to obtain optical colors for cirrus.

b) OPTICAL COLORS OF CIRRUS USING CTI

The CCD/Transit Instrument is a 1.8m, f/2.2 telescope on Kitt Peak, fixed at $+28^\circ$ declination. Its two charge-coupled devices (CCDs) operate in time-delay and integrate mode (TDI), with a total integration time of about one minute as the image of an object transits the

focal plane of the detector. The CTI data strip is 8.26 arcminutes wide, thus, in a year the instrument covers almost 44 square degrees of sky. While a V filter is used in front of one of the detectors every night, use of B, R and I filters on the second CCD varies, depending on sky brightness (McGraw et al., 1986). The virtues of using CTI to study cirrus include: the unbiased nature of the CTI strip, the availability of multiple nights of data, and the opportunity to look for optical cirrus that may (or may not) correspond to infrared features.

None of the PSC-selected cirrus sources in our sample lie in the CTI strip. We therefore selected regions for study by finding areas on the 100 μ m SKYFLUX images within the CTI strip that showed the greatest contrast at cirrus cloud edges. Such regions should be easier to pick out in the optical images than regions having bright cirrus but relatively constant surface brightness.

We chose to concentrate on the region $\alpha = 23^h 33^m$ to $\alpha = 23^h 42^m$ (1987.5) because of the number of nights of good data available. The CTI pixel data at B, V and R revealed a bright optical cirrus source near $\alpha = 23^h 36^m$. This region corresponds to an area of heavy cirrus on the IRAS 100 μ m SKYFLUX image. Moreover, comparison with a POSS plate showed this source to lie in a region of heavy optical cirrus, although the CTI feature does not stand out as especially bright or condensed. From the POSS plates, we find this cloud lies near, although not within, two Lynds Bright Nebulae (see Lynds, 1963).

We converted the CTI pixel data covering $\alpha = 23^h 35^m 00^s$ to $\alpha = 23^h 36^m 15^s$ into IRAF images for four nights of V data and two nights each of B and R data. A linear fit to the background of each file was then subtracted from the data to account for low frequency background trends such as moon brightness, terrestrial cirrus, and atmospheric variations. The individual images were then coadded and median filtered with a 45 x 45 pixel box to smooth the images and remove stars. The zero-level background was determined two ways using the unfiltered coadded data. First, we used the pixel value found most often over the entire image, which covered ~ 155 square arcminutes (B1, V1 and R1); second, we used the average of the three most frequently found pixel values in three different regions of "sky" (or minimum cirrus) near the cloud, covering a total of ~ 28 square arcminutes (B2, V2 and R2). The images were then cropped from $\alpha = 23^h 35^m 42.5^s$ to $\alpha = 23^h 36^m 05.9^s$ and $\delta = 27^\circ 57' 24.2''$ to $\delta = 28^\circ 00' 27.5''$ (1987.5).

We chose five regions within the CTI cloud to compare, shown, for illustration purposes, over the CTI coadded R pixel data in Figure 3. The mean and standard deviation of B, V and R magnitudes within each region are listed in Table 4, along with infrared measurements obtained from survey COADD data. Optical magnitudes are ~ 25 mag arcsec $^{-2}$, near the level of gross fog on the POSS plates. The optical colors appear red (B-V ~ 0.85 mag arcsec $^{-2}$, V-R ~ 0.54 mag arcsec $^{-2}$) and relatively constant over the cloud. The two methods for determining CTI background levels resulted in magnitude differences of about 0.2 mag arcsec $^{-2}$.

IRAS COADD images reveal a star in the CTI cloud at 12 μ m. Figure 4 shows the infrared and optical spectrum for this region. The CTI source is fainter than any of the COADD sources, with $F_{100} = 2.49 \pm 0.26$ Jy.

V. DISCUSSION

Because COADD data provide the most accurate method for obtaining flux densities for the cirrus sources, this discussion is based on COADD results.

Figure 5 shows F_ν vs. λ for the eleven COADD sources, as well as the CTI source; 12, 25 and 60 μm fluxes are normalized to the 100 μm fluxes. From this figure, we see evidence that cirrus is composed of at least one hot and one warm component and the amount of hot dust relative to the warm dust varies widely within this sample.

Assuming the cirrus is composed of hot and warm dust components, we used a simple two-temperature blackbody model to obtain estimates for the physical dust temperatures and for their luminosities. Emissivities of $\lambda^{-1.5}$ were used for both the warm and hot components, realizing that such approximations are at best quite crude. Temperatures are listed in Table 5 for the 60/100 μm color temperatures, the 12/25 μm hot dust temperatures, and the 60/100 μm warm dust temperatures. The average warm dust temperature is 22.5 ± 0.3 K and increases to only 22.8 ± 0.3 K if the four sources with no detectable hot dust are removed from the average. The average hot dust temperature in these clouds is 173 ± 8 K (if the anomalously hot source noted below, IRAS 00373+0947, is deleted from this average the result becomes 167 ± 2 K). Thus, when the contribution from hot grains is subtracted from the 60 μm emission there is no measurable variation in temperature of the warm dust component within this sample!

The 12 and 25 μm emission varies from cloud to cloud indicating a variation in the amount of hot dust relative to the more universal warm dust. From the ratio $F(12)/F(100)$ for the 11 sources in Table 3 we see almost an order of magnitude range in the amount of hot dust emission relative to the warm dust, just within this small sample. A better indicator of the relative amounts of hot and warm dust is the ratio of luminosities derived from our simple model. These results are listed in Table 4, where it is seen that the percentage of total IR luminosity emitted by the hot dust varies from 42% to less than 15%. This result is consistent with the work of Heiles et al. (1988).

To explain anomalously high 3.8 μm emission in some reflection nebulae, Sellgren (1984) applied a transient heating mechanism previously discussed by Duley (1973a,b), Greenberg and Hong (1974) and Purcell (1976). Upon absorption of energetic photons in the interstellar radiation field small grains can suffer large temperature transients, rising briefly to temperatures significantly above their equilibrium values. Grains made up of roughly 70-90 molecules, having sizes of ~ 9 Å (silicates) and ~ 6 Å (graphites), may account for grain temperature fluctuations of as much as 1000 K (Sellgren, 1984). The presence of a population of small, hot grains in addition to large, warm grains can explain the infrared emission of the cirrus sources. Based on spectral features and sublimation temperatures, other suggestions for the composition of these very small grains include PAH or QCC; both have similar spectral features. QCC has a single absorbance peak at 3.29 μm that matches exactly an unidentified infrared feature (UIR); most PAHs have multiple absorption peaks near 3.29 μm (Sakata et al., 1989). Most notably, however, both PAH and QCC have a strong emission feature near 11.3 μm . The ratios of cirrus emission at 12 to 100 μm and, to a lesser extent, at 25 μm to 100 μm , would depend on the relative abundance of small grains in each cirrus cloud and the details of the spectral energy distribution should depend on the composition.

We make note of the fact that one of the seven sources shown in Figure 5, IRAS 00373+0947, shows an apparent deep flux minimum at 25 μm . While there is only one such exceptionally hot source in the COADD sample, it may be indicative of a further compositional difference in the cirrus and clearly merits further study.

The shape of the CTI spectrum in Figure 5 follows the same pattern as the COADD cirrus sources, although the 60/100 μm color temperature of the CTI cirrus cloud is 5 K lower than the average color temperature of the infrared selected sample. Because of the difficulty in determining the baseline surrounding this relatively weak source we attribute this rather large discrepancy as measurement error. Comparing this source to the COADD cirrus sources at the shorter infrared wavelengths, there does not appear to be a high concentration of transiently heated grains, yet the source is bright and red optically. Guhathakurta and Tyson (1989) have also found red optical colors for four cirrus clouds, and have eliminated H-alpha emission as the cause.

Warm dust grains, at a physical temperature of ~ 22.5 K, radiate most of the energy detected by IRAS shortward of 120 μm , even in clouds with relatively large quantities of hot, presumably transiently heated, grains. The only evidence for a cold dust component is indirect; we find a significant range in the amount of scattered light observed at 0.5 μm relative to the 100 μm brightness, both within cloud complexes and from cloud to cloud. Thus, it seems possible that a third type of grain, which scatters and radiates efficiently and, therefore, is too cold to be detected by IRAS, may strongly influence the optical brightness of cirrus. A candidate for these < 15 K grains would be ice clad particles, or icy-mantels, once thought to be a major constituent of interstellar dust clouds.

In order to confirm our strong impression of large variations in the optical to 100 μm brightness of cirrus we have initiated a study of an optically selected sample of cirrus clouds, based on the list of Lynds Bright Nebulae (Lynds 1963). If our hypothesis is correct, this sample should show a larger range of optical to 100 μm brightness and the temperatures of these clouds should also be colder than those of our IR selected sample.

Low et al. (1984) and others explained the warm dust discovered by IRAS as a mixture of graphite and silicates with the observed differences in 60/100 μm color temperature produced simply by variations in the relative abundances of these two materials from cloud to cloud. The range of 60/100 μm color temperatures listed in Table 5 are typical of cirrus found by IRAS. Here we postulate that the hot grains may contribute significantly to the 60 μm emission (Herter et al., 1990) of specific clouds, and find that after taking this effect into account the temperature of the warm grains, as measured by the ratio of corrected 60 μm flux to 100 μm flux, is nearly constant from cloud to cloud to within measurement errors. This suggests to us that only a single type of warm dust particle, with a radiative equilibrium temperature of 22.5 K, is responsible for the bulk of the observed luminosity in these clouds. The idea of a universal mixing ratio for graphite and silicate particles, needed to account for the nearly constant warm dust temperature in these clouds, is difficult to reconcile with the stellar origins of these materials. However, our sample is small and selected in a specific way; it is important to study a larger variety of clouds to determine if this suggestion of a single type of warm dust particle applies to cirrus in general or is limited to condensations such as those in our sample.

With the exception of one significantly hotter cloud, IRAS 00373+0947, we find a small marginally significant range in 12/25 μm color temperatures for the hot dust particles in our sample, 163 to 173 K. This is easily explained by modest composition and/or grain size

variations. By comparing the luminosities of the hot and warm dust in each cloud we obtain an indication of the relative abundance of the two types of material, subject, of course, to more detailed modeling of the response of the two types of particles in the interstellar radiation field.

Our optical observations show both a range in optical brightness relative to 100 μm emission and a variation in color from blue to red. Presumably the blue light is produced by scattering of the interstellar radiation field by small particles. The red excess might be caused by the transiently heated hot particles. Because neutral PAHs are observed to show red luminescence (Allamandola et al., 1987), and similarities with red excesses in reflection nebulae studied by Witt and Schild (1988) may indicate the presence of Hydrogenated Amorphous Carbons (HAC), one might expect a correlation between the proportion of hot grains in a cirrus cloud and strong emission in the R band. Our observations do not support this hypothesis. Nor do we find correlation between the blue colors in the optical and the 12 μm /100 μm flux ratio, as would be expected if the smallest particles were strongly scattering the blue light.

ACKNOWLEDGEMENTS

The authors wish to thank Roseanne Hernandez and others at IPAC who made ADDSCAN and COADD data available on short notice, and Tom Hess for assistance with CTI software. This paper was improved as the result of helpful comments from Terry Herter, who served as referee.

The Infrared Astronomical Satellite was developed and operated by the Netherlands Agency for Aerospace Programs (NIVR), the US National Aeronautics and Space Administration (NASA) and the UK Science and Engineering Research Council (SERC). Use of POSS and ESO/SRC photographic plates was made possible by Kitt Peak National Observatory. This research was supported by NASA and by AFGRL.

This work utilized data from the CCD/Transit Instrument (CTI) which is supported by NSF Grant AST-8800298 and NASA Grant NAGW-804.

Table 1: Properties of 100 μ m Source Sample

Total number of 100 μ m sources	33157
Number of sources in sample	170
$b > +40^\circ$	42
$b < -40^\circ$	128
Number of cirrus sources	151
galaxies	13
sources in SMC	4
planetary nebulae	1
planets (Saturn)	1

Table 2: Peak ADDSCAN Flux Densities (Jy), Not Color-Corrected, and Optical Description for 28 Cirrus Sources

IRAS Name	F(100)	F(60)	F(25)	F(12)	Red ^a	Blue ^a
00154+0914	12.3±0.7	1.19±0.08	≤0.11	≤0.06	—	—
00269+1030	8.7±0.4	0.77±0.05	0.25±0.05	0.14±0.03	B	B
00371+0946	6.4±0.7	0.29±0.05	≤0.10	≤0.09	F	F
00373+0947	13.9±0.6	1.05±0.05	≤0.14	≤0.03	F	F
01044-0635	5.6±0.5	0.77±0.07	≤0.12	≤0.09	F	F
01268+1708	5.5±0.5	0.42±0.06	≤0.09	≤0.06	M	M
01554+1042	6.9±0.3	0.31±0.03	≤0.09	≤0.04	B::	B
02309+0839	6.1±0.3	0.95±0.05	≤0.07	≤0.04	M	M::
02318+1139	6.1±0.6	0.66±0.07	≤0.08	≤0.06	F	F::
02356-2959	7.9±0.2	0.88±0.09	0.14±0.03	0.10±0.03	B	B::
02387+1003	8.9±1.0	0.62±0.12	≤0.06	≤0.03	F	F::
03001+0841	4.0±0.2	0.62±0.05	0.15±0.04	≤0.05	M	M
03043+0812	4.5±0.5	0.32±0.05	≤0.07	≤0.03	M	M
03074+0744	6.1±0.9	0.50±0.08	≤0.09	≤0.06	—	—
03077+0814	5.3±0.6	0.48±0.09	≤0.09	≤0.07	—	—
03084+0827	13.5±0.5	1.56±0.09	0.36±0.05	0.16±0.04	—	—
09289+6621	4.1±0.4	0.22±0.02	≤0.03	≤0.03	B::	B
09302+6624	6.1±0.6	0.28±0.04	≤0.02	≤0.03	B::	B
09312+6551	3.6±0.4	0.33±0.04	≤0.05	≤0.04	B::	B
10373+7336	5.7±0.6	0.80±0.07	≤0.06	≤0.08	B::	B
11266-0420	4.8±0.5	0.56±0.06	≤0.07	≤0.06	F	F::
11467-0814	5.6±0.6	0.56±0.07	≤0.11	≤0.07	F	F
11573-1024	4.2±0.5	0.47±0.07	≤0.10	≤0.10	F	—
13528-1518	7.7±0.8	0.60±0.06	≤0.10	≤0.06	—	—
15547+0534	4.6±0.5	0.62±0.07	≤0.07	≤0.05	B	B
21191-3157	8.7±0.4	0.95±0.05	≤0.07	≤0.04	M	M
23410+0839	11.3±0.7	1.11±0.09	0.40±0.07	0.18±0.04	B::	B
23446-7202	11.2±0.3	1.08±0.04	0.23±0.06	0.15±0.03	B	B::

^a Key to optical descriptions:

— = Cirrus not apparent

F = Faint cirrus

M = Moderate cirrus

B = Bright cirrus

:: = Contrast is greater on this plate

Table 3: Color-Corrected Cirrus Flux Densities (Jy) from 2D Survey Coadd Data

IRAS Name	PSC(100)*	F(100)	F(60)	F(25)	F(12)
00154+0914	3.7	13.1 \pm 1.3	2.11 \pm 0.26	1.23 \pm 0.21	0.73 \pm 0.07
00269+1030	3.1	9.6 \pm 1.0	1.75 \pm 0.18	1.06 \pm 0.49	0.66 \pm 0.19
00373+0947	4.9	15.9 \pm 1.6	1.80 \pm 0.20	0.33 \pm 0.03	0.45 \pm 0.09
02356-2959	2.5	6.0 \pm 0.6	0.87 \pm 0.10	0.26 \pm 0.07	\leq 0.13
03001+0841	2.6	4.0 \pm 0.4	0.58 \pm 0.06	\leq 0.20	\leq 0.09
03074+0744	4.1	10.7 \pm 1.1	1.71 \pm 0.20	0.70 \pm 0.24	0.40 \pm 0.04
03084+0827	3.0	13.2 \pm 1.3	2.53 \pm 0.29	0.76 \pm 0.42	0.52 \pm 0.15
09312+6551	3.1	5.9 \pm 0.6	0.60 \pm 0.07	0.23 \pm 0.04	\leq 0.08
21191-3157	3.8	9.2 \pm 0.9	1.51 \pm 0.17	0.70 \pm 0.32	0.40 \pm 0.05
23410+0839	4.8	11.9 \pm 1.2	1.72 \pm 0.19	0.60 \pm 0.06	0.43 \pm 0.12
23446-7202	3.1	8.4 \pm 0.8	1.22 \pm 0.14	0.20 \pm 0.02	\leq 0.15

* – PSC 100 μ m flux density, without color correction.

Table 4a: Optical Surface Brightness Data for CTI Cirrus Source (mag arcsec⁻²)

Color	Region A	Region B	Region C	Region D	Region E
B1	25.51±0.10	25.56±0.09	25.36±0.07	25.48±0.10	25.54±0.05
V1	24.70±0.12	24.78±0.10	24.81±0.11	24.91±0.07	24.90±0.03
R1	24.01±0.08	24.06±0.08	24.03±0.05	24.19±0.07	24.22±0.03
B2	25.65±0.11	25.72±0.09	25.50±0.08	25.63±0.11	25.69±0.05
V2	24.53±0.10	24.60±0.08	24.62±0.09	24.70±0.06	24.69±0.03
R2	24.15±0.09	24.22±0.09	24.18±0.06	24.36±0.08	24.40±0.04
[B1-V1]	0.81±0.16	0.78±0.13	0.65±0.13	0.57±0.12	0.64±0.06
[V1-R1]	0.69±0.14	0.72±0.13	0.78±0.12	0.72±0.10	0.68±0.04
[B2-V2]	1.12±0.15	1.12±0.12	0.88±0.12	0.93±0.13	1.00±0.06
[V2-R2]	0.38±0.13	0.38±0.12	0.44±0.11	0.34±0.10	0.29±0.05

Note: The two sets of magnitudes and colors are based on different methods of estimating background level

Table 4b: Optical and Infrared Flux Densities for CTI Source

$\lambda(\mu\text{m})$	Flux (Jy/Sr)
100	$2.49 \pm 0.26 \times 10^6$
60	$1.78 \pm 0.21 \times 10^5$
25	$\leq 4.79 \times 10^4$
12	$\leq 2.56 \times 10^5$
.70 <R1>	$2.94 \pm 0.08 \times 10^4$
.70 <R2>	$2.54 \pm 0.09 \times 10^4$
.55 <V1>	$1.92 \pm 0.08 \times 10^4$
.55 <V2>	$2.29 \pm 0.08 \times 10^4$
.44 <B1>	$1.20 \pm 0.04 \times 10^4$
.44 <B2>	$1.05 \pm 0.04 \times 10^4$

Table 5: Derived Parameters for COADD Cirrus Sources

IRAS Name	$T_c(60/100)$	T_h	T_w	R^a
00154+0914	29 ± 1	164 ± 9	22.7 ± 0.9	$0.60 \pm .16$
00269+1030	30 ± 1	167 ± 25	23.4 ± 1.0	$0.74 \pm .37$
00373+0947	26 ± 1	213 ± 17	21.4 ± 0.7	$0.23 \pm .08$
03074+0744	29 ± 1	163 ± 16	22.8 ± 0.9	$0.41 \pm .17$
03084+0827	30 ± 1	171 ± 30	24.0 ± 1.0	$0.41 \pm .30$
21191-3157	29 ± 1	163 ± 21	22.9 ± 0.9	$0.48 \pm .26$
23410+0839	28 ± 1	173 ± 15	22.4 ± 0.8	$0.35 \pm .12$
02356-2959	28 ± 1	—	22.4 ± 0.9	≤ 0.26
03001+0841	28 ± 1	—	22.4 ± 1.0	≤ 0.28
09312+6551	25 ± 1	—	20.5 ± 0.8	≤ 0.18
23446-7202	28 ± 1	—	22.6 ± 0.8	≤ 0.17
Mean	28 ± 1	173 ± 8	22.5 ± 0.3	

^a – Ratio of hot-to-warm component emitted energy.

REFERENCES

- Allamandola, L. J., Tielens, A. G. G. M., and Barker, J. R. 1987, in *Infrared Processes*, eds. D. J. Hollenbach and H. A. Thronson, Dordrecht: Reidel, 471.
- Duley, W. W. 1973a, *Nature*, **244**, 57.
- Duley, W. W. 1973b, *Astrophys. Space Sci.*, **23**, 43.
- Explanatory Supplement to the IRAS Catalogs and Atlases*, ed. C. A. Beichman, G. Neugebauer, H. J. Habing, P. E. Clegg, and T. J. Chester. Washington, DC: US Govt. Print. Off., 1984.
- Greenberg, J. M., and Hong, S. S. 1974, in *Galactic Radio Astronomy*, eds. F. J. Kerr and S. C. Simonson III. Dordrecht: Reidel, 155.
- Guhathakurta, P. and Tyson, J. A. 1989, *Ap. J.*, **356**, 773.
- Heiles, C, Reach, W. T., and Koo, B. 1988, *Ap. J.*, **332**, 313.
- Herter, T., Shupe, D.L. and Cernoff, D.F. 1990, *Ap. J.*, **352**, 149.
- Keto, E. R., and Myers, P. C. 1986, *Ap. J.*, **304**, 466.
- Low, F. J., et al. 1984, *Ap. J.*, **278**, L19.
- Lynds, B. T. 1963, *Ap. J. Suppl.*, **105**, 163.
- McGraw, J. T., Cawson, M. G. M., and Keane, M. J. 1986, in *Instrumentation in Astronomy* (Proc. SPIE 627), ed. D. L. Crawford, 60.
- Pottasch, S. R., et al. 1984, *Astron. Astrophys.*, **138**, 10.
- Puget, J. L., Leger, A., and Boulanger, F. 1985, *Astron. Astrophys.*, **142**, L19.
- Purcell, E. M. 1976, *Ap. J.*, **206**, 685.
- Sakata, A., Wada, S., Onaka, T., and Tokunaga, A. T. 1989 preprint.
- Sandage, A. 1976, *Astron. J.*, **81**, 954.
- Sellgren, K. 1984, *Ap. J.*, **277**, 623.
- Smith, B. J., Kleinmann, S. G., Huchra, J. P., and Low, F. J. 1987, *Ap. J.*, **318**, 161.
- de Vries, C. P., and Le Poole, R. S. 1985, *Astron. Astrophys.*, **145**, L7.

de Vries, C. P. 1986, *Adv. Space Res.*, **6**, 35.

Witt, A., and Schild, R. E. 1988, *Ap. J.*, **325**, 837.

FIGURE CAPTIONS

1. Bright optical cirrus cloud in Fornax, seen on blue ESO/SRC photographic plate with IRAS 100 μm COADD contour overlay. North is up, east is to the left. The two emission peaks are IRAS 02356-2959 (southwest) and IRAS 02365-2950 (northeast). The image extends $\sim 1^\circ$ on each side.

2. Bright optical cirrus cloud in Tucana, seen on blue ESO/SRC photographic plate with IRAS 100 μm COADD contour overlay. North is up, east is to the left. IRAS 23446-7202 is the northwestern emission peak. The southeastern peak, located at $\alpha = 23^{\text{h}} 48^{\text{m}} 58^{\text{s}}$, $\delta = -72^\circ 20' 34''$, does not appear in the PSC. The image extends $\sim 1^\circ$ on each side.

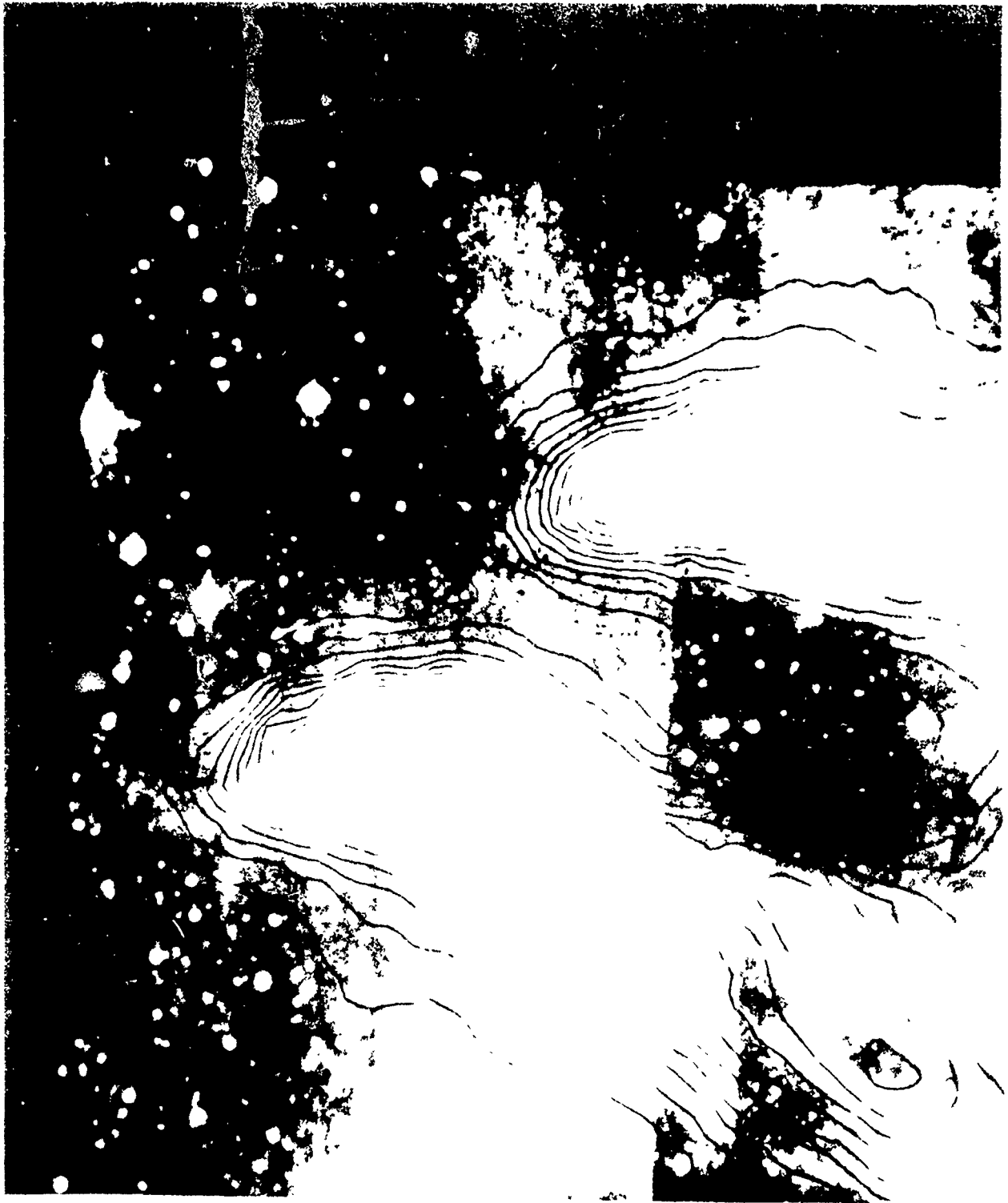
3. The CTI R coadded image data, showing regions from which CTI magnitudes were measured (see Table 4). North is to the left.

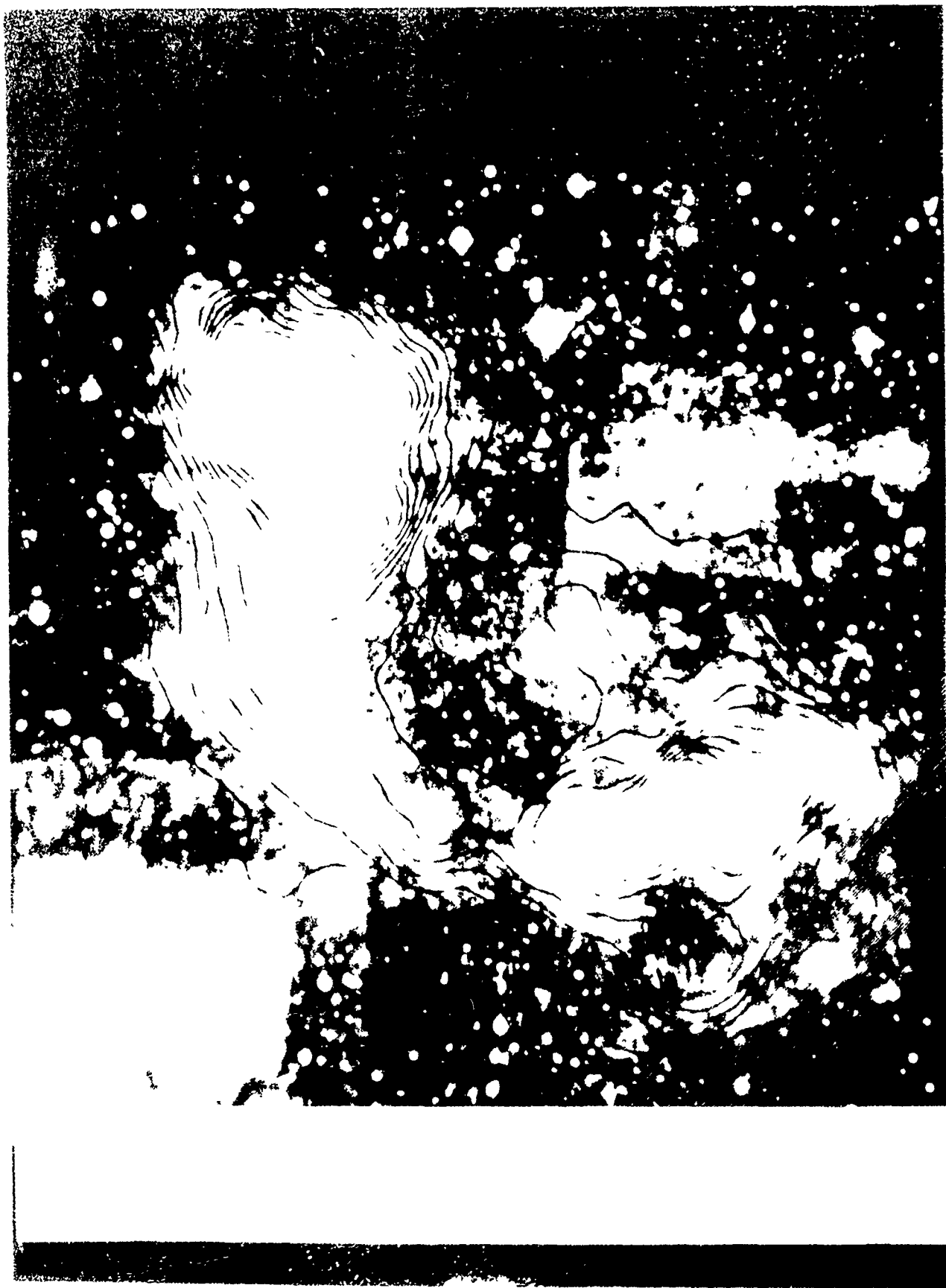
4. The infrared and optical spectrum of the CTI cirrus cloud, normalized to 100 μm flux. Shown are B(.44 μm), V(.55 μm), R(.70 μm), and 12, 25, 60 and 100 μm flux densities. 20 and 35 K blackbody curves are indicated by the dotted lines. 12 and 25 μm fluxes are upper limits.

5. F_{ν} vs λ for 11 COADD cirrus sources, normalized to F_{ν} at 100 μm . Data points for sources with only upper limits at 12 and/or 25 μm are connected by dashed lines. The dotted lines indicate blackbody curves for 20 and 35 K. Average errorbars for 12, 25 and 60 μm are shown in the lower right corner of the diagram.

POSTAL ADDRESS

Elizabeth S. Paley, Frank J. Low, John T. McGraw, Roc M. Cutri and Hans-Walter Rix: Steward Observatory, University of Arizona, Tucson AZ, 85721.

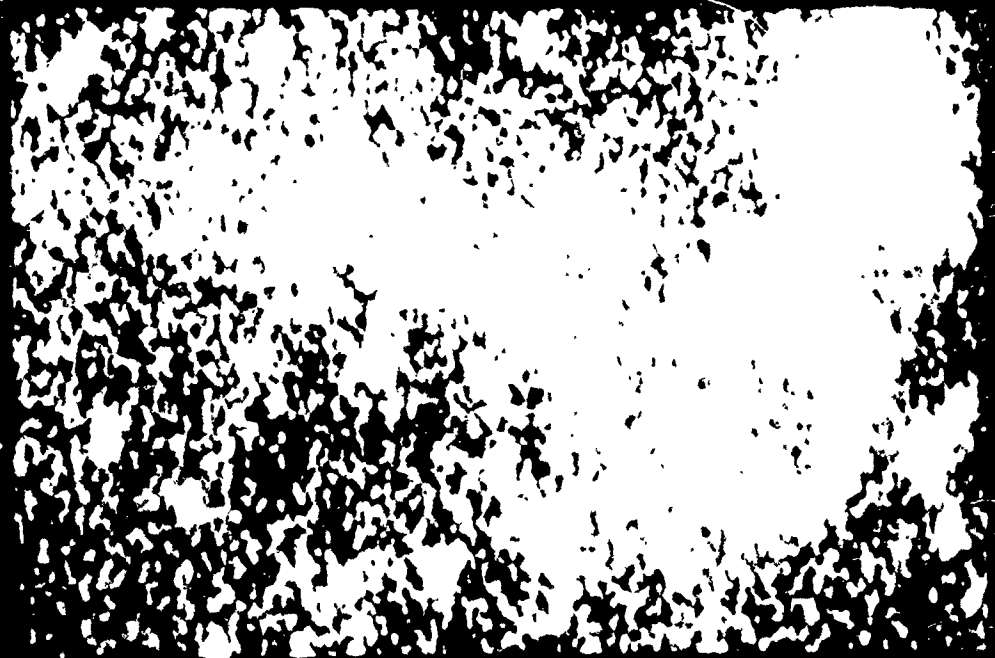


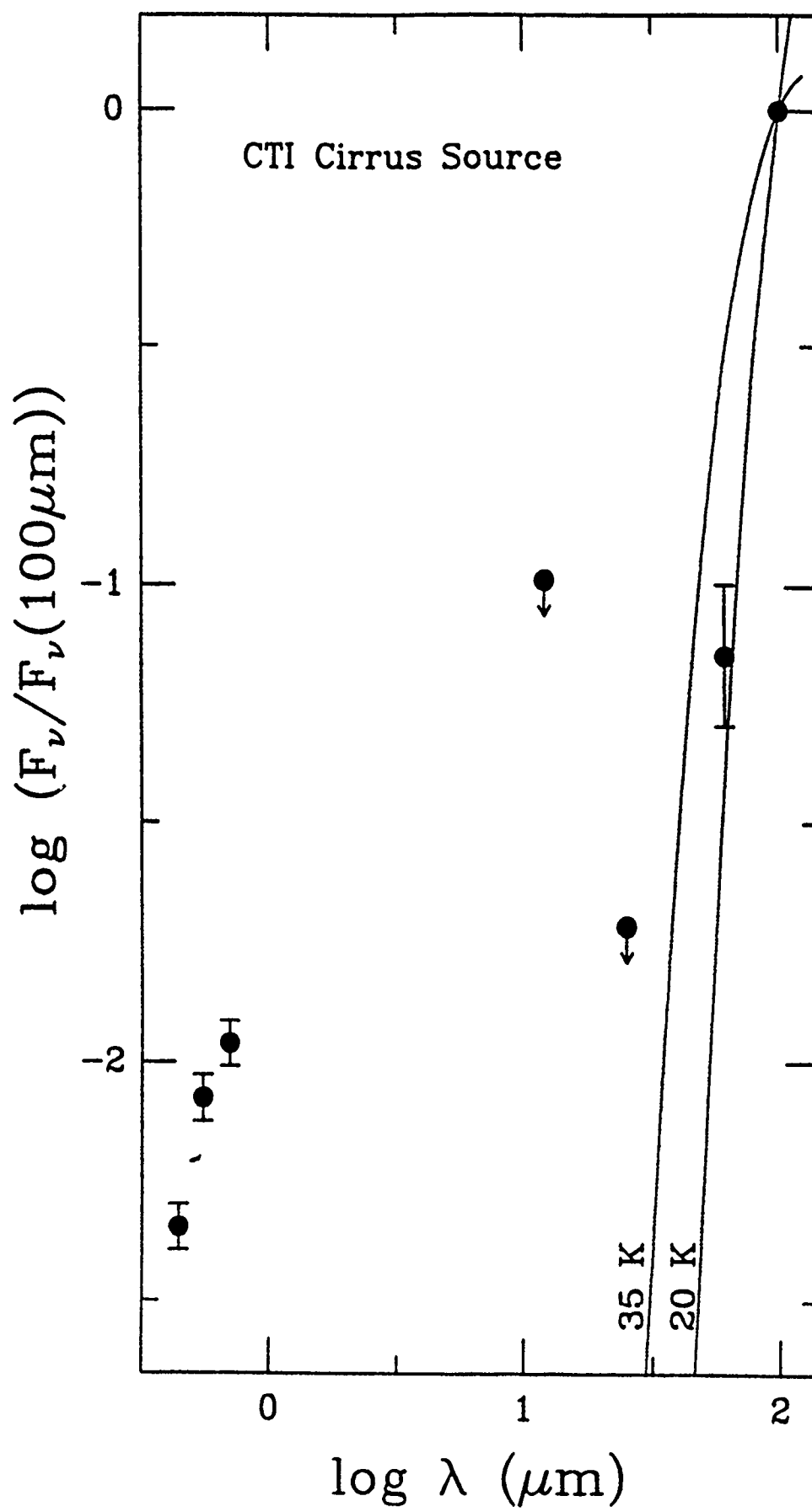


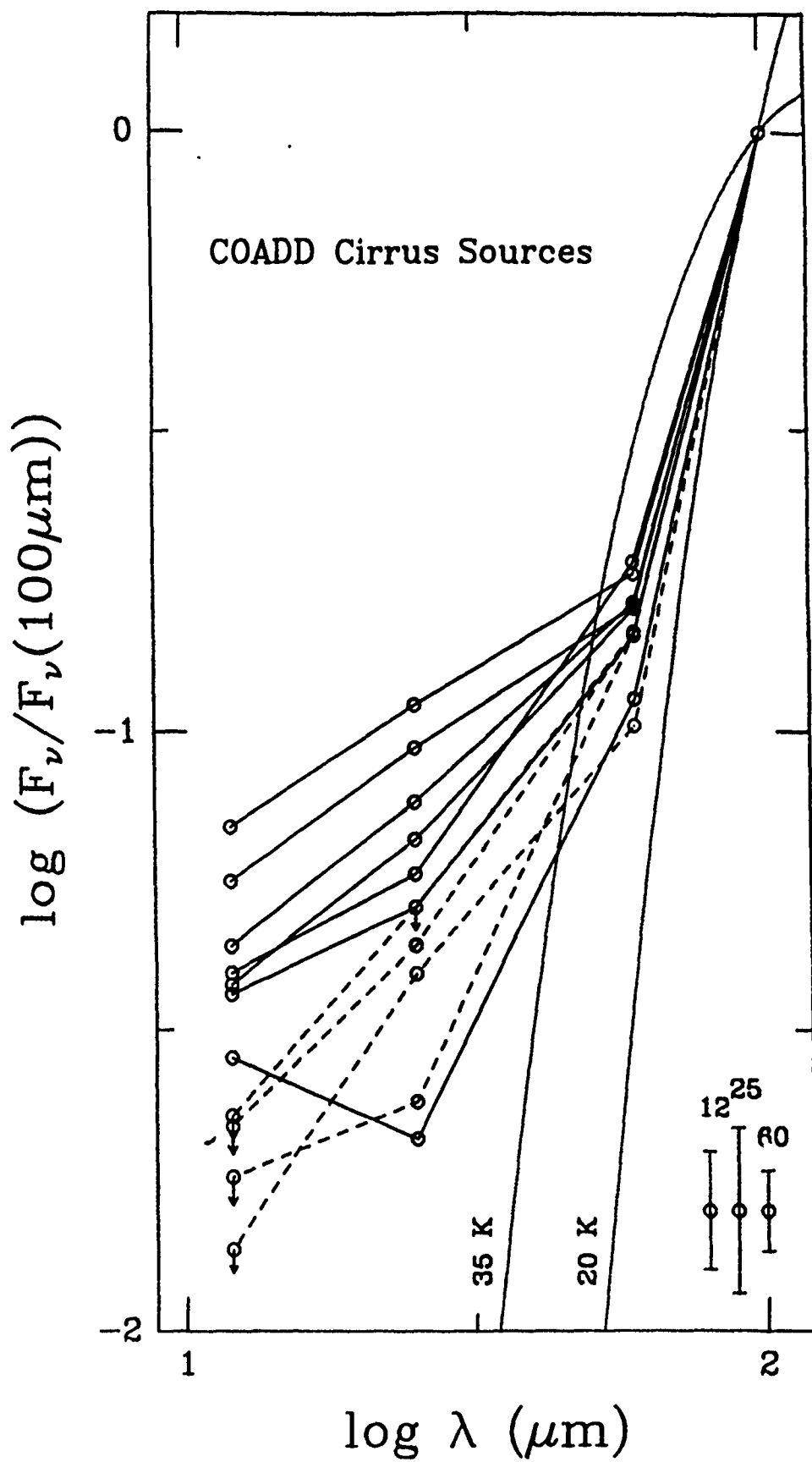
CTI R Data

23/36m05.9

23/35m42.5







APPENDIX III

POWER SPECTRAL ANALYSIS OF THE INFRARED CIRRUS

At high galactic latitudes, the emission from the interstellar clouds known as the "infrared cirrus" is the dominant fixed pattern celestial background component at wavelengths between $100\mu\text{m} < \lambda < 300\mu\text{m}$, and it is a significant component in the range $10\mu\text{m} < \lambda < 700\mu\text{m}$. Any infrared detection system which must be able to discriminate quickly between objects projected onto the sky, must do so against the backdrop of the cirrus emission. Consequently, it is critical that the characteristic spatial distribution of the cirrus filaments be well understood.

In both bright and faint cirrus regions, there appear to significant surface brightness modulations on scales down to the 2 arc-minute resolution of the Skyflux maps. Furthermore, in many clouds the cirrus seems to exhibit coherent spatial structure; large and small scale filaments appear co-aligned over large regions. Fundamental questions which must be addressed are how the spatial power of the cirrus is distributed in frequency space, and is the power distributed homogeneously within individual cirrus clouds.

To answer these questions, we have carried out Fourier analyses of selected prominent infrared cirrus complexes. 12 and $100\mu\text{m}$ power spectra of these clouds have been evaluated, and we note the characteristic spectral slopes and variations in the slopes among the sample.

A. LARGE SCALE CIRRUS DISTRIBUTION

We have made use of the database of enhanced IRAS Skyflux maps to examine the large and small-scale spatial appearance of the complexes of infrared cirrus. This database was generated by processing the raw IRAS Skyflux maps using the Steward Observatory Destripping software package. The enhanced images were cleaned of the fixed pattern "stripe" and low frequency "wave" artifacts, and in the case of the 12, 25 and $60\mu\text{m}$ maps, the contribution of the broad zodiacal emission was removed in a "flat-fielding" process.

Inspection of even the raw $100\mu\text{m}$ Skyflux maps shows that the infrared cirrus appears to be organized in complexes ranging in size from a few degrees to tens of degrees (e.g. see Appendix I). However, the cleaned maps reveal that even in regions between the prominent complexes there appears to be significant low surface brightness cirrus emission. There are frequently faint cirrus structures bridging prominent clouds suggesting that what appeared to be discrete complexes are actually physically associated clouds. Perhaps more significant is the fact that the enhanced $100\mu\text{m}$ maps show that it is likely that there are *no* regions of the sky which are completely free from cirrus emission. Areas which appeared to be clear in the original Skyflux maps exhibit low level surface brightness modulation in the cleaned maps marking the presence of faint cirrus structures virtually everywhere on the sky.

B. POWER SPECTRA

We selected 24 enhanced IRAS Skyflux maps which contained prominent $100\mu\text{m}$ cirrus structures for power spectral analysis. While hot ($12\mu\text{m}$) cirrus emission is visible in many Skyflux maps (see Appendix I), there are very few fields in which the emission is bright enough and the image data is of sufficiently uniform quality to assure reasonable signal-to-noise in the resulting power spectra. Consequently, only four $12\mu\text{m}$ maps were selected for study. The corresponding $100\mu\text{m}$ maps for these fields were included so the relative power distributions at the two wavelengths could be compared. The Skyflux plate numbers and coordinates of the selected fields are listed in Table 1.

Before the power spectra were evaluated, for each of the maps the value of the mean intensity over the entire image was subtracted from each pixel, thus minimizing the zero frequency "spike" in Fourier space. Two-dimensional power spectra were then evaluated using the STSDAS Fourier analysis packages within IRAF. Only those parts of the images which were free from artifacts or processing anomalies were utilized. This resulted in slightly different sized images going into each Fourier transform, and thus slightly different spectral resolutions for each power spectrum. The net size of the input image used for each frame is listed in Table 1. No filtering or apodization was used.

Representative examples of the two-dimensional power spectra are shown in Figures 1a-o. The spectra are displayed in false color using a logarithmic stretch to enhance the lower intensity structure. Many of the power spectra are dominated by strong low frequency peaks which extend in the cardinal directions. This occurs primarily because of the contribution of the broad zodiacal emission which was not removed from the $100\mu\text{m}$ images, and which may have not been perfectly removed from the $12\mu\text{m}$ maps. A portion of the very low frequency power may be produced by the abrupt truncation of the images and the lack of apodization. Despite having subtracted out total power in the image space, the images behave somewhat like rectangle functions which transform into sinc functions. Also apparent in many of the spectra is a linear artifact due to residual low level "stripes" in the images, left over from the cleaning process.

The power spectra of most of the fields in this study are similar to those of plates 110, 27 and 46, shown in Figures 1g-j. They are characterized by a nearly symmetrical angular power distribution extending from near the DC level out to the Nyquist limit ($0.25 \text{ arc-minutes}^{-1}$). This is contrary to the impression of coherent spatial structure obtained by the visual examination of the raw images. The exceptions to this are the power spectra of plates 1, 6 and 48 (12 and $100\mu\text{m}$), 50, 62 and 178, shown in Figures 1a-f and 1k-m, which are decidedly asymmetric. The unusual structure in all of these spectra appears to correlate with the presence of bright compact structure in the images. For example, plate 48 contains the image of M33, a prominent source in all four IRAS bands, and plate 50 covers a very bright infrared emission condensation associated with a large HII region/molecular cloud complex. The power spectra in plates such as 75 and 94, shown in Figures 1n and 1o, are only slightly elongated, suggesting a marginally preferred direction for the cirrus structure.

To carry out a comparative analysis of the power distributions of the selected images, we extracted radial profiles in two orthogonal directions through the spectra. The profiles were

taken at 20° and 110° position angles (measured clockwise from the vertical) selected to avoid the stripe residual artifacts. The profiles for the 12 and 100μm spectra of plates 1, 6, 48 and 110 are plotted together in Figures 2a-d, and the remaining 100μm profiles are shown in Figures 3a-u.

The power spectra of many of the 100μm maps can be well approximated by single power law functions ($P \propto f^\alpha$) over much of the spatial frequency range. However, there is a suggestion that the slopes of some of the spectra steepen with increasing frequency; this curvature is quite pronounced in a few cases, such as in plates 6, 50 and 178. There is little difference between the spectral profiles taken in orthogonal directions for most of the fields. When differences are apparent, such as in the 100μm spectra of plate 6, 27, 50, 110 and 131, they can be as large as an order of magnitude in power at a given spatial frequency, although they tend to be isolated to relatively narrow frequency ranges. The remaining sections of the spectra agree quite well, further suggesting that, while coherent structure such as linear features may exist in some clouds, that coherence does not extend over all spatial scales.

Despite the unusual structure in the two-dimensional power spectra, the radial profiles of the 12μm power spectra appear quite symmetrical and strikingly similar to each other. In addition, curvature in the short wavelength power spectra appears to be the norm. However, it is unlikely that this structure is due to the cirrus. The high frequency turnover is a signature of the point source contribution to the spatial power. Because stars are the dominant sources of emission in the 12μm Skyflux maps, rather than extended cirrus which dominates at 100μm, it follows that point sources will also dominate power spectra. To investigate the influence of stellar point sources on the resulting power spectra, synthetic images were constructed to simulate the Skyflux maps. The test images contained a "flat" gaussian noise background, with an RMS scatter equivalent to that observed in the background sky in typical 12μm images. An ensemble of 100 "stars" was distributed uniformly in one of the test images; the artificial stars had a distribution of brightness and image size roughly equivalent to those observed in the 12μm maps. Using the same procedure as described for the Skyflux maps, power spectra were then evaluated for the pure noise image and the image containing noise plus stars. Figure 4 illustrates the azimuthal averaged power spectral profiles for the two test images. As expected, the spectrum of the noise image is flat, but that of the image containing "stars" exhibits the same high frequency curvature that is seen in the 12μm Skyflux power spectra. These test images illustrate that uniformly distributed point-like sources can contribute to the power over a very broad range of spatial frequencies, including the very lowest. We must conclude, therefore, that the spatial power in the 12μm maps is *dominated by the contribution of point sources*. However, because the power spectra of the 12μm maps continue to rise towards low frequencies, unlike the spectrum of the synthetic star-field image in Figure 4, the emission from the cirrus still contributes a measurable fraction of the power.

The high frequency curvature observed in many of the 100μm spectra suggests that compact and point-like sources may contribute a non-negligible amount of power to those images, as well. The extreme example of this is plate 6 (Figure 1b) which contains the galaxies M81 and M82, two very high surface brightness, compact sources. If the 100μm power spectrum is evaluated for the regions of the plate 6 excluding M81 and M82, the result appears virtually identical to the spectrum of plate 46, shown in Figure 3. Because the cirrus is the

dominant emission source in most of the 100 μ m maps, the contribution of point sources generally should be small. In addition, it is possible that at least some of the curvature in the power spectra could be intrinsic to the cirrus, and not just an artifact of compact sources.

In order to recover the pure cirrus power spectrum we have investigated several methods for removing the point sources from the Skyflux maps. The most efficient procedure appears to be two-dimensional median filtering in image space. However, median filtering necessarily reduces the effective spatial resolution of the maps, and by suppressing point sources it also suppresses power over a broad range of frequencies. Included in Figure 4 is the azimuthal averaged radial profile of the synthetic star-field image after it has been median filtered using a filter window of 7x7 pixels (14'x14'), the minimum size empirically determined to effectively remove point-sources in the Skyflux maps. Median filtering recovers the slope of the input (pure noise) image at low frequencies fairly well, but the filtering actually suppresses power down to 0.04 arc-minutes⁻¹, which is nearly half the spatial frequency of the window size (1/14' \sim 0.07 arc-minutes⁻¹). The effects of the median filtering on real Skyflux data are illustrated in Figures 5 and 6. In Figure 5 is shown the two-dimensional power spectrum of the median filtered 12 μ m Skyflux map for plate 1. In contrast to the spectrum of the unfiltered image shown in Figure 1a, this spectrum exhibits virtually none of the non-circular structure. Median filtering suppresses such structure in the spectra of other 12 and 100 μ m maps, as well, implying that the bulk of the asymmetry seen in the two-dimensional power spectra arises from structure on small spatial scales, either in the form of bright compact sources or small-scale cirrus filaments. Figure 6 compares the azimuthal averaged radial profiles of the power spectra of the filtered and non-filtered 12 and 100 μ m plate 1 Skyflux maps. As predicted, the filtering effects the 12 μ m data to a much greater degree. Both spectra show residual curvature, but most of it is an artifact of the "break" near 0.04 arc-minutes⁻¹ induced by the filtering (see Figure 4). It is encouraging that the slope of the low frequency region of the filtered 12 μ m map is comparable to that of the 100 μ m map, although the 12 μ m spectrum is still somewhat flatter ($\alpha \sim -2.9$ compared to $\alpha \sim -3.3$ at 100 μ m). Figures 7a-d show the azimuthal averaged radial profiles of the power spectra of the four 12 μ m fields included in this study. The spectrum of plate 6 was evaluated for the sub-region excluding M81 and M82 which resulted in somewhat lower power spectral resolution.

It is important that the limitations of filtering the Skyflux maps be properly understood. In addition to filtering out point sources, global median filtering also suppresses fine scale structure in the cirrus. In Fourier space, this will result in *too much power* being removed over a broad range of spatial frequencies. Furthermore, residuals from slightly resolved sources, which cannot be effectively removed through median filtering "tuned" for point sources, will still weakly influence the power spectra. This is liable to be more critical in the 100 μ m maps which contain a larger proportion of galaxies. Finally, median filtering can introduce low level periodic artifacts due to the modulating influence of the filter. In general, the biggest hazard in filtering the 100 μ m maps in which the cirrus is usually the dominant emission source (there are certainly exceptions to this), is that there is no way to selectively remove only stellar and extragalactic sources. This can produce gross errors in measurements of the cirrus power at high spatial frequencies. Such errors are especially critical if estimates of the power at frequencies well above the Skyflux resolution are to be made by extrapolating these data. Because of these limitations, and because

in most of the 100 μ m maps selected for this study the integrated cirrus emission is much greater than that from non-cirrus sources, no filtering was carried out on the 100 μ m data.

To characterize the slopes of the cirrus power spectra, power law functions were fit to the radial spectral profiles in the frequency ranges .01-.025 arc-minutes⁻¹, .025-.063 arc-minutes⁻¹, .063-.01 arc-minutes⁻¹, and .01-.02 arc-minutes⁻¹. This was carried out using the azimuthal averaged filtered 12 μ m spectra, and the unfiltered 100 μ m spectra at position angles of 20° and 110°. The distribution of power law indices, α , in each frequency region for the images are shown in the histograms in Figure 8. In the figure, the entries for those spectra which qualitatively appeared to show the least high frequency curvature are indicated by filled squares. The large dispersion in the distribution of 100 μ m slopes reflects the relatively poor signal-to-noise of the spectra, since no azimuthal averaging was employed for that data. The average power law indices in each spectral regime have been evaluated for the 12 μ m spectra, and for both the full set of 100 μ m spectra and the least-curved subset of 100 μ m spectra, and are listed in Table 2. At low spatial frequencies (<.063 arc-minutes⁻¹) the 12 and 100 μ m power spectral slopes agree fairly well, indicating that a value of $\alpha \sim -2.9$ to -3.0 accurately describes both the distribution of the hot and cold cirrus components. At higher frequencies the 12 μ m spectra offer no valid slope information because of the effects of filtering. As a class, the 100 μ m spectra steepen towards higher frequencies most likely because of the contribution of point-like non-cirrus sources in the images.

C. PROBING HIGHER SPATIAL FREQUENCIES

The quality of the power spectral data presented above is ultimately limited by the 2' resolution of the IRAS Skyflux maps and the point source contamination. In virtually all cases, the declining spectra merge in frequency space with the noise slightly above the Nyquist frequency. This is particularly apparent in the 12 μ m data because the surface brightness of the cirrus emission is so low. We have attempted to obtain an improved measure of power at higher frequencies by utilizing data from the Pointed Observations of IRAS.

The Pointed Observations were carried out by repeatedly scanning the IRAS detector array over small regions (1-3 deg²) of the sky at rates 2-8 times slower than that used in the all-sky survey. The slower scans resulted in much higher spatial sampling rates which, in turn, yielded better resolution than survey mode observations. Data samples were obtained on scales of 8-30 arc-seconds at 100 μ m and 2-8 arc-seconds at 12 μ m. However, the practical limit to the resolution available from any IRAS data is ~ 3 -5 arc-seconds because of the wobble induced in the satellite due to the free-play in the gyroscope bearing (gyro pivotal clearance). Multiple scans and slower rates also resulted in longer net integration times than typical survey observations, and the Pointed Observations achieved sensitivities 3-7 time better than the survey mode. This would hopefully improve the signal-to-noise of cirrus detections at 12 μ m.

The major limitation in using the Pointed Observations for this application is that, of course, none intentionally targeted bright cirrus regions. However, we have identified a number of scans which serendipitously covered regions with reasonably high surface brightness 100 μ m cirrus emission. We have obtained Calibrated Reconstructed Detector Data (CRDD) for several

of those observations, and here we present the analysis for the three which cover the brightest regions of cirrus, BS63, SY52 and DF16. As an example of the improved resolution offered by the Pointed Observations, Figure 9 compares a single column of data from the 100 μ m IRAS Skyflux map 171 to the corresponding co-added scans of the BS63 Pointed Observation CRDD from a single 100 μ m detector. Much more detail is visible in the CRDD data, and the contrast in features is greatly enhanced. The difference in surface brightness between the Skyflux and CRDD scans is a result of larger effective area of the Skyflux beam as well as calibration differences between the two data sets.

In Figures 11 and 12 are shown the co-added 12, 25 60 and 100 μ m single detector scan data for the BS63 and SY52 Pointed Observations. For each field, three sets of scans are given, representing three separate "rows" of detectors seen by sources as they scanned across the IRAS focal plane. Referencing Figure 10 which shows a schematic of the IRAS focal plane, the three detector sets are: 47, 39, 31 and 55 which are small, "edge" detectors located at the bottom of the figure; 23, 16, 8 and 1 located just inboard the preceding edge detectors; and 54, 46, 11 and 62 which are the "edge" detectors at the top of Figure 10. Use of the edge detectors has the benefit that these were generally the most sensitive because their smaller angular size resulted in their seeing fewer background photons. While the cirrus emission is prominent in the 60 and 100 μ m scans shown in the above Figures, it is still at a very low contrast in the short wavelength data, despite the improved sensitivity of the Pointed Observations. In addition, structural features in the cirrus emission can be seen to vary substantially across the focal plane.

Figures 13-15 illustrate the one-dimensional power spectra for each detectors' data in the BS63 and SY52 fields. Also included are the spectra for the DF16 Pointed Observations field. As for the Skyflux data, the power spectra were evaluated by first subtracting the average intensity for each from each pixel in the scan. Although it is apparent that the Pointed Observation data are severely limited by signal-to-noise, 100 μ m power spectral information is available up to spatial frequencies of $\sim .005$ arc-seconds⁻¹, which is a slight improvement over the Skyflux data. More importantly, because individual scans of the Pointed Observation data can be examined, non-cirrus sources can be selectively removed without suppressing the small scale structure in the cirrus. At 12, 25 and 60 μ m, no significant sign of power can be seen above the noise limits. The power spectra of detectors 16 and 23 (25 and 12 μ m) in the SY52 field illustrate the familiar signature of the point sources detected in the scans shown in Figure 12b. In addition, a peak is present in the 25 μ m spectrum, which is produced by the periodic noise seen in the raw scan (this noise is likely due to crosstalk between detector 16 and one of the onboard clocks).

If the assumption is made that the spatial power distributions will be similar across the cirrus field covered by the Pointed Observation, some improvement is possible by co-adding scans in frequency space. As shown in the Skyflux data, this assumption is typically correct, however there are exceptions in which the power distribution can be asymmetric. Figures 16-18 show the co-added power spectra for the three Pointed Observation fields. The shape and level of the spectra from each field is remarkably consistent, within each IRAS band. At 100 μ m, the spectra can be coarsely fit with an average power law of slope ~ -1.9 which becomes indistinguishable from the noise below $\sim .006$ arc-seconds⁻¹. When the correction for a one-dimension to two-dimension Fourier transform is made ($\alpha(2d) \sim \alpha(1d)-1$), this agrees well with the average low frequency slopes of the 100 μ m Skyflux spectra listed in Table 2. This similarity

suggests that the high frequency spectral curvature observed in the Skyflux data is virtually all due to the point source contribution. The co-added 12 μ m spectra show little useful information.

It is possible that if the power spectra from all detectors is co-added, the Pointed Observation data could still yield useful details of the high frequency cirrus structure. Again, this relies on the assumption that the spatial structure is consistent across the field, and care must be taken to reject, or filter scans which exhibit non-cirrus source detections. The latter condition severely limits the amount of available 12 μ m data. Because further refinements of the data may be possible, we hope to pursue the analysis of Pointed Observation data, even though it is not strictly part of this contract work.

D. SUMMARY

Fourier analysis has yielded a number of quantitative results concerning the characteristic spatial distribution of the infrared cirrus.

- The two-dimensional power spectra of 12 μ m IRAS Skyflux maps are virtually dominated by the influence of stars in the maps. The power spectra of the 100 μ m cirrus fields are also influenced by point sources, although to a much smaller degree. Two dimensional median filtering of the 12 μ m maps can suppress the contribution of the point sources, but such filtering produces artifacts which must be taken into account.
- The two-dimensional power spectra of most 12 and 100 μ m cirrus fields are symmetrical, indicating that the spatial power is distributed homogeneously. That is, the spatial structure of the cirrus is generally *not* coherent over large spatial scales.
- In 20% of the fields studied, the two-dimensional power spectra exhibit some asymmetries. However, these asymmetries extend over relatively small ranges in spatial frequencies. This suggests that although certain coherent cirrus structures can be present, such as large linear features, the bulk of the cirrus structure is distributed with no preferred spatial orientation. At least some of the asymmetries observed in the power spectra may be caused by the presence of discrete, compact non-cirrus sources.
- At frequencies below ~ 0.05 arc-minutes $^{-1}$, both the 12 and 100 μ m two dimensional power spectra typically have power law slopes, α , of -2.9 to -3.0 . Above 0.05 arc-minutes $^{-1}$, the slopes of the 100 μ m steepen to values of ~ -3.3 to -3.5 . Although we cannot rule out the that steepening is indicative of the small-scale structure of the cirrus, analysis of the Pointed Observation data strongly suggest that the curvature is caused by the contribution of point sources in the images. Because of the compromising effects of median filtering, the high frequency behavior of the 12 μ m spectra is unknown.
- Because only moderately bright cirrus was serendipitously scanned during the Pointed Observations of IRAS, the cirrus data and resulting power spectra are of relatively low signal-to-noise. The ability to verify that point sources are not present in the scan

allows much higher confidence to be placed on the interpretation of the power spectral slopes at the highest frequencies. For the three brightest cirrus regions covered by Pointed Observations, the slopes of the 100 μ m power spectra up to spatial frequencies of ~ 0.2 arc-minutes⁻¹ agree well with the lower frequency slopes observed in the Skyflux data ($\alpha \sim -2.9$). The hot cirrus emission is too faint in these areas to produce useful power spectral information.

These analyses point out the strengths and limitations of the IRAS Skyflux maps and Pointed Observations database for studies of the spatial power distribution of the cirrus. The Skyflux maps cover essentially the entire sky so regions of the brightest cirrus emission may be selected for study. The individual scans of Pointed Observations, although limited in spatial coverage, can be screened for point sources. If all non-cirrus sources, including stars, galaxies and compact HII regions and molecular clouds, could be selectively removed from the two-dimensional Skyflux maps, uncontaminated power spectra could be accumulated. However, we suggest that a better data set to employ for spatial power studies of the cirrus may be the IRAS Survey CRDD. CRDD scans for selected regions covering the brightest cirrus complexes can be selected. As with the Pointed Observation data, these individual scans can be selectively filtered for non-cirrus sources and then combined into two-dimensional images, thus alleviating many of the problems incurred in post-processing the existing Skyflux maps.

Table 1.

Enhanced IRAS Skyflux Maps Used in the Power Spectral Analysis

IRAS Plate	RA	Dec	Band	Size(')
1	00:00	+90	1	780x780
1			4	900x900
6	09:36	+75	1	530x530
6			1 ^a	360x360
6			4	880x880
9	16:48	+75	4	880x880
27	00:00	+45	4	900x900
46	22:48	+45	4	900x900
47	00:00	+30	4	900x900
48	01:00	+30	1	840x840
48			4	900x900
50	03:00	+30	4	900x900
62	15:00	+30	4	900x900
70	23:00	+30	4	900x900
71	00:00	+15	4	900x900
72	01:00	+15	4	900x900
73	02:00	+15	4	900x900
75	04:00	+15	4	900x900
92	21:00	+15	4	900x900
94	23:00	+15	4	840x840
110	15:00	+00	1	900x900
110			4	900x900
116	21:00	+00	4	900x900
119	00:00	-15	4	900x900
122	03:00	-15	4	900x900
124	05:00	-15	4	900x900
131	12:00	-15	4	860x860
140	21:00	-15	4	900x900
176	10:48	-45	4	880x880
178	13:12	-45	4	820x820

Notes:

^a - Subsection of plate 6 excluding the galaxies M81 and M82.

Table 2
Mean Power Spectral Slopes

	Spectral Range (arc-minutes ⁻¹)			
	.01-.025	.025-.063	.063-.10	.10-.20
<u>Skyflux Data:</u>				
$\langle\alpha(100)\rangle$	-2.5 ± 0.2	-2.8 ± 0.2	-3.7 ± 0.2	-4.1 ± 0.3
$\langle\alpha(100)\rangle^a$	-2.9 ± 0.2	-3.2 ± 0.2	-3.6 ± 0.2	-3.1 ± 0.2
$\langle\alpha(12)\rangle^b$	-2.7 ± 0.4	-3.2 ± 0.1	—————	—————
<u>Pointed Observations:</u>				
$\langle\alpha(100)\rangle^c$	—————	—————	-2.9 ± 0.3	-2.9 ± 0.3

Notes:

^a – Mean spectral indices for the set of 100 μ m power spectra exhibiting the least amount of curvature.

^b – No valid high frequency slopes are available for the 12 μ m spectra because of spatial median filtering of the images.

^c – Spectral slope from Pointed Observations deduced from one-dimensional power spectrum in the region .05-.20 arc-minutes⁻¹. Slope corrected to two-dimensions ($\alpha(2d) \sim \alpha(1d) - 1$).

Figure 1a. - Power spectrum of temp

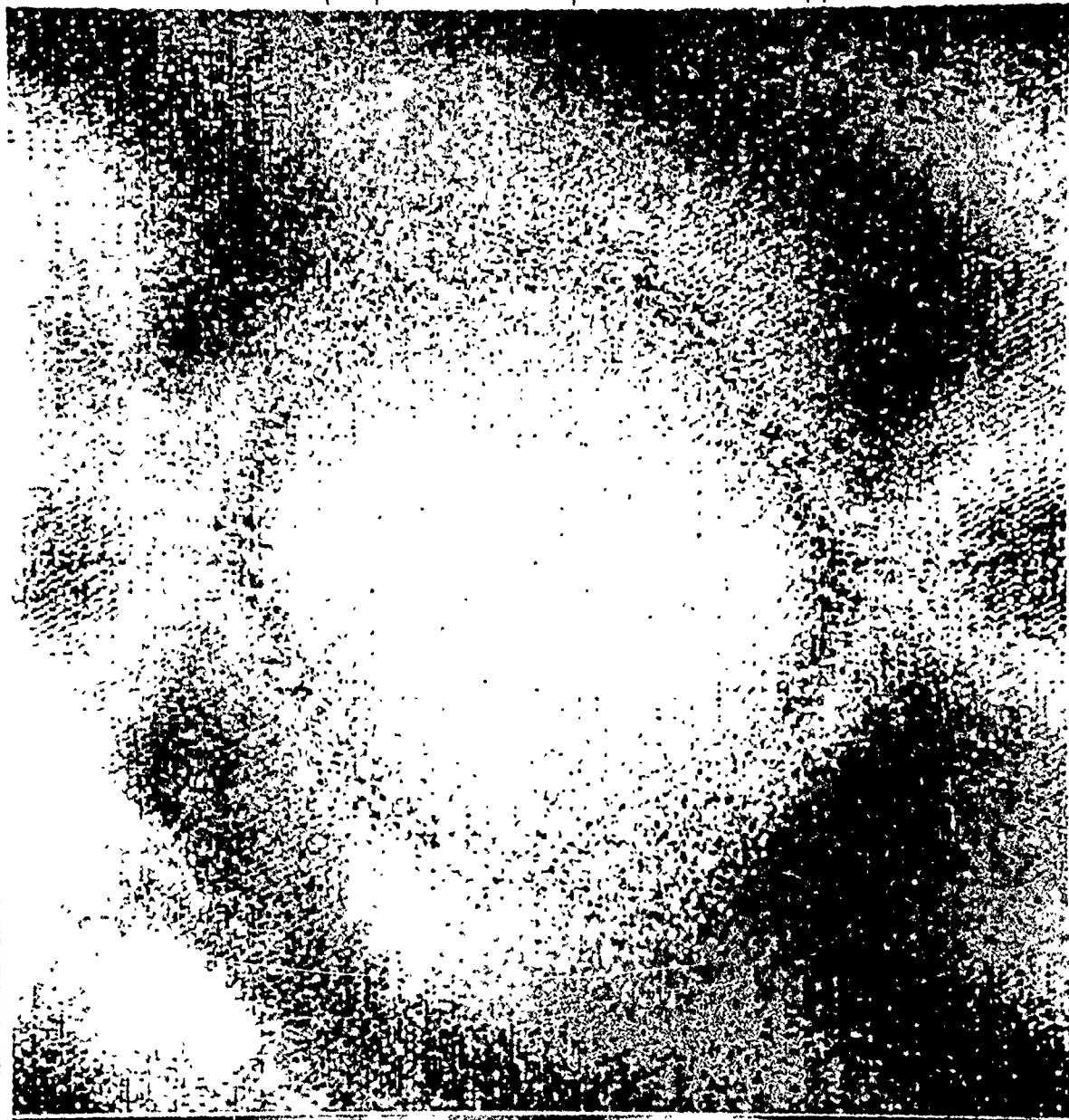


Figure 1a. - The two-dimensional power spectrum of the enhanced $12\mu\text{m}$ IRAS Skyflux plate 1. The strong vertical and horizontal features running through the center of this images and those that follow are caused by the finite size of the transformed image, and the contribution of very low spatial frequency power arising from the broad zodiacal emission.

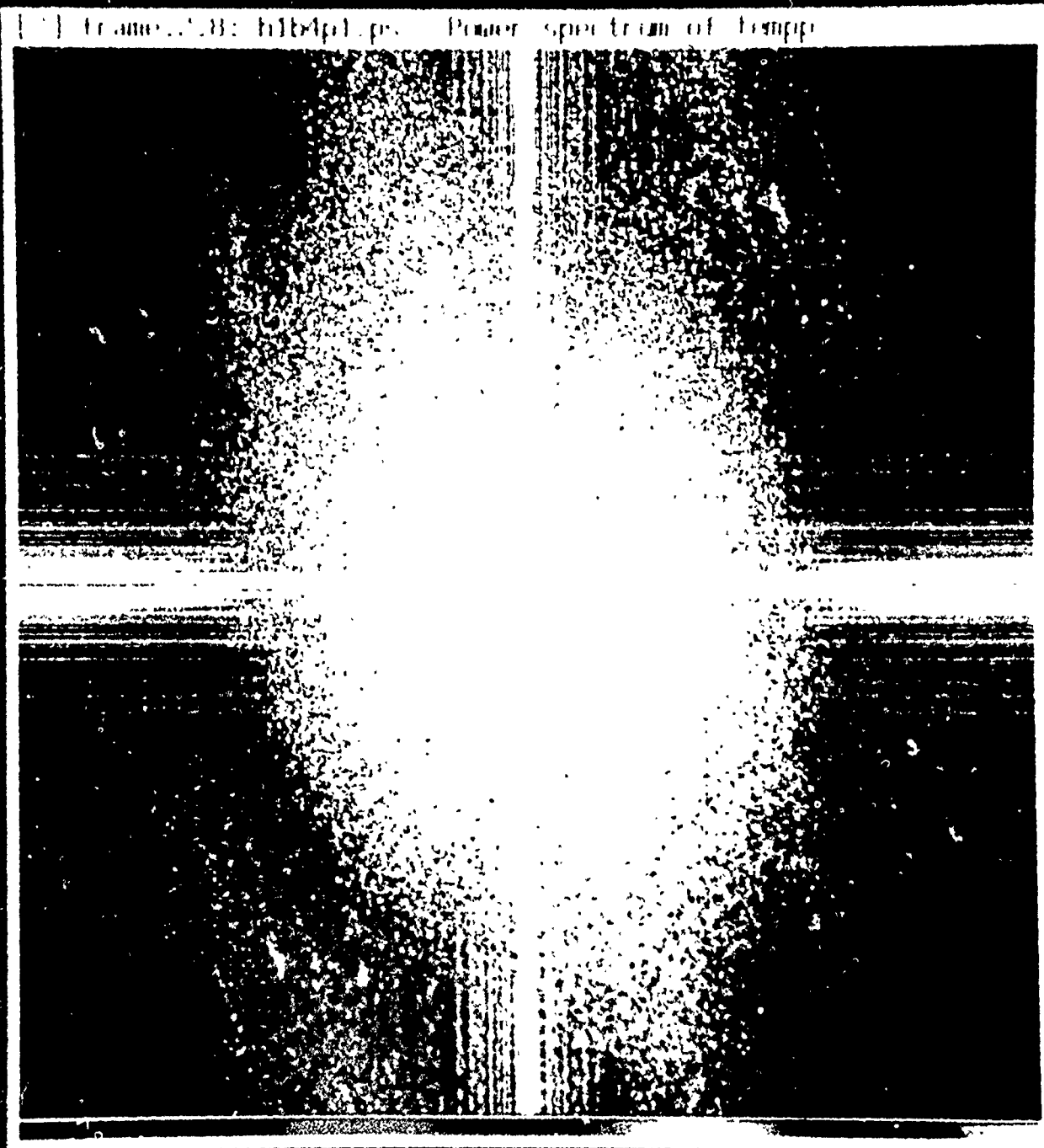


Figure 1b. – The two-dimensional power spectrum of the enhanced 100μm IRAS Skyflux plate 1. The weak linear feature, at position angle 160° in this spectrum, is caused by residual stripe artifacts in the original image.

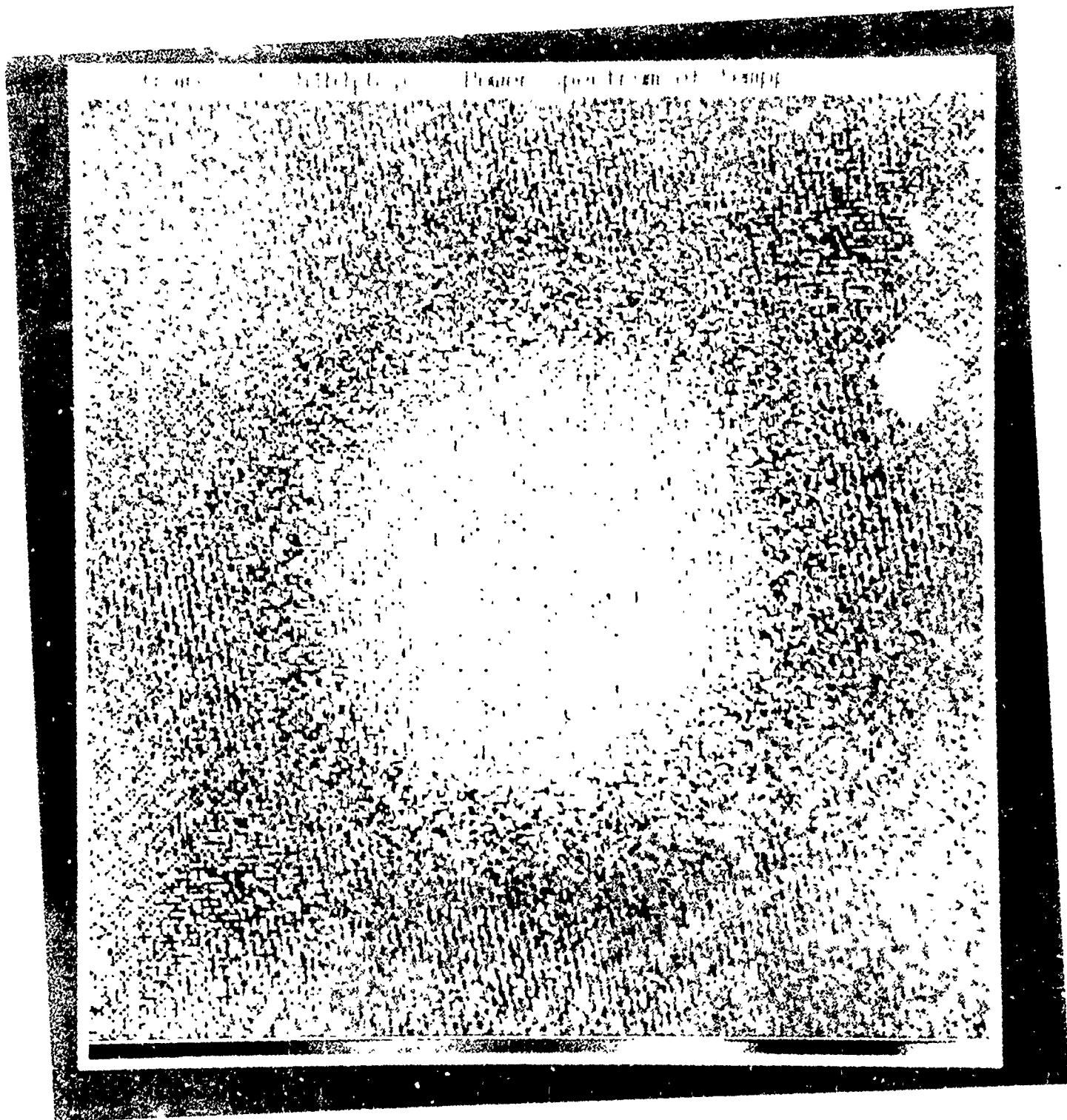


Figure 1c. – The two-dimensional power spectrum of the enhanced 12 μ m IRAS Skyflux plate 6.

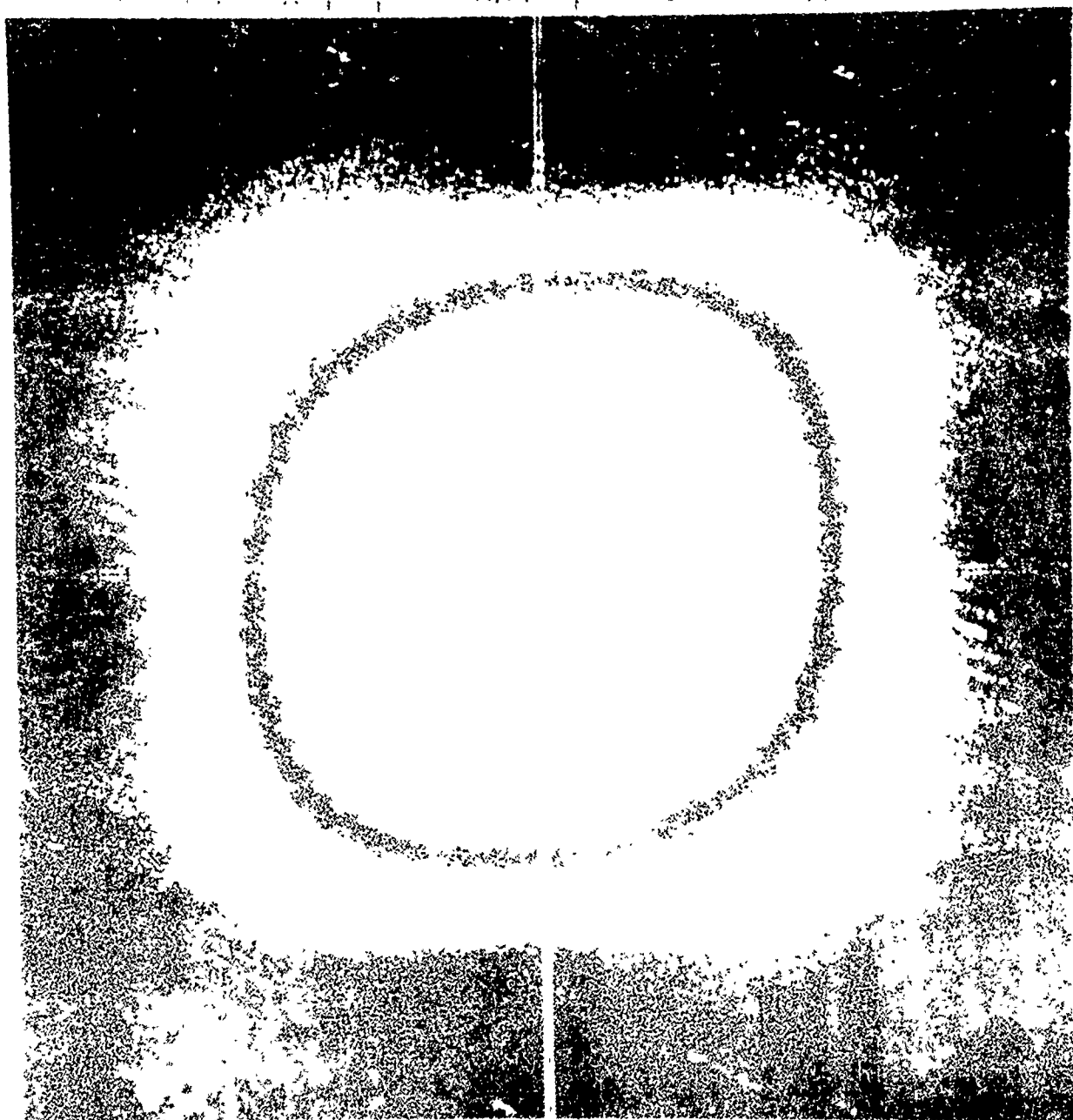


Figure 1d. The two-dimensional power spectrum of the enhanced 100 μ m IRAS Skyflux plate 6.

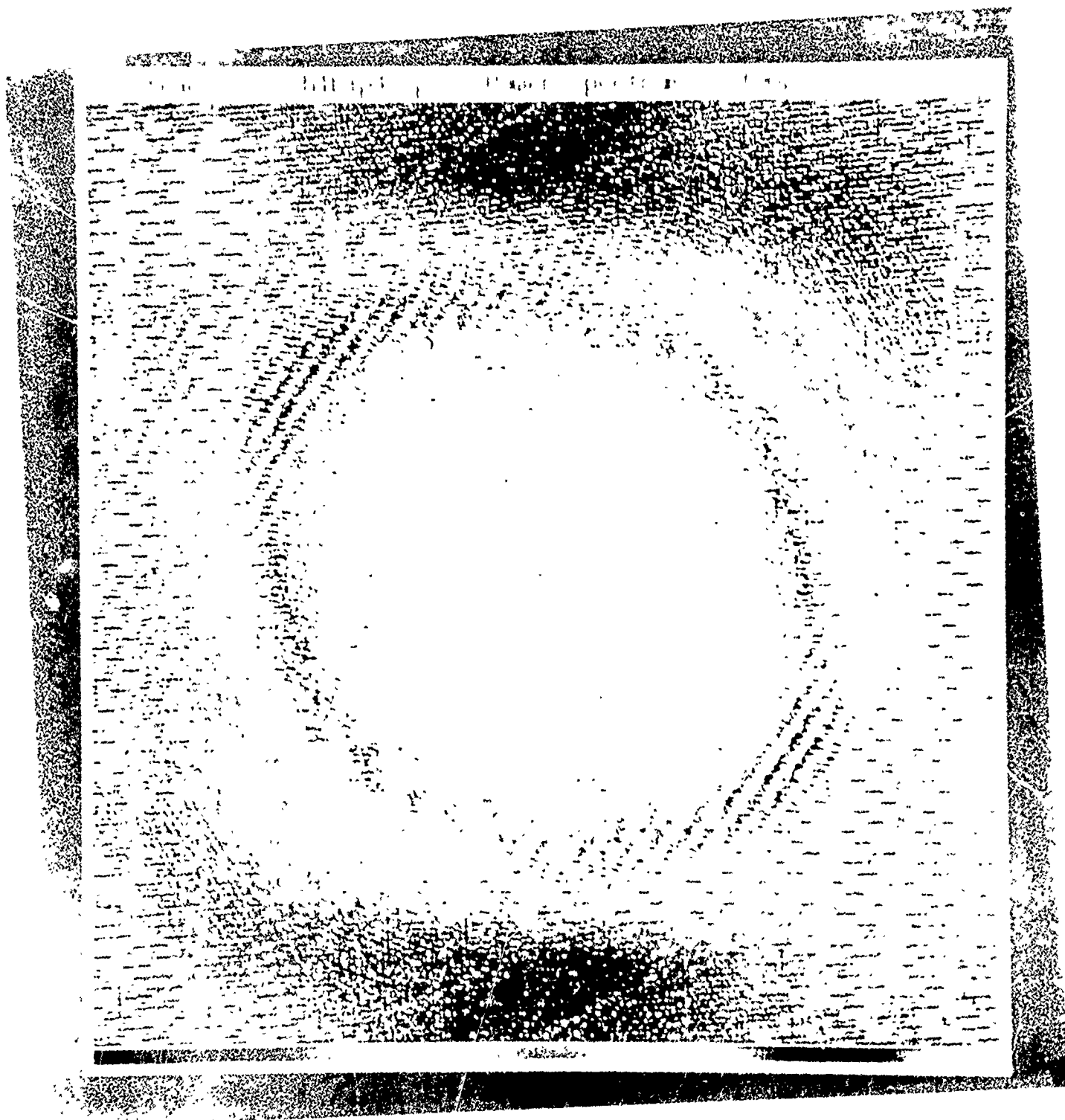


Figure 1e. The two-dimensional power spectrum of the enhanced 12 μ m IRAS Skyflux plate 48.

Frame 19, bits 10-18 pr. Power spectrum of temp

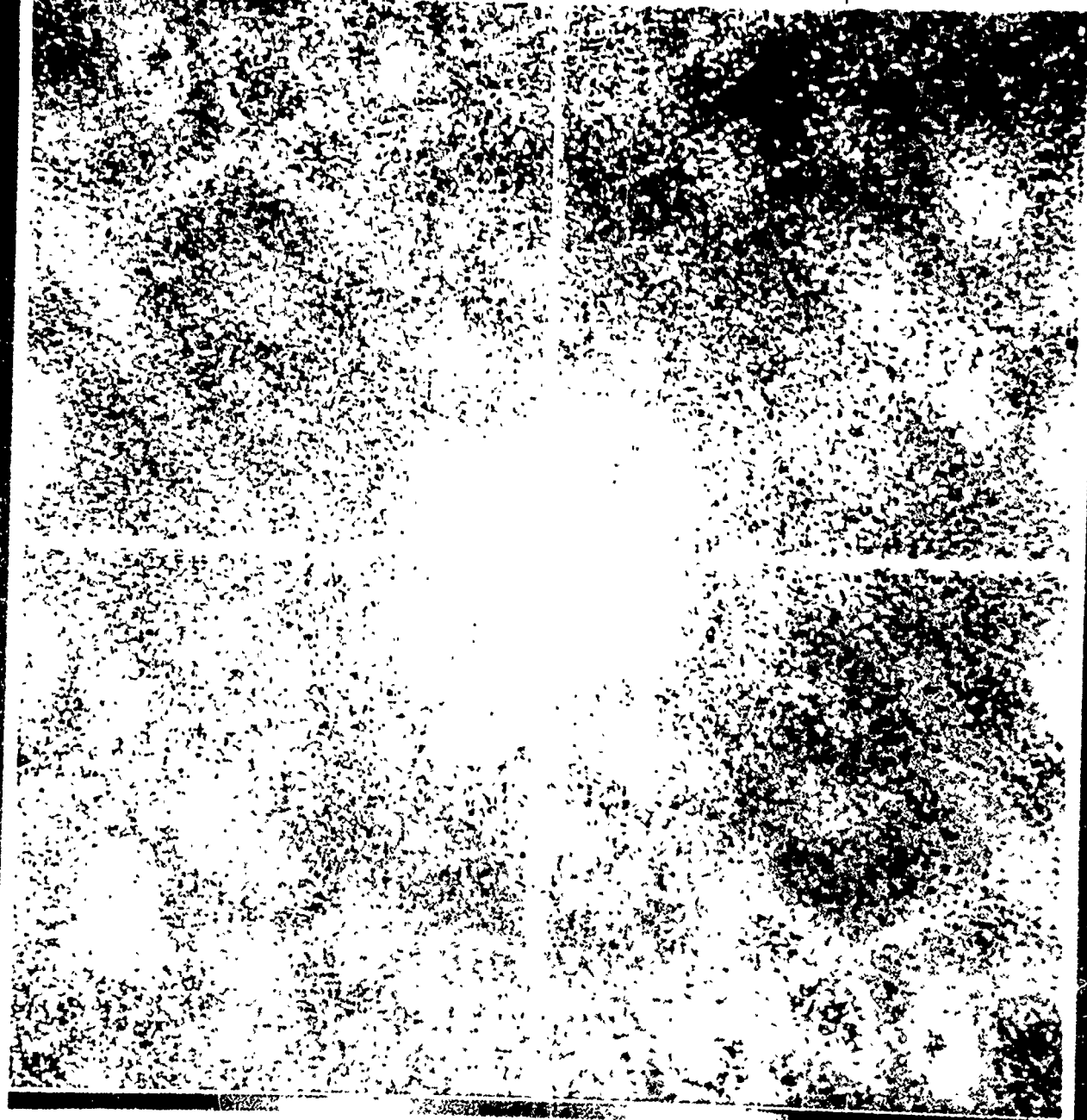


Figure 1f. – The two-dimensional power spectrum of the enhanced 100 μ m IRAS Skyflux plate 48.

Figure 1g. - Power spectrum of 12μm IRAS Skyflux plate 110.

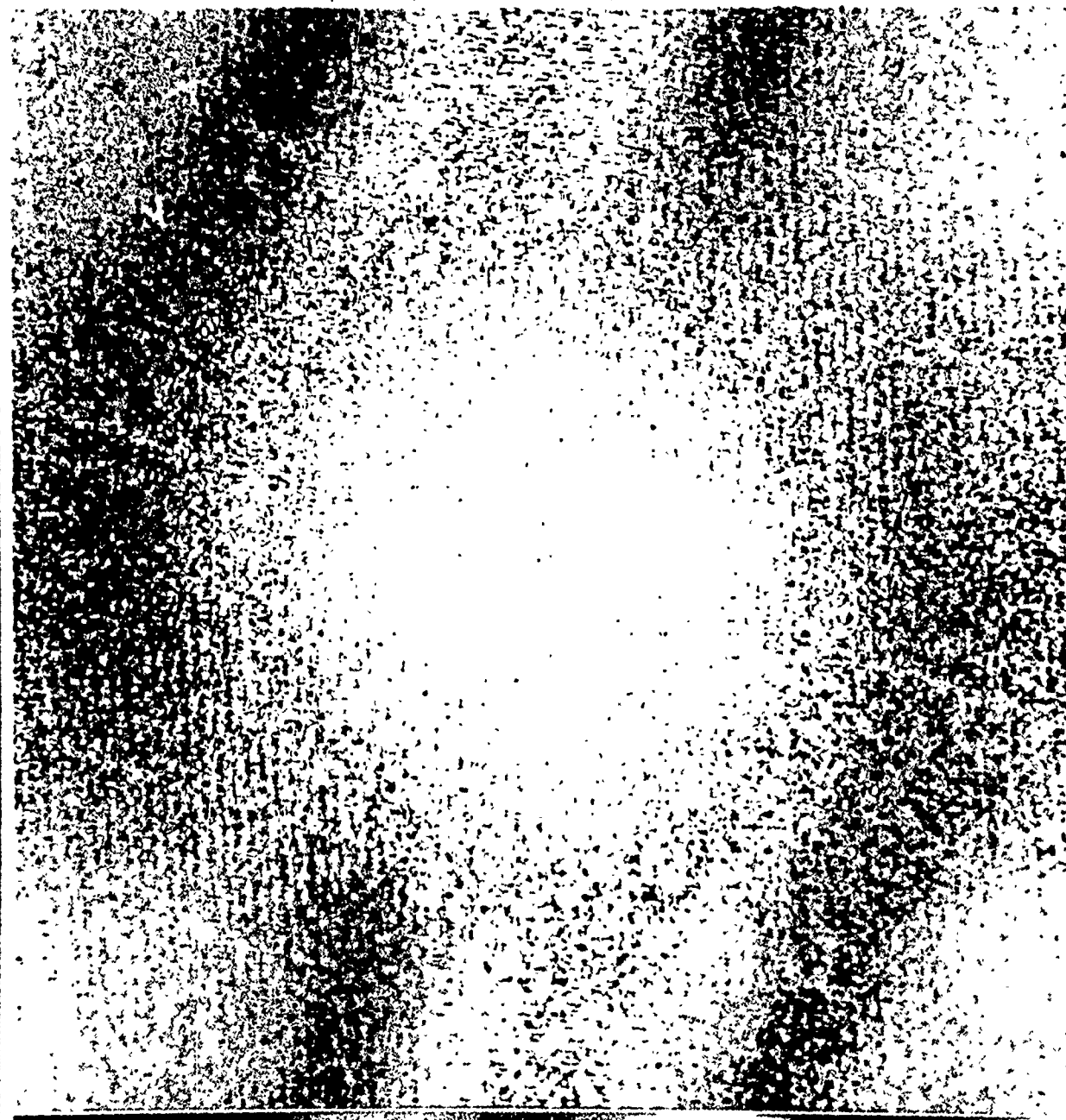


Figure 1g. - The two-dimensional power spectrum of the enhanced 12μm IRAS Skyflux plate 110.

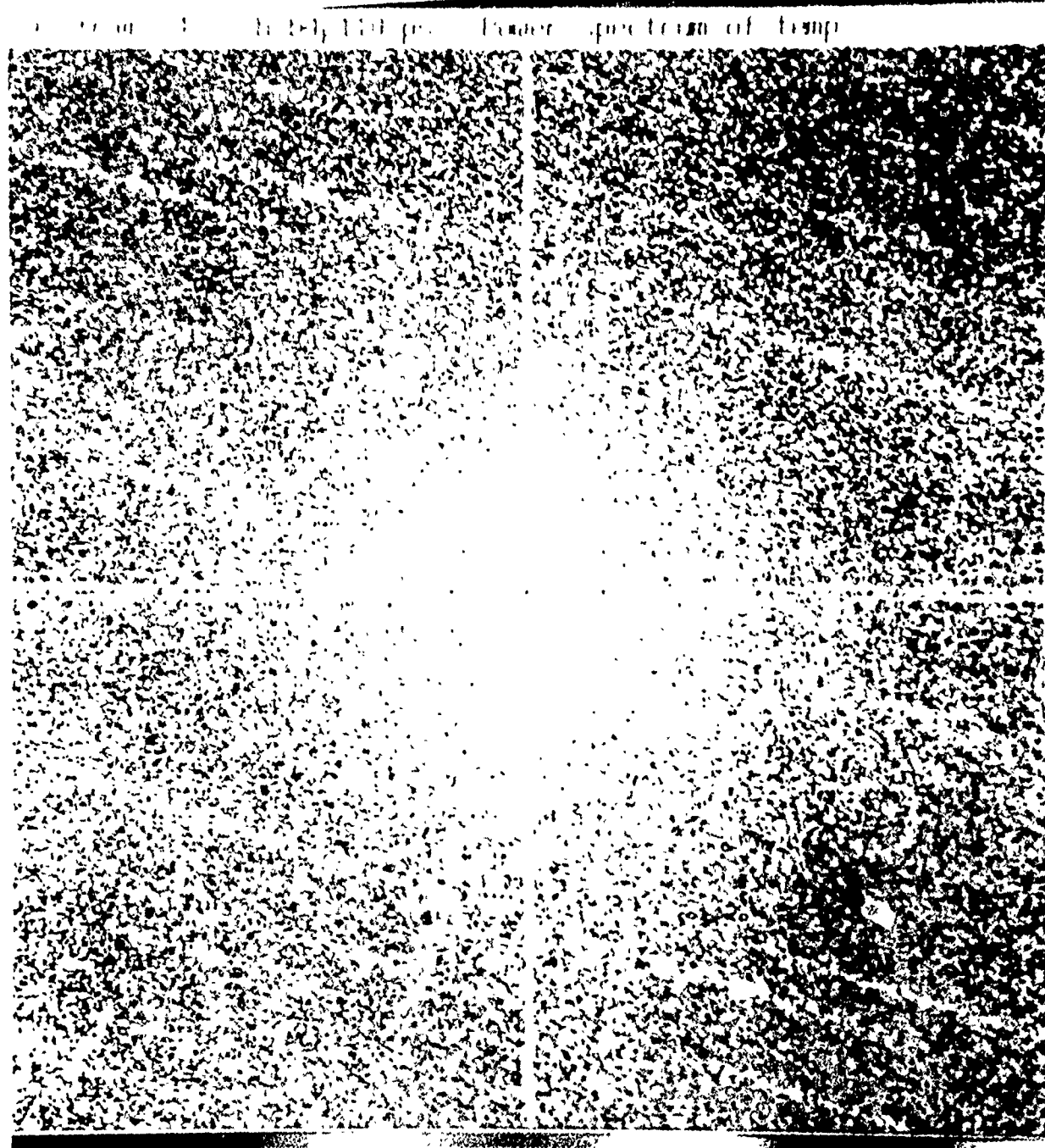


Figure 1h. - The two-dimensional power spectrum of the enhanced 100 μ m IRAS Skyflux plate 110.

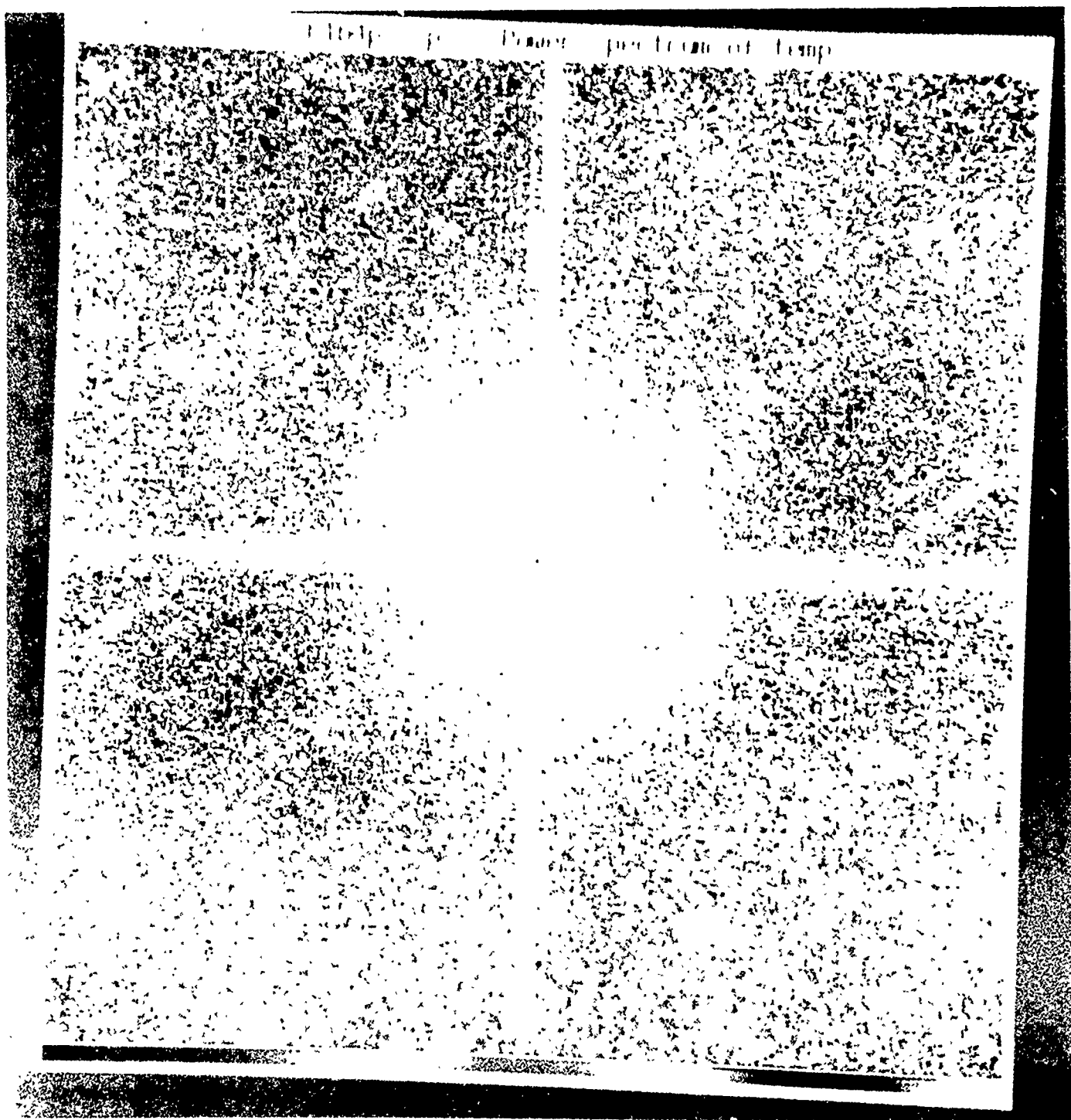


Figure 11. – The two-dimensional power spectrum of the enhanced 100 μ m IRAS Skyflux plate 27.

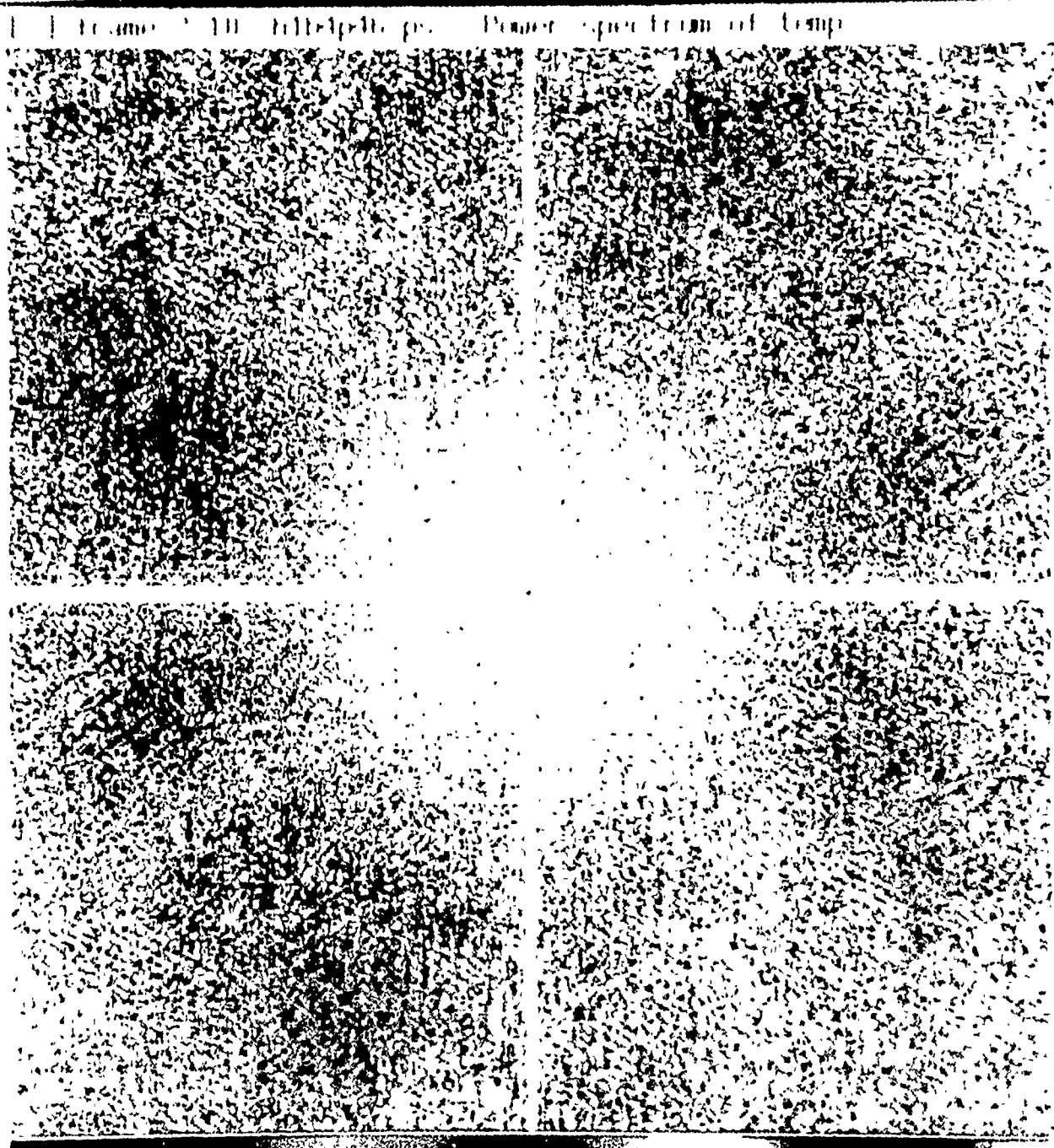


Figure 1j. - The two-dimensional power spectrum of the enhanced 100 μ m IRAS Skyflux plate 46.

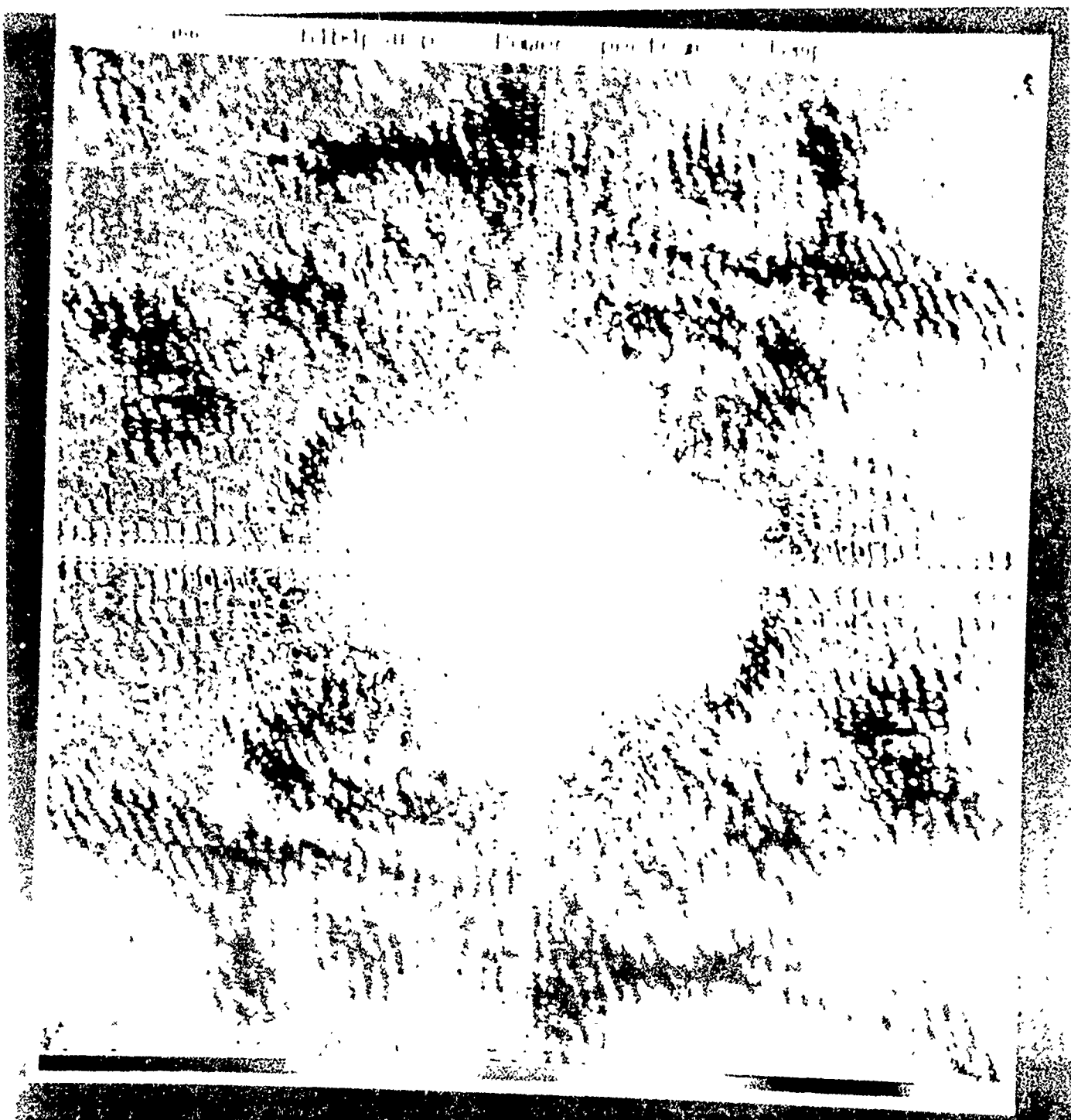


Figure 1k. – The two-dimensional power spectrum of the enhanced 100 μ m IRAS Skyflux plate 50.

Figure 11. – The two-dimensional power spectrum of the enhanced 100μm IRAS Skyflux plate 62.



Figure 11. – The two-dimensional power spectrum of the enhanced 100μm IRAS Skyflux plate 62.

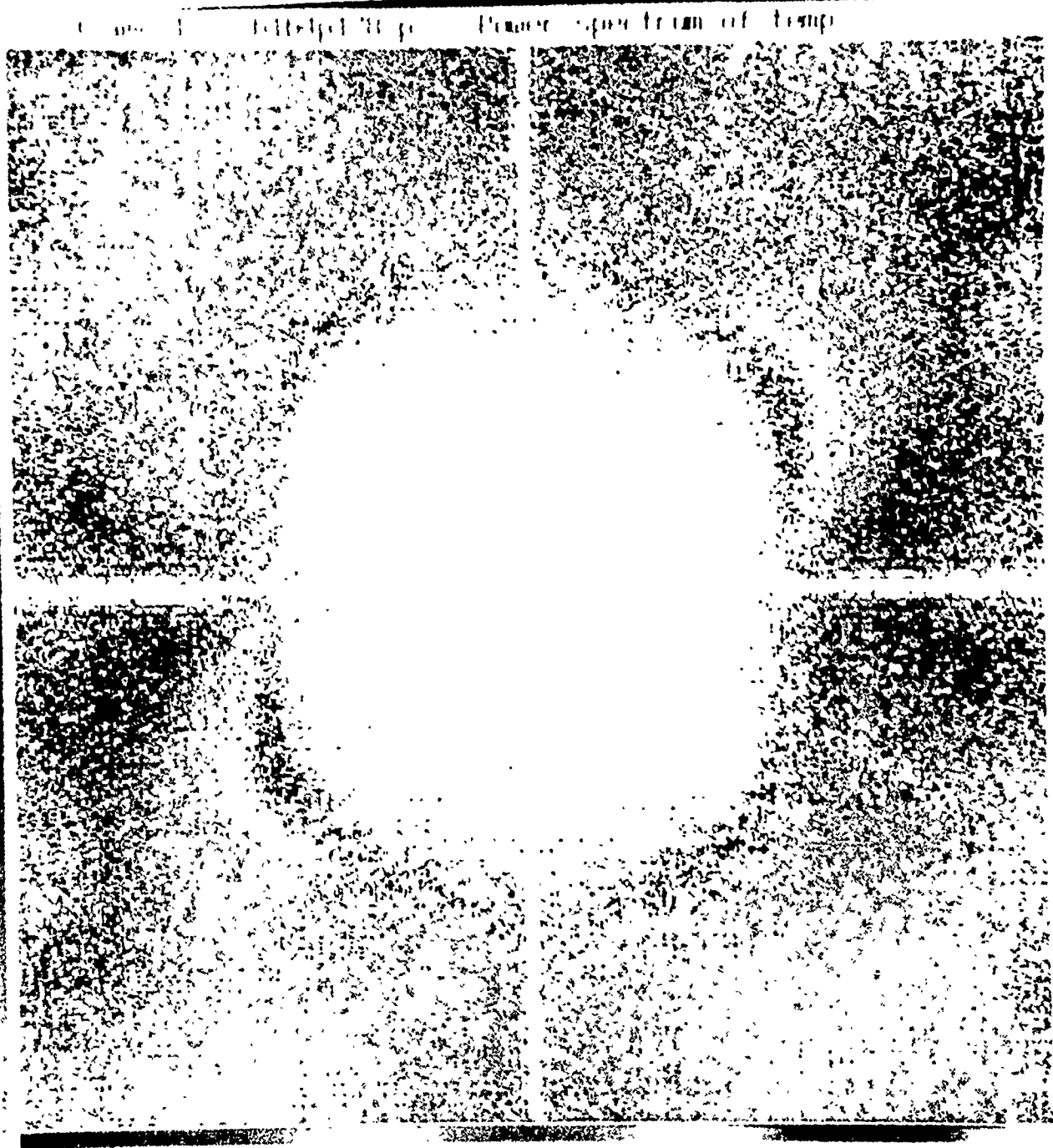


Figure 1m. – The two-dimensional power spectrum of the enhanced 100μm IRAS Skyflux plate 178.

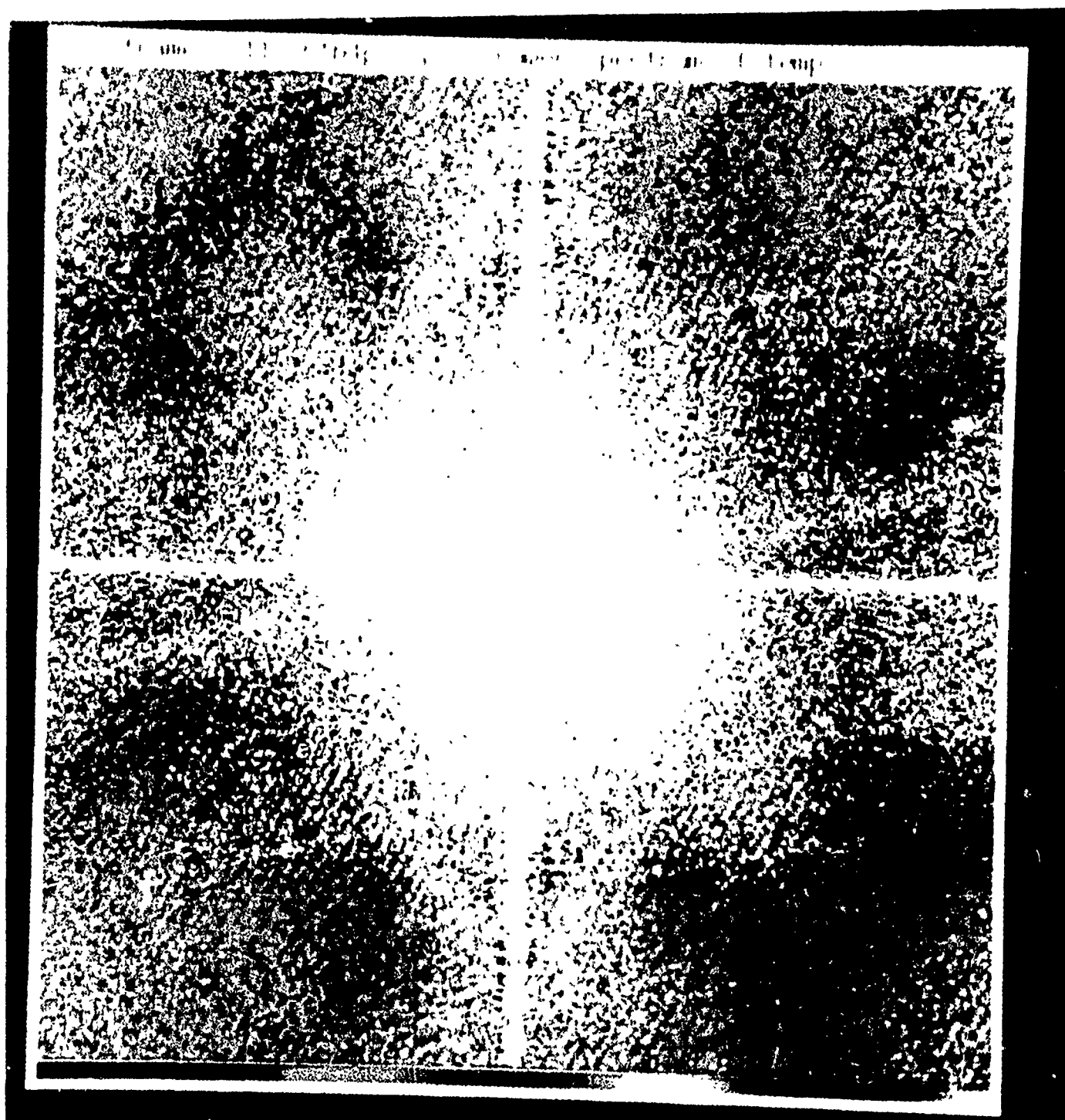


Figure 1n. – The two-dimensional power spectrum of the enhanced 100 μ m IRAS Skyflux plate 75.

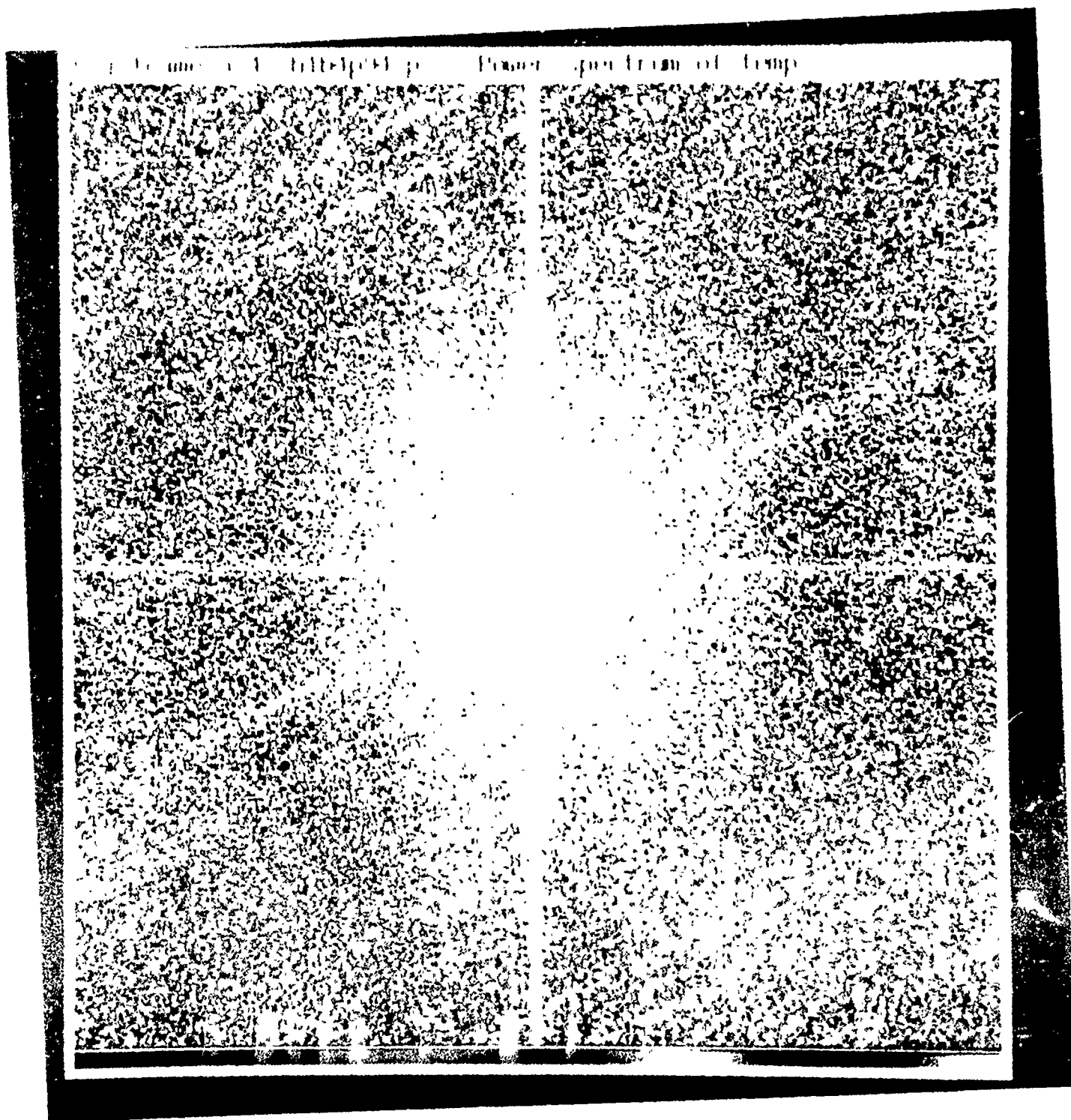


Figure 10. – The two-dimensional power spectrum of the enhanced 100 μ m IRAS Skyflux plate 94.

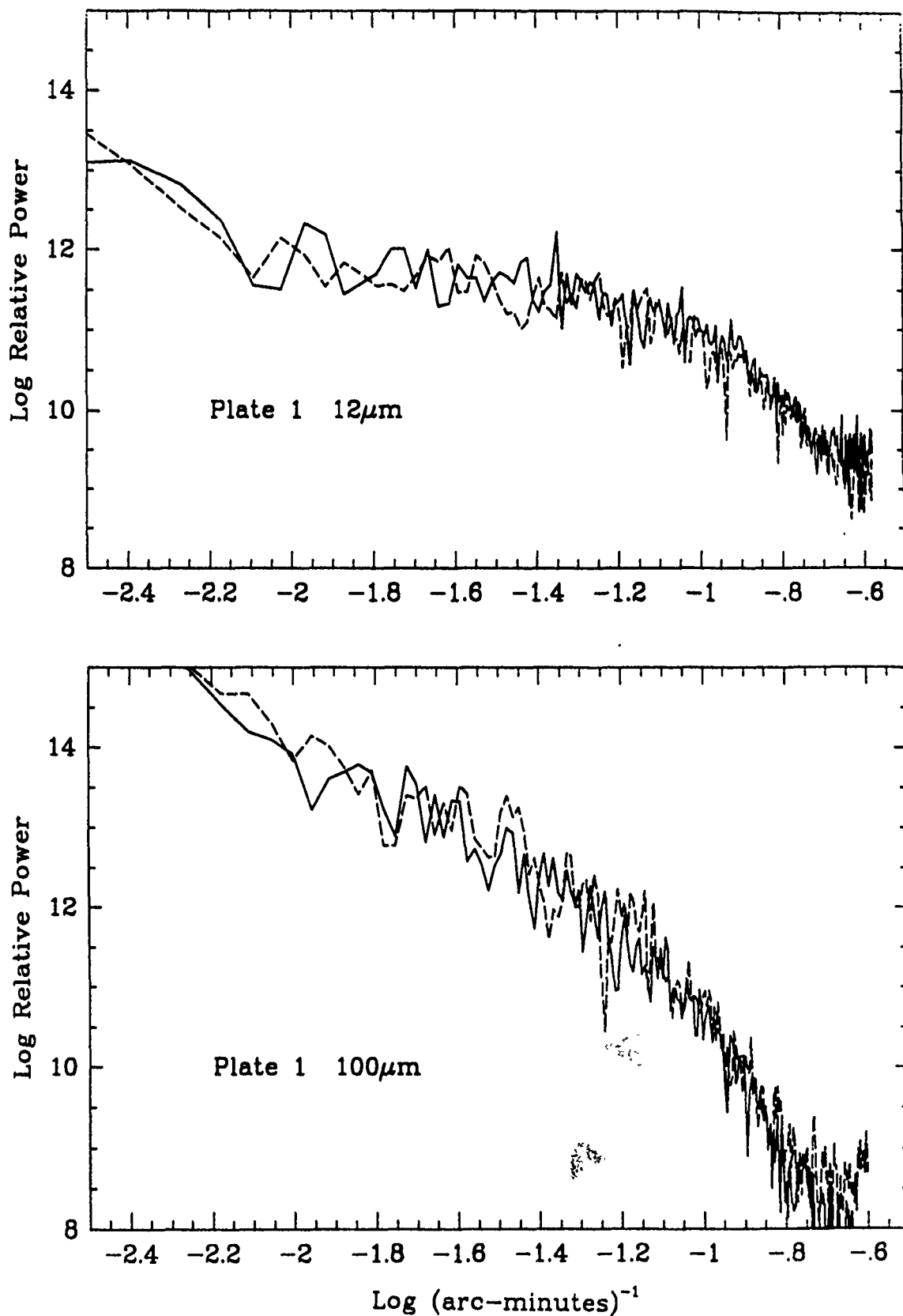


Figure 2a. – Radial profiles of the 12 μ m (top) and 100 μ m (bottom) two-dimensional power spectra of IRAS Skyflux plate 1. The solid line represent a cut taken at a position angle of 20° measured clockwise from the vertical, and the dashed line represents the profile taken at 110°.

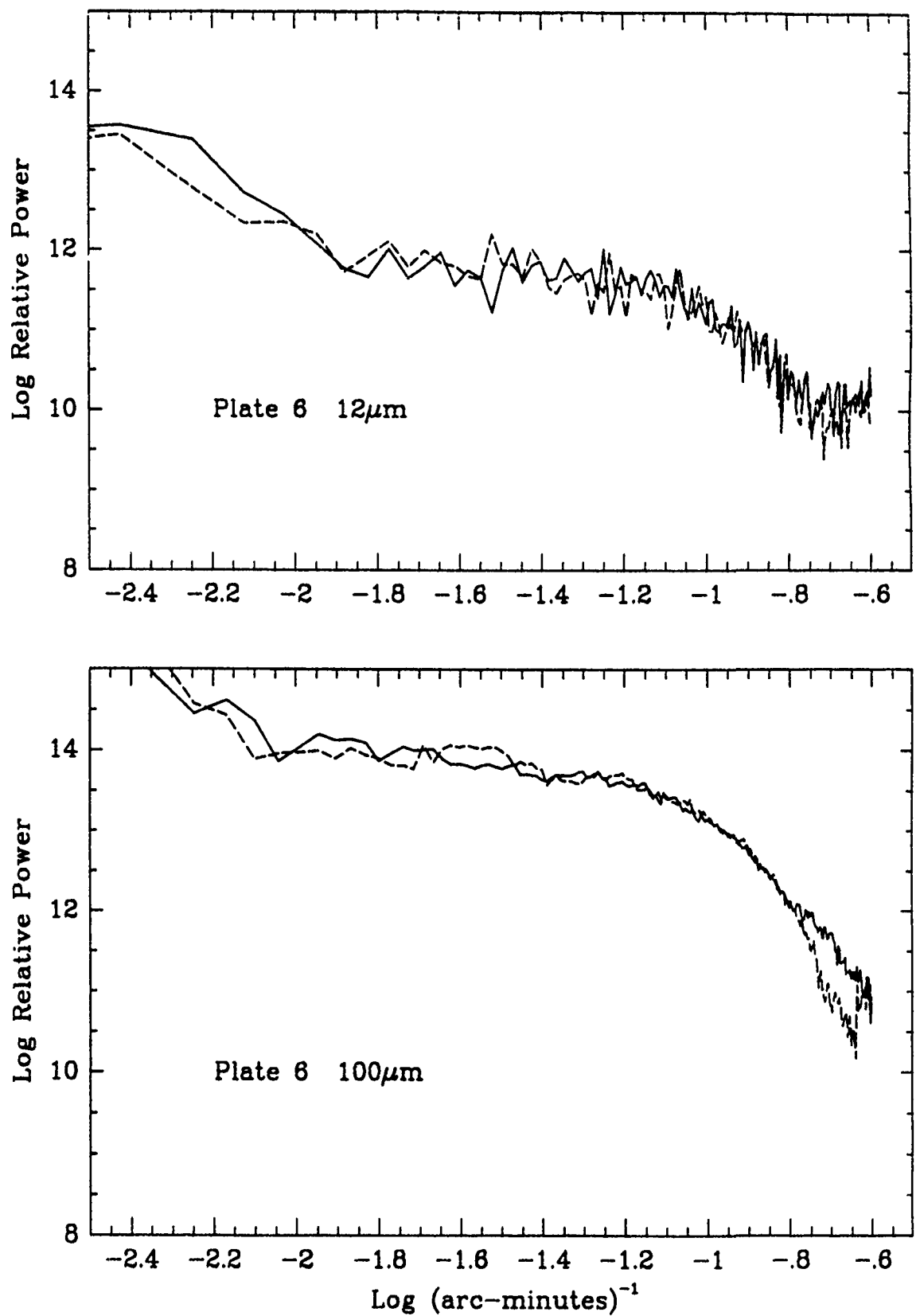


Figure 2b. — Cross-sectional cuts through the 12 μ m (top) and 100 μ m (bottom) two-dimensional power spectra of IRAS Skyflux plate 6. The solid line represent a cut taken at a position angle of 20° measured clockwise from the vertical, and the dashed line represents the profile taken at 110°.

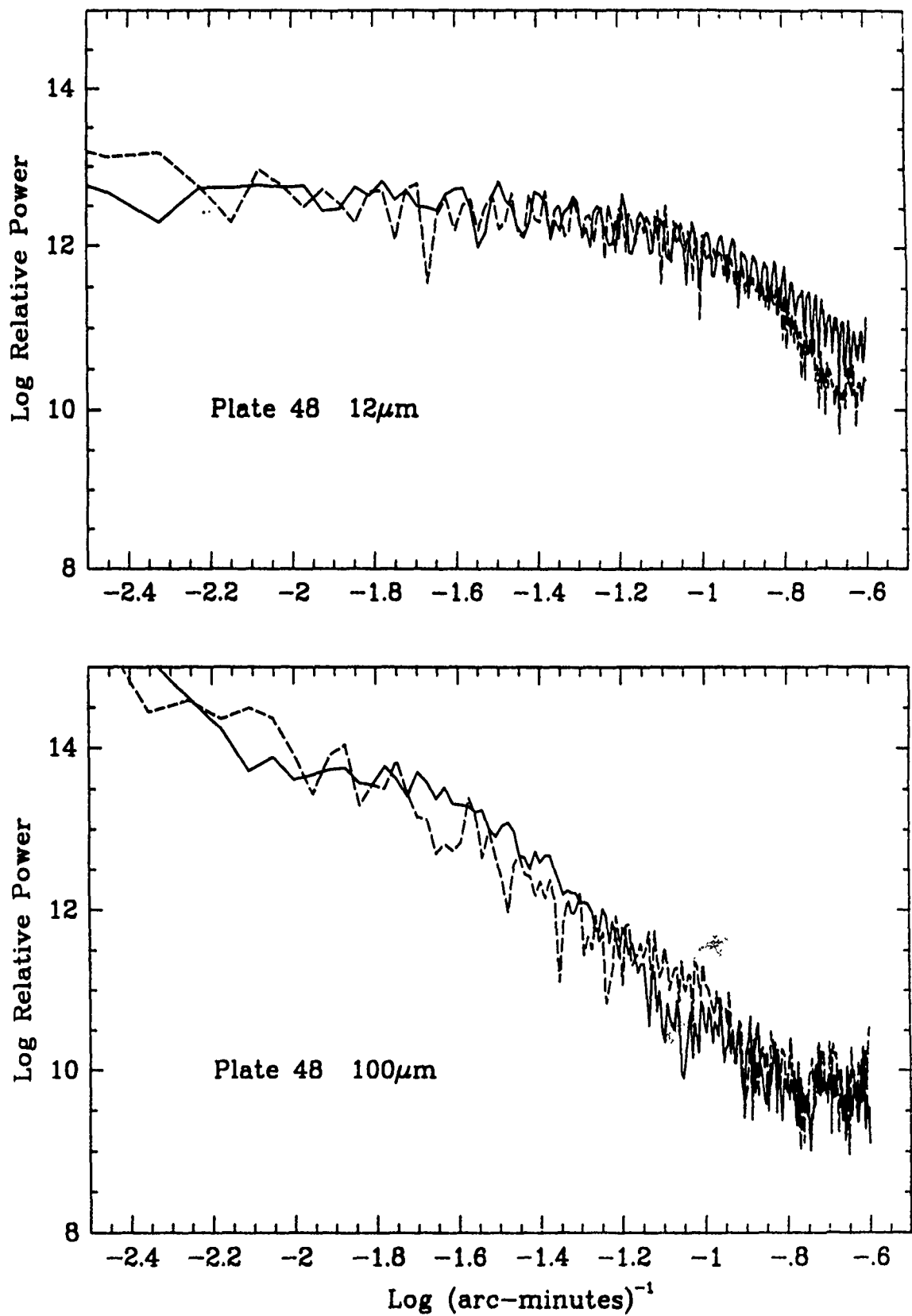


Figure 2c. – Cross-sectional cuts through the 12 μ m (top) and 100 μ m (bottom) two-dimensional power spectra of IRAS Skyflux plate 48. The solid line represent a cut taken at a position angle of 20° measured clockwise from the vertical, and the dashed line represents the profile taken at 110°.

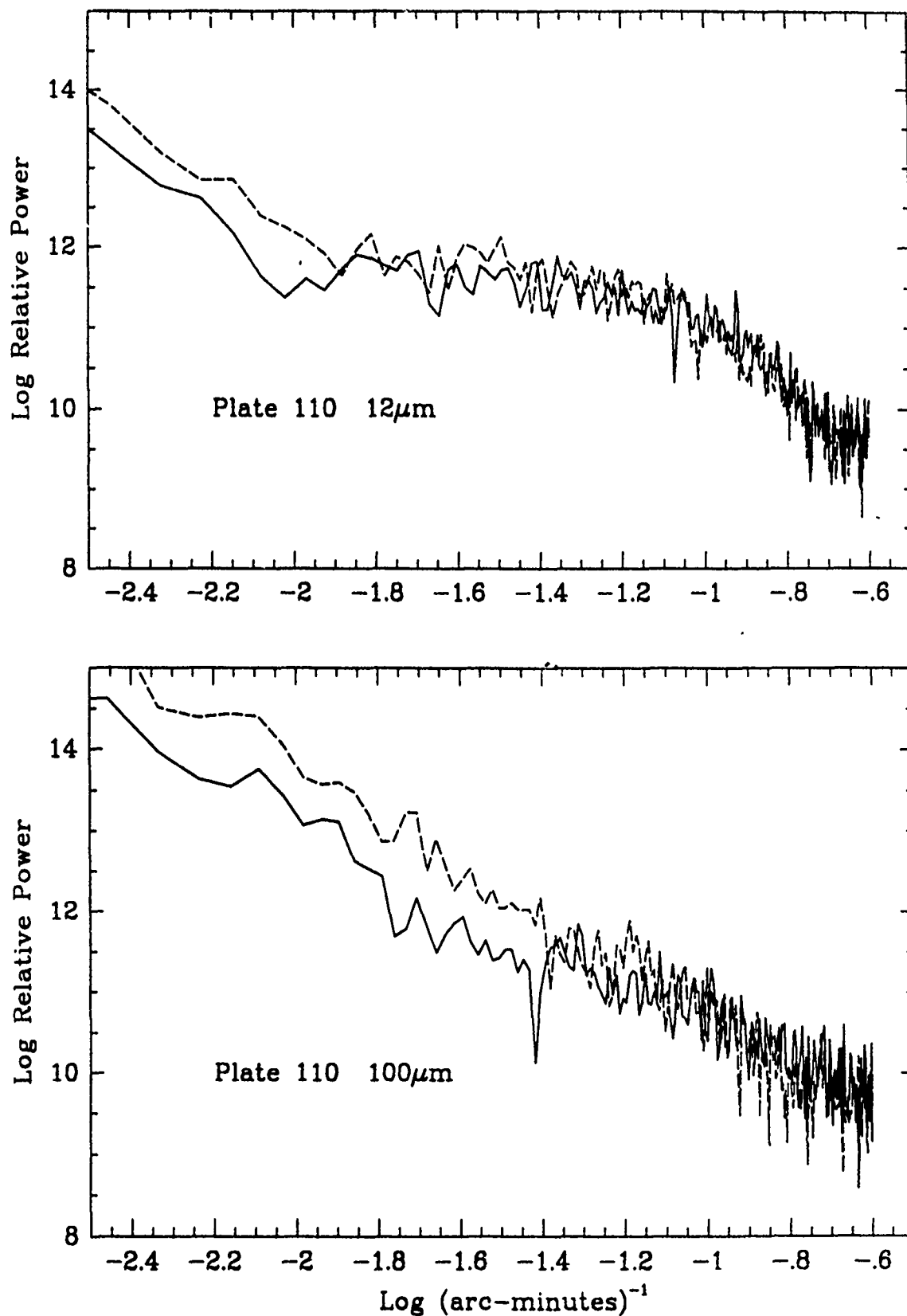
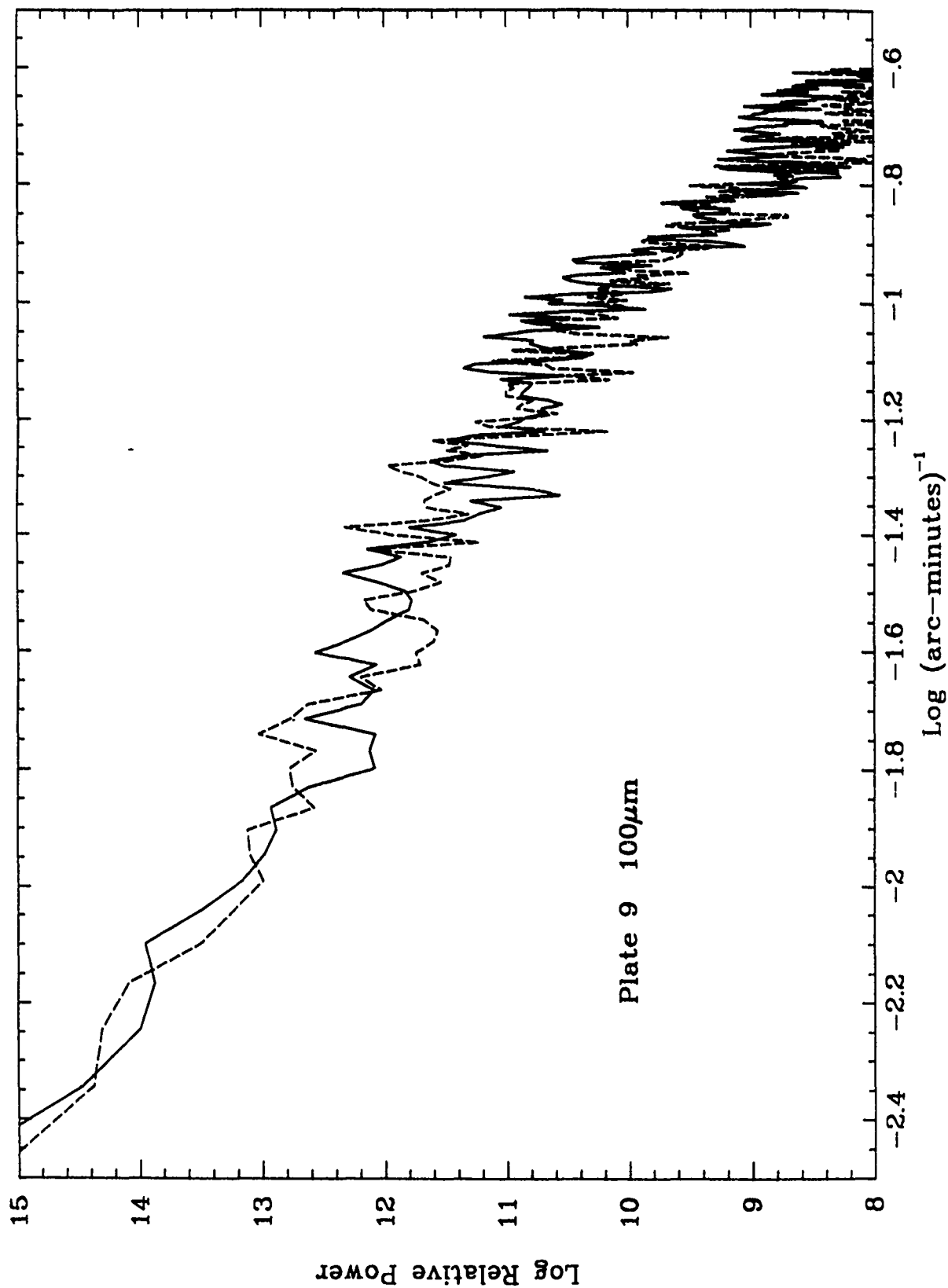


Figure 2d. – Cross-sectional cuts through the 12 μ m (top) and 100 μ m (bottom) two-dimensional power spectra of IRAS Skyflux plate 110. The solid line represent a cut taken at a position angle of 20° measured clockwise from the vertical, and the dashed line represents the profile taken at 110°.



Figures 3a-a. - Cross-sectional cuts through the 100 μ m two-dimensional power spectra of 21 different IRAS Skyflux plates. As in Figures 2a-c, the cross sections taken at position angles of 20° are shown as solid lines, and those at 110° are shown as dashed lines.

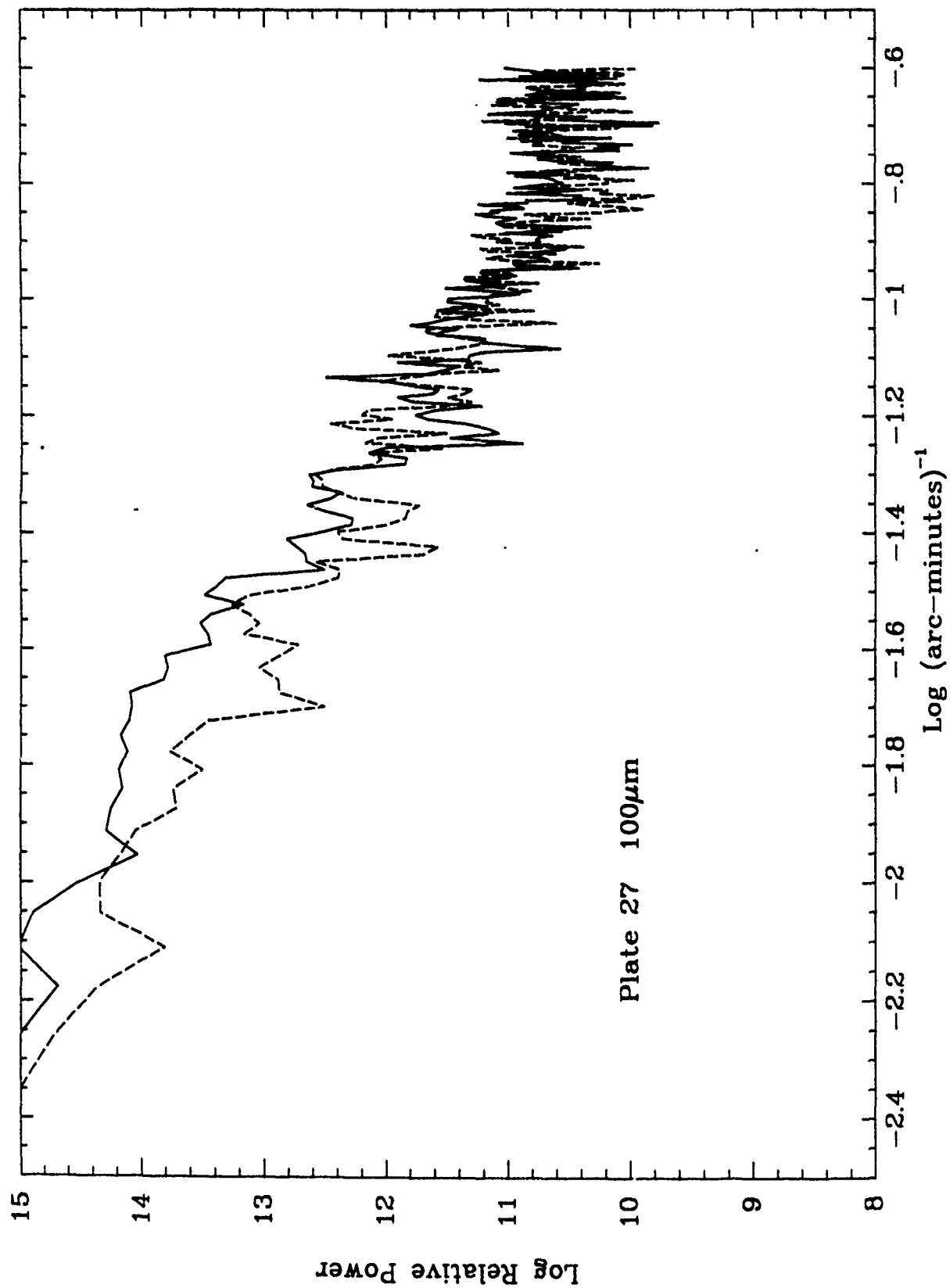


Figure 3b.

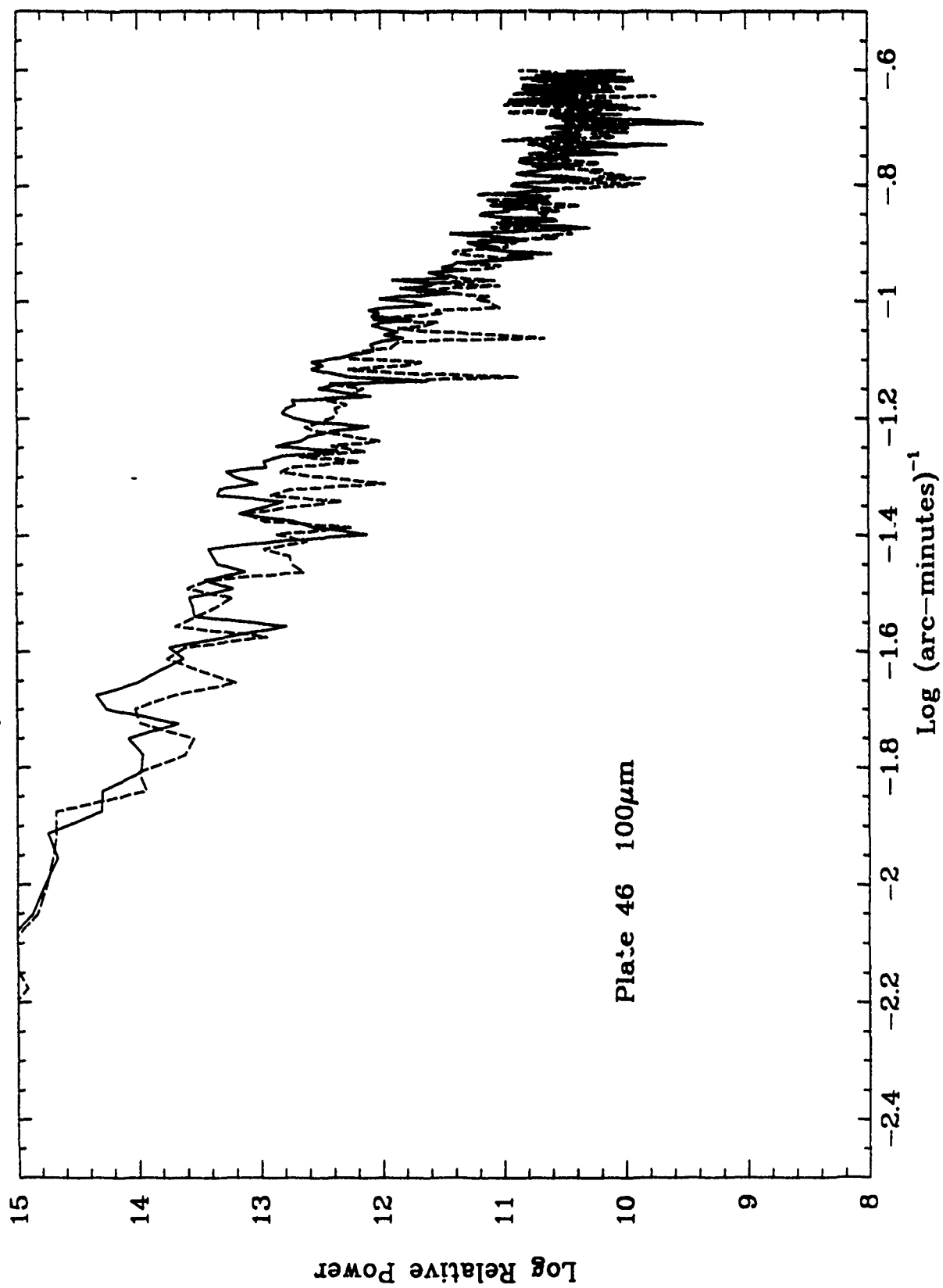


Figure 3c.

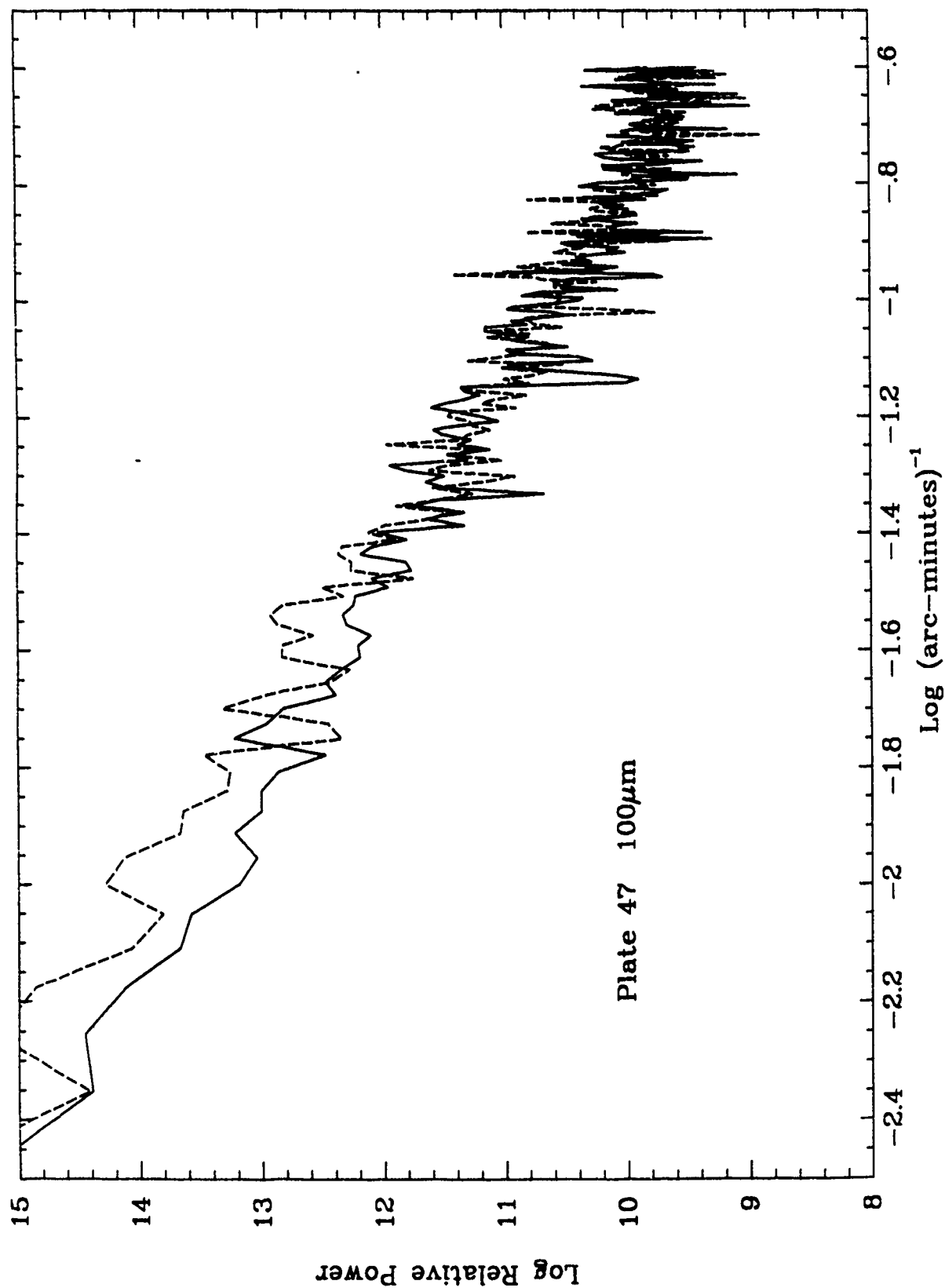


Figure 3d.

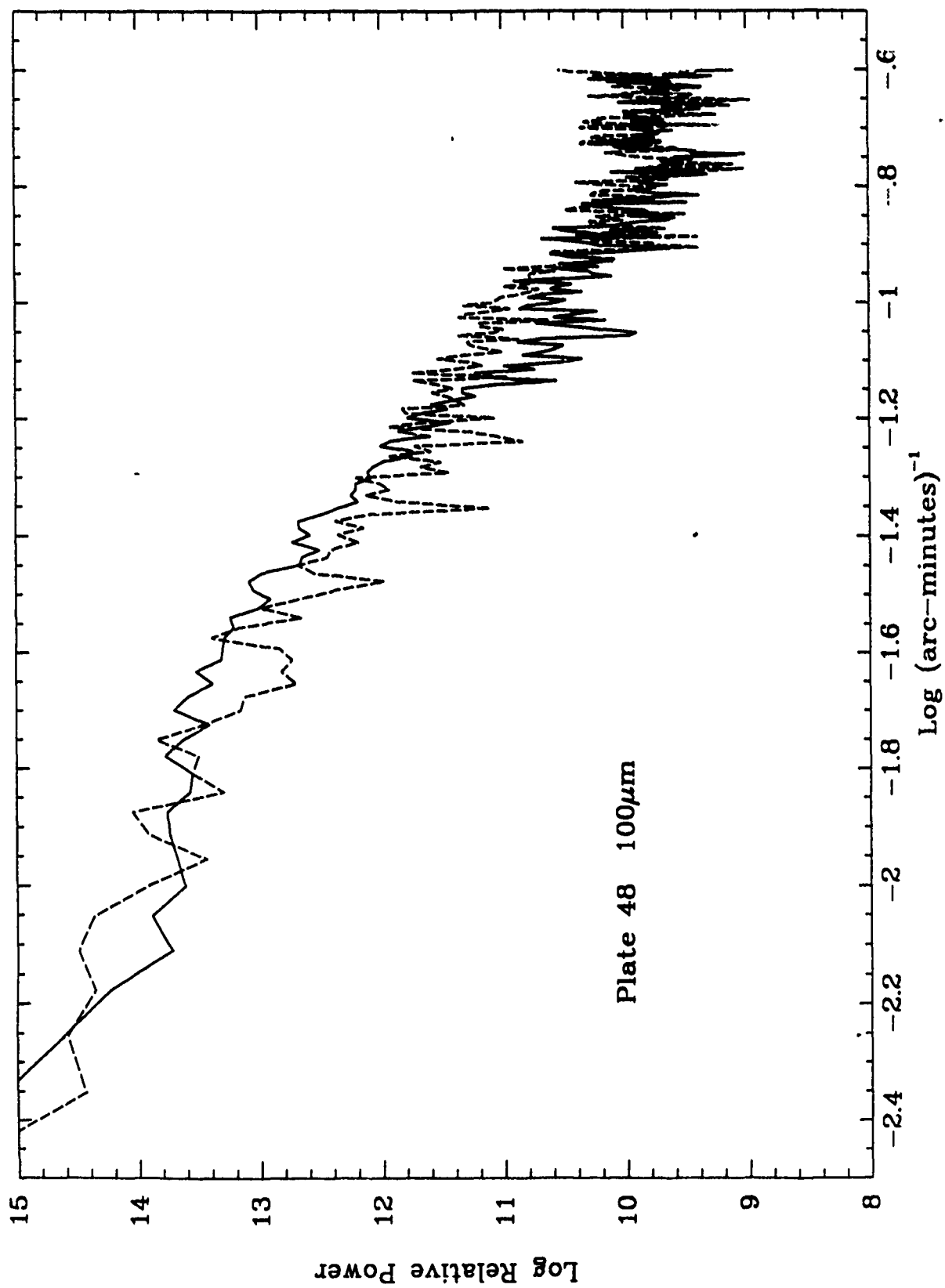


Figure 3e.

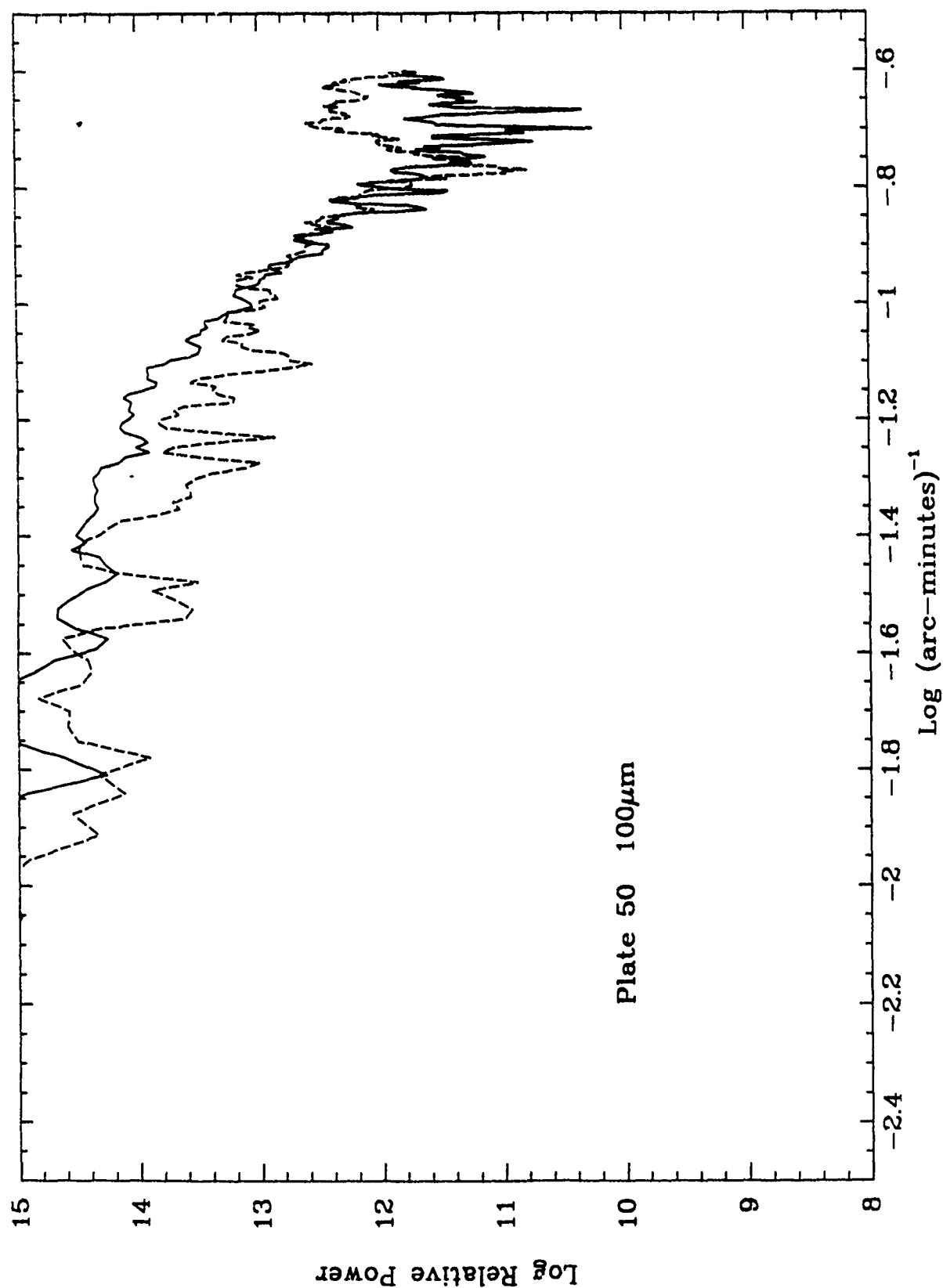


Figure 3f.

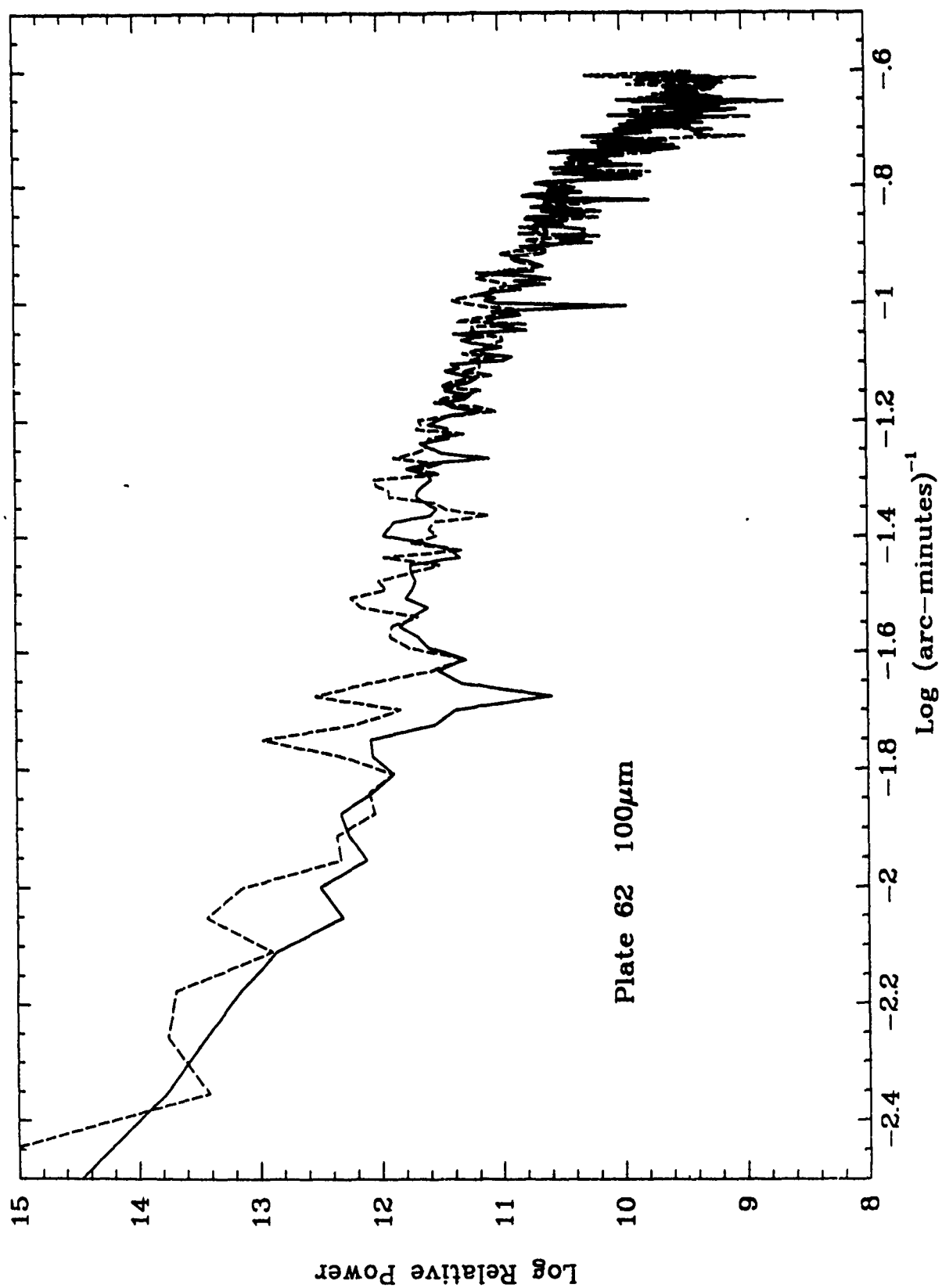


Figure 3g.

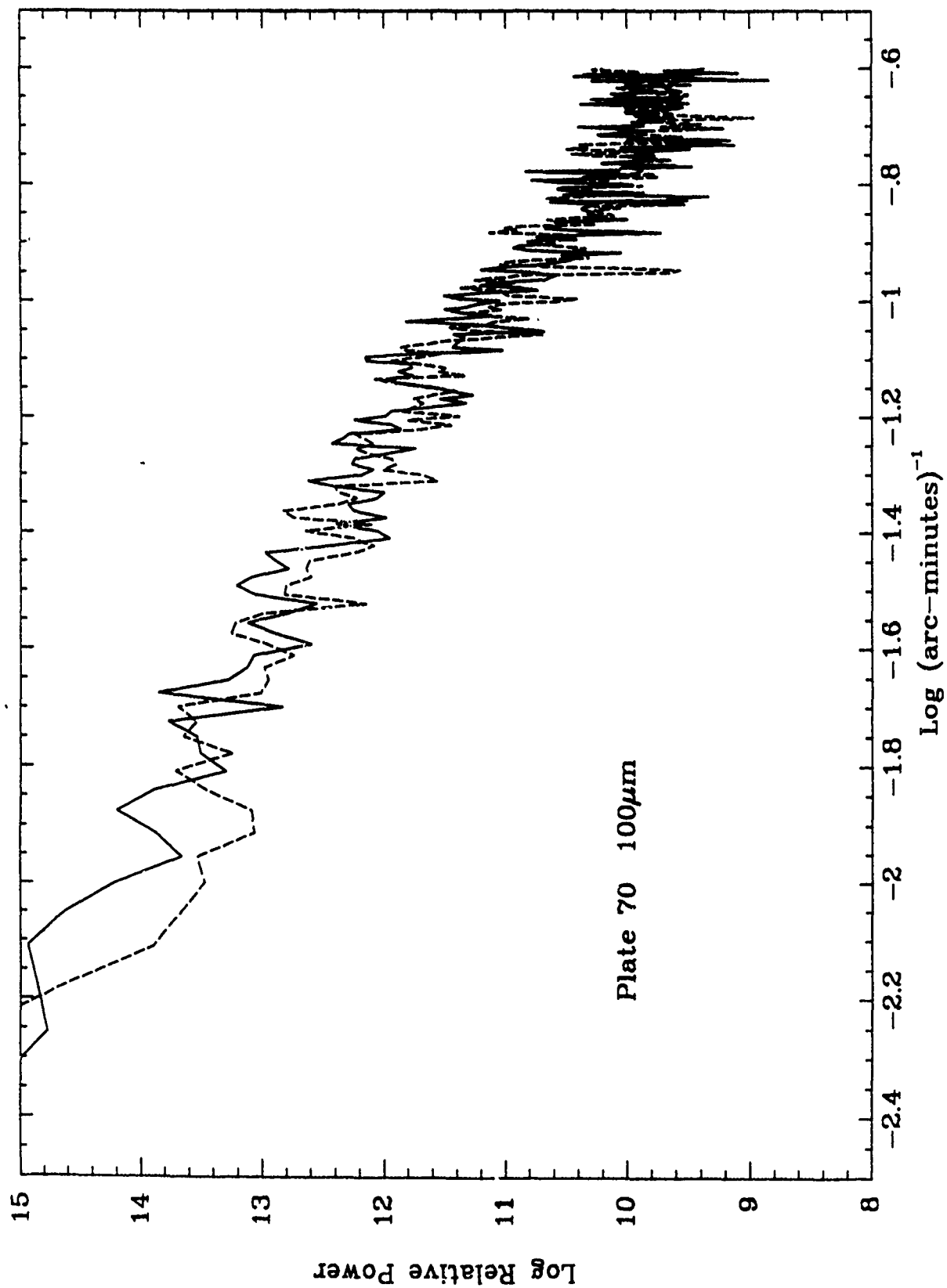


Figure 3h.

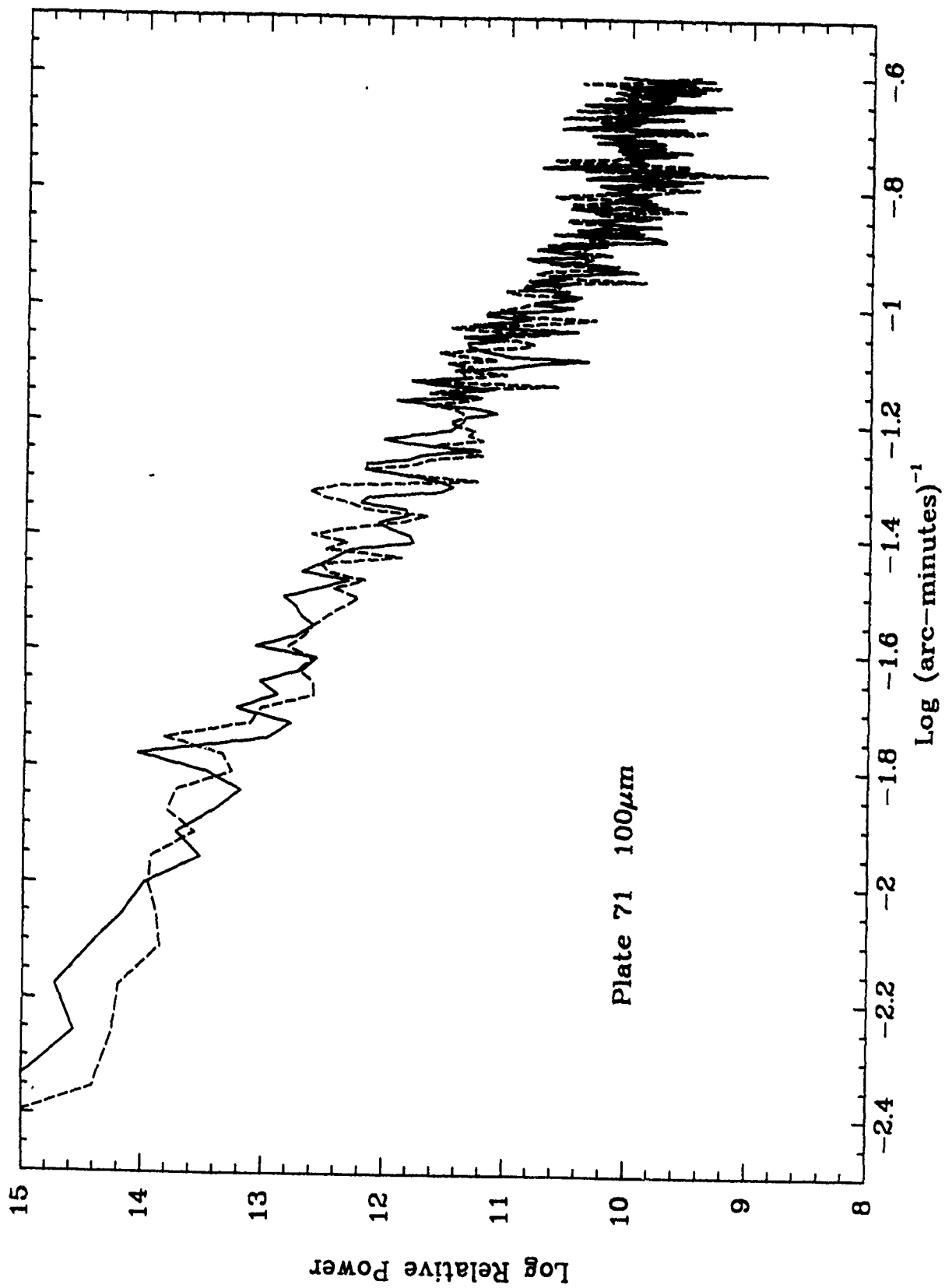


Figure 31.

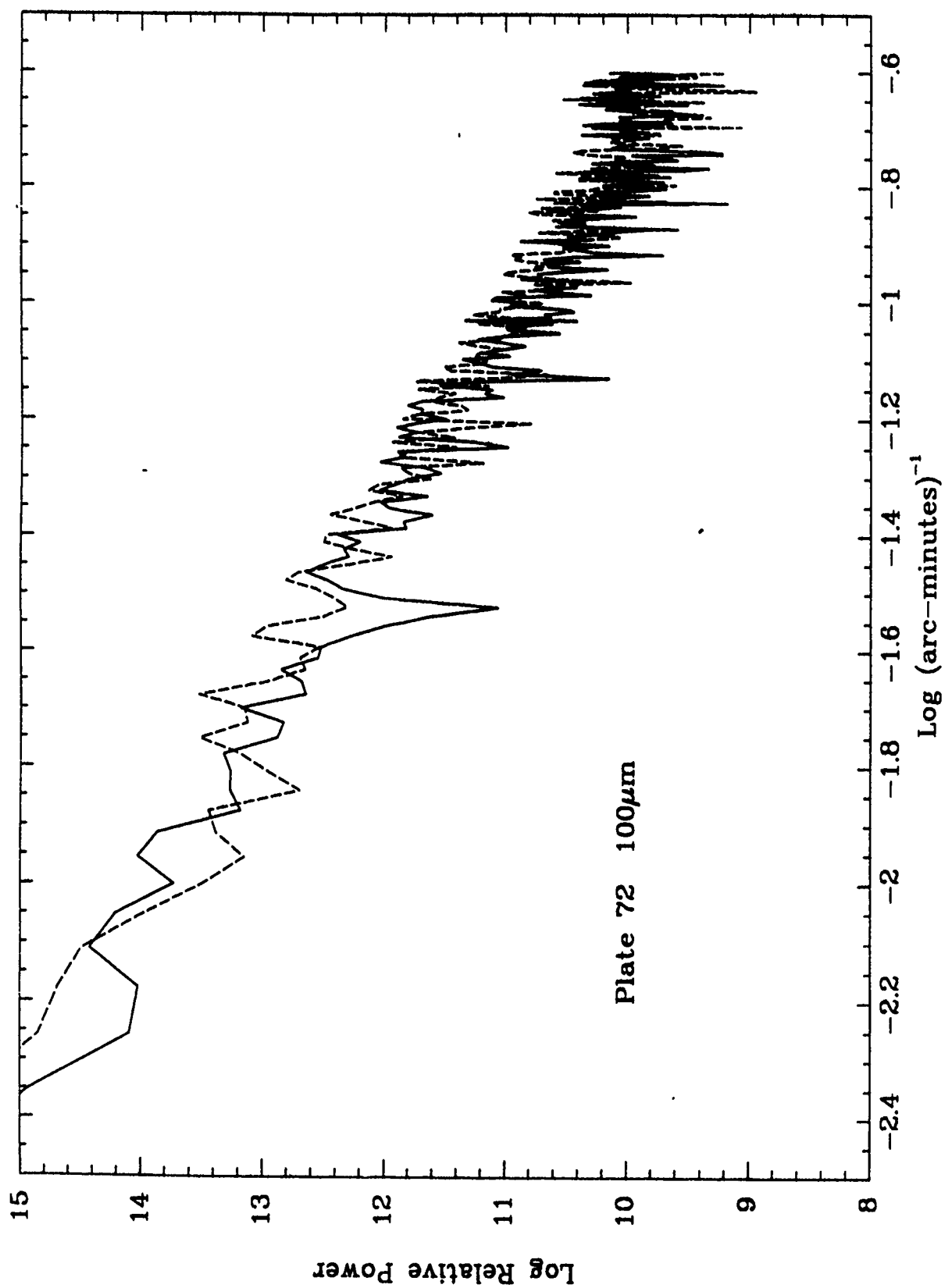


Figure 3j.

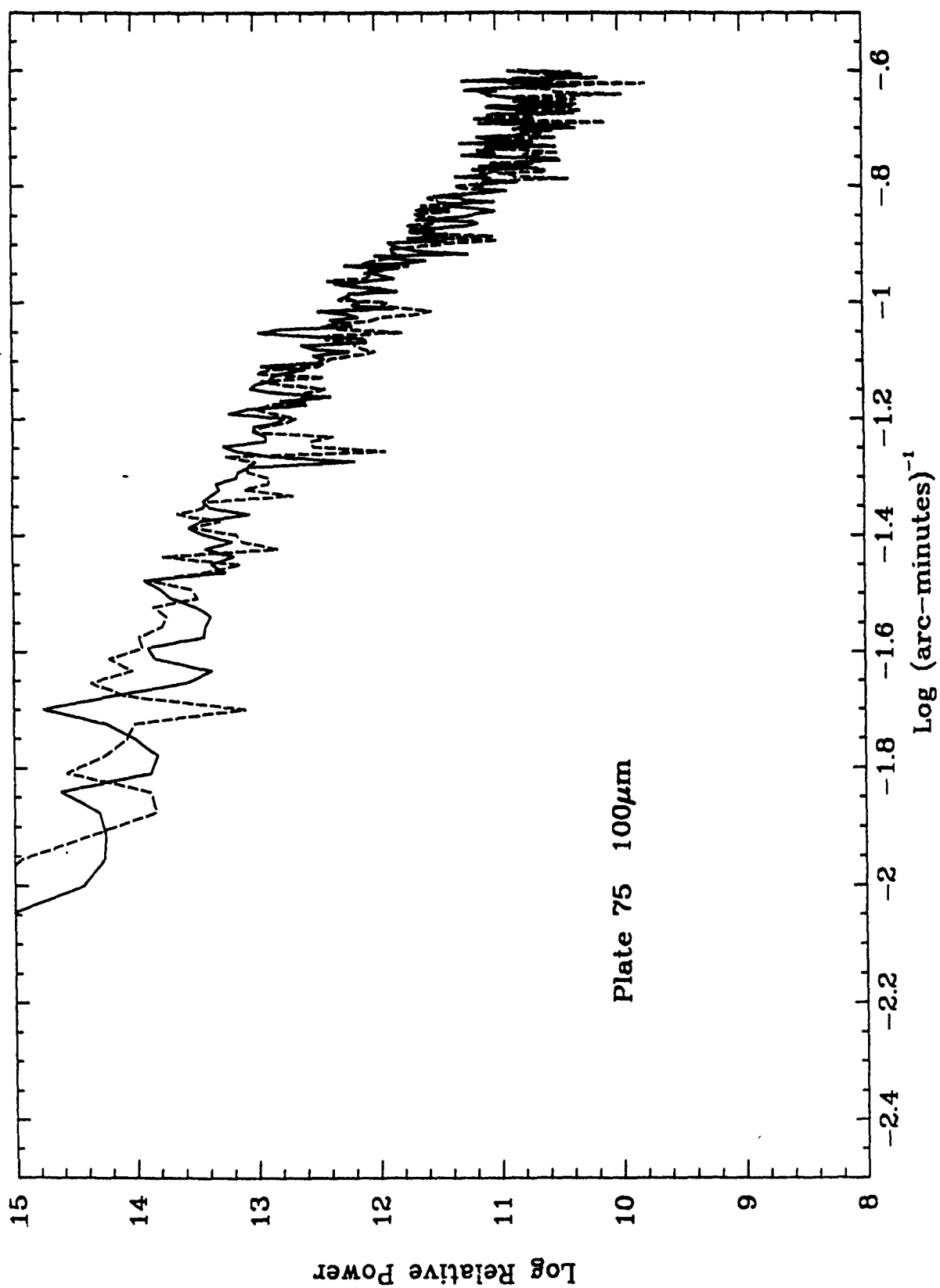


Figure 3k.

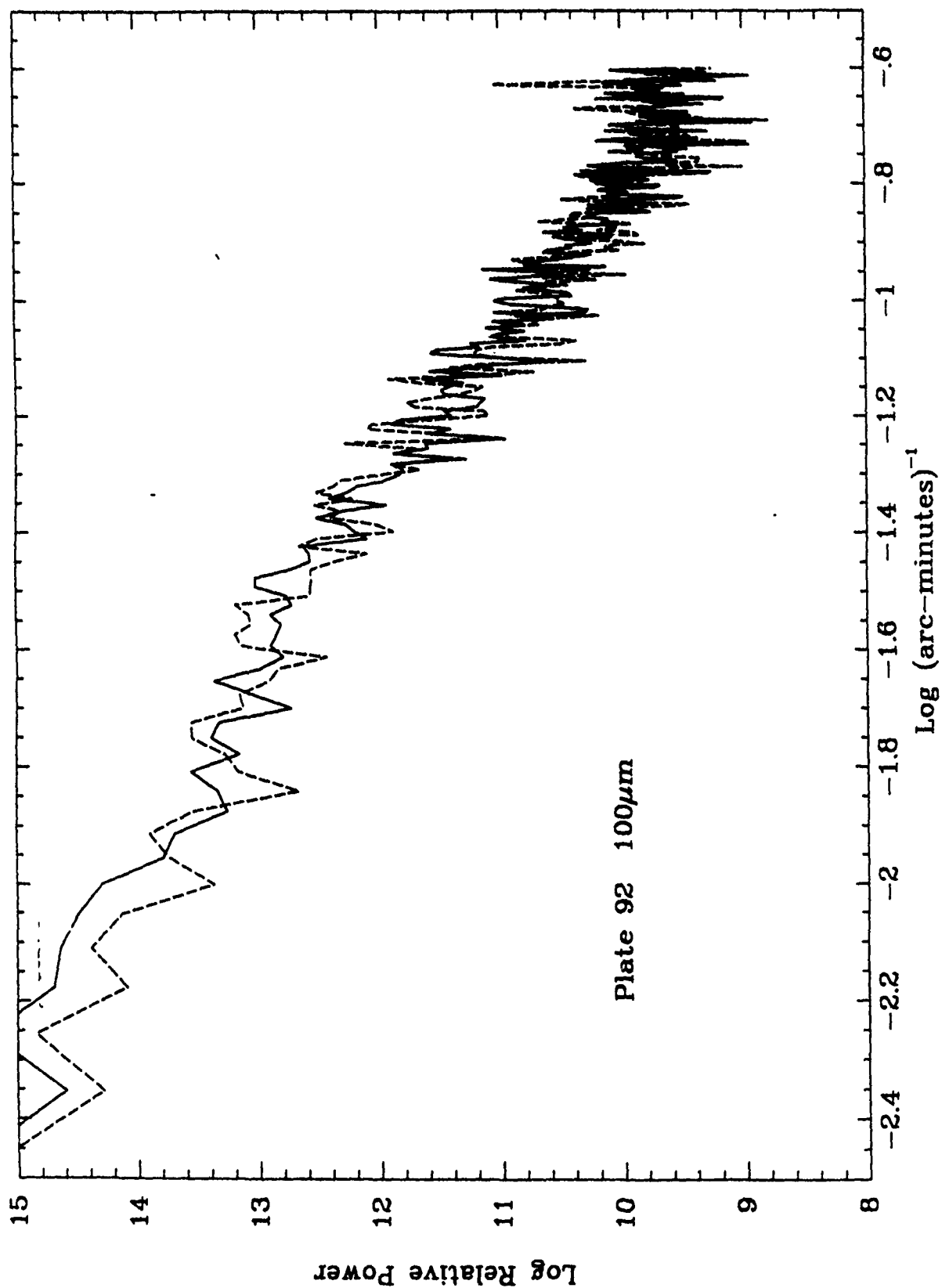


Figure 31.

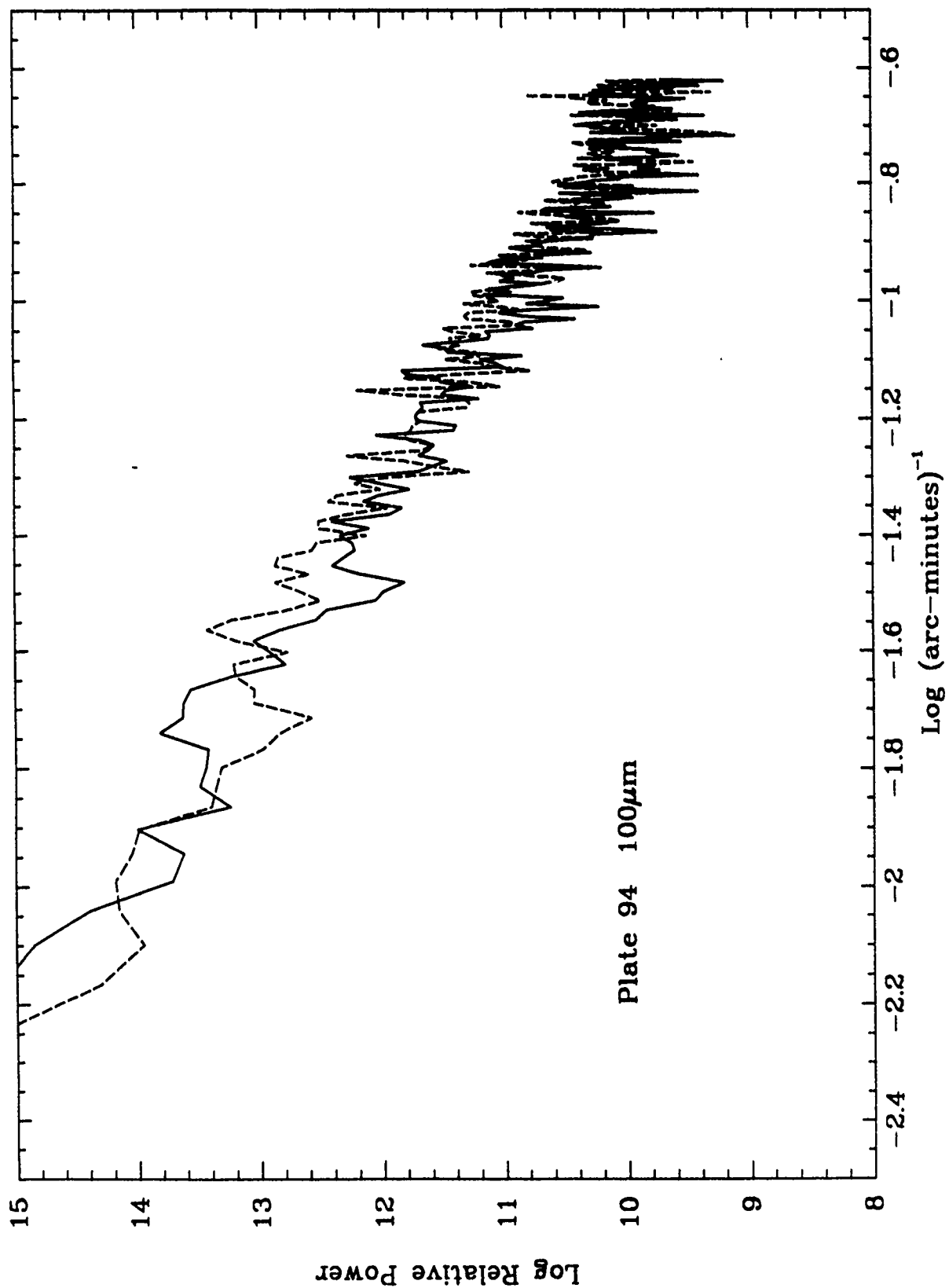


Figure 3m.

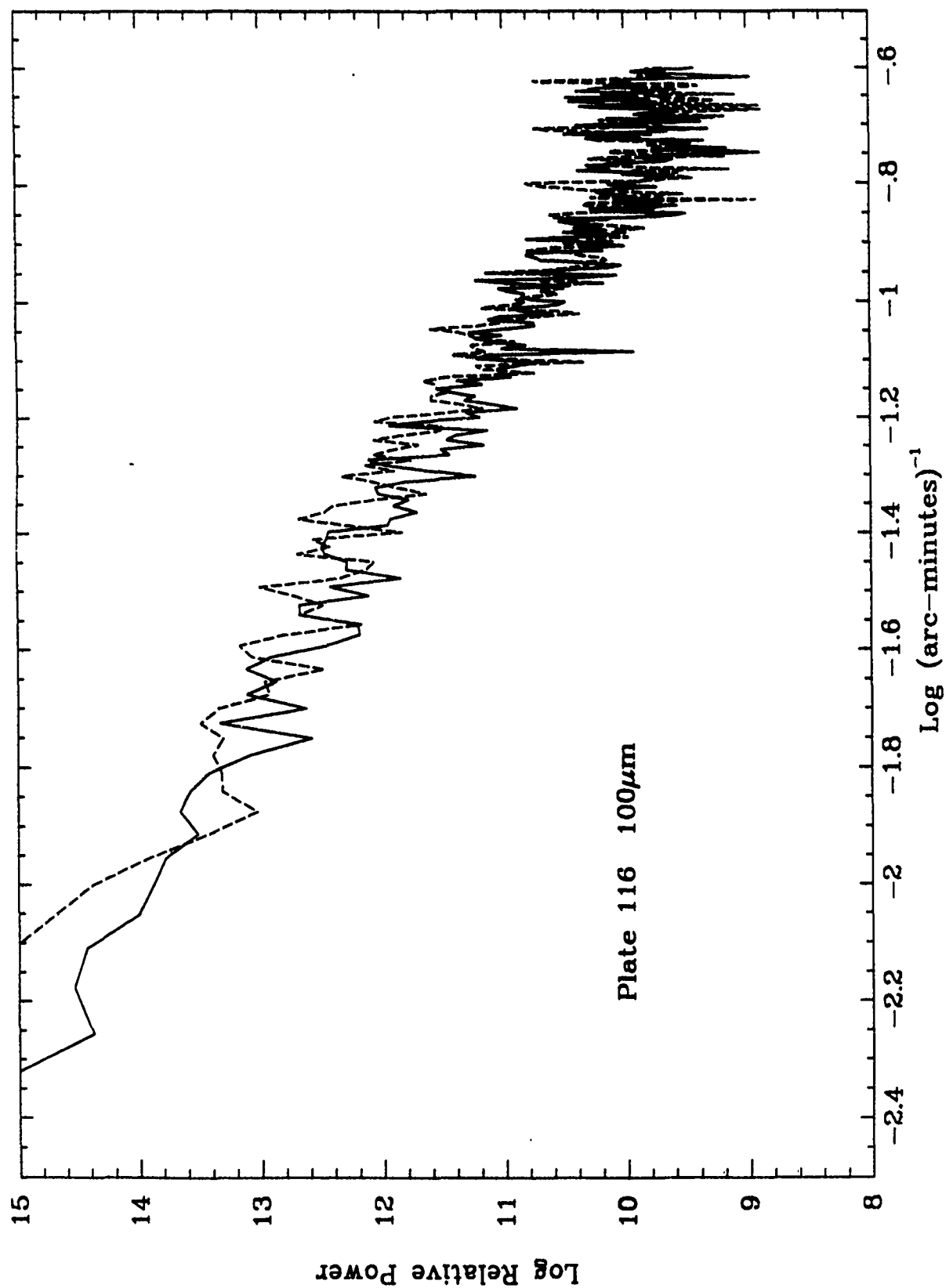


Figure 3n.

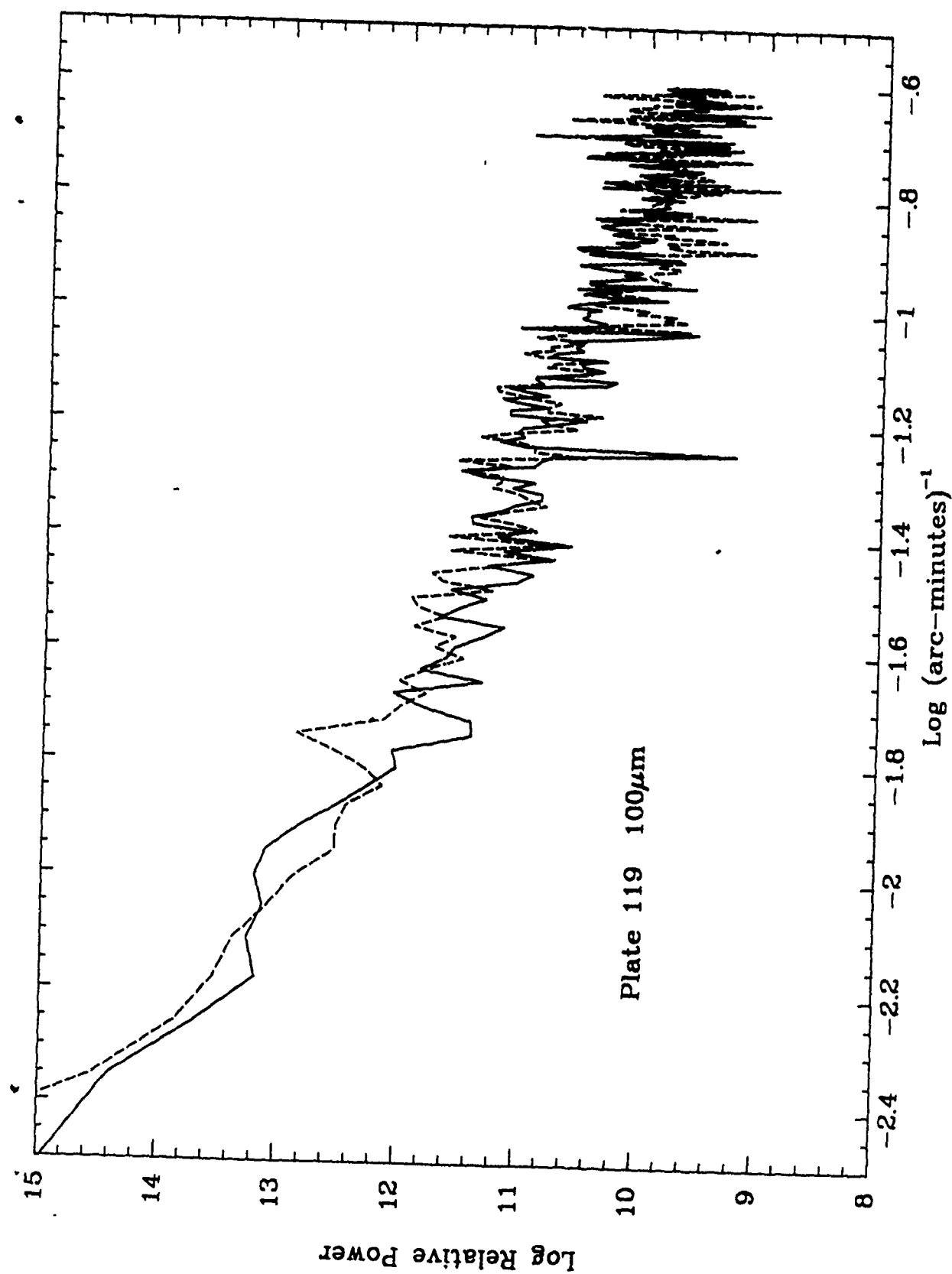


Figure 30.

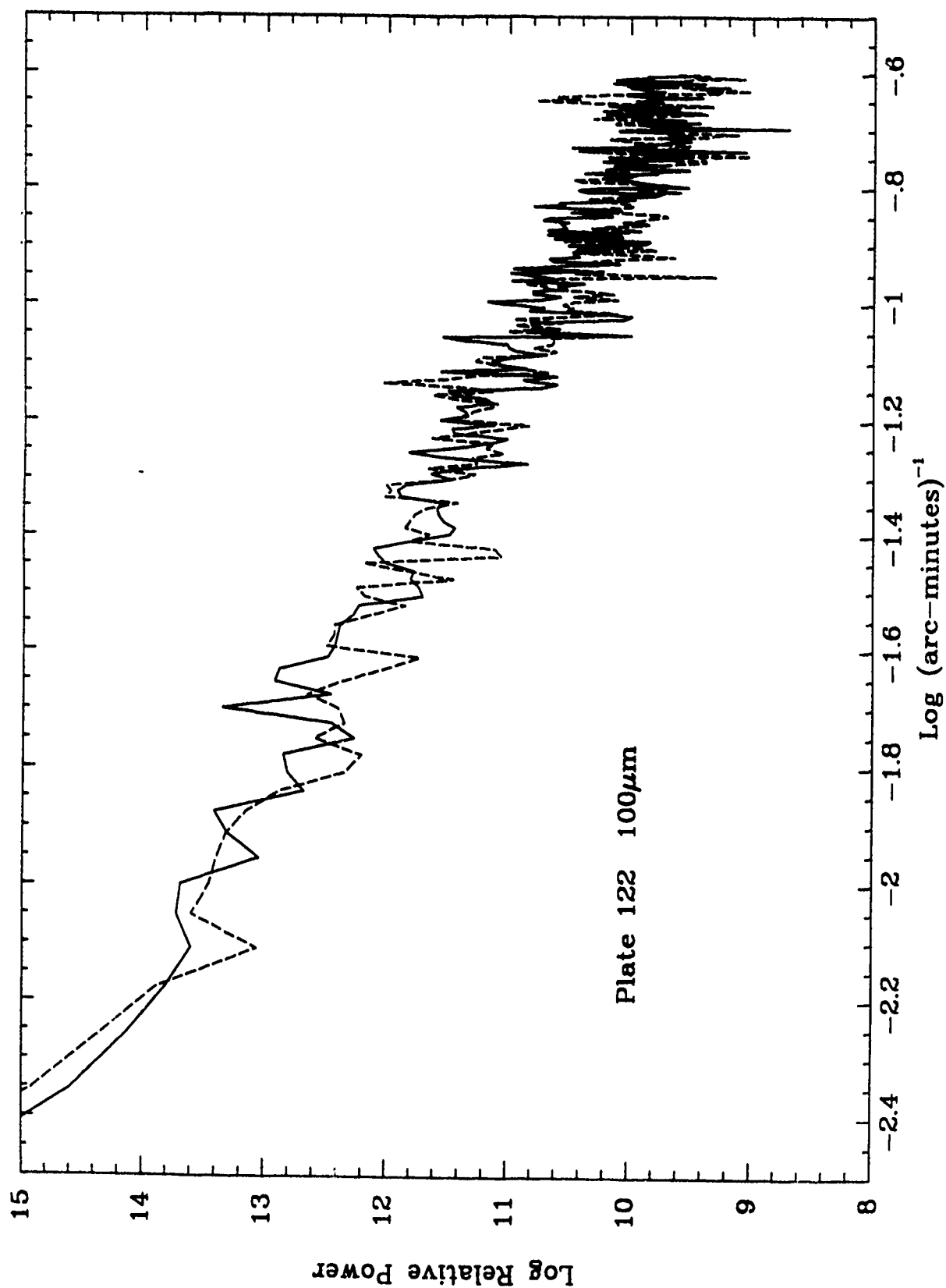


Figure 3p.

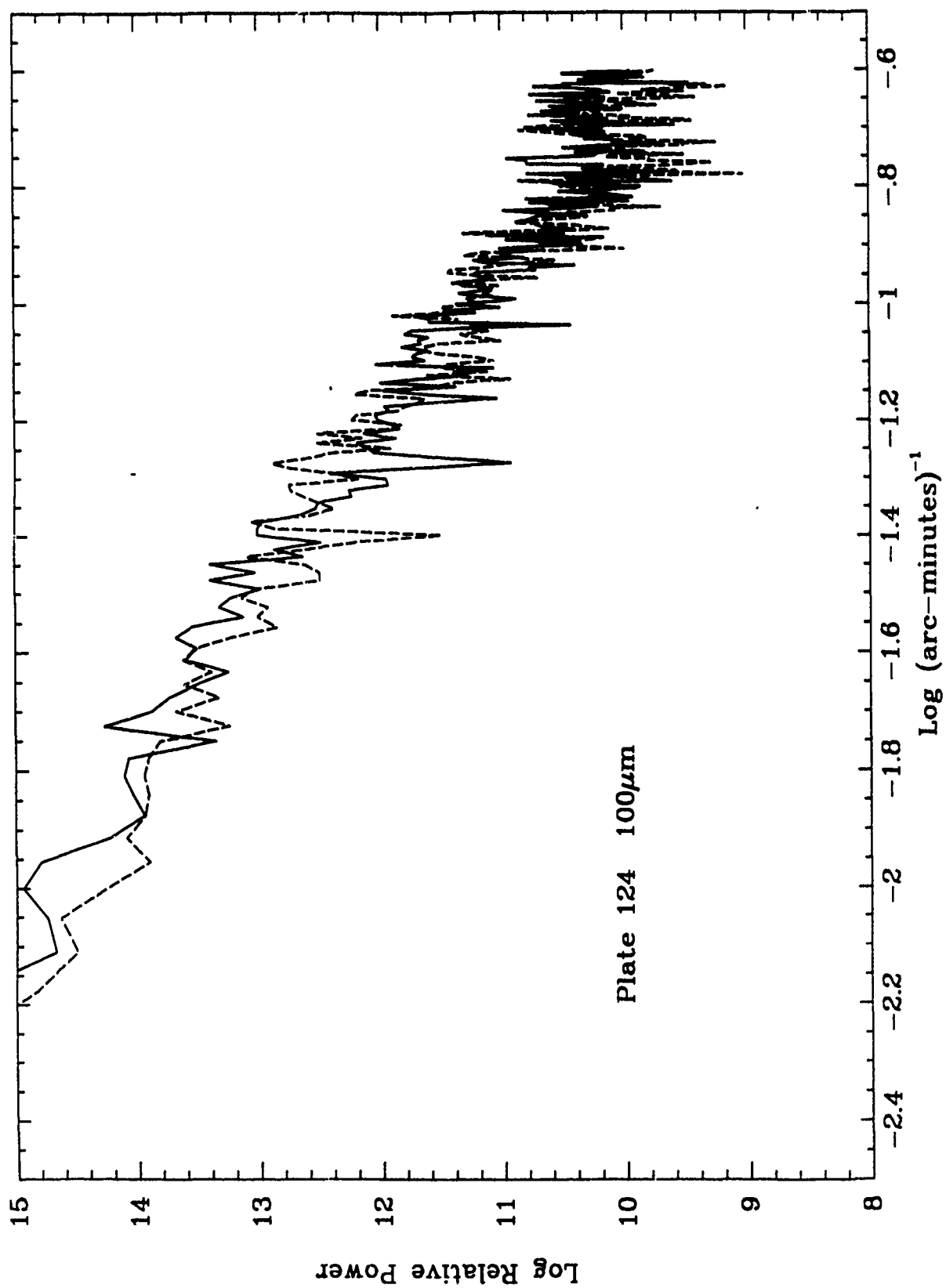


Figure 3q.

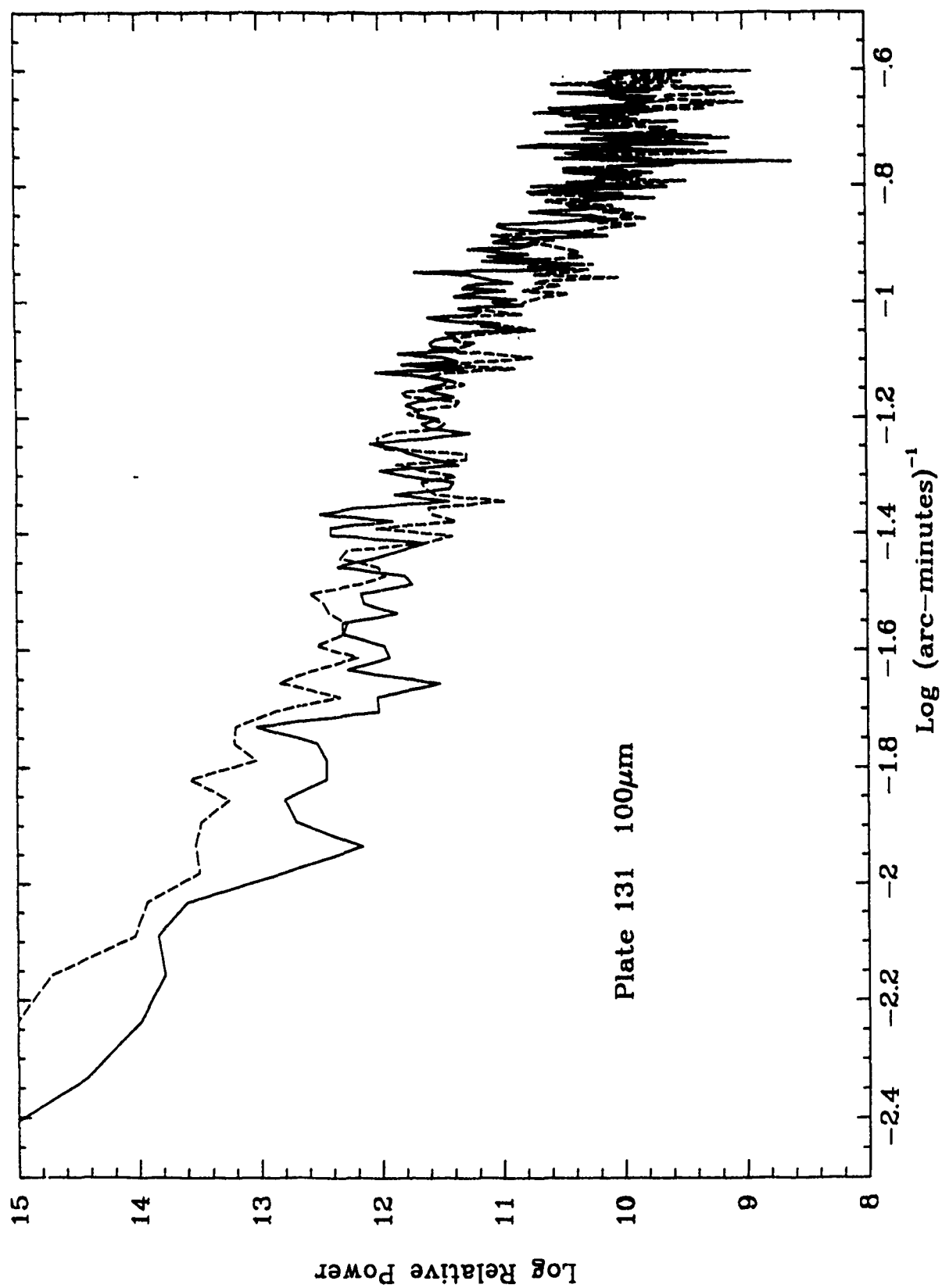


Figure 3r.

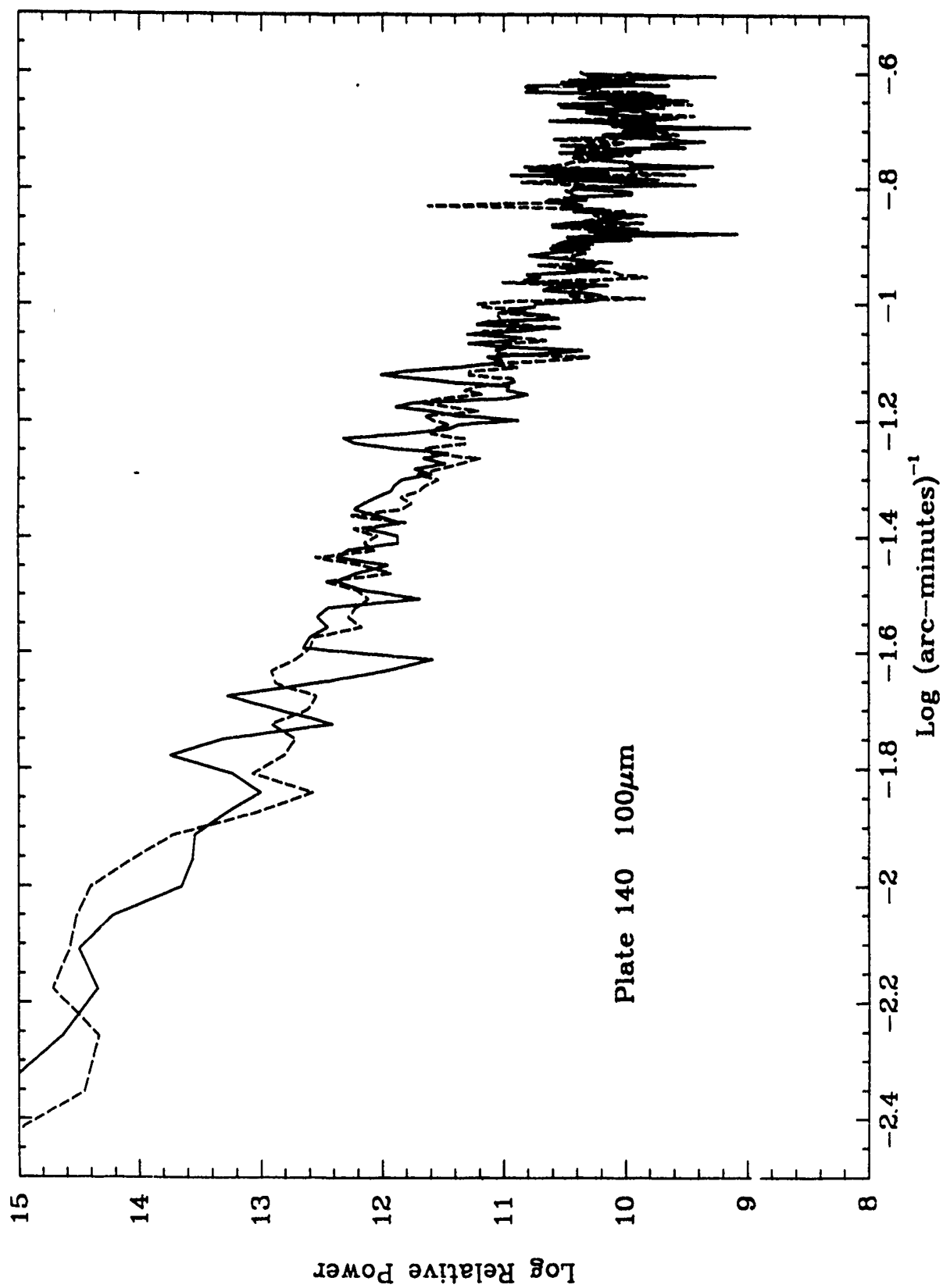


Figure 3s.

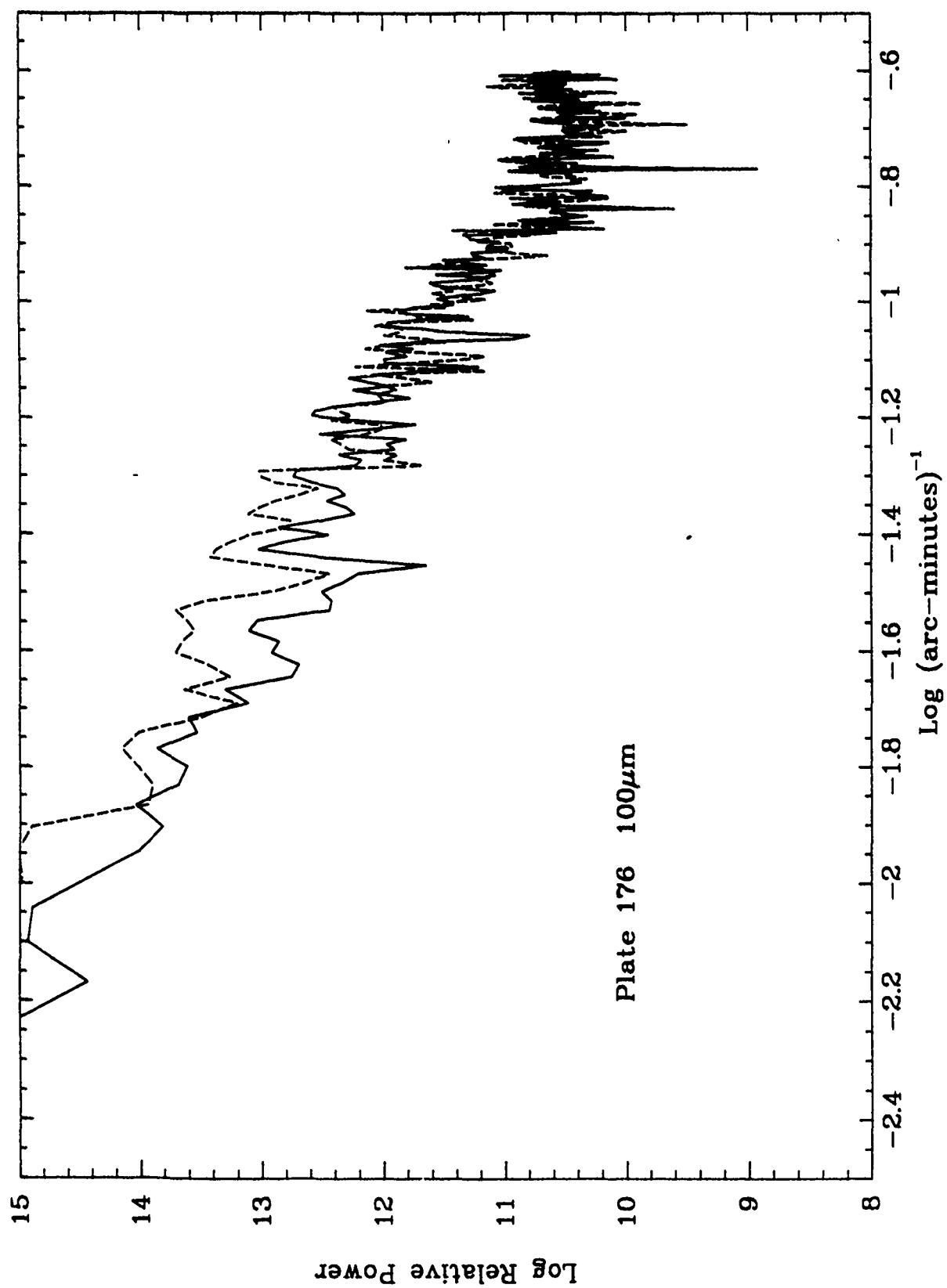


Figure 3t.

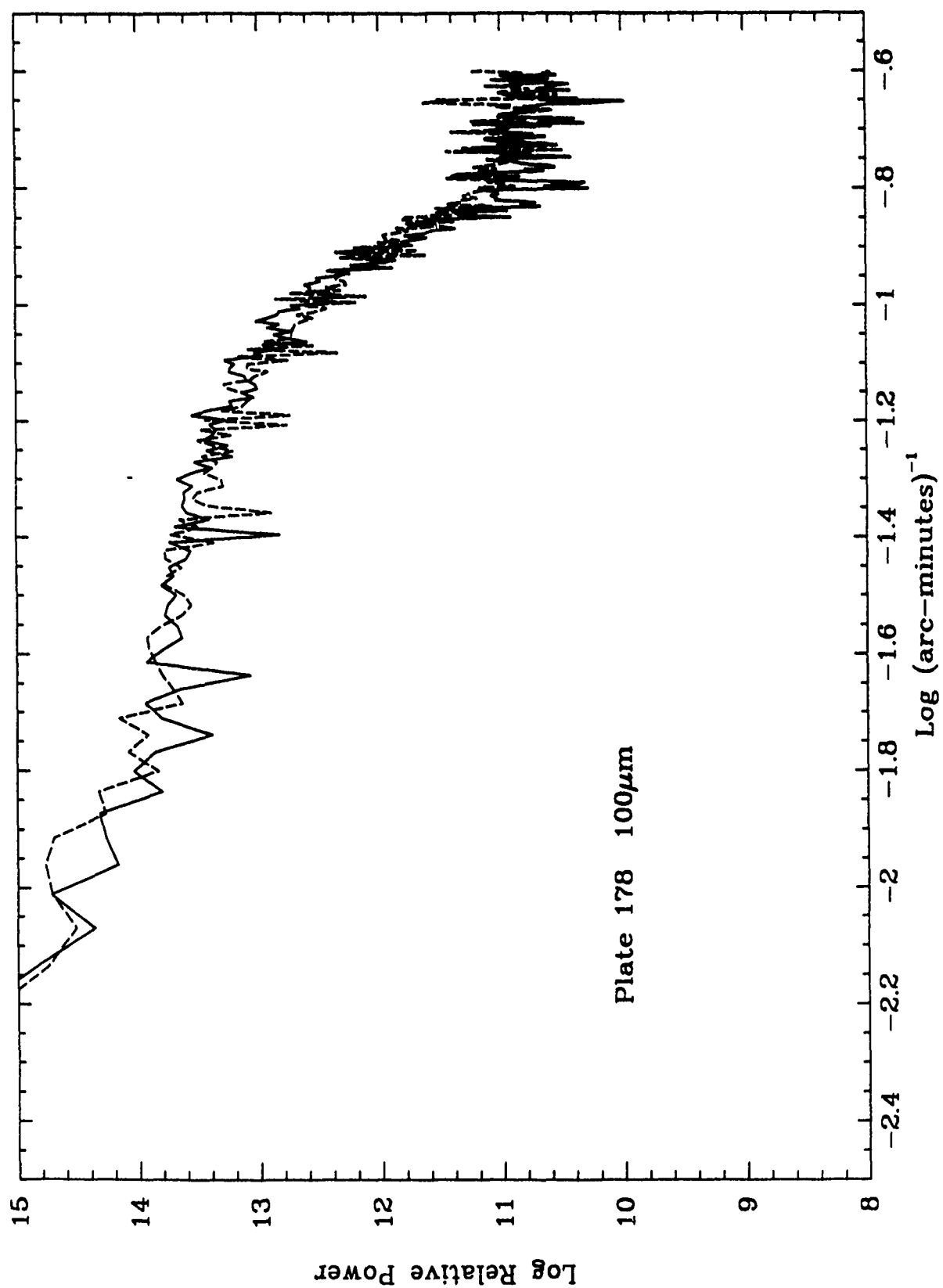


Figure 3u.

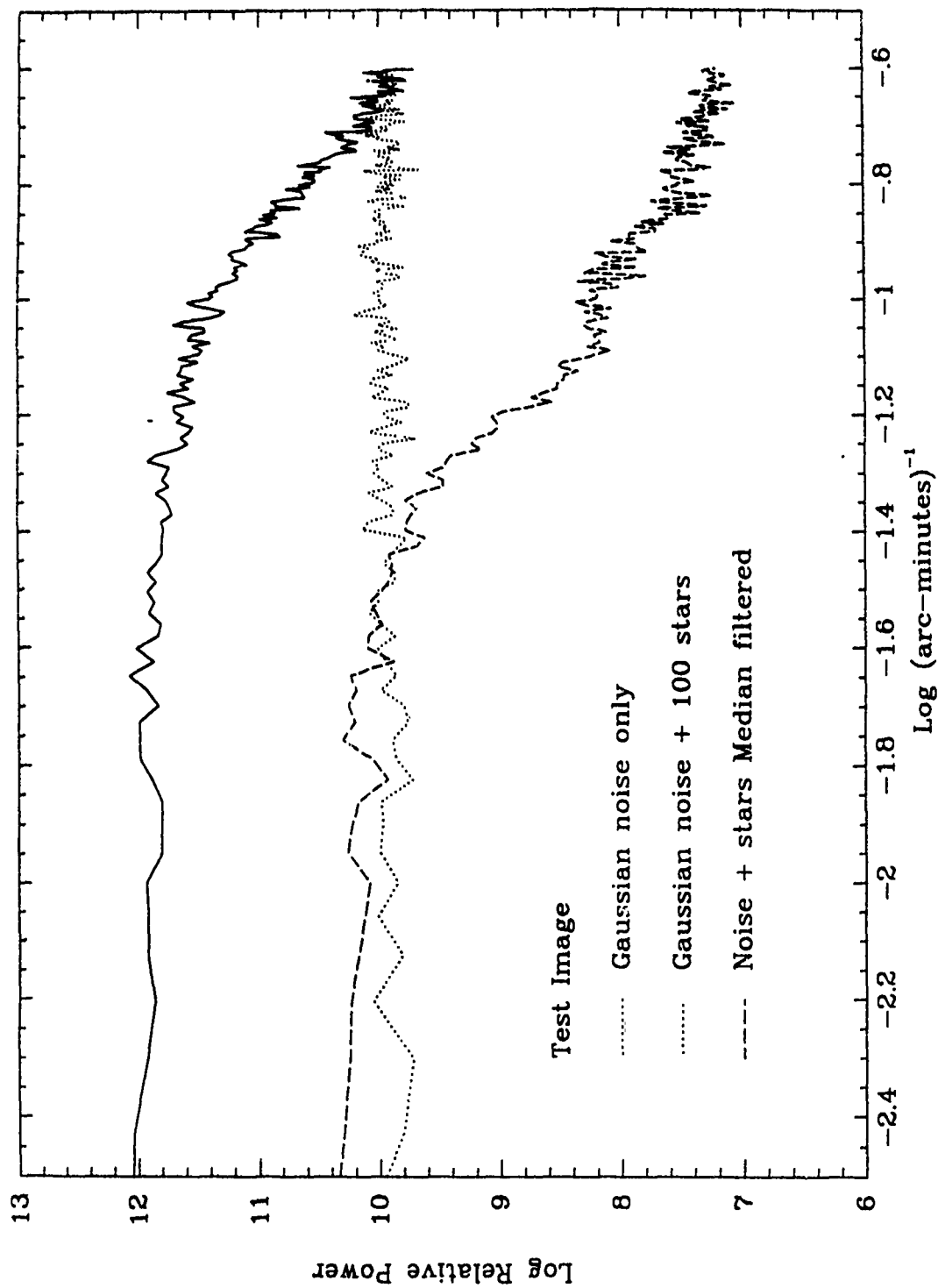


Figure 4. - The azimuthal averaged radial profile of the two-dimensional power spectra of artificial 12μm "images." The dotted line represents the power spectral profile of a test image with pure Gaussian noise with an RMS amplitude similar to 12μm Skyflux images. The solid line is the profile of the power spectrum of the noise image with 100 point sources uniformly distributed. The "stars" have profiles and brightness distribution identical to point sources in 12μm Skyflux maps. The dashed line represents power spectral the profile of the median filtered star field image.

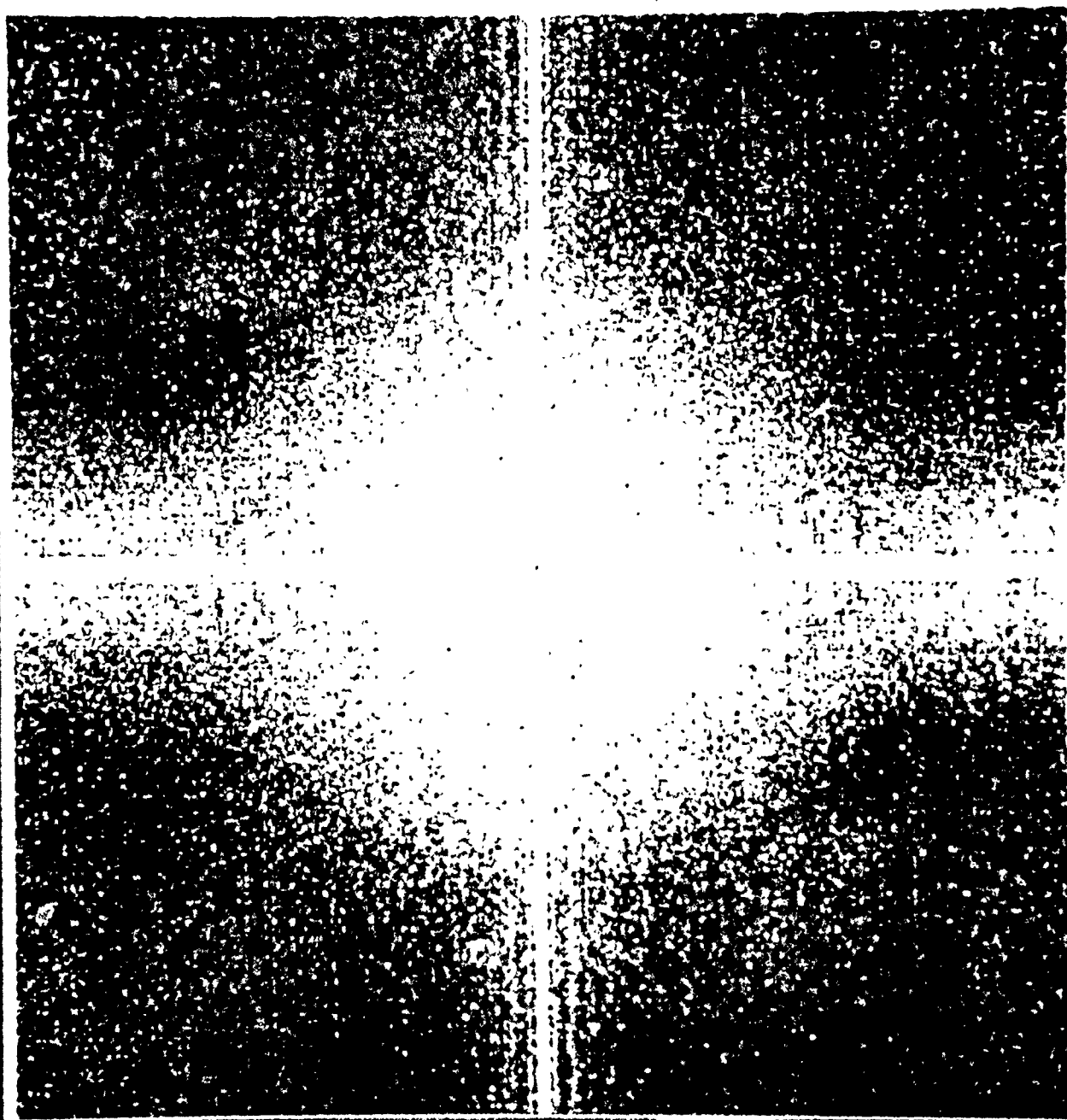


Figure 5. – The two-dimensional power spectrum of the median filtered $12\mu\text{m}$ IRAS Skyflux plate 1. The filter window size was $14'\times 14'$. Compare this image with the spectrum of the unfiltered image shown in Figure 1a.

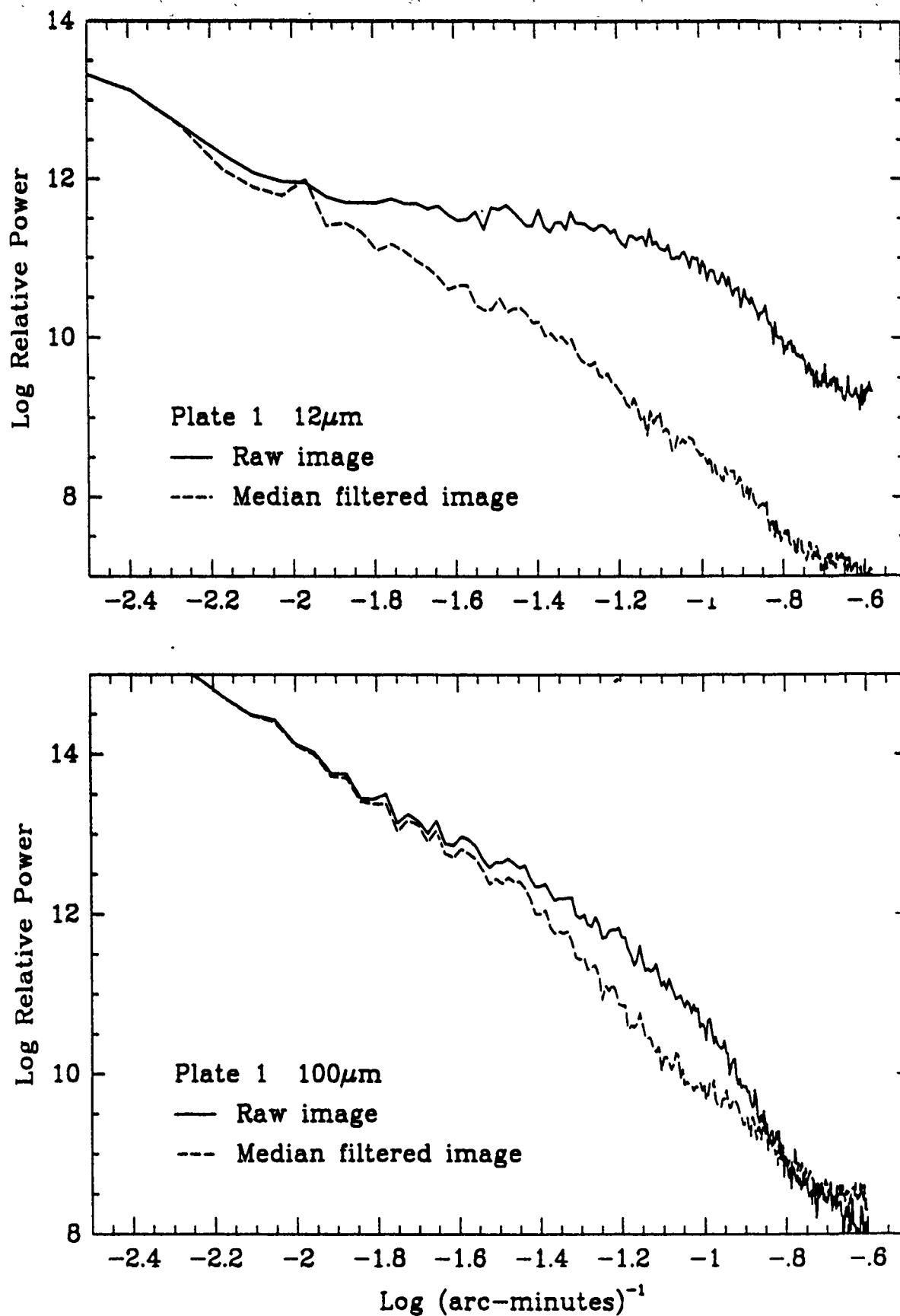


Figure 6. – Azimuthal averaged radial profiles of the 12 μ m (top) and 100 μ m power spectra of Skyflux plate 1. The solid lines are the profiles from the spectra of the raw images, and the dashed lines are profiles of the spectra of median filtered images.

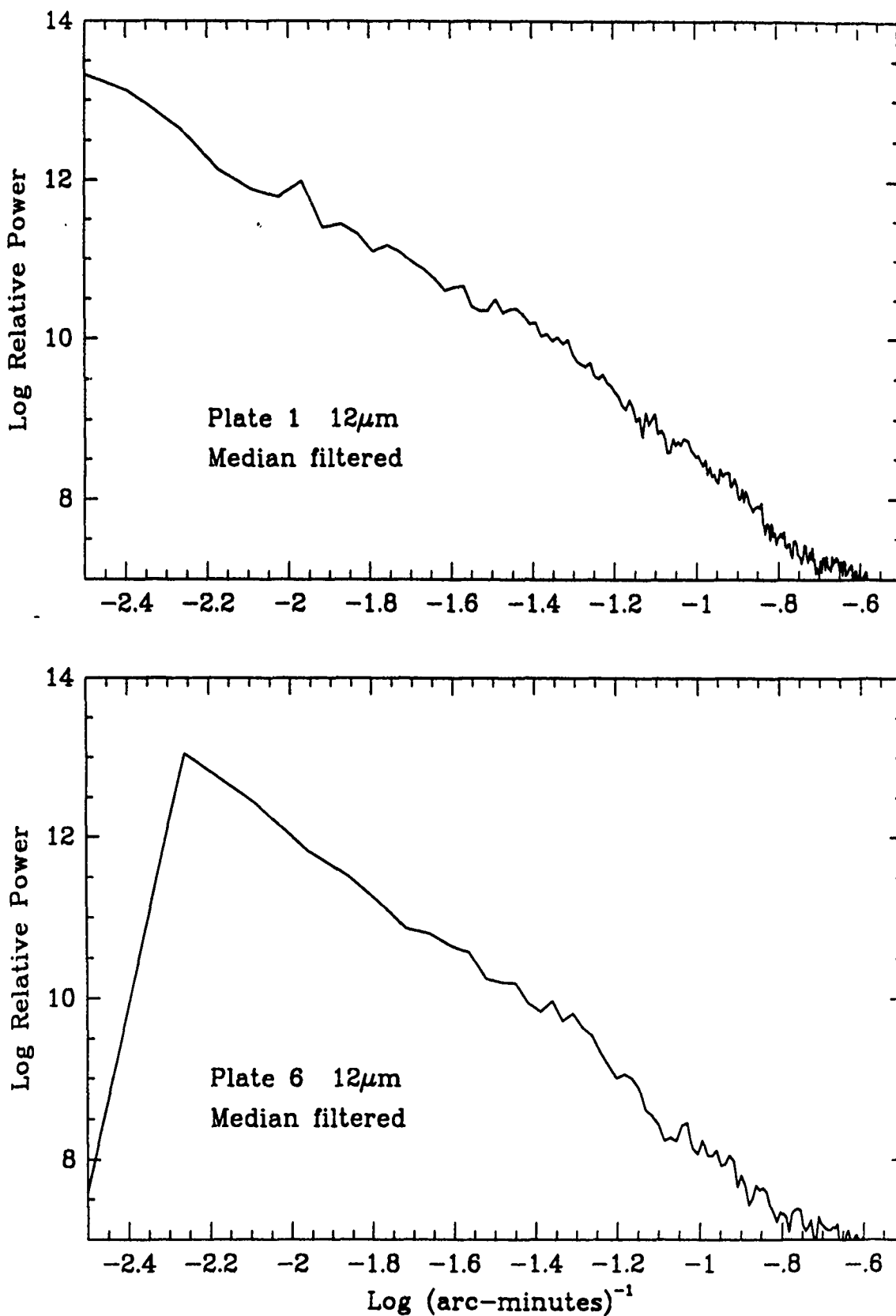


Figure 7a. — The azimuthal averaged radial profiles of the two dimensional power spectra of the median filtered 12μm Skyflux plates 1 (top) and 48 (bottom).

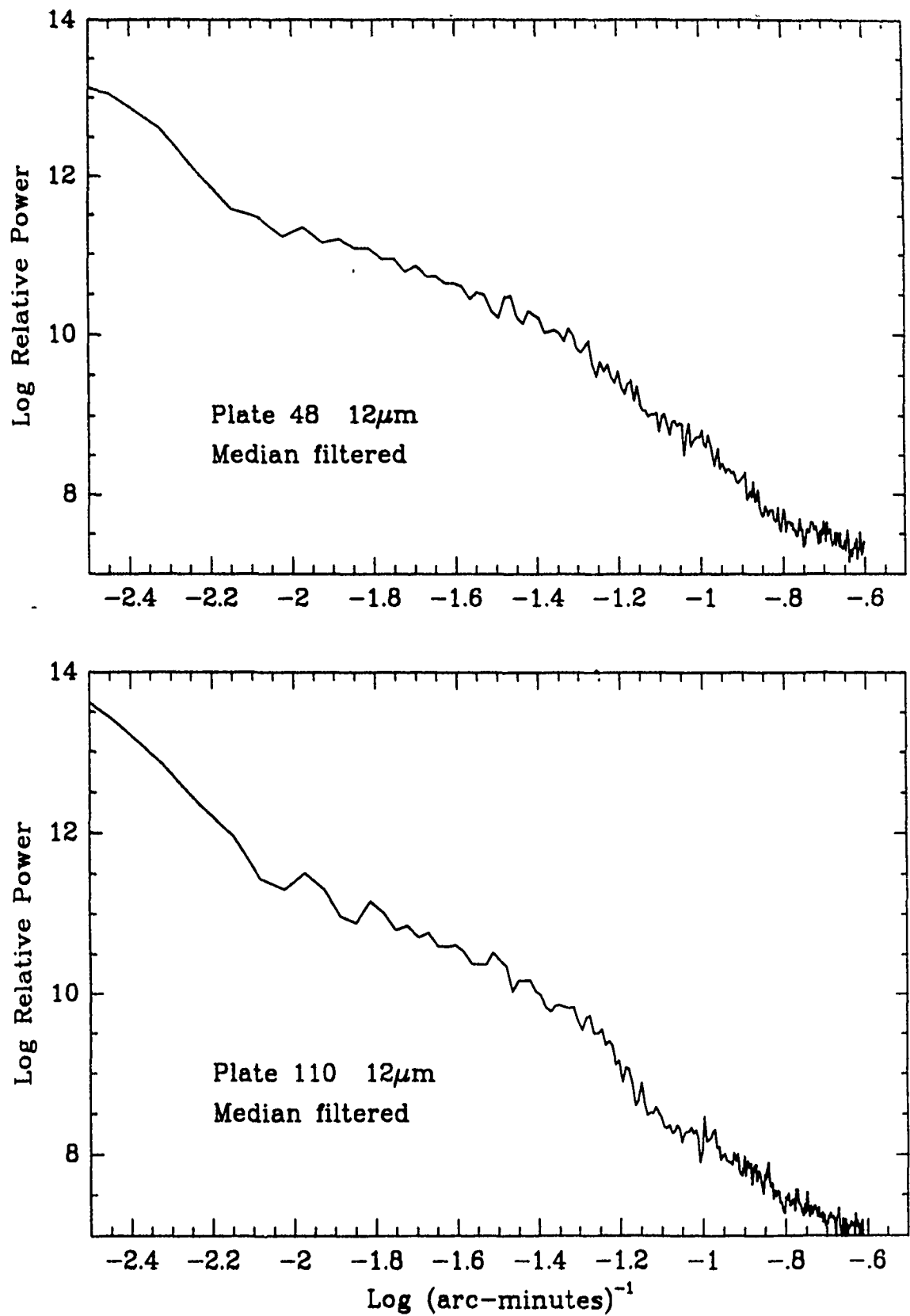


Figure 7b. – The azimuthal averaged radial profiles of the two dimensional power spectra of the median filtered 12μm Skyflux plates 1 (top) and 48 (bottom).

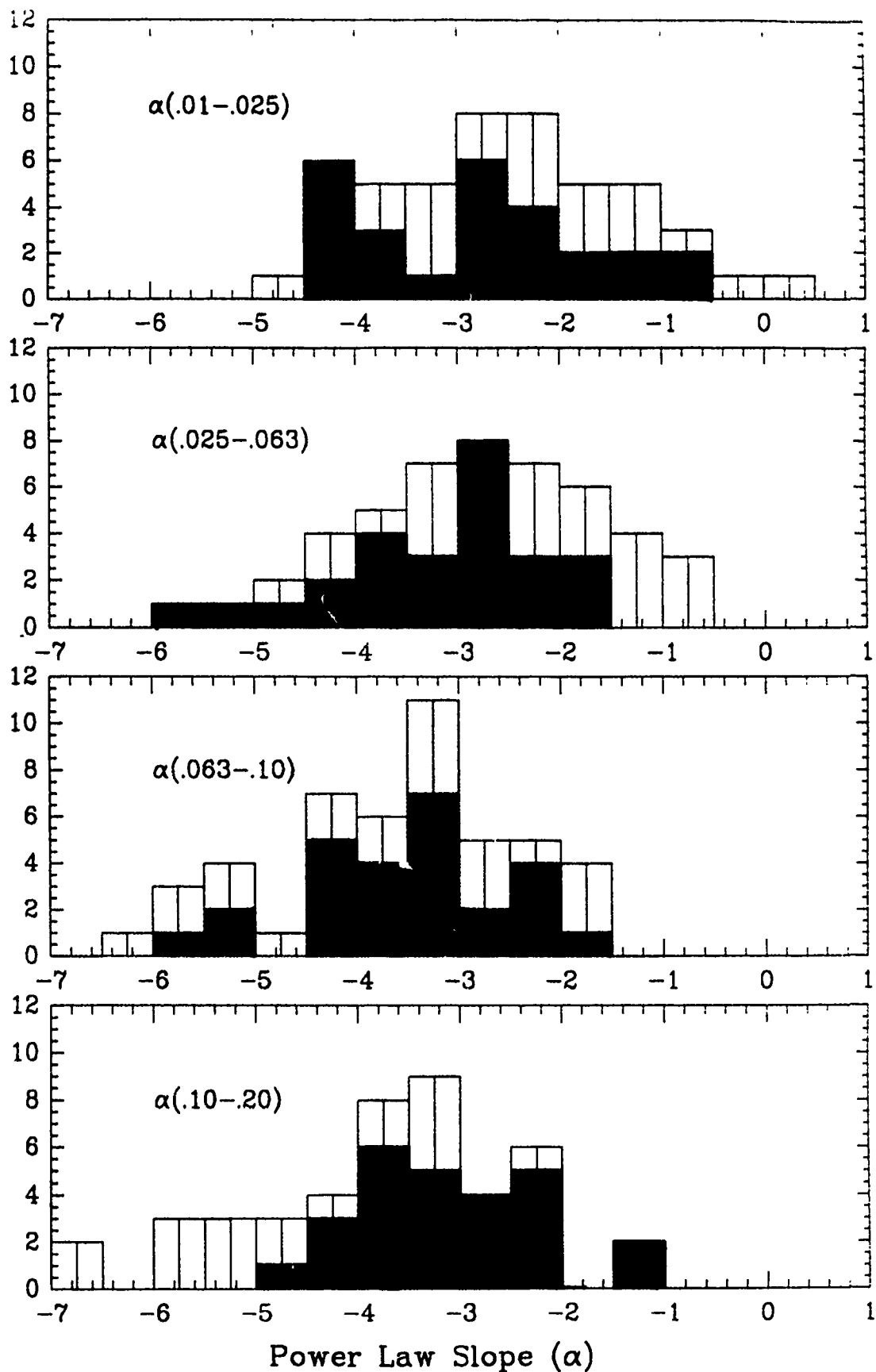


Figure 8. – The distribution of power law slopes fit to the 100 μ m power spectral cross-sections shown in Figures 2 and 3. Slopes are shown for fits made in the spatial frequency ranges of (a) .01-.025 arc-minutes⁻¹, (b) .025-.063 arc-minutes⁻¹, (c) .063-.10 arc-minutes⁻¹, and (d) .10-.20 arc-minutes⁻¹. The slopes of the spectra which qualitatively appeared to show the least amount of curvature are denoted by filled squared. Note the large dispersion in the fit slopes, and the trend toward steeper slopes with increasing frequency range.

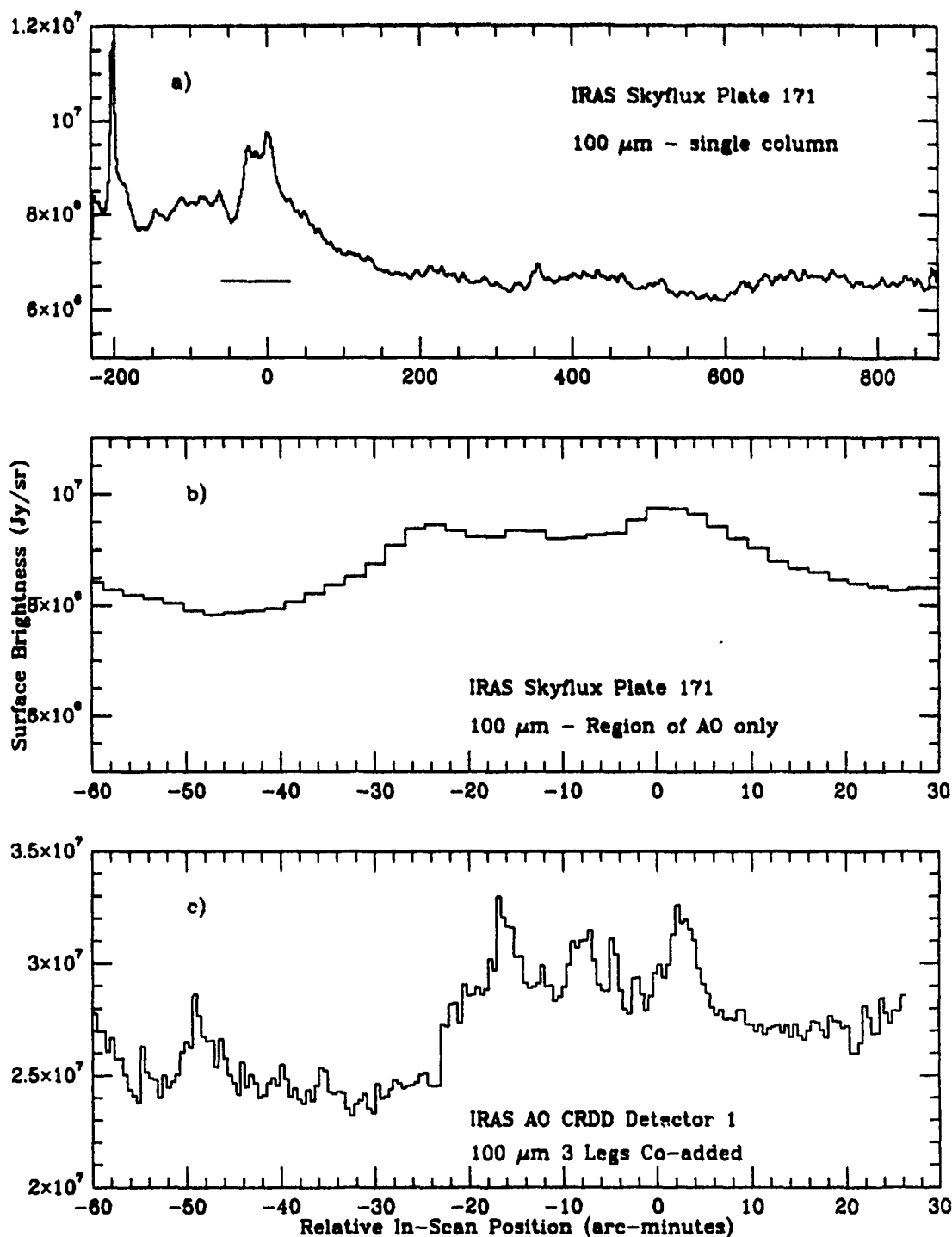


Figure 9. - A comparison of the spatial resolution and sensitivity of IRAS Skyflux and Pointed Observation data. a) A single pixel-wide slice taken from the 100 μm Skyflux plate 171, through a prominent cirrus cloud which was serendipitously scanned during a Pointed Observation by the satellite. The Pointed Observation covered the region indicated by the horizontal line near 0 arc-minute relative in-scan position. b) An enlargement of the Skyflux data in the region covered by the Pointed Observation. c) The Pointed Observation single detector data covering the prominent cirrus cloud. Three passes by the satellite have been co-added. Note the improved resolution and contrast in the cirrus structure.

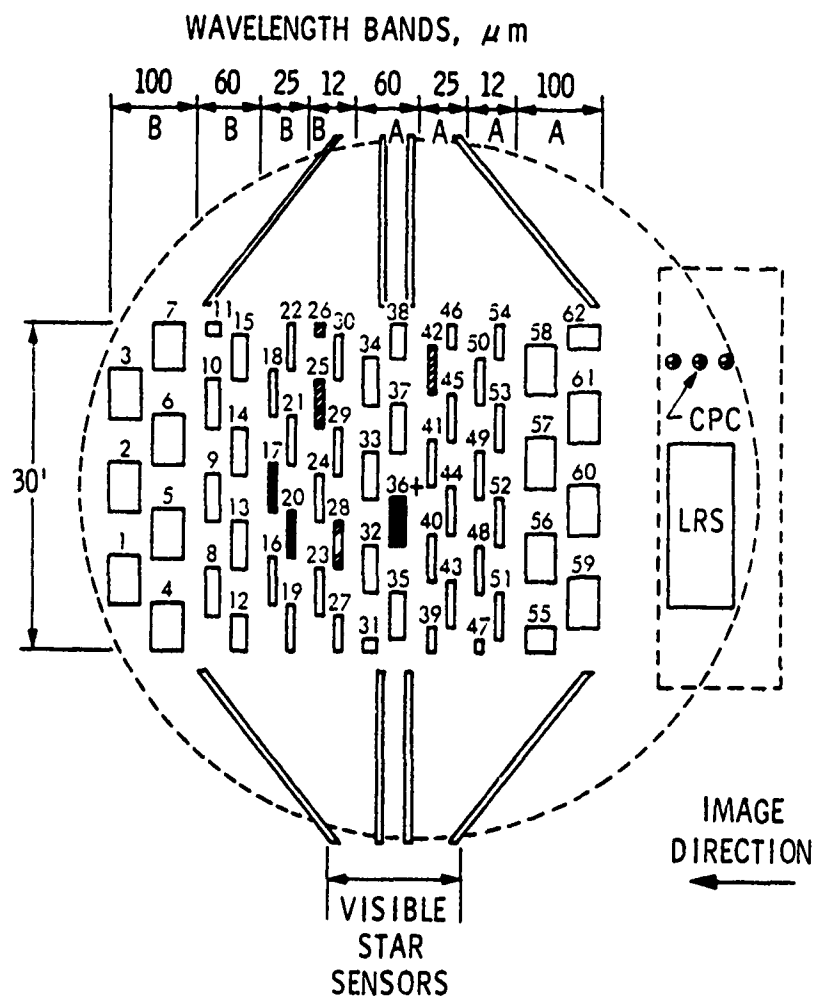


Figure 10. – Schematic of the IRAS Focal Plane detector array. Reprinted from Figure II.C.6 in the IRAS Catalogs and Atlases Explanatory Supplement.

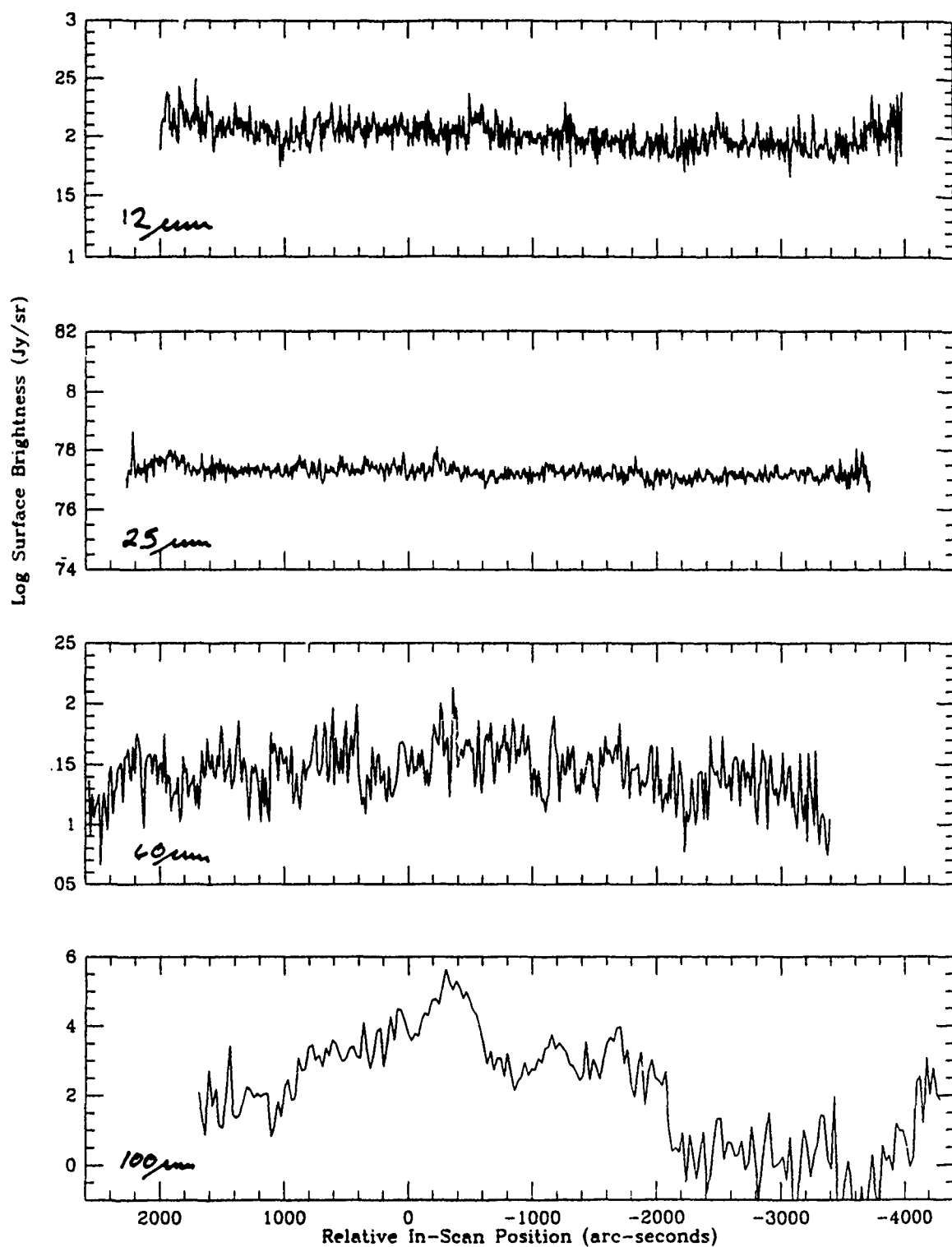


Figure 11a. – The co-added single detector data from the Pointed Observation BS63. Descending from the top are the 12μm data from detector 47, the 25μm data from detector 39, the 60μm data from detector 31, and the 100μm data from detector 55.

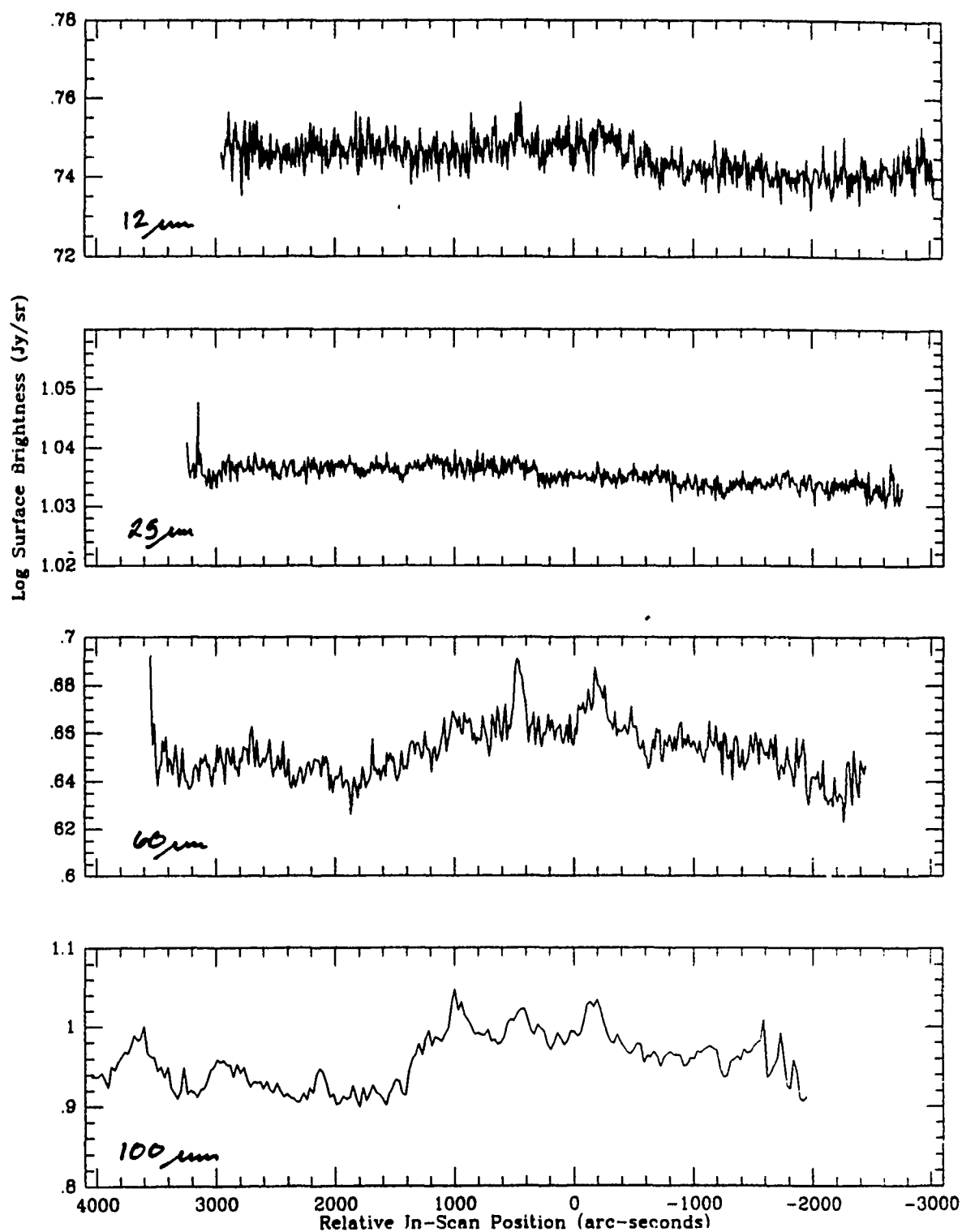


Figure 11b. – The same as Figure 11a, but for detectors 23 (12 μm), 16 (25 μm), 8 (60 μm) and 1 (100 μm).

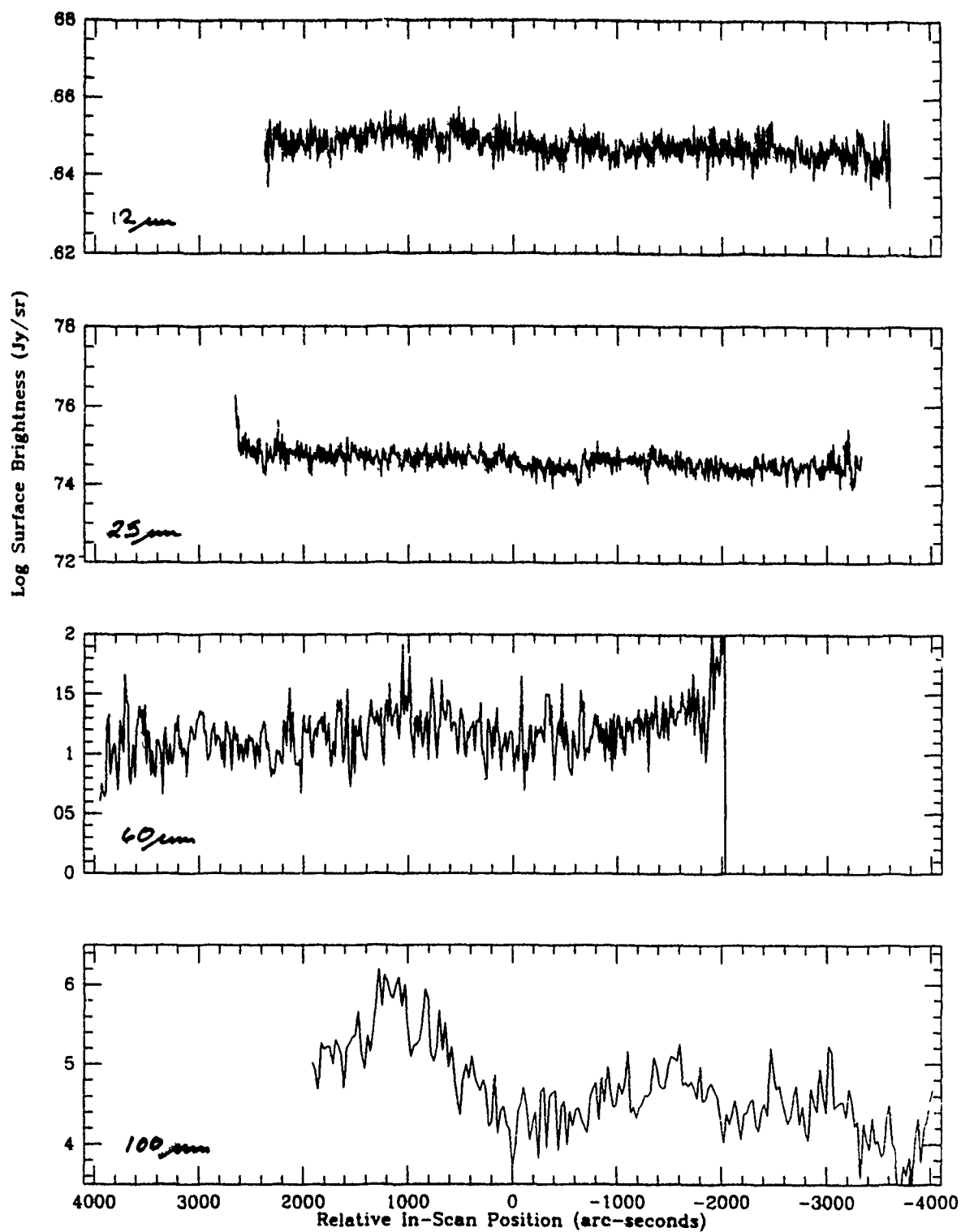


Figure 11c. – The same as Figure 11a, but for detectors 54 (12 μm), 46 (25 μm), 11 (60 μm) and 62 (100 μm).

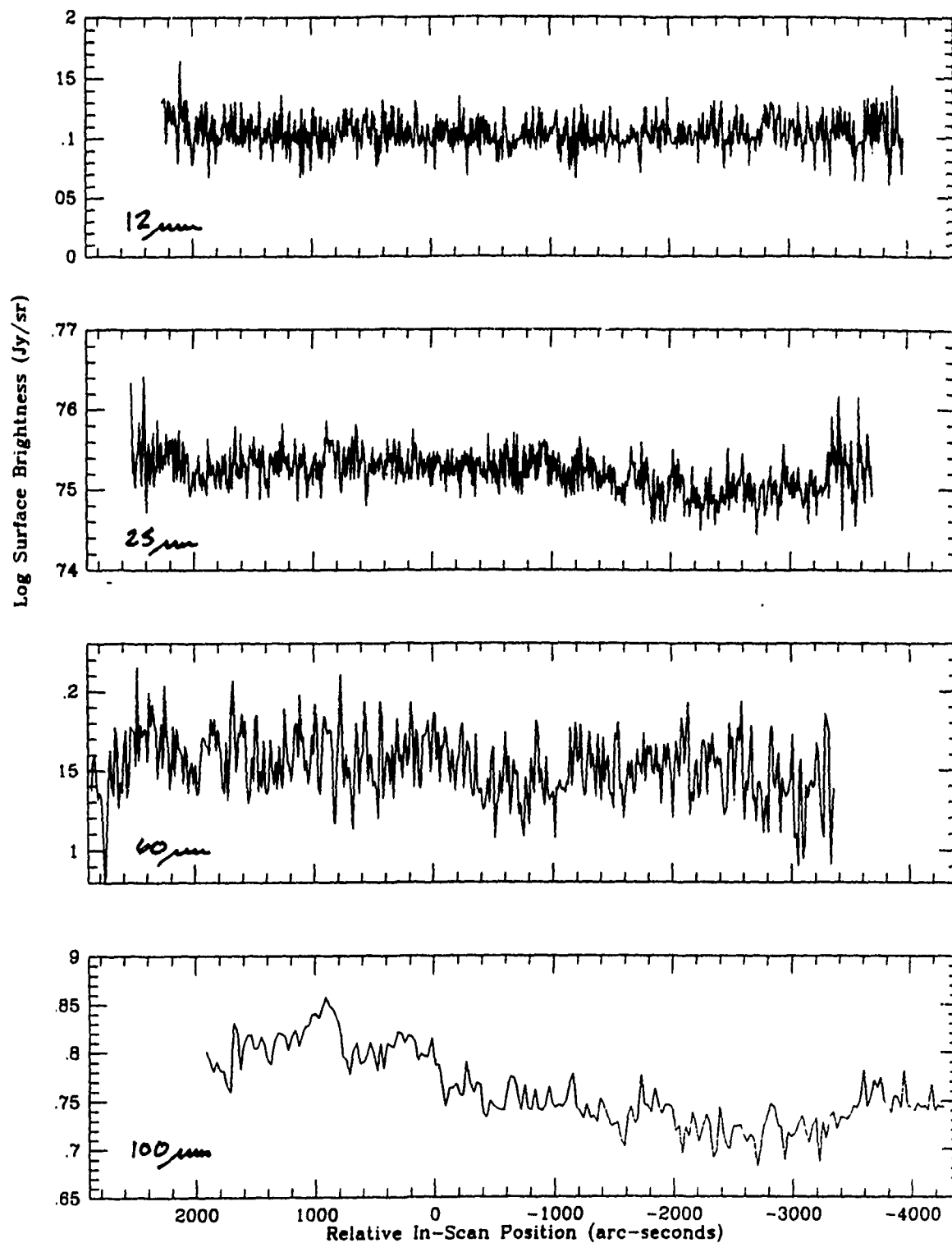


Figure 12a. – The co-added single detector data from the Pointed Observation SY52. Descending from the top are the 12μm data from detector 47, the 25μm data from detector 39, the 60μm data from detector 31, and the 100μm data from detector 55.

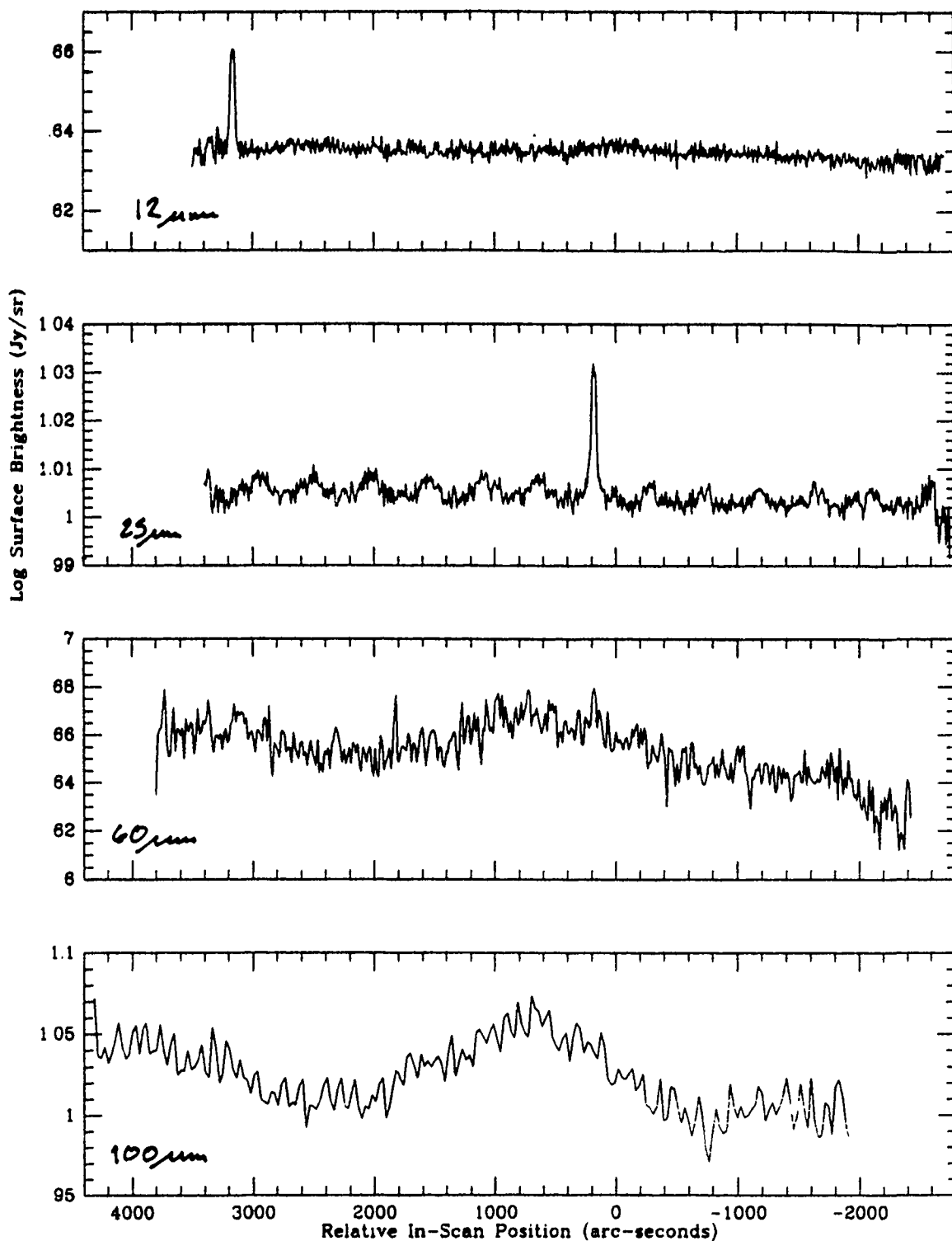


Figure 12b. – The same as Figure 12a, but for detectors 23 (12 μm), 16 (25 μm), 8 (60 μm) and 1 (100 μm). Notice the two point sources detected at 12 and 25 μm , and the periodic noise signal in the 25 μm data.

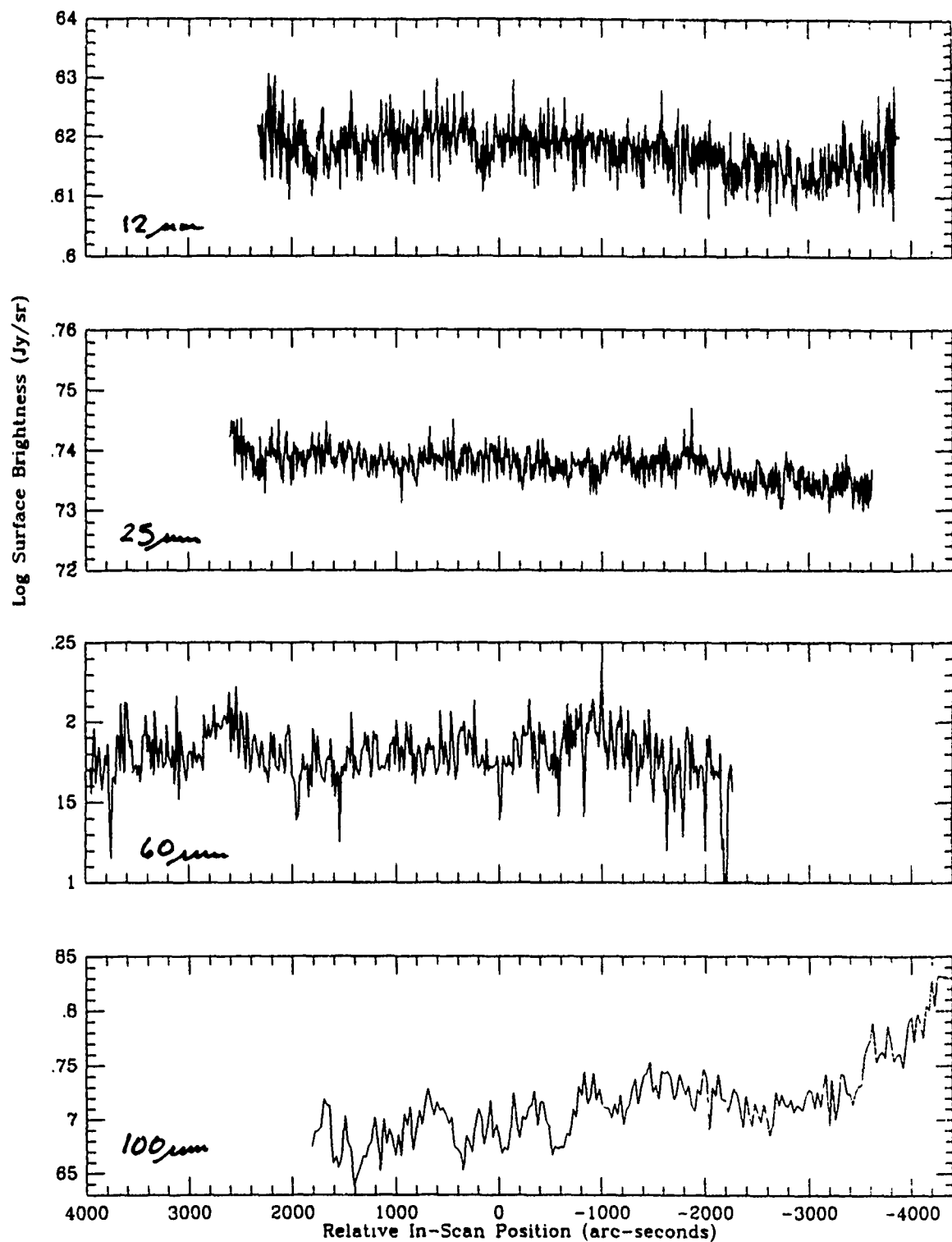


Figure 12c. – The same as Figure 12a, but for detectors 54 (12 μm), 46 (25 μm), 11 (60 μm) and 62 (100 μm).

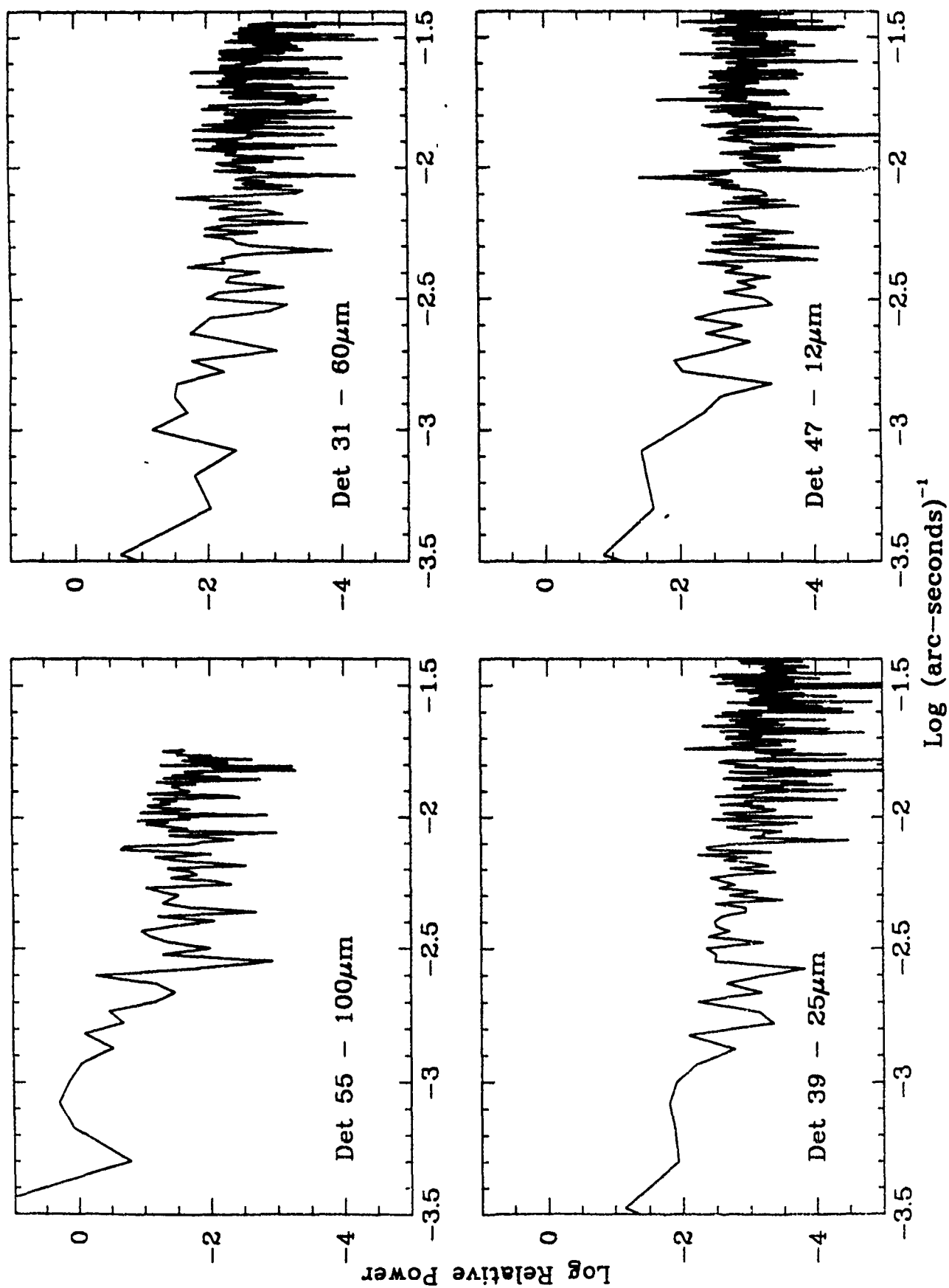


Figure 13a. - The one-dimensional power spectra for each of the single detector scan data in Pointed Observation BS63 shown in Figure 11a.

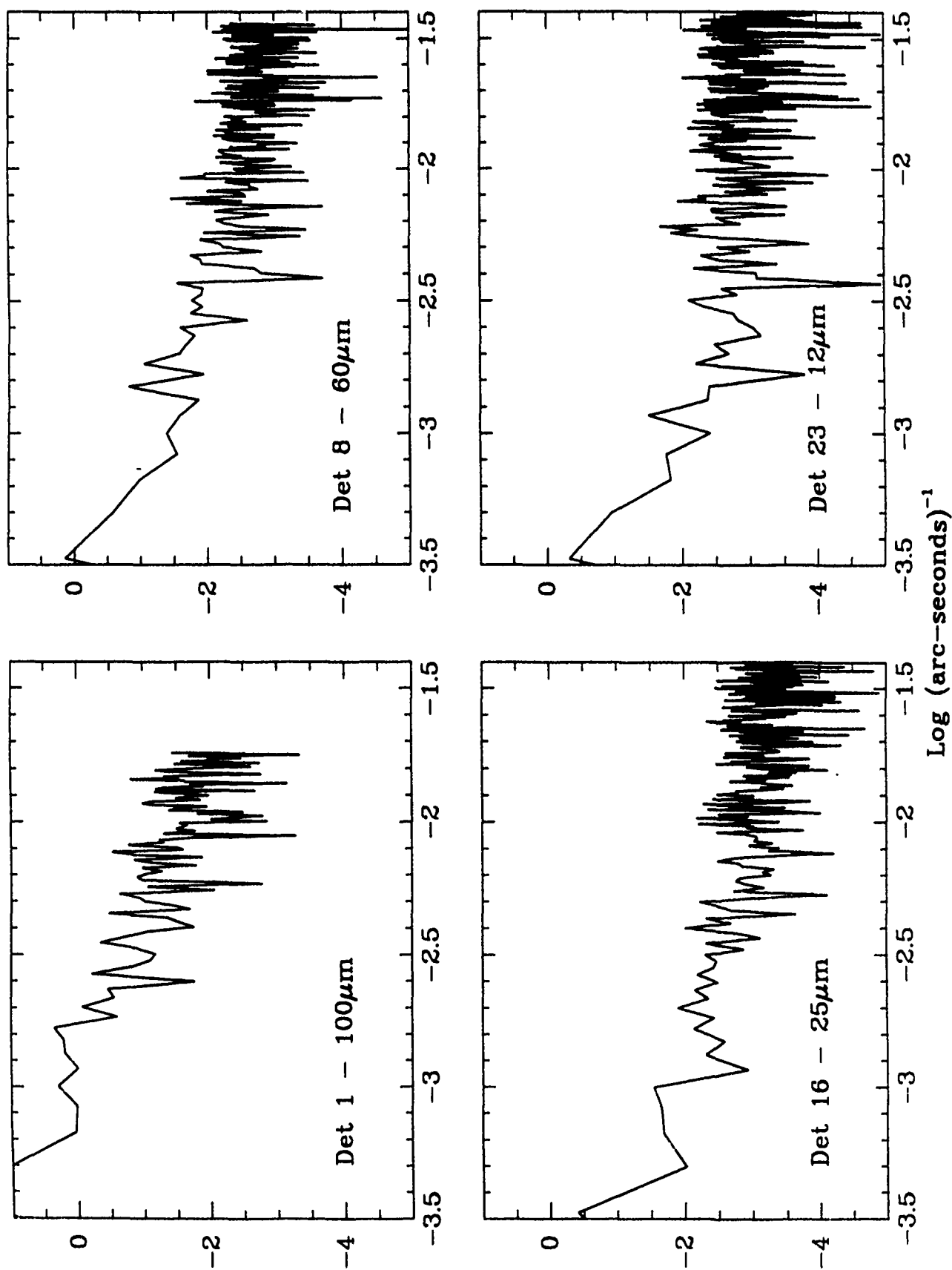


Figure 13b. - The one-dimensional power spectra for each of the single detector scan data in: Pointed Observation BS63 shown in Figure 11b.

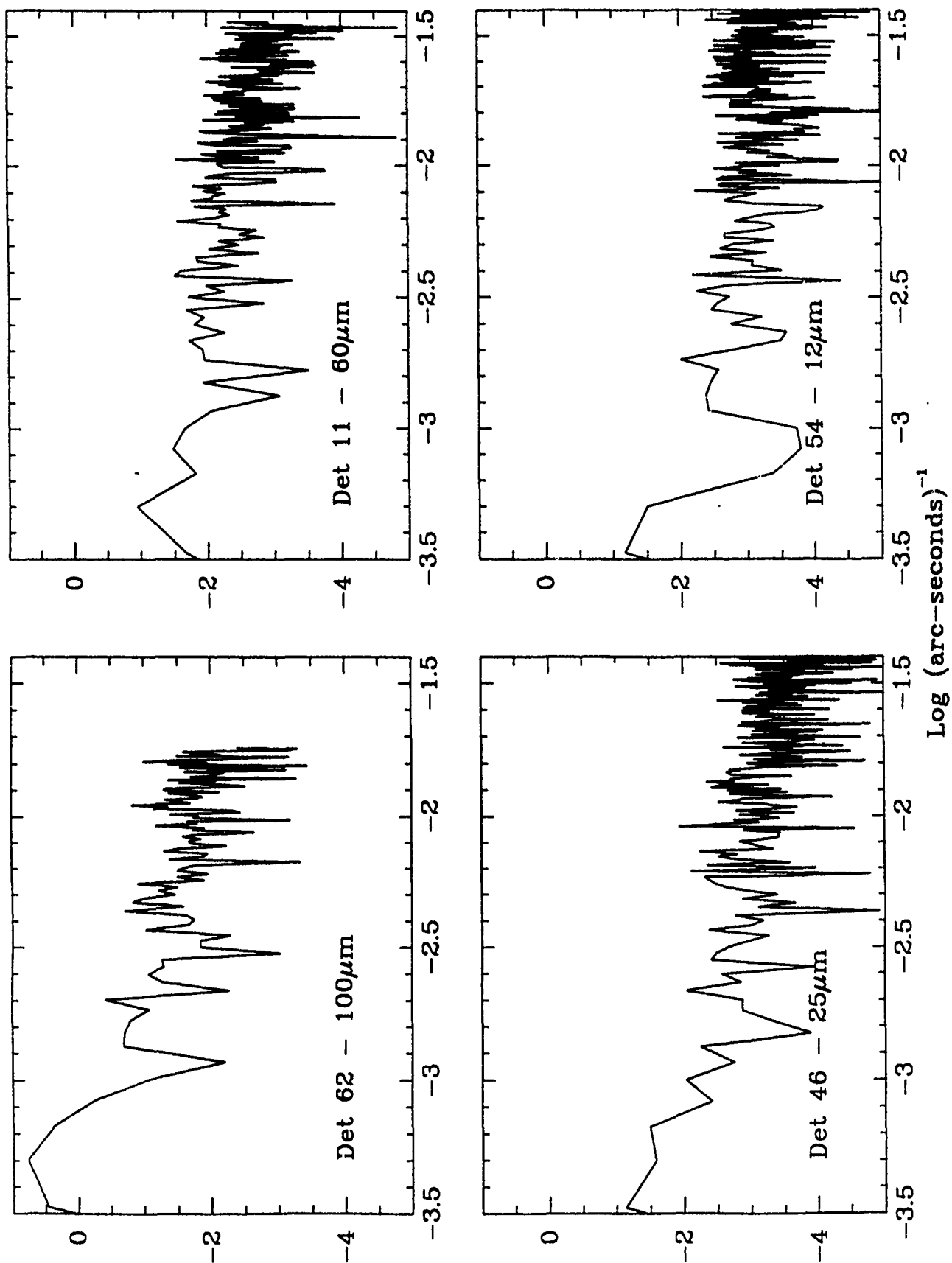


Figure 13c. - The one-dimensional power spectra for each of the single detector scan data in
Pointed Observation BS63 shown in Figure 11c.

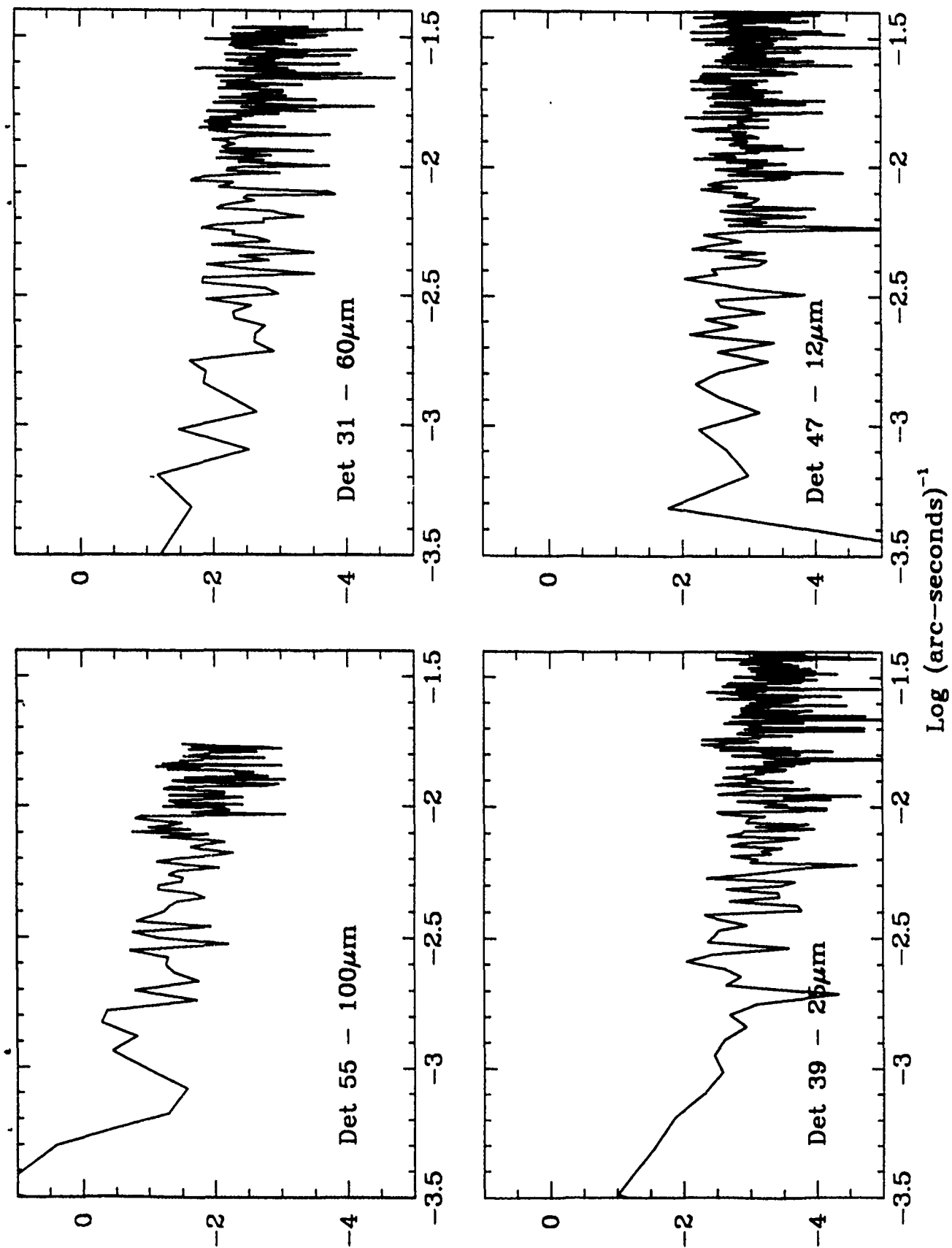


Figure 14a. - The one-dimensional power spectra for each of the single detector scan data in Pointed Observation SY52 shown in Figure 12a.

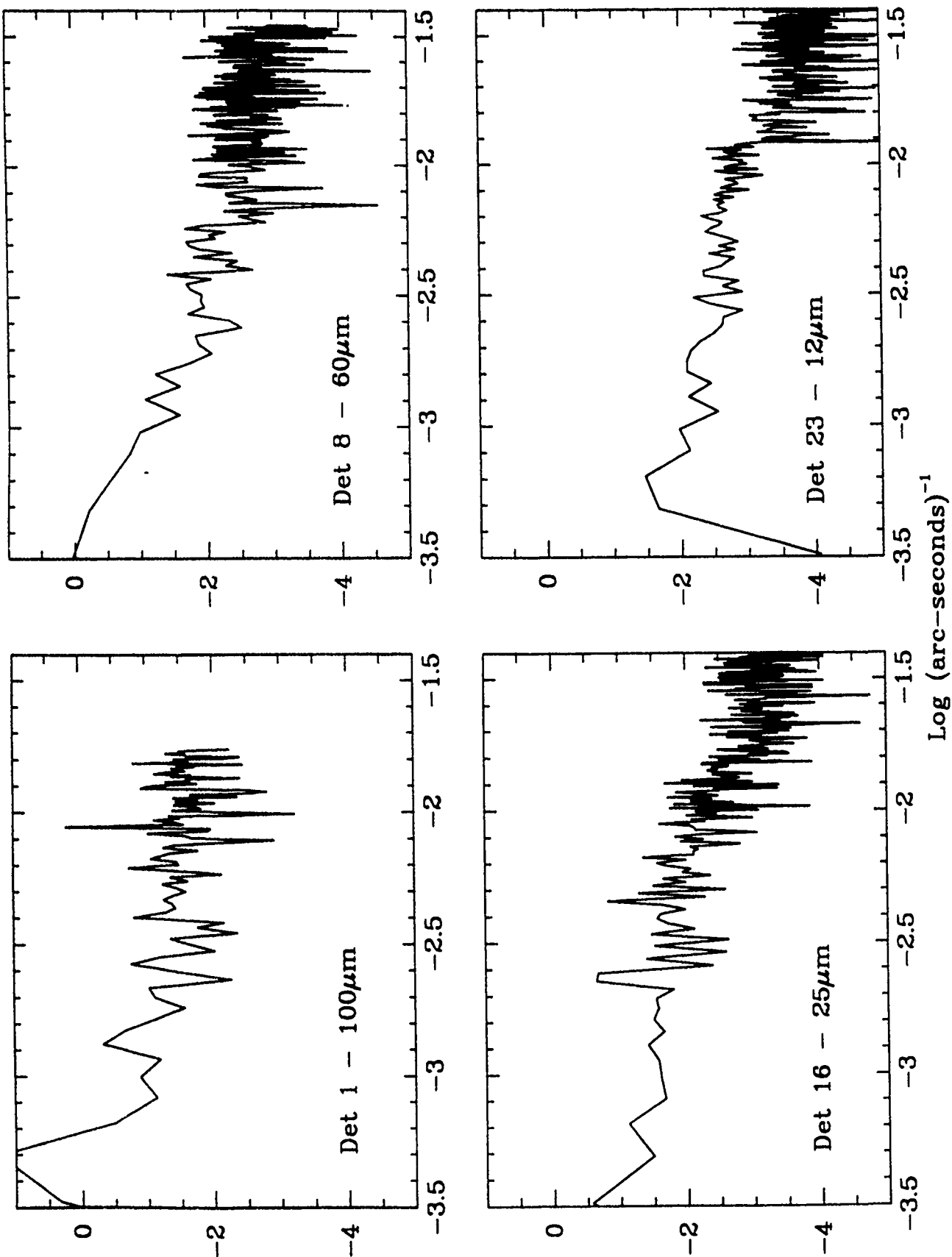


Figure 14b. - The one-dimensional power spectra for each of the single detector scan data in Pointed Observation SY52 shown in Figure 12b.

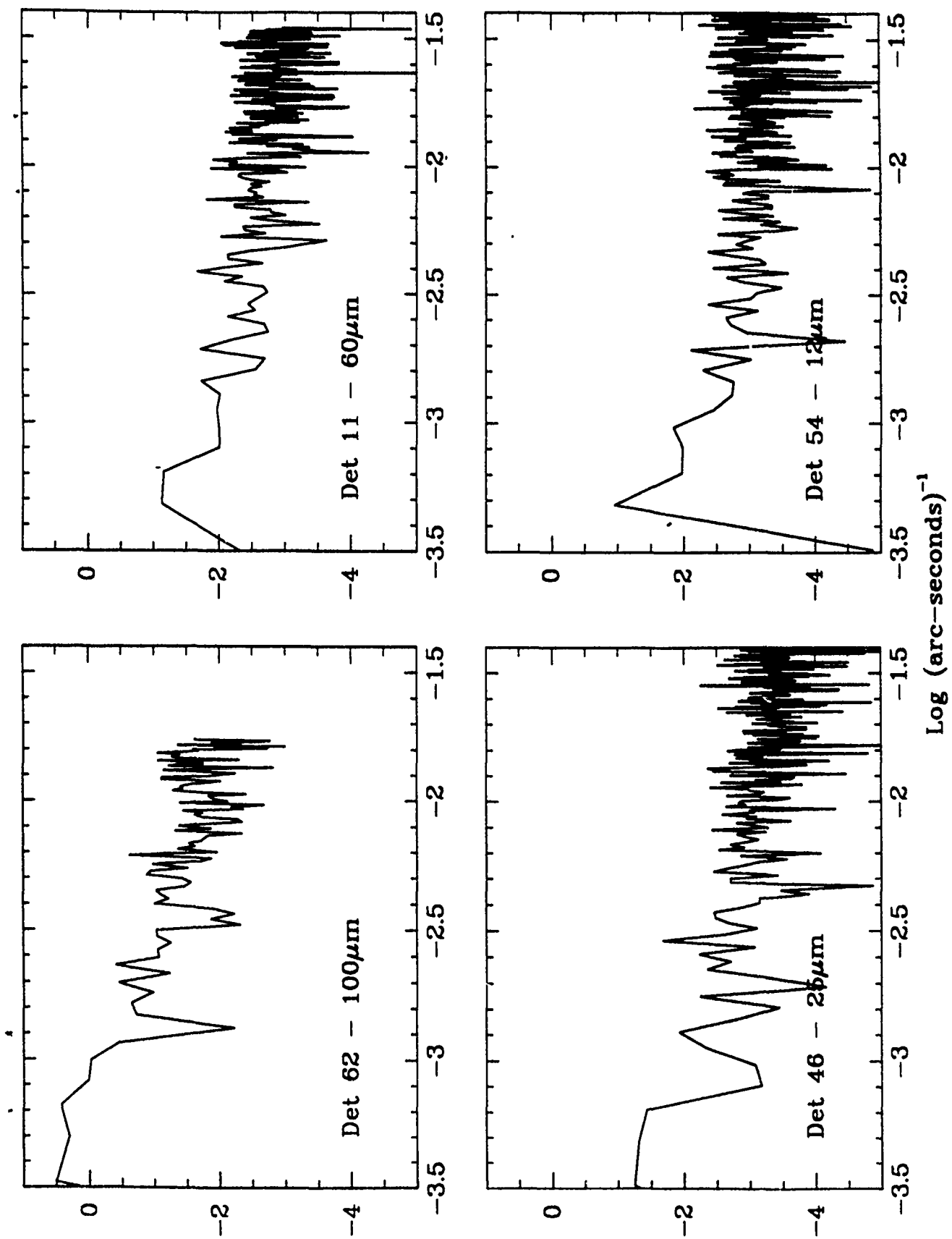


Figure 14c. - The one-dimensional power spectra for each of the single detector scan data in Pointed Observation SY52 shown in Figure 12c.

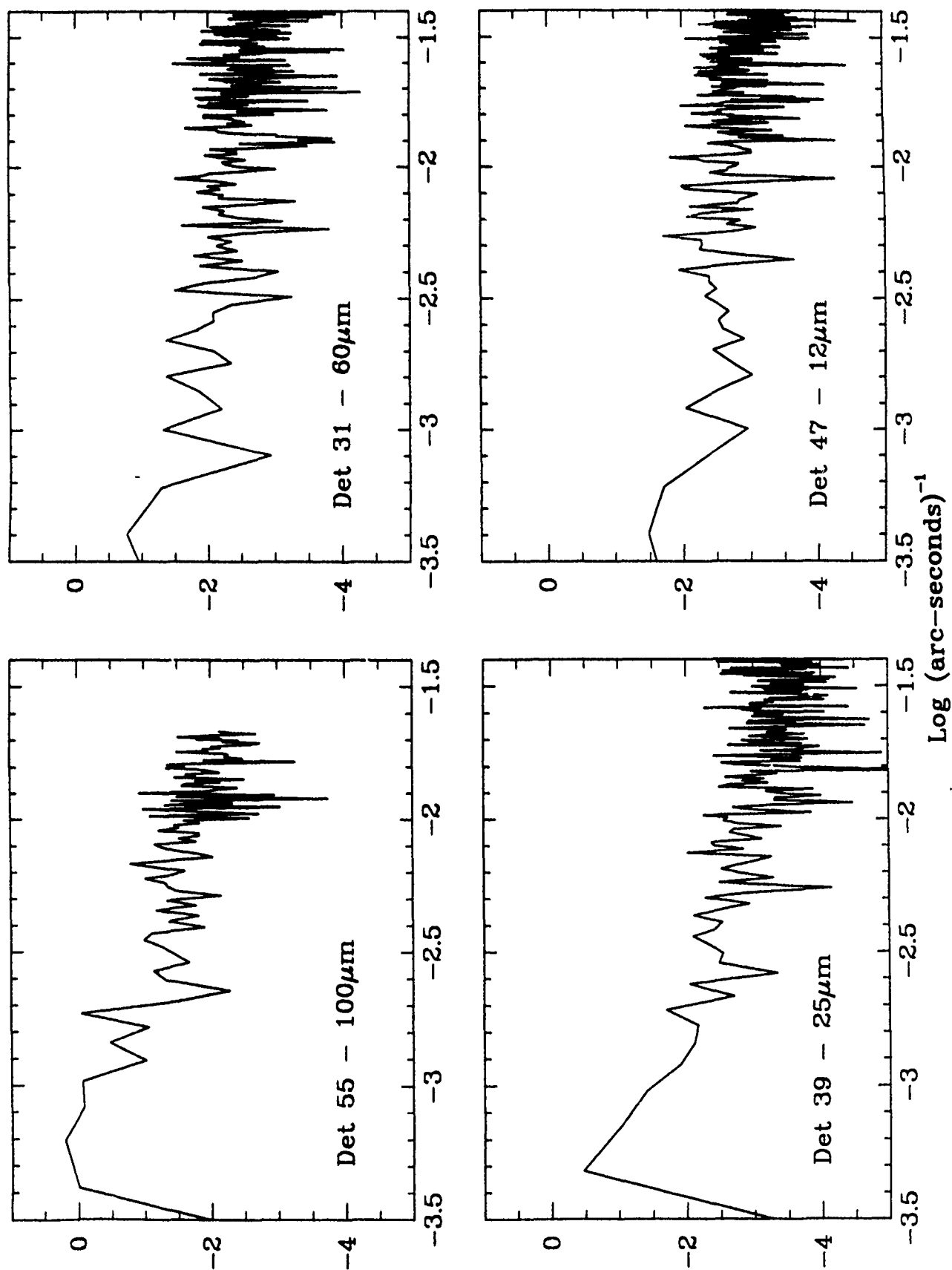


Figure 15a. - The one-dimensional power spectra of the scan data of Pointed Observation DF16 for detectors 1, 8, 16 and 23. The raw scan data are not shown.

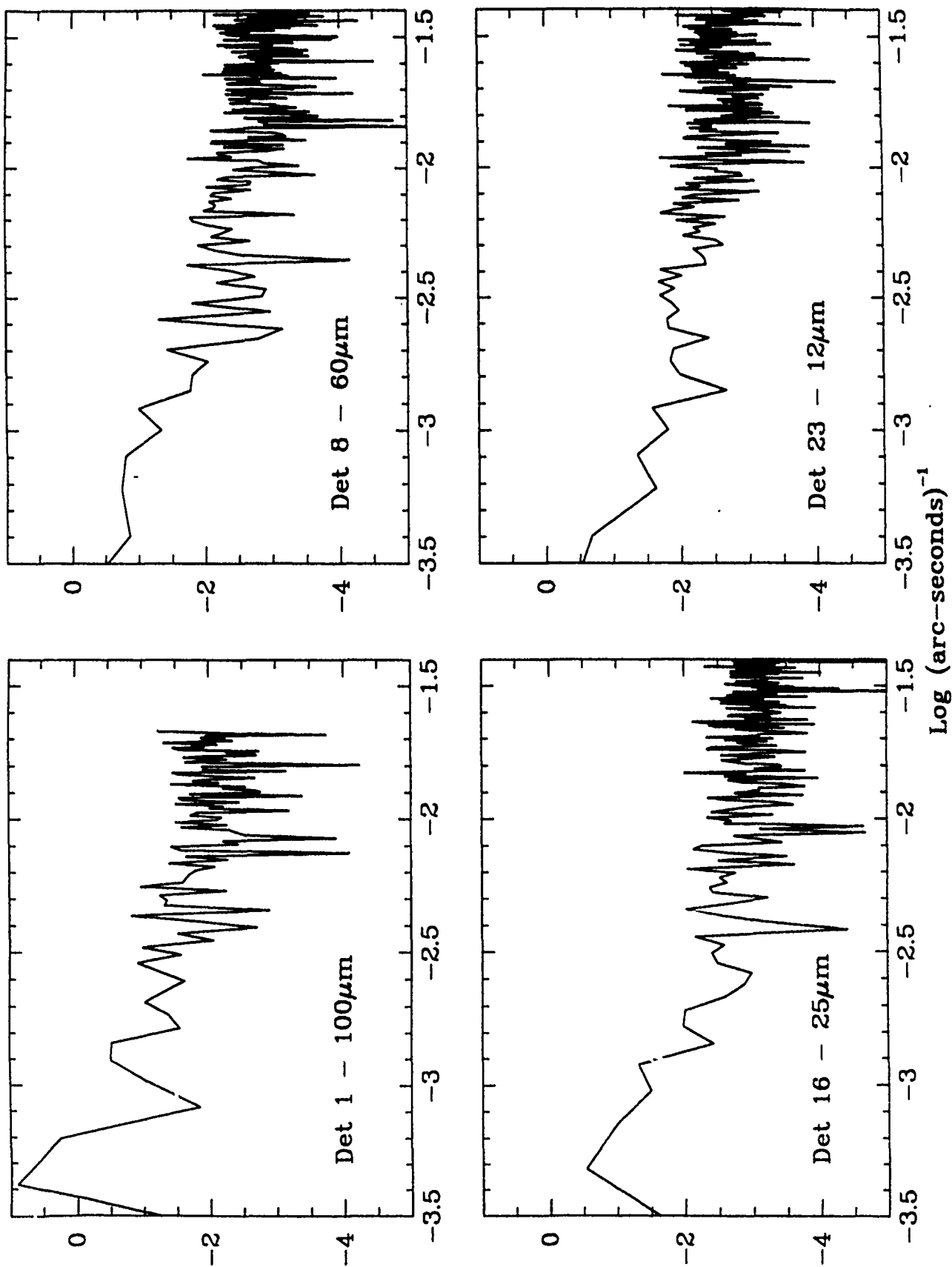


Figure 15b. - The one-dimensional power spectra of the scan data of Pointed Observation DF16 for detectors 55, 31, 39 and 47. The raw scan data are not shown.

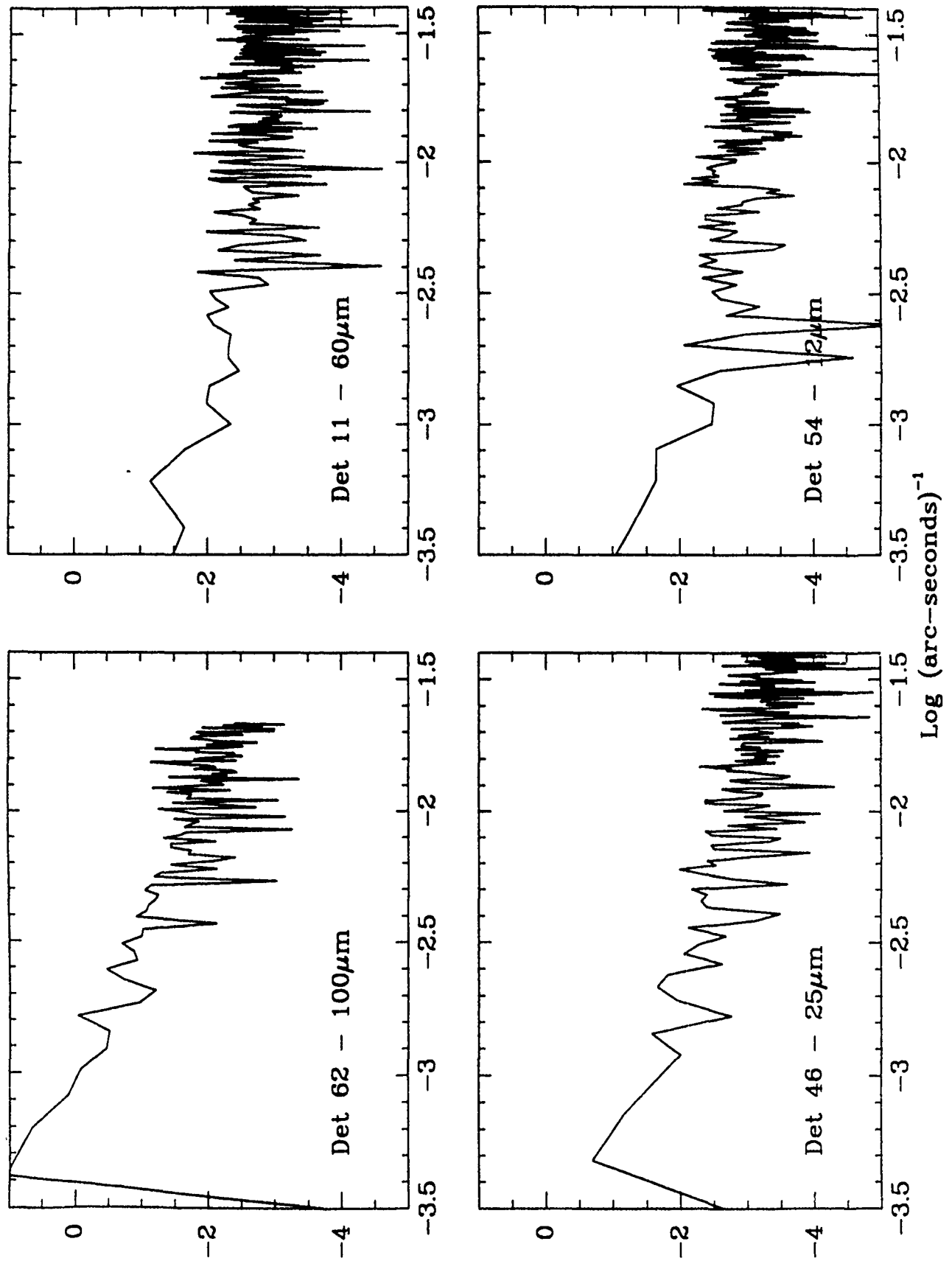


Figure 15c. - The one-dimensional power spectra of the scan data of Pointed Observation DF16 for detectors 62, 11, 46 and 54. The raw scan data are not shown.

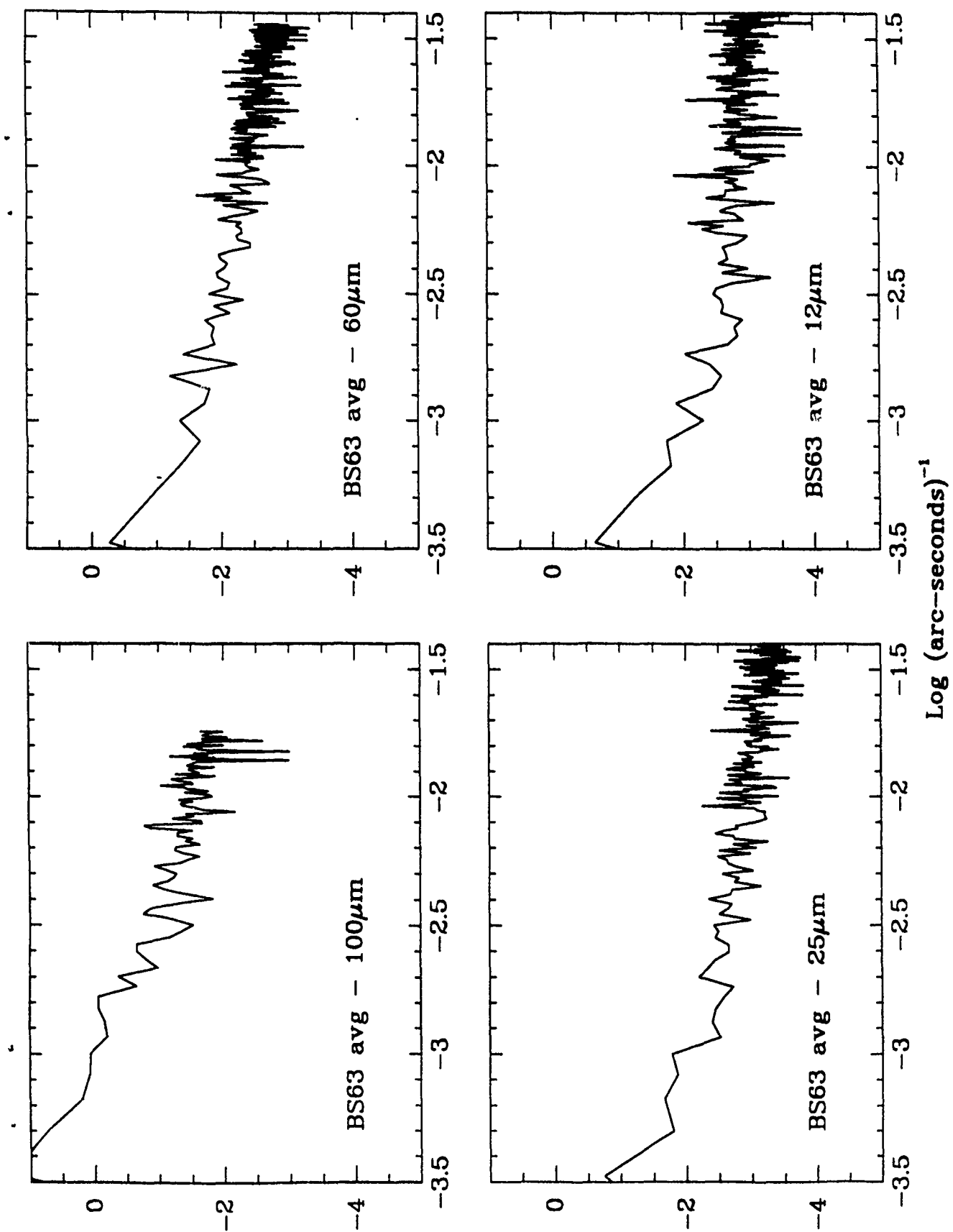


Figure 16. - The average one-dimensional power spectra for BS63. The power spectra of three individual 12, 25 60 and 100 μm detector data have been averaged to produce these.

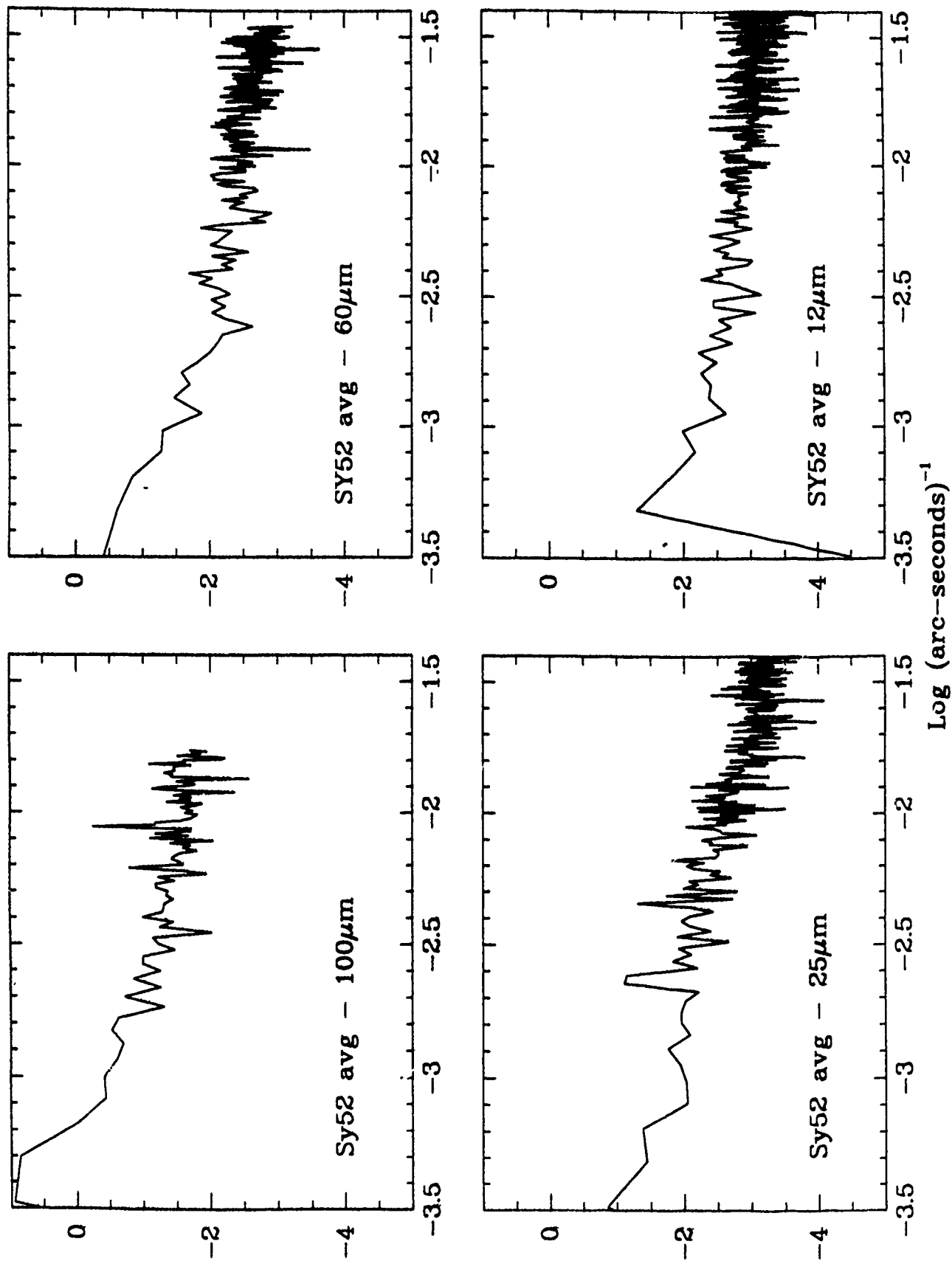


Figure 17. - The average one-dimensional power spectra for SY52. The power spectra of three individual 12, 25 60 and 100 μm detector data have been averaged to produce these.

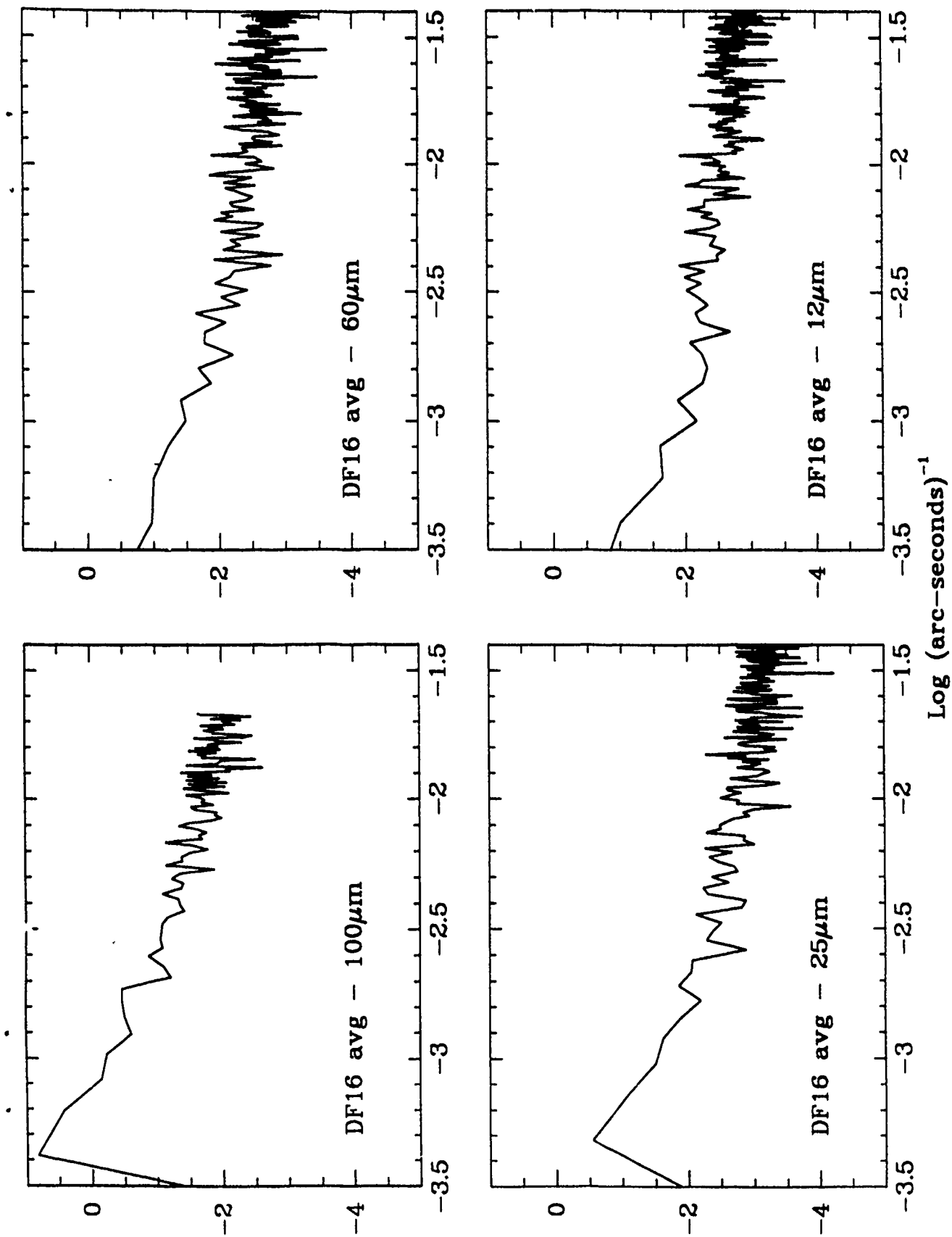


Figure 18. - The average one-dimensional power spectra for DF16. The power spectra of three individual 12, 25 60 and 100 μm detector scans have been averaged to produce these.

APPENDIX IV

A SURVEY OF COMETARY DUST TRAILS

by M. Sykes and R. Walker

To be submitted to *Icarus*

I. Introduction

When we think of dust from comets, we think primarily of the tails sweeping away from the Sun, along with ion tails, forming the flowing "hair" from which comets derive their name. These particles tend to be micron-sized and are very sensitive to radiation pressure. Dust *trails*, on the other hand, consist of large particles, are relatively insensitive to radiation pressure, and cover portion of the orbits of short-period comets (Fig. 1). Trails were first detected by the Infrared Astronomical Satellite (Sykes *et al.* 1986), and were notable for their long, narrow appearance - sometimes extending tens of degrees across the sky while having a width of only a few arcminutes.

In 1983 the Tempel 2 dust trail was by far the most prominent such structure, as it came within 0.4 AU of the Earth during its perihelion passage. It was first detected as a string of 25 μm sources seeming related to periodic comet Tempel 2 (Davies *et al.* 1984). Subsequent analysis of these detections indicated that they may be low-velocity emissions of submillimeter particles (Eaton *et al.* 1984). Sykes *et al.* (1986) found that these point sources were actually part of a continuous stream of material extending behind as well as ahead of the comet. They also found trails associated with other short-period comets. Subsequent analysis determined that all trails consisted of large, refractory particles with small (m/sec) velocities relative to their parents (Sykes, Hunten and Low 1986).

Early estimates of the trail population, estimated by extrapolating from a small area of sky, indicated that there should be more than 100 trails, many of which might be associated with periodic comets not yet discovered (Sykes *et al.* 1986). Later, as more of the IRAS data was examined, as many as 57 trails were identified that were without known parents (Sykes and Dow, 1988?). In this paper we show this last to be in error due primarily to confusion with infrared cirrus.

The Tempel 2 trail has been the focus of a recent study (Sykes, Lien and Walker 1990) showing it to consist primarily of millimeter-sized particles, emitted at velocities of a few meters/sec over the past few hundred years. It also exhibits a small, but significant, enhancement in color temperature relative to that expected for a blackbody at the heliocentric distances observed. This is explained as either evidence for a population of small particles released from large particles, or for a temperature gradient across the large particle surfaces such that they are warmer towards the Sun. Number densities are such that the Tempel 2 trail could pose a hazard to CRAF-type spacecraft moving within it (Sykes 1988a).

Trails provide insight into the nature and evolution of comets, and their relationship to asteroids and the zodiacal dust complex. The present work represents a several year effort to find and identify all trails that were detected by IRAS, determine their parent bodies, and understand the trail phenomenon in general. A second paper will provide a more exhaustive analysis of individual trails identified in this survey.

II. The Survey

A description of the IRAS mission is given by Neugebauer *et al.* (1984). From its polar orbit, IRAS made three surveys of the sky designated HCONs 1, 2, and 3. The first two surveys covered about 96% of the sky, and were interleaved so that the same location of sky was observed from 7 to 10 days apart on average. The last survey (HCON 3) covered only 72% of the sky, and observed a given location several months later on average than the first two surveys.

Scans made during each of these surveys were averaged and binned into 16.5×16.5 images of the sky (having 512×512 2-arcminute pixels) called the IRAS Skyflux Maps (Beichman *et al.* 1988). The sky was divided into 212 such fields, and three sets were constructed, one for each HCON. There are only 188 HCON 3 Skyflux Maps due to incomplete coverage. The distribution of these fields in equatorial coordinates may be found in Beichman *et al.* (1988). Each field consists of 4 images, one for each of the IRAS bandpasses (centered on 12, 25, 60, and $100 \mu\text{m}$, respectively). It should be remembered that these images are not "snapshots" of the sky at thermal wavelengths, but are constructed from individual overlapping scans made over some period of time. Near the ecliptic plane, images are built up of scans taken over a period of a few weeks. At higher latitudes the period of time spanned may be longer. A solar system object in a prograde orbit moves in the same direction that IRAS scans shift in longitude from orbit to orbit. Thus, the same object or trail segment may be observed on consecutive orbits.

The $100 \mu\text{m}$ images are dominated everywhere by infrared cirrus, and since the thermal spectrum of inner-solar system objects should peak within the 12 or $25 \mu\text{m}$ IRAS bandpasses, only 12, 25, and $60 \mu\text{m}$ images were inspected for trails for a total of 1836 images. Trails were sought by individually processing and visually inspecting each of these images for long, narrow features characteristic of trails.

Trail contrast was enhanced by either performing a linear stretch on the image, or "flattening" the image by subtracting a plane fit to the zodiacal background. Occasionally, zero-sum high-pass filtering along the scan direction was employed, as were other "destriping" algorithms (e.g. Cutri *et al.* 1991), but these did not provide any significant advantage in the detection of trails over the simple methods generally employed.

When a trail was detected its source was identified by comparison with the projection of a known orbit onto the IRAS Skyflux Map. This is difficult because header files associated with Skyflux Maps have no timing information other than an identification of the SOP number of the first and last scan used in the image. A SOP designates a specific 12-hour time period during the IRAS mission (Beichman *et al.* 1988). Initially (Sykes *et al.*, 1986; Sykes and Dow, 1988), two positions of a potential source orbit were projected onto the Skyflux Map corresponding to the times of the first and last scans. If the trail was bracketed by these two projections, a tentative identification was said to have been made. Since most trails were located near the ecliptic, and the times spanned by the scans were generally a few weeks or less, this method generally provided unique solutions.

Since it was not known *a priori* whether dust trails were a phenomenon associated with only one class of object, several sources were considered (Table 1). These included

108 short-period comets (Marsden 1986), 28 long-period comets (having orbital periods greater than 200 years) (Marsden 1986), 36 asteroids thought to have comet-like orbits, and 58 meteor streams (Cook 1978). Long-period comets were chosen which had perihelion passage times between January 1, 1981, and July 30, 1985, bracketing the period of the IRAS mission by a couple of years on either side.

Later, we developed software in which the time and position of the intersection of a single scan by IRAS and an arbitrary orbit were calculated. Using a listing of all the scan geometries and times provided by the IRAS Zodiacal History File (Beichman *et al.* 1988), orbits could be projected onto each IRAS Skyflux Map scan by scan, incorporating all the effects of parallax. This was used to confirm the initial identification of trail parents, and was also used to provide additional information on heliocentric and geocentric distances of an observed segment of trail, as well as the angular distance of that segment from the parent comet.

Care had to be taken in the identification of some extended structures as trails. In Sykes *et al.* (1986), two trails, one of which had been tentatively identified as belonging to Shoemaker 2, the other belonging to an unidentified source, turned out to be diffraction spikes due to Jupiter (the planet was avoided in the scanning procedure, leaving a squarish void on the images from which the "trails" appeared to emerge). Similarly, diffraction spikes from Saturn were seen on an adjacent Map. Cirrus structures could also mimic the narrow appearance of trails over short distances, but were identified by their location remaining fixed between HCONs, while orbital motions of both the comet and the Earth would result in a parallactic shift between HCONs. Many faint candidate trails (e.g. Sykes and Dow 1988), seen in only one HCON, were rejected because of their correlation with the edges of cirrus structures seen at 100 μm .

Some low-resolution maps of the sky (having 0.5×0.5 pixels) were generated in support of an analysis of zodiacal dust band structures by one of the authors (Sykes 1988b). Examination of these images resulted in the discovery of a new type of dust trail (Type II) having no known parent, and characterized by a large apparent angular width (a few degrees versus a few arcminutes). Only four examples were identified (Sykes 1988b). These images were found to be useful also in the detection of known Type I trails (such as Tempel 2) over a greater range of longitudes since the coaddition into larger-area pixels results in greater signal-to-noise observations of the trail. This study focusses on the original Type I trails.

III. Results

A. Spatial Distributions

Short-period comets are the only solar system objects which were found to have trails. In all, eight trails were detected in association with known short-period comets (Table 2), and several faint trails were detected which did not appear to be associated with the orbit of any known object (a comparison with the projected orbits of all known

main-belt asteroids, however, has not been made). The location of all detected trails projected onto the plane of the ecliptic on July 1, 1983 is shown in Fig. 2. The most extended trails are Encke, Schwassmann-Wachmann 1, and Tempel 2. The distribution of the "orphan" trails are shown in Fig. 3. Whenever the coma of a short-period comet was observed on a Skyflux Plate, a trail was also detected. On the other hand, no long-period comet had a detectable trail. Comet Bowell (1982 I) was seen to have a large *tail* (Walker and Rowan-Robinson 1984), but otherwise, the long-period comets appeared as fuzzy point sources.

The portions of a given trail that IRAS would scan from orbit to orbit depended upon many factors, including the time of year, the orbital elements of the trail, and the solar elongation angle. Since the physical separation between two particles in one orbit also changes as a function of time, we characterize the segment of trail observed at any given time by its difference in mean anomaly from the mean anomaly of the parent comet. This difference does not vary with orbital phase, and allows us to keep track of the same particles as they orbit the sun.

In Figures 6-29 we show, for each HCON and each trail, scan by scan, where IRAS observed across each trail orbit. Trail positions identified in the IRAS Skyflux Maps are marked in bold, and comet positions (when scanned, or nearly scanned) are indicated. These plots are in ecliptic cylindrical coordinates, and are scaled in dimension to match the aspect ratio of the high-pass filtered, low-resolution images of Sykes (1989, 1990). Below each ecliptic coordinate map is a companion figure which shows the distance in mean anomaly relative to the parent comet of each orbital segment scanned. In most cases, we can see that only a small segment of orbit (within $\sim 20^\circ$ mean anomaly of the comet position) is scanned over most of the mission. This is a consequence of telescope scans that generally shift in the direction of increasing ecliptic longitude as the trails move in that direction. Breaks and shifts in the plots are parallactic effects resulting from changes in the pointing geometry of IRAS.

B. Thermal and Physical Characteristics

Individual detector scans of each trail have been processed and analysed using the procedure described in Sykes, Lien and Walker (1990). Observational parameters for the scans analysed in this paper are given in Table 3, along with the fluxes in each of the IRAS bandpasses where measured. Trail width is determined from the full-width at half-maximum of the trail profile and a knowledge of the heliocentric distance of the trail at the time of observation. The color temperatures were determined by fitting a graybody curve to the IRAS observations using a least-squares fit. The optical depth corresponds to the ratio of the observed trail surface brightness to that expected for a uniform surface of the same temperature. Finally, we compare the color temperature with that expected for a blackbody at the same heliocentric distance, expressed by the ratio $\epsilon/(1 - A)$ (Table 3).

Many trails exhibited a small but significant excess color temperature over that expected for a blackbody. This had been noted by Sykes *et al.* (1990) for the Tempel 2 trail. Possible explanations include low-emissivity materials, small particles, or temperature

gradients on large particles. The low emissivities required do not match that of any known non-metallic materials. Most terrestrial materials have emissivities in excess of 0.9 (Kahle 1977). In comet coma observations, color temperature excesses are generally ascribed to the presence of a sub-micron particle population (Ney 1982). Thermal observations of such comets generally exhibit silicon emission features in the spectrum - which are not evident in the broadband IRAS data. These small particles would also have to have $\beta < 10^{-3}$, corresponding to diameters $\leq 100 \text{ \AA}$ (e.g. Burns, Lamy, and Soter 1979). Such particles would have strongly coupled to the gas outflow from the comet nucleus, resulting in velocities $\sim 1 \text{ km/sec}$ relative to the comet - far removed from trail orbits. This scenario would require small particles to originate from large particle carriers, either as fragments of those larger particles or imbedded in volatile material within those particles which is subsequently released. Another explanation is that the particles are large enough to support a temperature gradient on their surfaces, so the sunlit side is warmer than the dark side, resulting in the observed excess color temperatures when observed from the Earth at low phase angles.

There are variations in the amount of temperature excess among the comets. This does not seem to be correlated with phase angle or heliocentric distance, and may represent real physical or compositional differences among refractory particles of different comets.

C. Trail Ages

The ranges of mean anomalies (in degrees) over which the trails were observed to extend in front and behind each comet are listed in Table 4. Each trail is similar in that they are seen to extend predominantly behind the parent comet in its orbit, and, over the extent to which it is detected, they decrease in surface brightness smoothly and monotonically as one moves away from the position of the parent comet. There are no breaks or significant changes in surface brightness on short spatial scales (other than those due to observational effects mentioned above).

Assuming isotropic emission, the velocity of trail particles can be related to the physical width of the trail (Sykes, Hunten, and Low 1986; Sykes, Lien, and Walker 1990). Assuming for each comet that the particles tend to be ejected near perihelion (which will maximize our resultant velocity), we calculate the particle velocities for each trail (v_{peri}) and list them in Table 4. With the exception of Encke, all trail particles have velocities of a few meters/sec. The large perihelion velocity of the Encke trail particles arises from the very small perihelion distance of P/Encke. Emissions occurring further away from perihelion, resulting in the same trail widths, correspond to lower velocities, and is shown in Table 4 in the case of aphelion emissions (v_{ap}).

Given the speed with which trail particles are moving away from their parent comets, we can estimate the age of trails from the calculated rate of change of mean anomaly (in radians/sec) of the particles relative to their parent comets. This is given by the relation

$$\dot{\theta} = \frac{1}{2} \left[\frac{GM_{\odot}}{a^3} \right]^{1/2} \left(\beta + 3 \frac{\Delta a}{a} \right) \quad (1)$$

where,

$$\Delta a = \beta a \left(\frac{1+e}{1-e} \right) + 2a\Delta v \left[\frac{a}{GM_{\odot}} \frac{1+e}{1-e} \right]^{1/2} \quad (2)$$

where the two components of Δa correspond, to first order, to the change in semi-major axis due to the effects of radiation pressure and ejection velocity. In order to maximize the effect of ejection, Δv is chosen to be in the direction of motion of the parent body at perihelion.

The age of a trail would then be

$$T = \frac{\Delta\theta}{\dot{\theta}} \quad (3)$$

Ages for each trail are given in Table 4 assuming a maximum $\beta = 10^{-3}$ (hence minimum age) determined from syndyne analysis of the Tempel 2 trail (Sykes, Lien, and Walker, 1990). Emissions are assumed to be at perihelion, further minimizing trail ages. Trail ages were also calculated using an estimated "minimum β " (β_{min}), which corresponds to the largest particle capable of reaching the forwardmost extent of the trail at the same time it reaches the hindmost portion of the observed trail:

$$\beta_{min} = 3\Delta v \left[\frac{a}{GM_{\odot}} \frac{1+e}{1-e} \right]^{1/2} \left(\frac{1-e}{2+e} \right) \left(\frac{\Delta\theta_+ - \Delta\theta_-}{\Delta\theta_+ + \Delta\theta_-} \right) \quad (4)$$

For comparison we also list the orbital period of the trails. Some trails are definitely the result of recent emissions near the time of observation, whereas other comets, in particular Tempel 2 and Encke, are the results of emissions taking place over several or more orbital periods. The continuity of these trails suggests that large particles are being emitted over a significant fraction of the comet orbits, if not the entire orbits. Even though surface activity may have essentially shut down on the nucleus, there might exist a long-lived coma consisting of large particles which "bleed-off" into trail orbits as a consequence of collisional activity or gravitational perturbations. Such a large particle coma around a comet nucleus may have been detected by radar observations of IRAS-Araki-Alcock, though it was not thought to be gravitationally bound (Goldstein *et al.* 1984).

D. Comet Mass Loss

If we assume the trail profile is triangular, that the optical depth of the trail falls linearly with increasing $\Delta\theta$ over the range detected, and that all particle are a single size or β , then we can calculate the mass of the trail particles from the relation

$$M_{\text{trail}} = 6.6 \times 10^{-7} a W \tau (\Delta\theta) / \beta \quad (\text{cgs}) \quad (5)$$

where a is the semimajor axis, W is the trail width, and τ is the peak optical depth (from Table 3). The trail masses, assuming a maximum $\beta = 10^{-3}$ are listed in Table 4.

Given the age of the trails calculated above, a refractory mass loss rate is estimated for each trail comet and given in Table 4. Decreasing β (increasing particle sizes) increases both trail mass and ages, but in a way which results in a slowly increasing rate of refractory mass loss. When we compare these numbers with mass loss rates estimated from visual wavelength observations (Kresák and Kresáková 1987) (Table 4), we find that, in general, as much or more material is lost in large refractory particles than has been estimated previously for all gas and dust together. Moreover, this refractory mass loss appears to be in a narrow size range roughly spanning a decade from 1 mm to 1 cm (or less).

IV. Why These Comets?

One can understand why trails might not be seen in association with long-period comets. By the time such a comet returns to the inner solar system, the large debris ejected near perihelion would have spread out over such a large distance that its surface brightness would be much reduced. But why were these particular short-period comets found to have trails? More specifically, are these comets peculiar or do all short-period comets possess trails?

We know that several trail comets are, indeed, unusual. Encke has the smallest known perihelion distance of all short-period comets, and is historically very active. Schwassmann-Wachmann 1 is well known for its large random outbursts which result in an increase of 5 to 8 magnitudes at visual wavelengths. Gunn, in the 19th century had an orbit completely outside that of Jupiter's, and now has an orbit completely within Jupiter's. Pons-Winnecke and Churyumov-Gerasimenko have also experienced significant decreases in their perihelion distance this century (Belyaev *et al.* 1986). So perhaps the existence of an observable trail is related to the intrinsic level of activity of these comets.

Kresák and Kresáková (1987) calculated the total mass of dust lost by 122 comets over the past century, based on assumptions of dust production rates inferred from estimates of absolute magnitude, a heliocentric distance dependence of that rate, and careful consideration of orbital changes over the period covered. Their results are summarized in a histogram (Fig. 30), where the mass of dust generated by trail comets are indicated. If we put aside the values for Encke and Schwassmann-Wachmann 1, since their behavior is already known to be anomalous relative to the population of short-period comets, we see that trail comets do appear to be among the more "active" short-period comets. This has been confirmed by the preliminary results of Schliecher *et al.* (1991) who have been rereducing comet photometry of the past 15 years to produce an internally consistent measure of gas and dust production rates over approximately 80 comets. A comparison of trail comets with other short period comets show them, again, to be among the more active

comets in both gas and dust production (Schleicher, private communication). This is not sufficient, however, to explain why these particular comets were found to have trails, while others, presumably as or more active had no trails detected.

A reasonable answer is found by considering where in their orbits the dust trails were scanned. Fig. 31 shows the heliocentric distance, in each HCON, at which a segment of orbit within 2° mean anomaly of a comet was scanned by IRAS. This was done for 104 short-period comets, and the results were plotted against the perihelion distance of the comet. Excluding Encke and Schwassmann-Wachmann 1, the dust trails were associated with comets having the lowest perihelion distances that were also scanned during perihelion passage. Many additional comets had similarly low perihelion distances, but tended to be scanned at aphelion. This is understandable since an object in an elliptical orbit will spend most of its time at aphelion, and the least time at perihelion. At greater heliocentric distances trail material will have colder temperatures, and hence will be fainter at thermal wavelengths. This is illustrated in Fig. 32, where the variation of IRAS inband flux as a function of heliocentric distance is shown for a blackbody in radiative equilibrium with sunlight. In the IRAS 12 and 25 μm bands (1 and 2), the difference between perihelion and aphelion inband flux can be more than a factor of 10. Since the surface brightness of these structures is low compared to noise associated with the zodiacal background, relatively small decreases in brightness can make their identification in the Skyflux Maps difficult. In combination with the investigations of their relative activity, we conclude that IRAS detected these particular comet trails because they were well supplied by their parents and were the hottest comet particles (hence brightest at thermal wavelengths, for a given optical depth) available at the time of the mission. This implies that future orbiting infrared detectors such as the Infrared Space Observatory will see a different ensemble of trails at different times (with the possible exceptions of Encke, SW1, and Tempel 2) as other comets cycle through perihelion.

V. DISCUSSION

A. Trails and Meteor Streams

Meteor streams are extremely large structures consisting of material spread over an entire cometary orbit (or in the case of the Geminids, the orbit of a possible asteroid). Rather than uniformly filling a toroid, meteoroids (generalizing from McIntosh and Hajduk 1983) are distributed over a "shell-like surface traced out by the long-term evolution of the comet", further complicated by the long-term evolution of individual meteoroid orbits. Though trails extend over only small portions of a comet orbit, and are less than hundreds of years in age (compared to thousands of years for meteor streams), they represent the very beginning of meteor stream formation.

Cross-sectional dimensions of meteor streams can be fairly large. McIntosh and Hajduk (1983) estimate that the belt comprising the Orionid and η -Aquarid streams (associated with P/Halley) to be 0.44 AU perpendicular to the orbital plane and ~ 0.05 AU

in the plane. This compares with typical trail widths of $< 10^{-3}$ AU. As a consequence of their young age, trails have not been scattered significantly by gravitational perturbations (primarily due to Jupiter) and are extremely well defined in space. Any such scattering would greatly decrease trail surface brightness, resulting in non-detection by IRAS). That no known meteor streams were identified in the IRAS image data is not surprising when one considers that their peak optical depths may range from 3 to 5 orders of magnitude smaller than that of the Tempel 2 trail (assuming the number densities of Rendtel 1989, and a path length of 0.1 AU), and that the dust trails seen by IRAS were fairly low signal-to-noise structures.

Meteor streams are detected when the Earth passes through them and the particles leave luminous streaks in the sky as they burn up. During some of the most spectacular displays, such as the Leonids, there were more than 10,000 meteors per hour. Were the Earth to pass through the Tempel 2 trail, near the comet, we would see more than 100,000 meteors per second!

Orbital perturbations result in shifts in short-period comet orbits on timescales of decades. The strength of the perturbation is an increasing function of the proximity of a body to Jupiter. So, while a comet may experience a significant perturbation by Jupiter, a particle at another location in the same orbit may experience a significantly smaller perturbation, resulting in the two objects having different orbits. This is why trails are not seen to extend completely around a comet's orbit. A close encounter with Jupiter, such as that experienced by P/Oterma in the 1930's, would effectively scatter any associated trail particles in the vicinity of the comet (Carusi *et al.* 1981). Any remaining, more distant trail segment would be "disconnected" from its parent and slowly fade with time as the particles continue to spread over the older orbit (and are subject to future perturbations by Jupiter). It is possible that several of the "orphan" trails may be the disconnected remnants of just such events.

At the ejection velocities listed in Table 4, it would take $\sim 10^3$ years for particles released from a comet to distribute themselves completely around the orbit, in which time the parent comet may have had its orbit shifted several times. The time between the IRAS observations and the last significant shift in orbit due to a close encounter with Jupiter for each of the trail comets is listed in Table 5 (Baelaev *et al.* 1986). We see that in several cases these comet orbits have shifted on timescales less than the maximum trail ages in many cases. Detailed dynamical modeling will be required to determine whether to what extent these orbital perturbations shift trail particle orbits, or require a resetting of the trail "clock." In some instances we may have a situation where an observed trail represents the complete emission history of large particles from a comet over a known time interval.

B. Comets and the Origin of Zodiacal Dust

The origin of the zodiacal cloud has long been thought to be primarily cometary (Whipple 1955, 1967, 1976). Estimates of dust production by short-period comets at the current epoch, however, have fallen an order of magnitude or more short of that needed to maintain the cloud against losses by radiation forces (after collisional evolution) (Delsemme

1976, Röser 1976). A cometary cloud would be replenished by the occasional capture of "new", highly active comets into short-period orbits. Whipple (1967) has suggested P/Encke as having been such a source in the past.

Asteroid collisions also have been considered to be a source of interplanetary dust, but the lack of observational constraints on the population of boulder-sized precursors to dust, and uncertainties in the mechanics of collisional disruption of these and larger bodies, have made it difficult to estimate the asteroidal contribution. When the Pioneer spacecraft failed to detect an enhancement in the spatial density of interplanetary dust as they passed through the asteroid belt, the contribution of asteroid collisions to the zodiacal complex consequently was thought to be small compared to comets (Dohnanyi 1976). This has undergone extensive revision since the discovery of the asteroid dust bands by IRAS (Low *et al.* 1984) and work suggesting that asteroid collisions may in fact be the principal source of zodiacal dust (Sykes and Greenberg 1986, Reach 1991).

The generality of the dust trail phenomenon is important when considering the rate at which short-period comets supply mass to the interplanetary dust complex. A comparison with total mass-loss rates estimated from groundbased observations (Table 4) indicates that several times more mass is lost in refractory trail particles alone. Assuming a canonical dust-to-gas mass ratio of ~ 1 , the contribution of comets to the zodiacal cloud should be increased by at least a half an order of magnitude. While this still falls short of comets being capable of supplying the entire cloud, their significance is greatly increased.

In its observations of the zodiacal cloud, IRAS was most sensitive to particle radii of several microns at 12 and 25 μm (Reach 1988). Since trail particles are much larger, the cometary component of this cloud would arise from the collisional comminution of trail particles over time. However, IRAS also observed the cloud to have a high degree of azimuthal symmetry about the sun (to within a few percent of predicted surface brightness at 12 and 25 μm) (Good 1991). As trail particles are comminuted into smaller sizes, they would be increasingly sensitive to radiation pressure and at some point might find themselves in Jupiter-crossing orbits. Numerical simulations of the dynamical evolution of such particles directly ejected from P/Encke, suggests that their orbital nodes would be distributed over all longitudes as a consequence of gravitational interactions with Jupiter (Gustafson, Misconi, and Rusk 1987). This could result in the cometary component of the zodiacal cloud having reasonable azimuthal symmetry about the sun. Otherwise, a cometary cloud would be very "bumpy".

C. The Nature of Short-Period Comets

Comets contain a far greater fraction of refractory material than has been previously imagined. This is inferred from the mass loss rates of the trails and that expected for their parent comets on the basis of visual wavelength observations (Table 4). Historically, the refractory/volatile mass ratio has been estimated between 0.5 and 1 (Delsemme 1983, Greenberg 1983). Using a ratio of 1 (Kresák and Kresáková 1987) to determine the mass of volatiles released in one century from the trail comets (Table 4) and ratioing that into the mass injected into the trail over the same period, the refractory/volatile mass ratio is

~ 4.

The larger cometary mass loss rates inferred from trail studies suggests that short-period comets are evolving more rapidly and have shorter active lifetimes than previously thought. A large refractory component also suggests that it is easier for comets to evolve into asteroidal bodies than had been previously thought. This may be the case in a number of asteroids thought to be extinct comet nuclei.

If this represents the cosmogonic mass ratio, then our view of comets as "dirty snowballs" needs to be revised to perhaps "icy mudballs". In the dirty snowball case, cometary refractory material would make up from 33%–50% of the mass and 10%–20% of the volume of the nucleus. In the icy mudball model, cometary refractory material would comprise ~80% of the mass and ~50% of the volume.

Greatly increasing the refractory fraction of comets does not necessitate a similar increase in their bulk density. Estimates of the density of P/Halley from the *Giotto* encounter are less than 1 g/cm³. The mass density of meteor stream particles (which are refractory) range between 0.2 and 1 g/cm³ (Lindblad 1976). Stratospheric dust collection experiments find many very low density particles. In this case, the combination of low-density dust structures and high refractory/volatile mass ratios would imply that comets are "foamy" objects, whose internal structure is dominated by interstitial spaces - more like styrofoam than a block of ice.

Another explanation for the origin of trail particles is that they could be fragments of a thick and well-developed mantle covering the canonical dirty snowball nucleus. However, such a mantle would have to be cyclic. There would have to be a period dominated by devolatilization of the outer layer of the nucleus, leaving a residual mantle, followed by a period during which the mass loss would be primarily refractory as the mantle is fragmented and carried off, followed by another period of devolatilization. This is required to explain the current excess of refractory mass loss over that expected from a dirty snowball. One problem with this scenario is that half the comets should be losing mass primarily in gas, which is not evident.

A large refractory mass fraction is inconsistent with comets originating in the cold regions of interstellar space and molecular clouds (e.g. Greenberg 1983), implying rather that they derive from relatively warmer regions of the primordial solar nebula. For dynamical reasons, the region in which comets formed prior to ejection into the Oort cloud is thought to be the vicinity of proto-Uranus and proto-Neptune (Fernández and Ip 1981). Since these planets would have formed from cometary bodies, their compressed mass densities of 1.58 and 2.30 g/cm³ [what happens if hydrogen and helium are removed?] suggest that comets having such a large refractory component could(?) not have been the principal source of volatiles for these planets. Of course, ease of dynamical transport to Oort cloud alone is insufficient as determinant of comet formation location. A "mudball" would have formed closer to the Sun than Uranus and Neptune, but it is possible that formation efficiency and population densities of these objects closer in to the Sun may have been greater than that needed to offset the inefficiencies of transport to Oort cloud orbits.

Appendix I. Notes on Individual Trails

Churyumov-Gerasimenko

This extremely faint trail was detected over a very small portion of the parent orbit (Fig. 4 - 6). Neither coma nor trail were detected in HCON 2. In the case of the latter, this was probably due to a decrease in contrast against the background. The coma was not detected in HCON 2 (Fig. 5) because it was barely missed by IRAS, which scanned within a few tenths of a degree on either side of it. The apparent break in the trail in Fig. 4 is actually due to the satellite, at a later time, scanning back over the same orbital segment (including the coma) which shifts position in the interim. The coma and trail are missed completely during HCON 3 (Fig. 6).

Encke

The Encke trail was one of the most extensive detected by IRAS (Fig. 7 - 9). It is particularly interesting in the light of speculation by several authors that P/Encke alone might account for the bulk of the interplanetary dust complex. It is curious, therefore, that while having a large trail, the Encke coma was not detected when its position was scanned by IRAS, perhaps indicating a relative lack of activity at the times of observation, when the comet was at distances of 2.8 and 2.9 AU, beyond the distance at which water-driven activity turns on.

The extent of the trail is in part due to the stability of the Encke orbit, which is very little influenced by Jovian perturbations. The ascending node, argument of perihelion, and inclination have all slowly decreased by a few degrees or less over the last 200 years (Belyaev *et al.* 1986), which suggests that the trail particle orbits have been similarly affected.

Gunn

IRAS coverage of the Gunn orbit is shown in Figures 10 - 12. Trail observations forward of the comet coma in HCON 1 (Fig. 10) were truncated by a change in the IRAS scan pattern. Similarly, in HCON 2 (Fig. 11) the coma itself was not scanned by IRAS.

P/Gunn is another comet with an interesting dynamical history. In 1800, the orbit of P/Gunn was completely outside that of Jupiter (Belyaev *et al.*, 1986). By 1900 its orbit was completely within that of Jupiter, and its perihelion distance was around 3.5 AU. In 1965 perturbations by Jupiter resulted in a further decrease in perihelion distance to its current 2.4 AU with an increase in eccentricity from 0.18 to 0.32. The orbital inclination was changed by less than half a degree. Thus, by 1983 the Gunn trail should have built up emissions from only 3 perihelion passages.

Kopff

While extensively observing the Kopff dust trail, the Kopff coma was missed during HCONs 1 and 2 (Fig. 13, 14), but was observed during HCON 3 (Fig. 15). The break in trail coverage seen in HCON 3 (Fig. 15) was due to the trail being washed out by background cirrus in the vicinity of the galactic center.

In 1954 the Kopff orbit was shifted by Jupiter, changing its perihelion distance and eccentricity very little, but decreasing its inclination by a few degrees and decreasing the longitude of the ascending node by 133° (Belyaev *et al.*, 1986). Thus, trail emissions are not likely to be older than 29 years.

Pons-Winnecke

IRAS coverage of the Pons-Winnecke orbit are shown in Figures 16 - 18. The trail was one of the fainter trails observed, and heavily broken up on the IRAS Skyflux Maps as a consequence of several changes in viewing geometry by IRAS.

Schwassmann-Wachmann 1

The Schwassmann-Wachmann 1 trail was the most distant observed (6.2 AU), and is associated with a comet noted for its peculiar and violent outbursts at random times resulting in increases in brightness of 5 - 8 magnitudes at visual wavelengths (Marsden 1986). As a consequence of the large orbital radius, IRAS fairly evenly scanned the orbit relative to the comet's instantaneous position (Fig. 19, 20, 21). In HCON 3, the vicinity of the comet was not scanned by IRAS.

Tempel 1

IRAS coverage of the Tempel 1 orbit is shown in Figures 22 - 24. The trail and coma were not detected in HCON 3 because of cirrus in the direction of the galactic center.

The Tempel 1 orbit was perturbed by Jupiter in 1941 and 1953 resulting in a net decrease of semi-major axis from 2.1 to 1.5 AU and small shifts in the other orbital elements.

Tempel 2

It almost seemed that IRAS could not look anywhere without seeing the Tempel 2 dust trail (Figs. 25 - 27). This was a consequence of the proximity of the trail to the earth and the small change in the relative positions of the earth and the dust trail as both moved about the Sun. Breaks in the coverage of the observed trail were due to cirrus in the direction of the galactic center.

As with Encke, Tempel 2 has a very stable orbit, which accounts for the fact that we may be seeing cometary emissions as old as several hundred years.

Orphans

With one exception, these trails are all at the limits of detection very faint and are seen in only one or two wavelength bands.

Acknowledgments

We would like to thank D. Schleicher, B. Millis, T. Bowell, and M. A'Hearn for sharing their recent work on comet gas and dust production rates prior to its publication. L. McFadden and F. Vilas provided lists of asteroids in comet-like orbits early on in the current work. An ephemeris program generously provided by D. Tholen was used in the initial trail-parent identification effort. This work has benefited from discussions with D. Lien, F. Low, R. Cutri, S. Larson, and R. Rudy. This work was supported in part by the NASA Astrophysics Data Program and Air Force Geophysics Laboratory Contract F19628-87-K-0045.

References

- A'Hearn, M., H. Campins, D. Schleicher, and R. Millis 1989. The nucleus of comet P/Tempel 2. *Astrophys. J.* **347**, 1155-1166.
- Beichman, C., G. Neugebauer, H.J. Habing, P.E. Clegg, and T. Chester (Eds.) (1988). *IRAS Catalogs and Atlases: Explanatory Supplement*. Government Printing Office, Washington D.C.
- Belyaev, N., L. Kresák, E. Pittich, and A. Pushkarev 1986. *Catalog of Short-Period Comets*. Bratislava.
- Burns, J.A., P. Lamy, and S. Soter 1979. Radiation forces on small particles in the solar system. *Icarus* **40**, 1-48.
- Carusi, A., L. Kresák, and G. Valsecchi 1981. Perturbations by Jupiter on a chain of objects moving in the orbit of Comet Oterma. *Astron. Astrophys.* **99**, 262-269.
- Cook, A. 1973. A working list of meteor streams. In *Evolutionary and Physical Properties of Meteoroids*. Eds., C. Hemenway, P. Millman, and A. Cook (U.S. Government Printing Office, Washington D.C). NASA SP-319, 183-191.
- Davies, J.K., S.F. Green, B.C. Stewart, A.J. Meadows, and H.H. Aumann 1984. The IRAS fast moving object search. *Nature* **309**, 315-319.
- Delsemme, A. H. 1976. The production rate of dust by comets. In *Lecture Notes in Physics No. 48, Interplanetary Dust and Zodiacal Light*, H. Elsässer and H. Fechtig, eds., Springer-Verlag (New York), pp. 314-318.
- Delsemme, A. H. 1982. Chemical composition of cometary nuclei. In *Comets* (L. Wilkening, ed.), pp. 85-130. University of Arizona Press, Tucson.
- Dohnanyi, J. S. 1976. Sources of interplanetary dust: Asteroids. In *Lecture Notes in Physics No. 48, Interplanetary Dust and Zodiacal Light*, H. Elsässer and H. Fechtig, eds., Springer-Verlag (New York), pp. 187-205.
- Draine, B.T. and E.E. Salpeter 1979. On the physics of dust grains in hot gas. *Astrophys. J.* **231**, 77-94.
- Eaton, N., J.K. Davies, and S.F. Green 1984. The anomalous tail of comet P/Tempel 2. *Mon. Not. R. Astron. Soc.* **211**, 15P-19P.
- Fernández, J. A. and W.-H. Ip 1981. Dynamical evolution of a cometary swarm in the outer planetary region. *Icarus* **47**, 470-479.
- Goldstein, R., R. Jurgens, and Z. Sekanina 1984. A radar study of comet IRAS-Araki-Alcock 1983d. *Astron. J.* **89**, 1745-1754.

- Gombosi, T. 1987. An orbital evolution model of the nucleus-coma interface region of comet P/Tempel 2. CRAF Project Document, private communication.
- Good, J. 1991. Zodiacal dust cloud modelling using the IRAS data. Preprint.
- Greenberg, J. M. 1982. What are comets made of? A model based on interstellar dust. In *Comets* (L. Wilkening, ed.), pp. 131-163. University of Arizona Press, Tucson.
- Gustafson, B., Misconi, N. and Rusk, E. 1987. Interplanetary dust dynamics. II. Poynting-Robertson drag and planetary perturbations on cometary dust. *Icarus* **72**, 568-581.
- Kahle, A. 1977. A simple thermal model of the Earth's surface for geologic mapping by remote sensing. *J. Geophys. Res.* **82**, 1673-1680.
- Keller, H., C. Arpigny, C. Barbieri, R. Bonnet, S. Cazes, M. Caradini, C. Cosmovici, W. Delamare, W. Huebner, D. Hughes, C. Jamar, D. Malaise, H. Reitsema, W. Schmidt, P. Siege, F. Whipple, and K. Wilhelm 1986. First Halley Multicolour Camera imaging results from Giotto. *Nature* **321**, 320-325.
- Koschack, R. and J. Rendtel 1988. Number density in meteor streams. *Werkgroepnieuws-meteoren* **16**, 149-157.
- Kresák, L. and M. Kresáková 1987. The mass loss rates of periodic comets. In Symposium on the Diversity and Similarity of Comets. ESA SP-278, 739-744.
- Lamy, P. and J.M. Perrin 1988. Light scattering of large rough particles: Applications to cometary grains. In *Infrared observations of comets Halley and Wilson and properties of the grains*. ed. M. Hanner, NASA CP-3004 (U.S. Government Printing Office; Washington D.C.), 156-157.
- Lien, D.J. 1990. Dust in comets. I. Thermal properties of homogeneous and heterogeneous grains. *Astroph. J.* **335**, 680-692.
- Lindblad, B.A. 1976. Meteoroid densities. In *Interplanetary Dust and Zodiacal Light*, eds. H. Elsasser and H. Fechtig, Springer-Verlag (New York), 373-378.
- Marsden, B. G. 1986. *Catalog of Cometary Orbits*. 5th edition. International Astronomical Union.
- McIntosh, B.A. and A. Hajduk 1983. Comet Halley meteor stream: a new model. *Mon. Not. R. Astron. Soc.* **205**, 931-943.
- McIntosh, B.A. and J. Jones 1988. The Halley comet meteor stream: numerical modelling of its dynamic evolution. *Mon. Not. R. Astron. Soc.* **235**, 673-693.
- Moshir, M., G. Kopan, T. Conrow, H. McCallon, P. Hacking, D. Gregorich, G. Rohrbach, M. Melnyk, W. Rice, L. Fullmer, J. White, and T. Chester 1989. *Explanatory Supplement to the IRAS Faint Source Survey*. Jet Propulsion Lab, Pasadena.
- Neugebauer, G., H. Habing, R. van Duinen, H. Aumann, B. Baud, C. Beichman, D.

- Beintema, N. Boggess, F. Clegg, T. de Jong, J. Emerson, T.N. Gautier, F. Gillett, S. Harris, M. Hauser, J. Houck, R. Jennings, F. Low, P. Marsden, G. Miley, F. Olton, S. Pottasch, E. Raimond, M. Rowan-Robinson, B. Soifer, R. Walker, P. Wesselius, and E. Young 1984. The Infrared Astronomical Satellite (IRAS) mission. *Astrophys. J.* **278**, L1-L6.
- Ney, E.P. 1982. Optical and infrared observations of bright comets in the range $0.5\ \mu\text{m}$ to $20\ \mu\text{m}$. In *Comets* (L. Wilkening, ed.), pp. 323-340. University of Arizona Press, Tucson.
- Reach, W. 1988. Zodiacal emission. I. Dust near the Earth's orbit. *Astrophys. J.* **335**, 468-485.
- Reach, W. 1991. Asteroidal dust and the zodiacal emission. In *The Origin and Evolution of Interplanetary Dust*, A.-C. Levasseur-Regourd, ed., Kluwer (Dordrecht), in press.
- Rendtel, J. 1989. Number densities in Eta Aquarids and Orionids, preprint.
- Röser, S. 1976. Can short period comets maintain the zodiacal cloud?'. In *Lecture Notes in Physics No. 48, Interplanetary Dust and Zodiacal Light*, H. Elsässer and H. Fechtig, eds., Springer-Verlag (New York), pp. 319-322.
- Sagdeev, R., J. Blamont, A. Galeev, V.I. Moroz, V. Shapiro, V. Shevchenko, and K. Szego 1986. Television observations of comet Halley from Vega spacecraft. *Nature* **321**, 262-266.
- Sekanina, Z. 1979. Expected characteristics of large dust particles in comet Halley. In *Comet Halley Micrometeorite Hazard Workshop*, ESP SP-153, Paris, 25-34.
- Sykes, M.V. 1988a. The albedo of large refractory particles from P/Tempel 2. In *Comets to Cosmology* (A. Lawrence, ed.), pp. 66-72. Springer-Verlag, New York.
- Sykes, M.V. 1988b. IRAS observations of extended zodiacal structures. *Astrophys. J.* **334**, L55-L58.
- Sykes, M.V. and K. Dow 1988. The cometary dust trail survey. *Bull. Am. Astr. Soc.*, **840**.
- Sykes, M.V. and R. Greenberg. The formation and origin of the IRAS zodiacal dust bands as a consequence of single collisions between asteroids. *Icarus* **65**, 51-69.
- Sykes, M.V., D.M. Hunten, and F.J. Low 1986b. Preliminary analysis of cometary dust trails. *Adv. Sp. Res.* **6**, 67-78.
- Sykes, M.V., L.A. Lebofsky, D.M. Hunten, and F.J. Low 1986a. The discovery of dust trails in the orbits of periodic comets. *Science* **232**, 1115-1117.
- Sykes, M.V., D. Lien, and R.G. Walker 1990. The Tempel 2 dust trail. *Icarus* **86**, 236-247.
- Walker, R.G. and H.H. Aumann 1990. IRAS comet observations: The continuing saga. *Adv. Sp. Res.* **10**, 151-158.

Walker, R.G. and M. Rowan-Robinson 1984. The peculiar tail of comet Bowell. *Bull. Am. Astron. Soc.* **18**, 816.

Whipple, F. 1955. A comet model. III. The zodiacal light. *Astroph. J.* **121**, 750-770.

Whipple, F. 1967. On maintaining the meteoritic complex. In *The Zodiacal Light and the Interplanetary Medium* (J.L. Weinberg, ed.), NASA SP-150, pp. 409-426.

Whipple, F. 1976. Sources of interplanetary dust. In *Lecture Notes in Physics No. 48, Interplanetary Dust and Zodiacal Light*, H. Elsässer and H. Fechtig, eds., Springer-Verlag (New York), pp. 403-415.

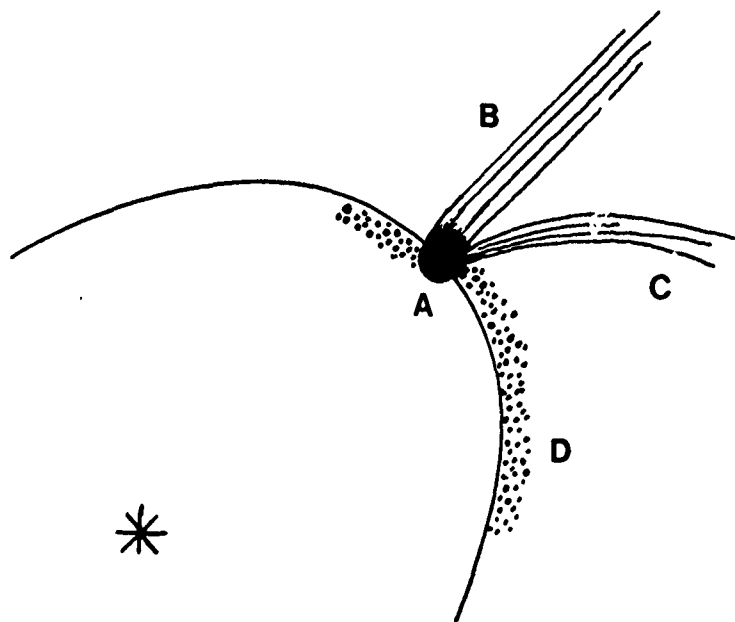


Figure 1. Comets generally exhibit a variety of phenomena at visual wavelengths including (a) the coma, (b) an ion tail, and (c) a dust tail. At thermal wavelengths a new phenomenon becomes apparent: (d) the dust trail, consisting of large particles moving slowly away from the nucleus along orbital paths very close to that of the parent comet.

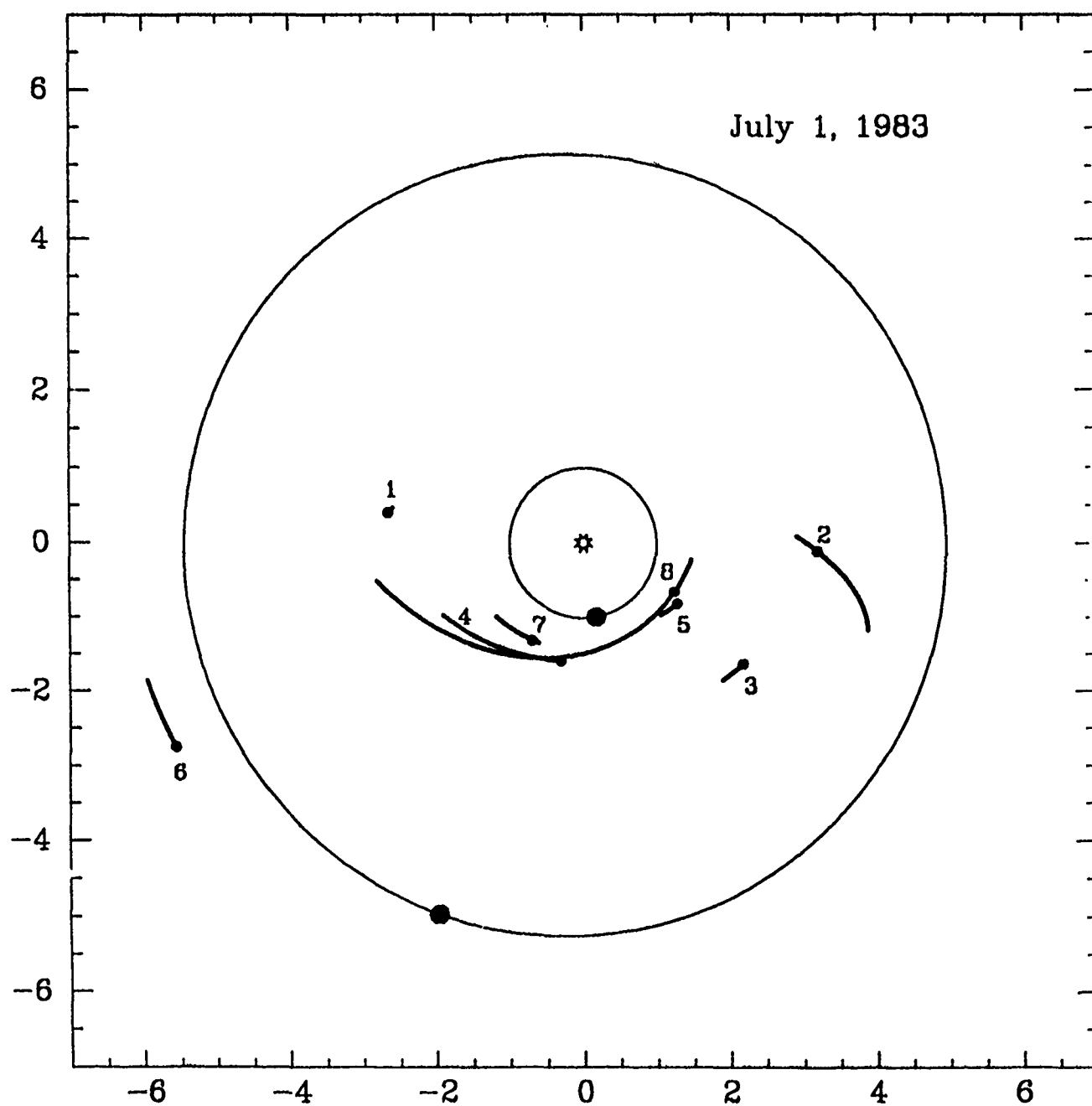


Figure 2. The location of the observed dust trails projected onto the ecliptic plane on July 1, 1983. The orbits and positions of the Earth and Jupiter are also shown. The trails are (1) Churyumov-Gerasimenko, (2) Encke, (3) Gunn, (4) Kopff, (5) Pons-Winnecke, (6) Schwassman-Wachmann 1, (7) Tempel 1, (8) Tempel 2. Large dots within the trails indicate the positions of the comet nuclei.

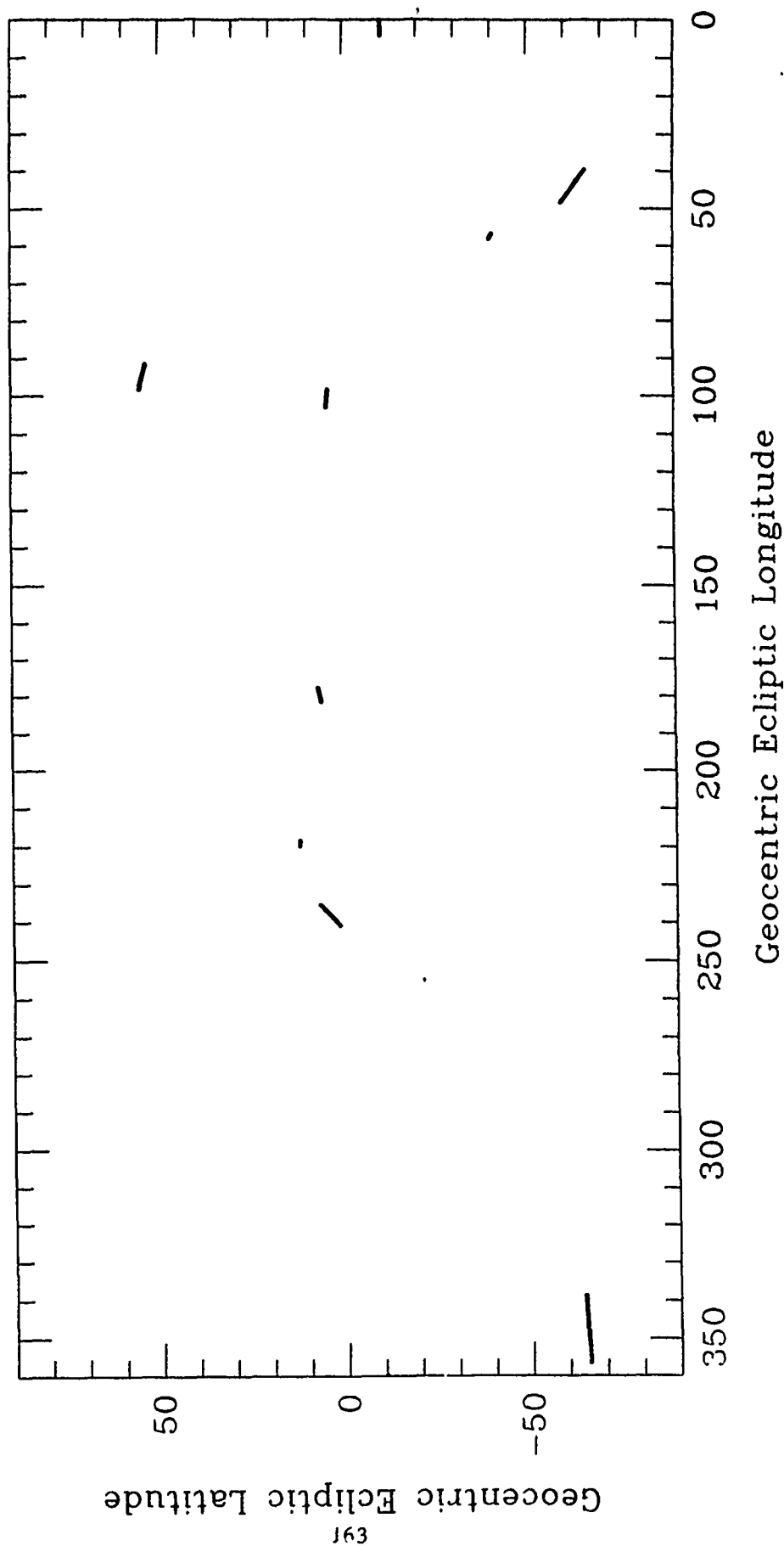


Figure 3. The observed locations of the orphan trails in geocentric ecliptic coordinates.

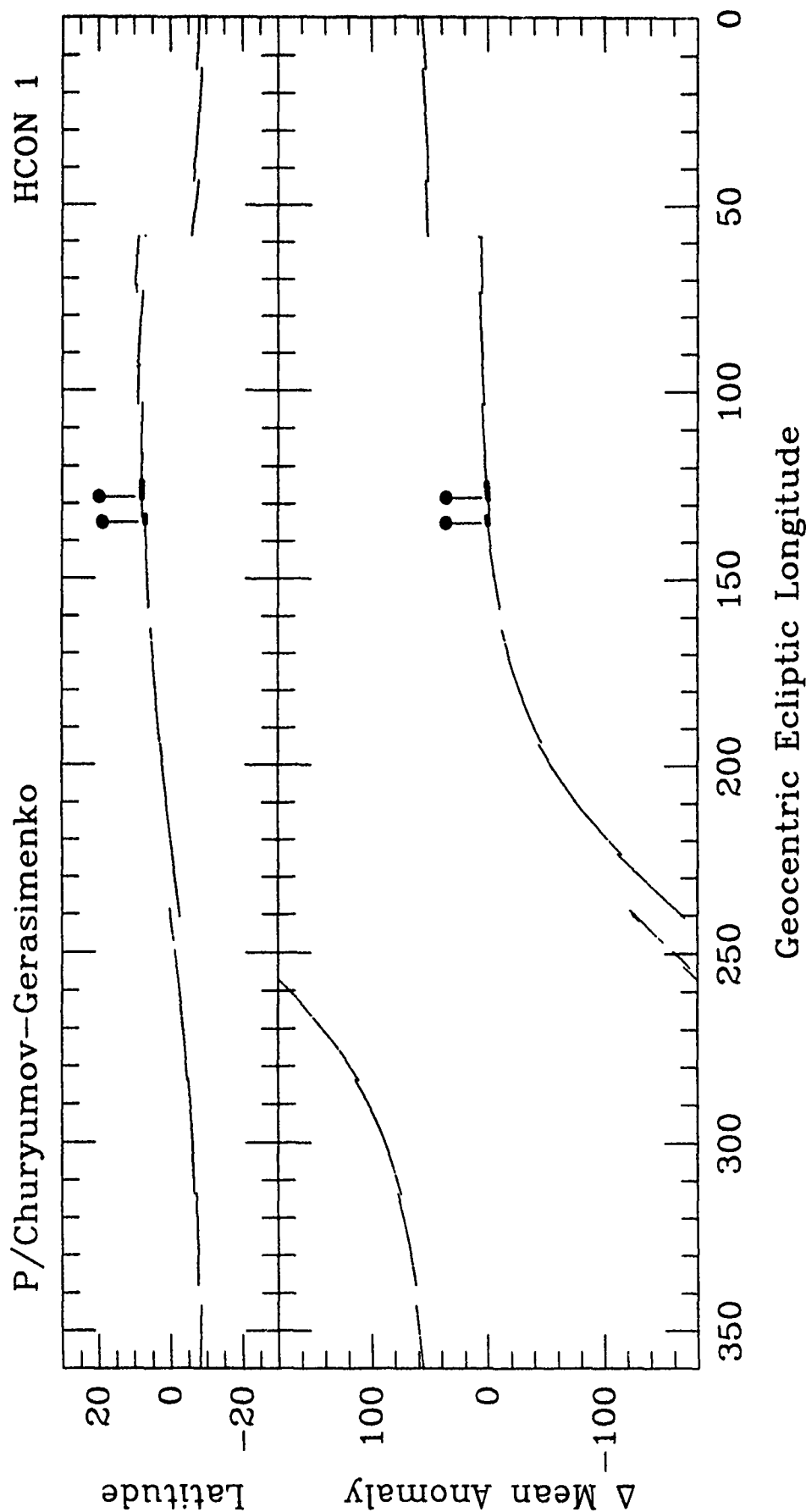


Figure 4. The geocentric ecliptic coordinates of each scan of the Churyumov-Gerasimenko during HCON 1 (light line). The heavy line indicates where a trail was observed on the IRAS Skyflux Maps. A filled circle (●) shows where the parent coma was detected. A cross (×) indicates either where IRAS scanned the comet position without detecting it, or where IRAS came close to scanning the comet position, but did not scan it. Also shown is the angular distance in degrees of mean anomaly of the orbit segment scanned from the position of the parent comet at the time of observation. A negative value indicates a location forward of the comet's position in its orbit.

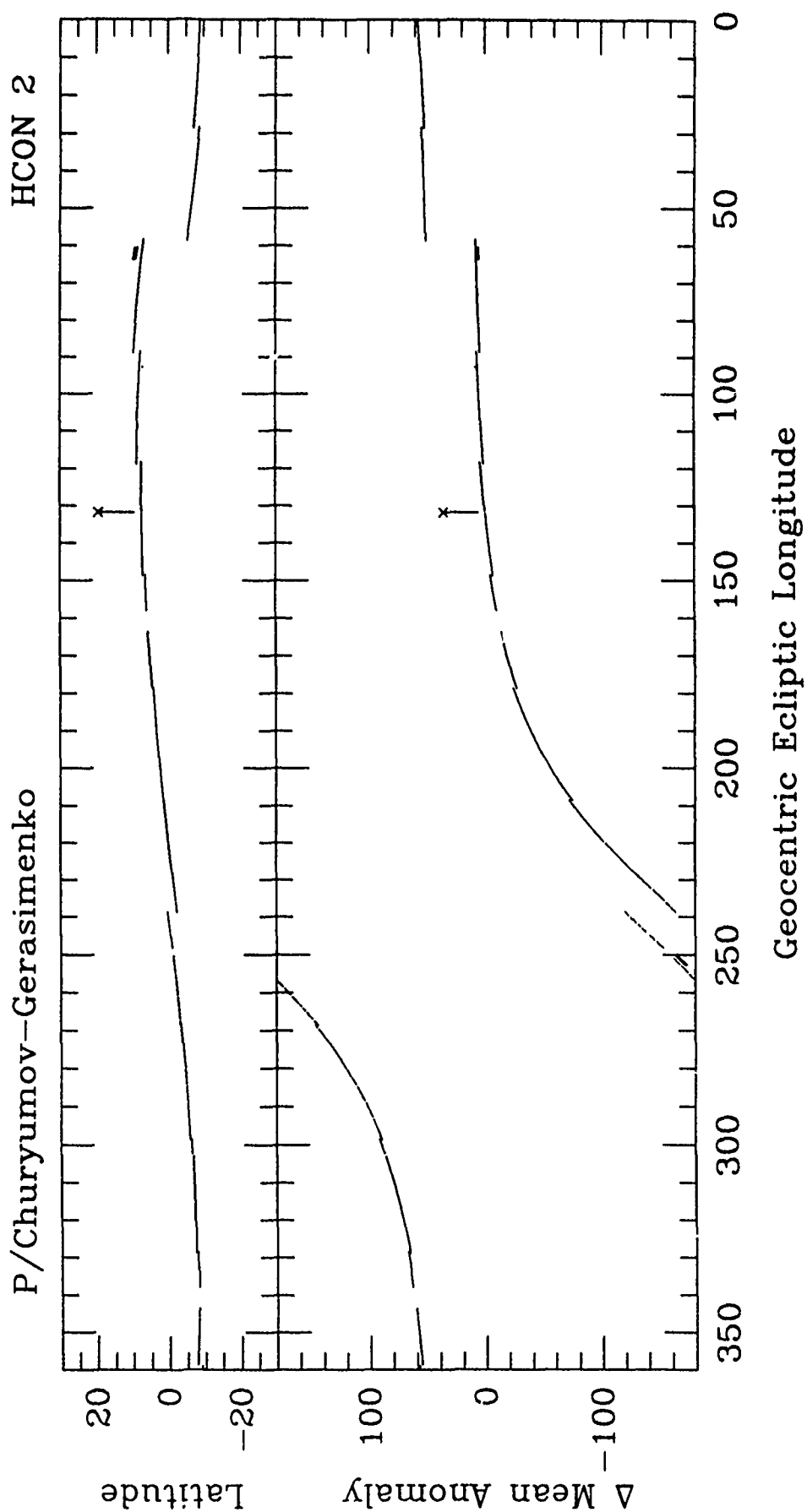


Figure 5. Churyumov-Gerasimenko, HCON 2. See Fig. 4.

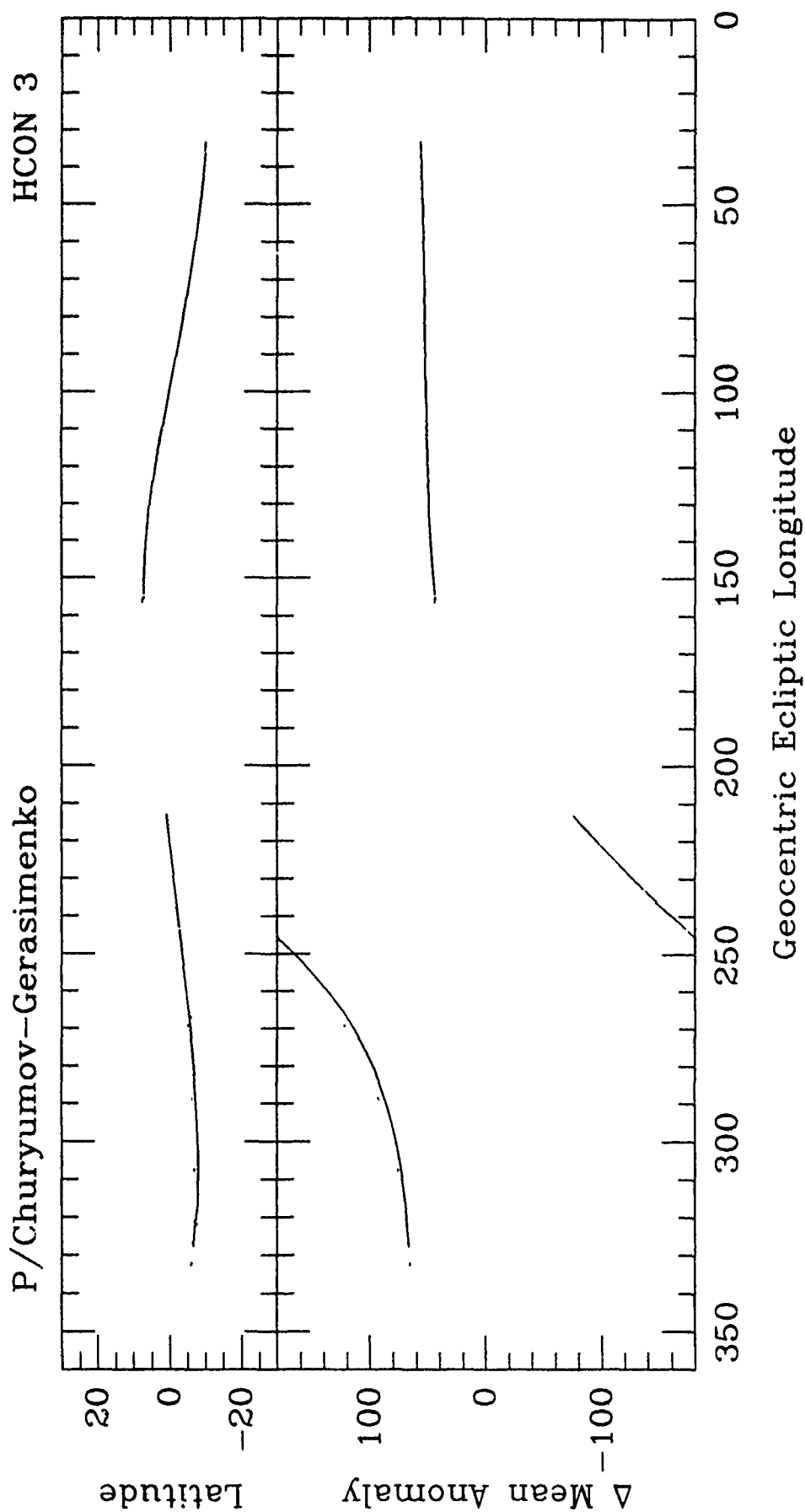


Figure 6. Churyumov-Gerasimenko, HCON 3. See Fig. 4.

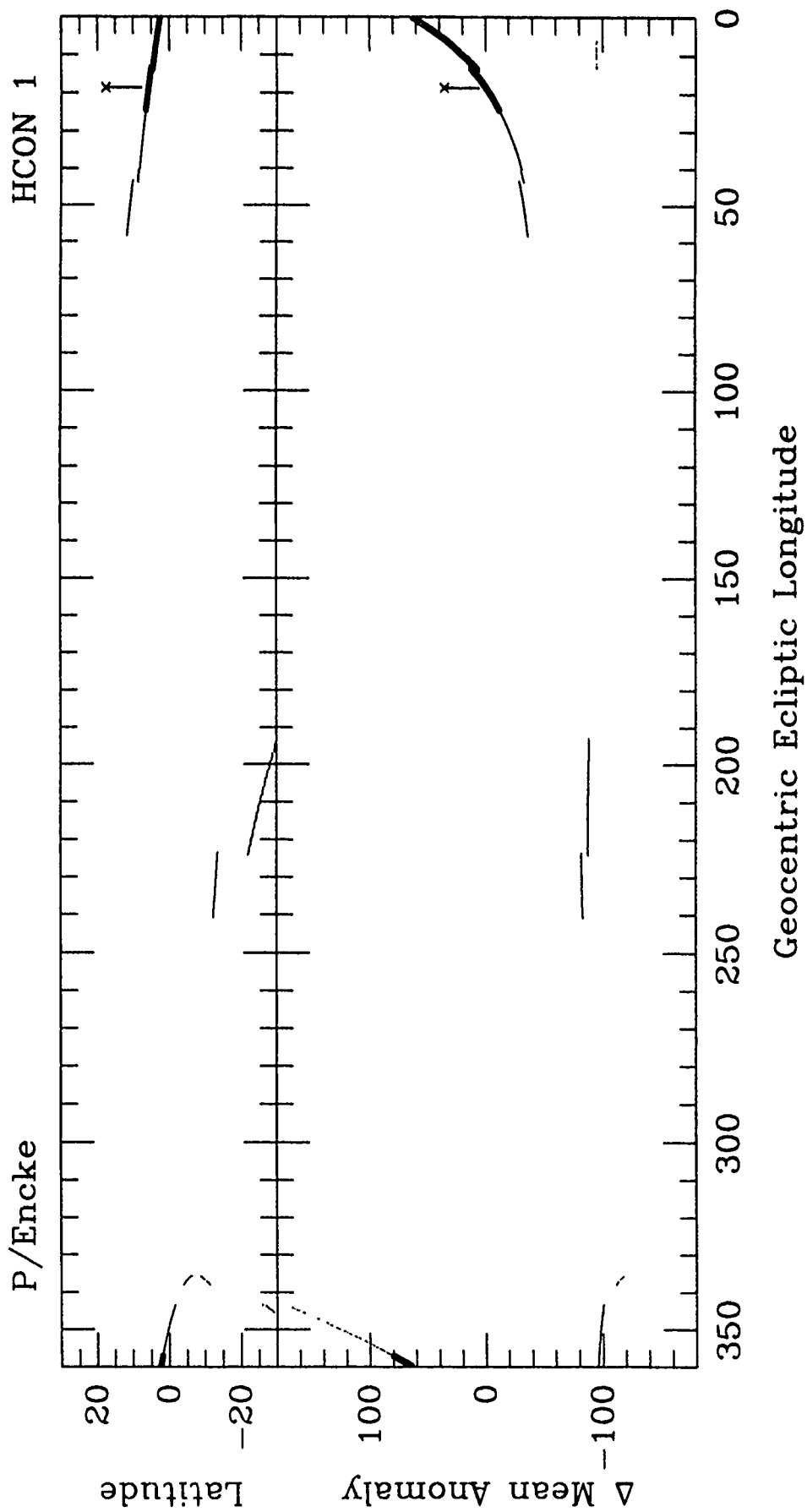


Figure 7. Encke, HCON 1. See Fig. 4.

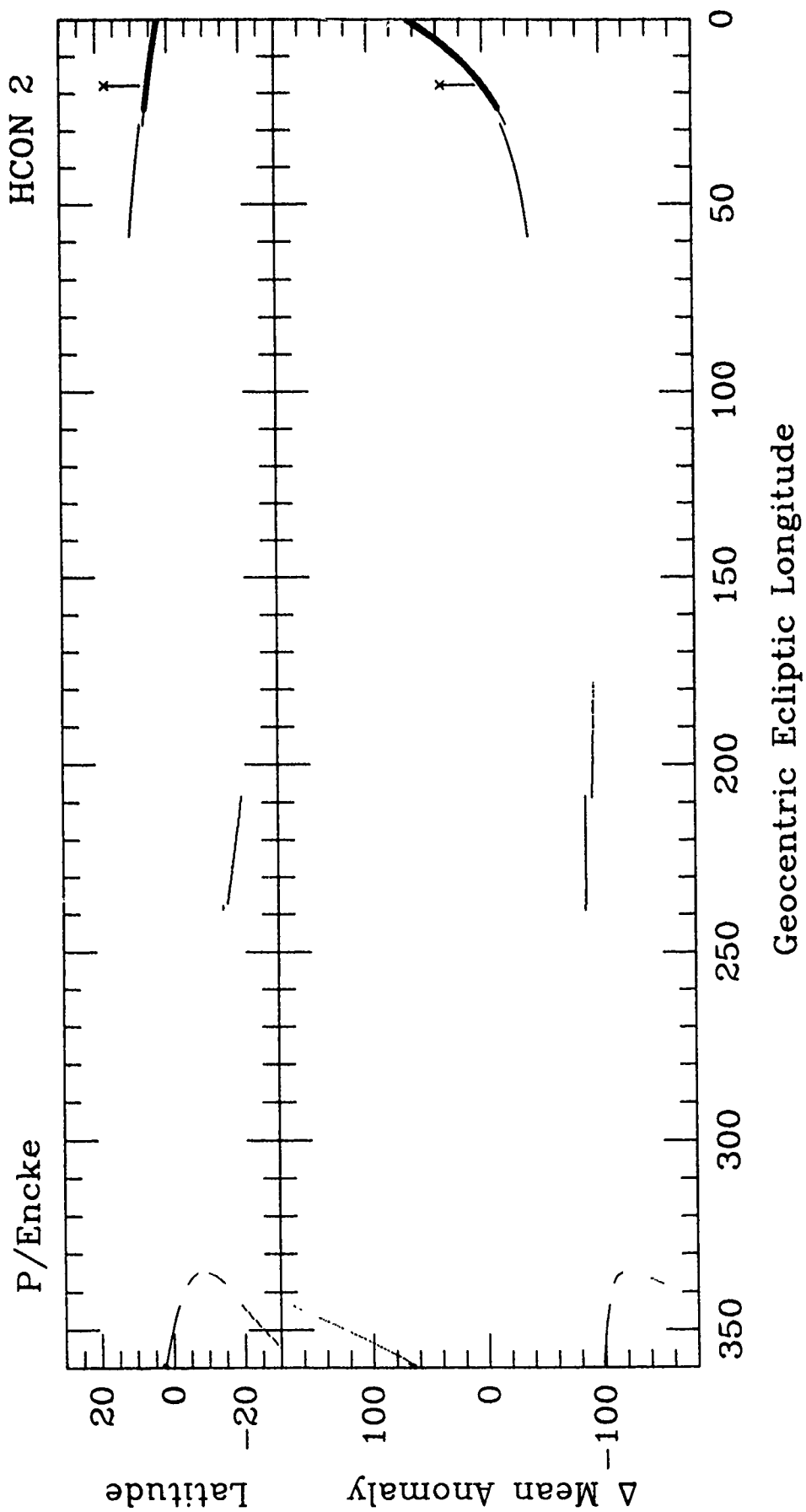


Figure 8. Encke, HCON 2. See Fig. 4.

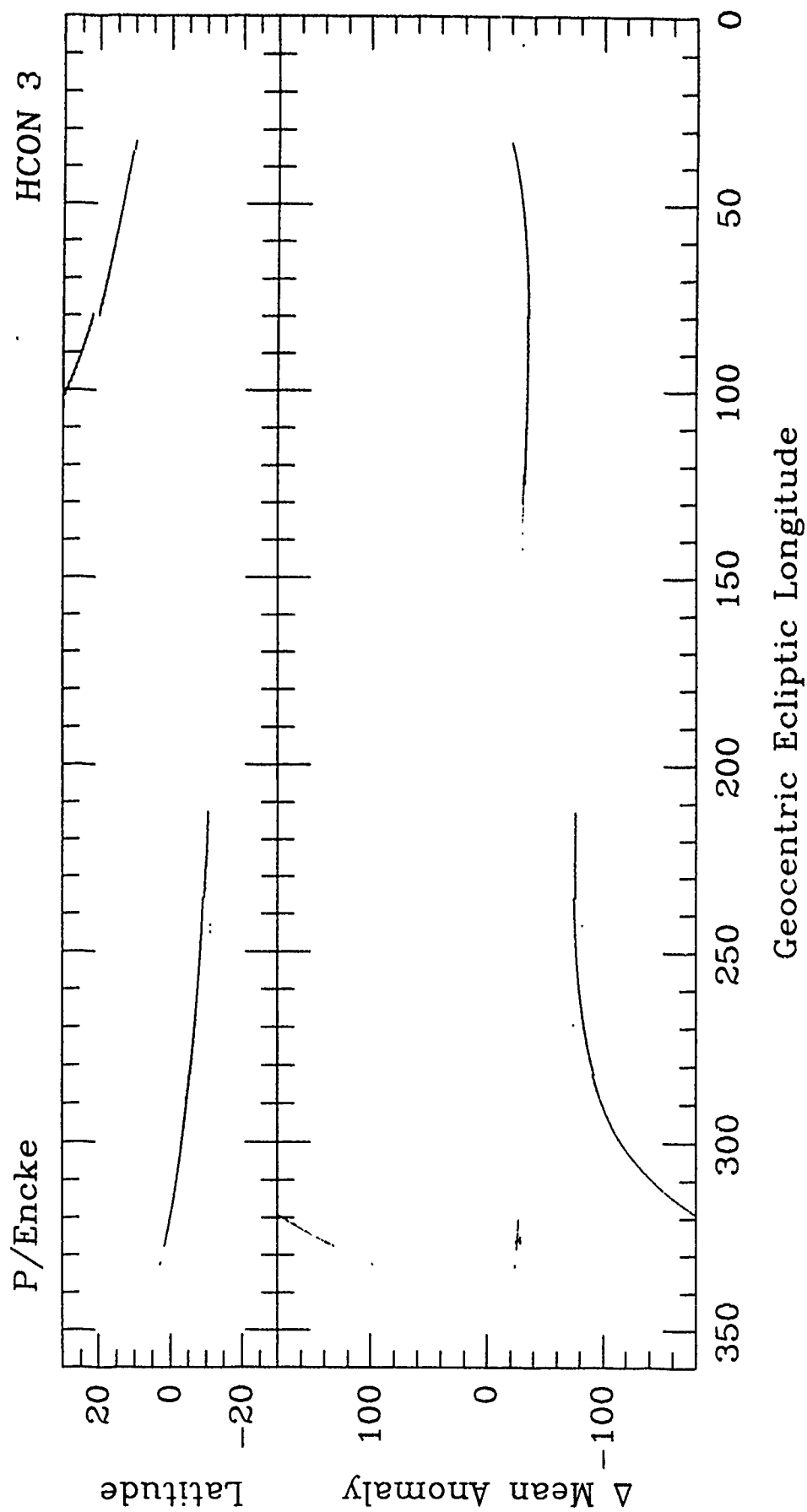


Figure 9. Encke, HCON 3. See Fig. 4.

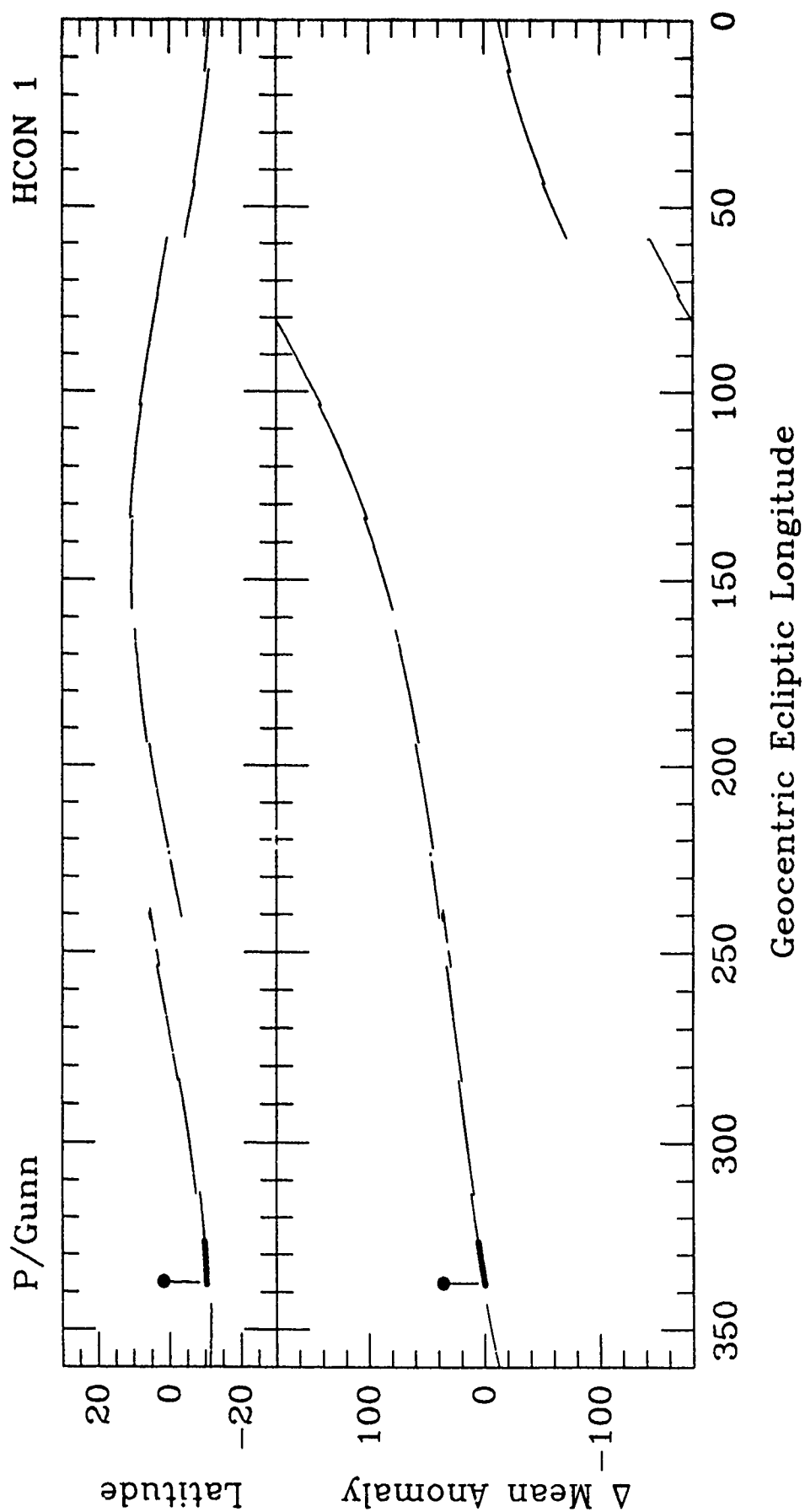


Figure 10. Gunn, HCON 1. See Fig. 4.

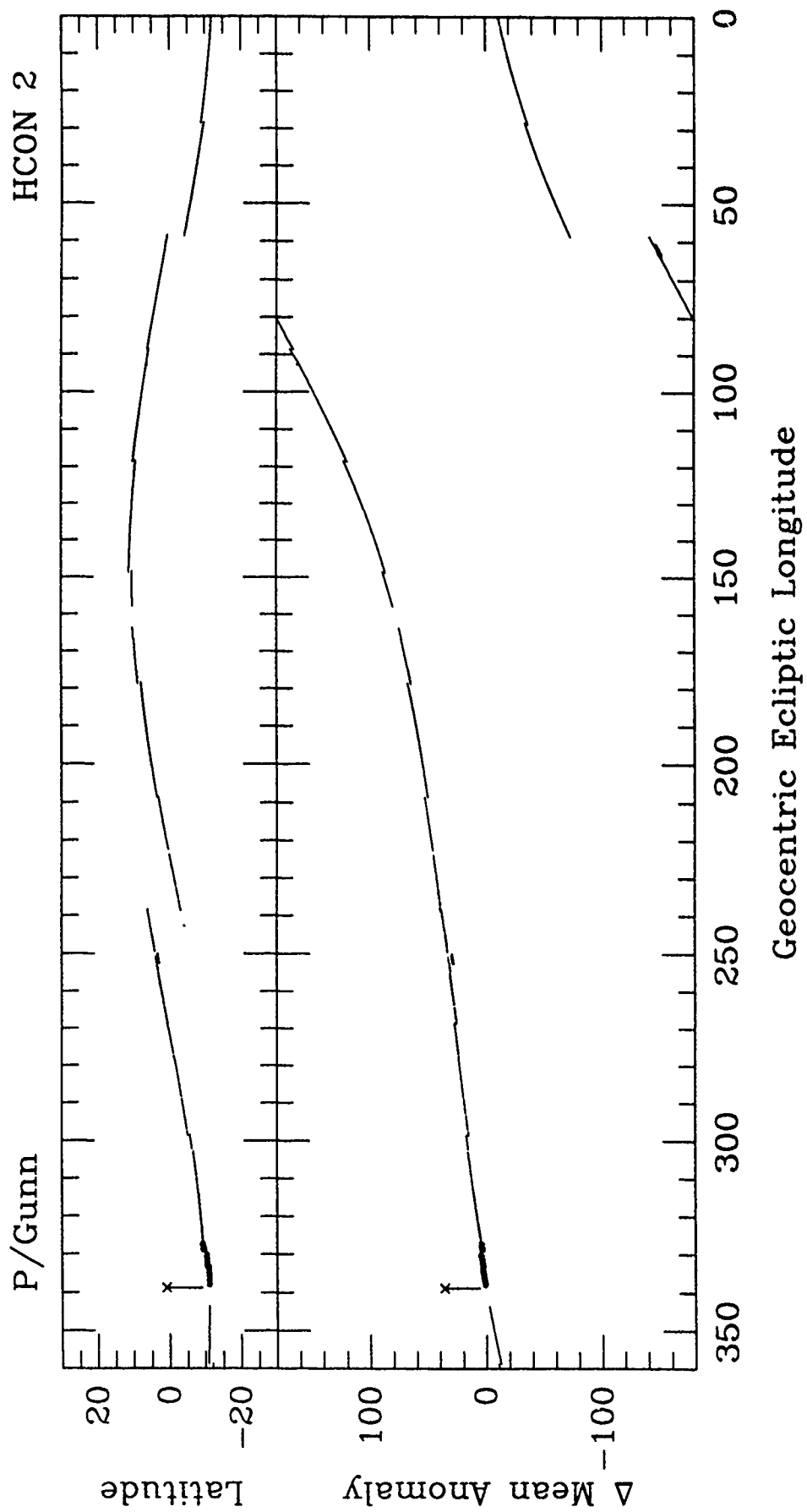


Figure 11. Gunn, HCON 2. See Fig. 4.

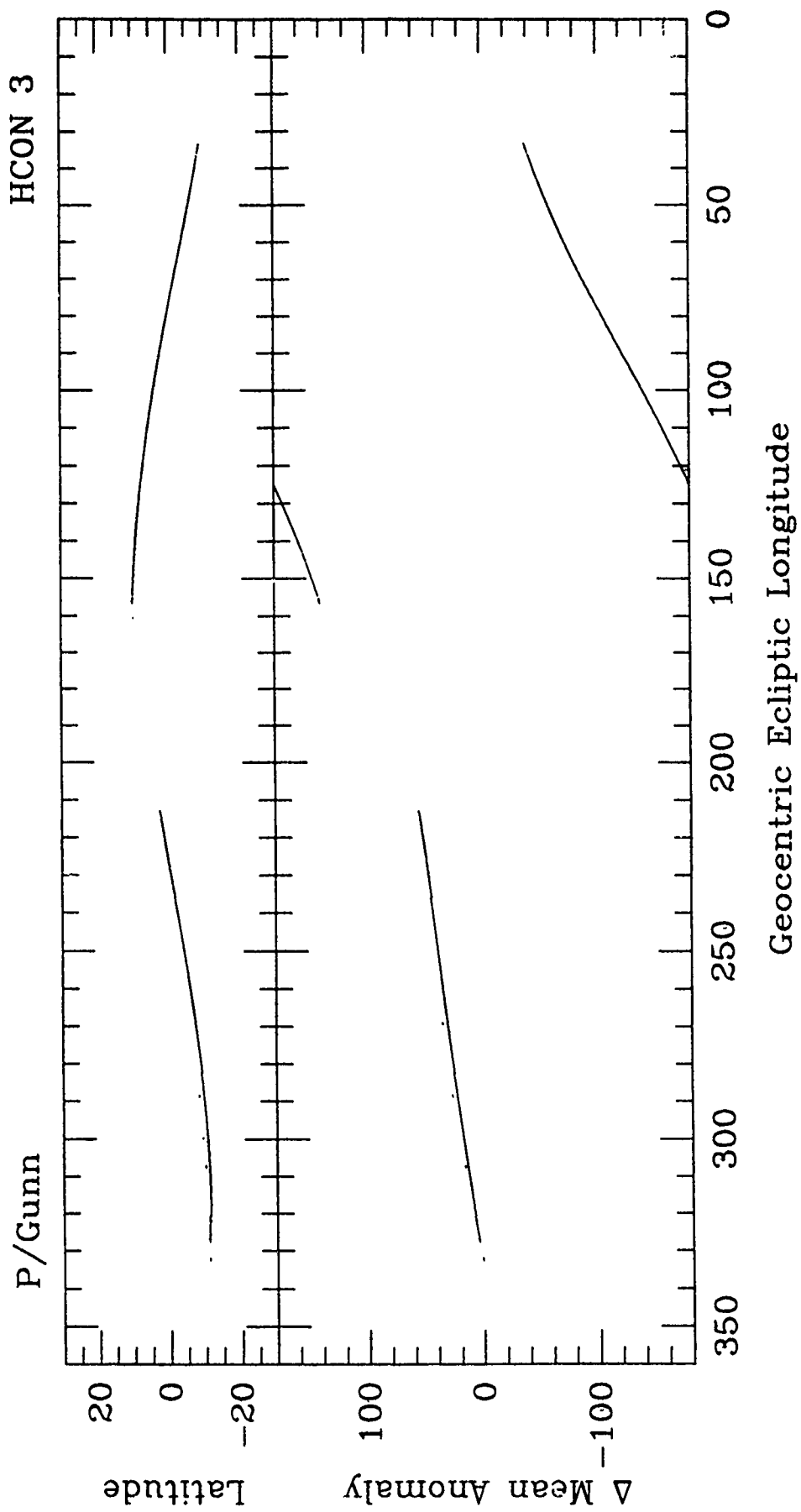


Figure 12. Gunn, HCON 3. See Fig. 4.

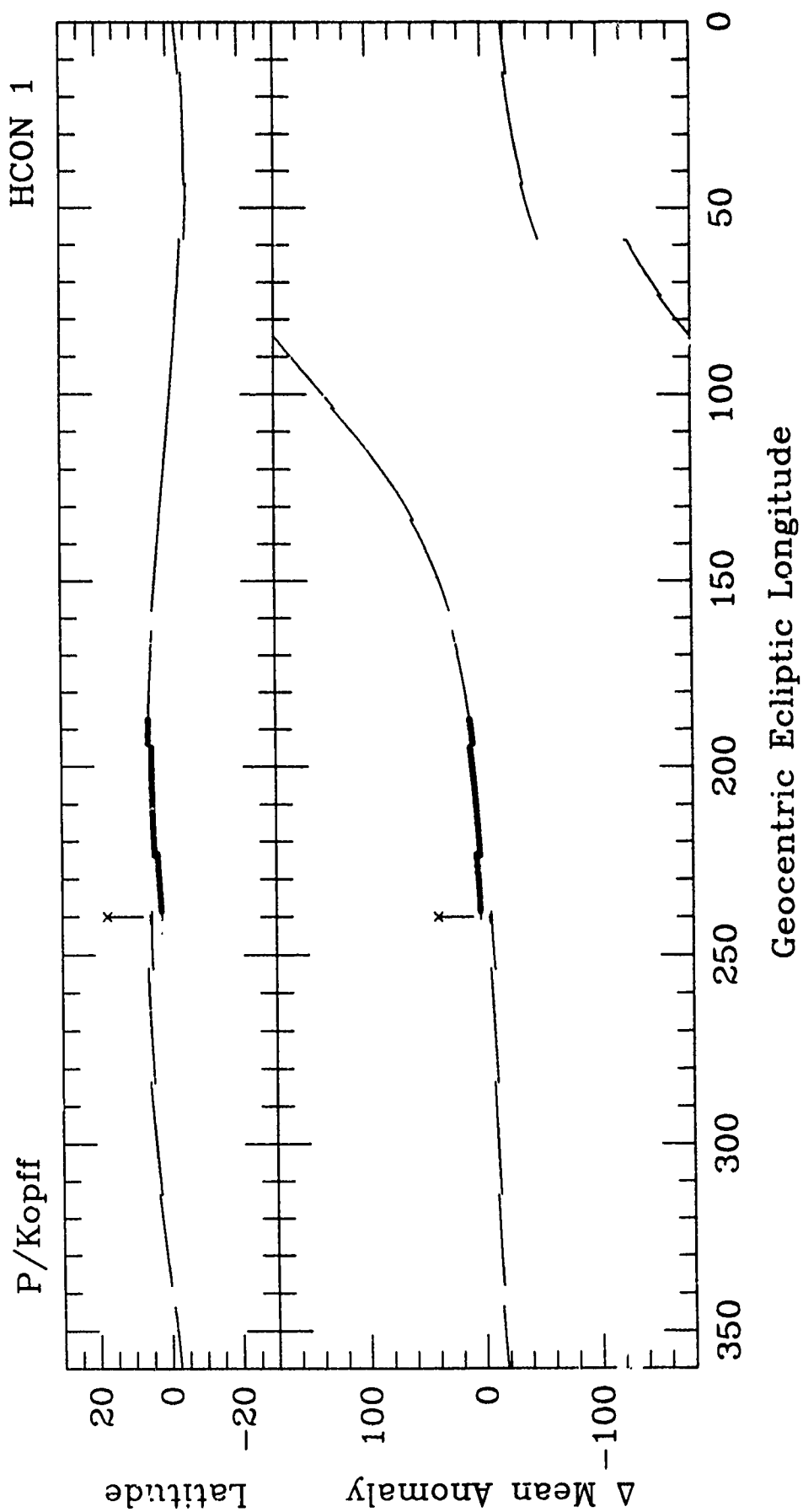


Figure 13. Kopff, HCON 1. See Fig. 4.

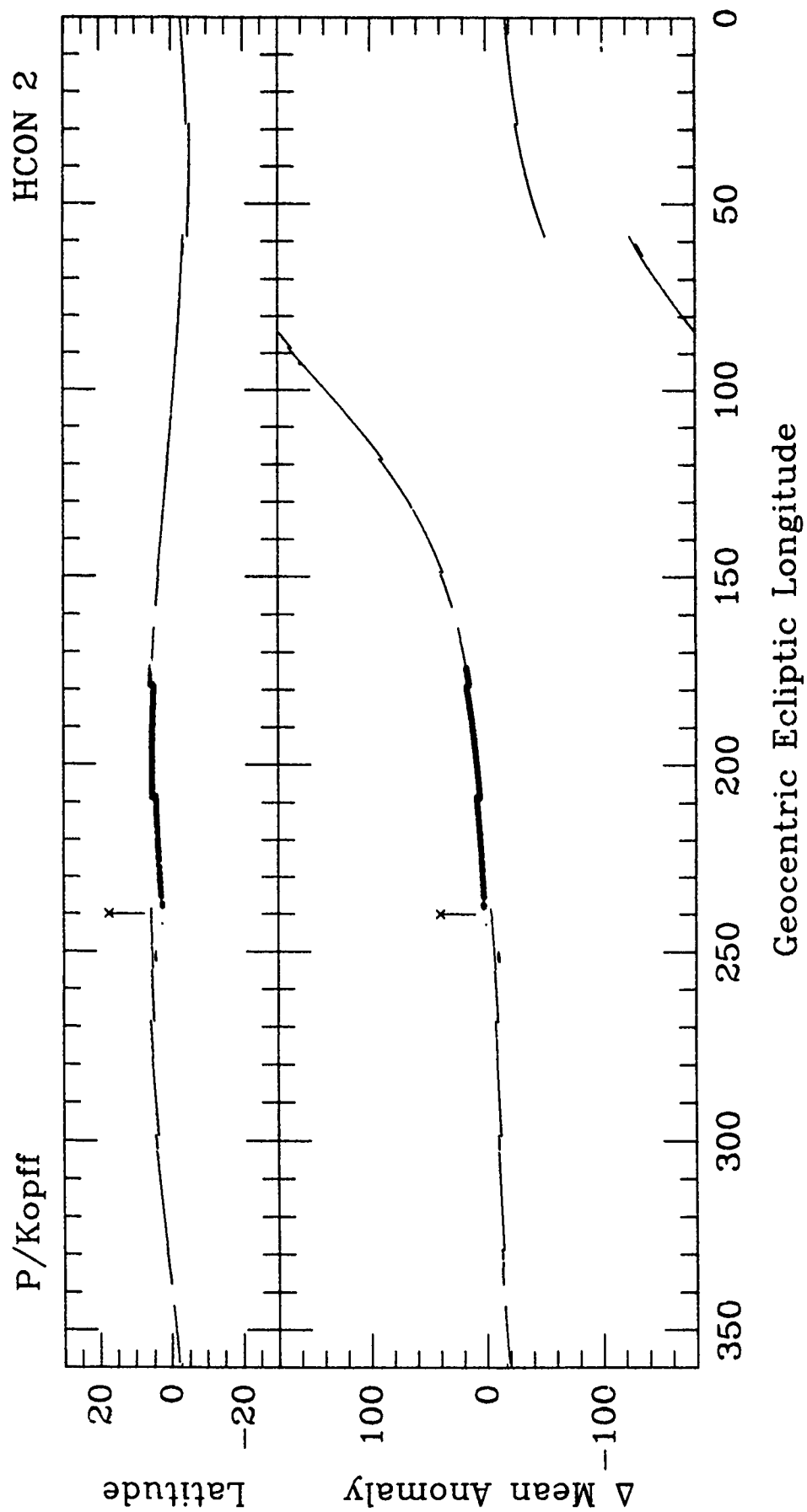


Figure 14. Kopff, HCON 2. See Fig. 4.

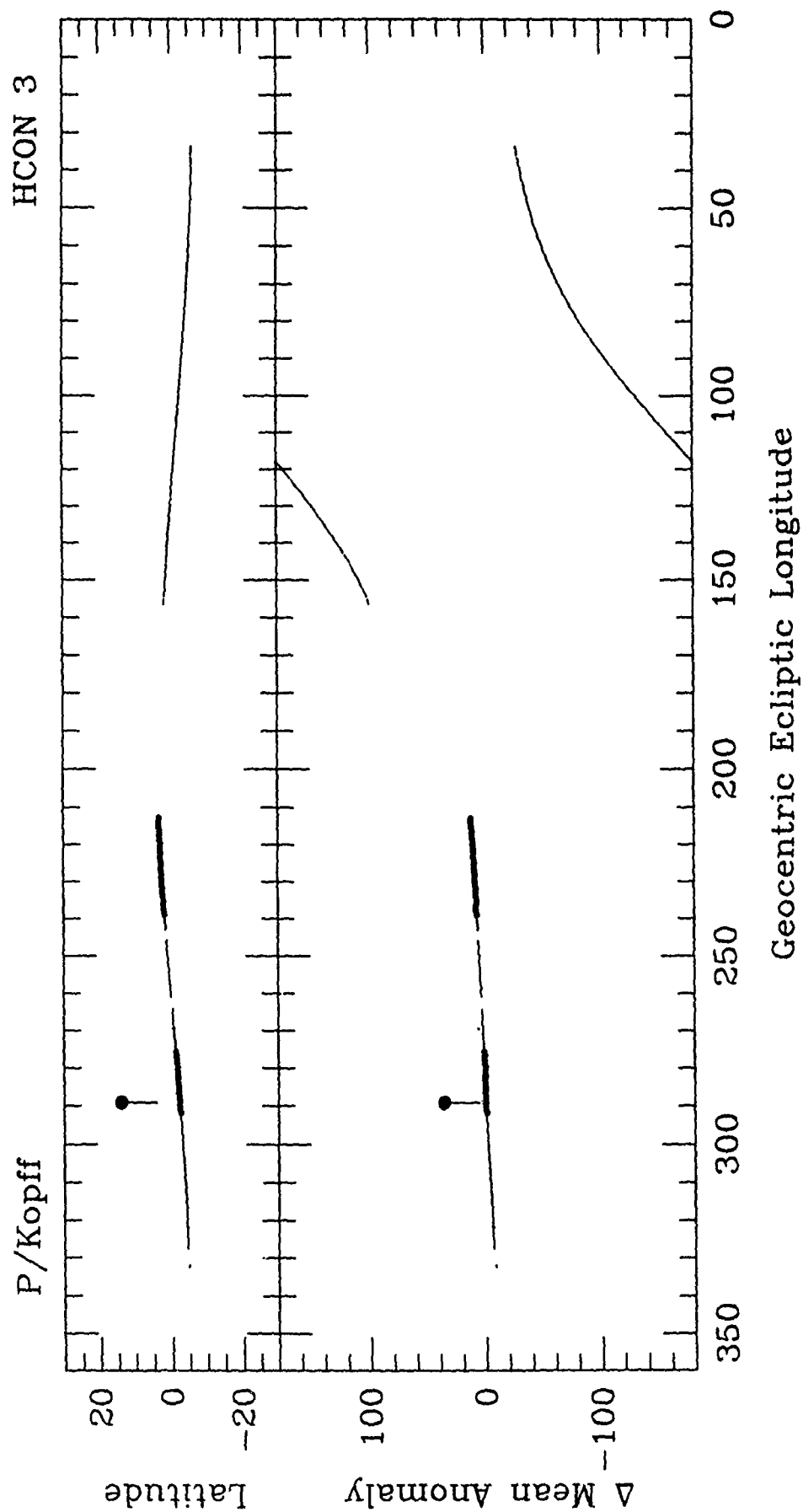


Figure 15. Kopff, HCON 3. See Fig. 4.

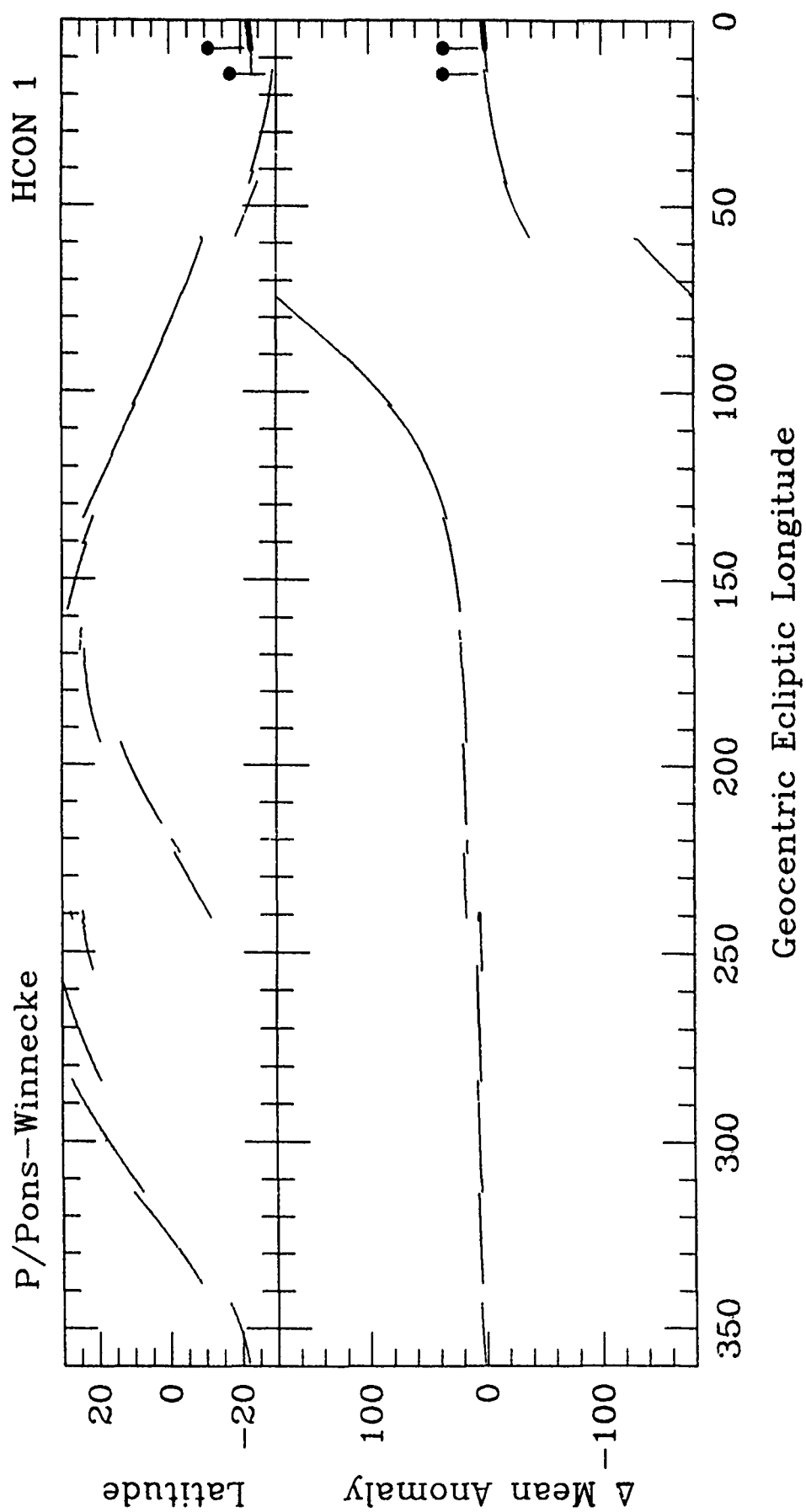


Figure 16. Pons-Winnecke, HCON 1. See Fig. 4.

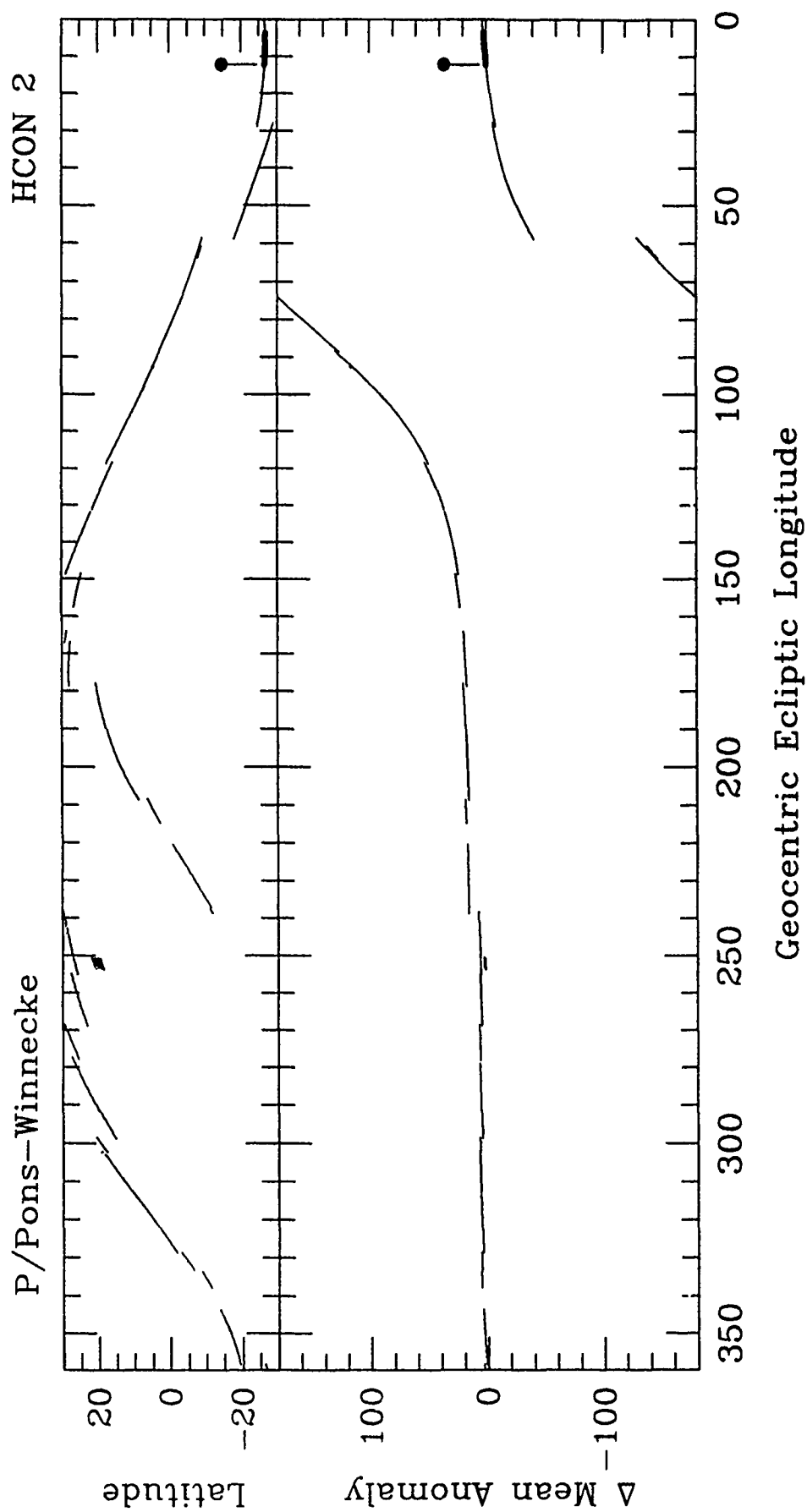


Figure 17. Pons-Winnecke, HCON 2. See Fig. 4.

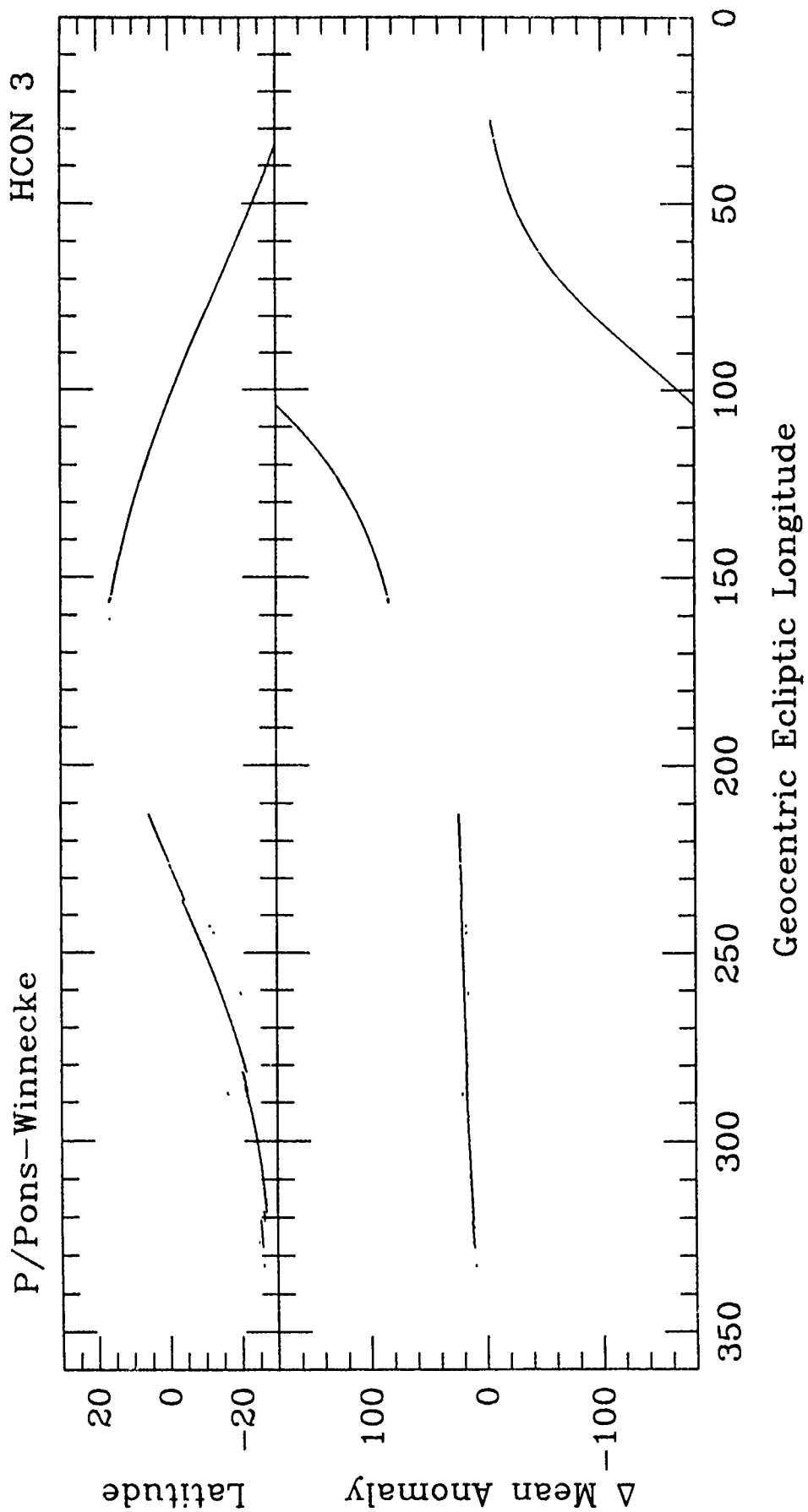


Figure 18. Pons-Winnecke, HCON 3. See Fig. 4.

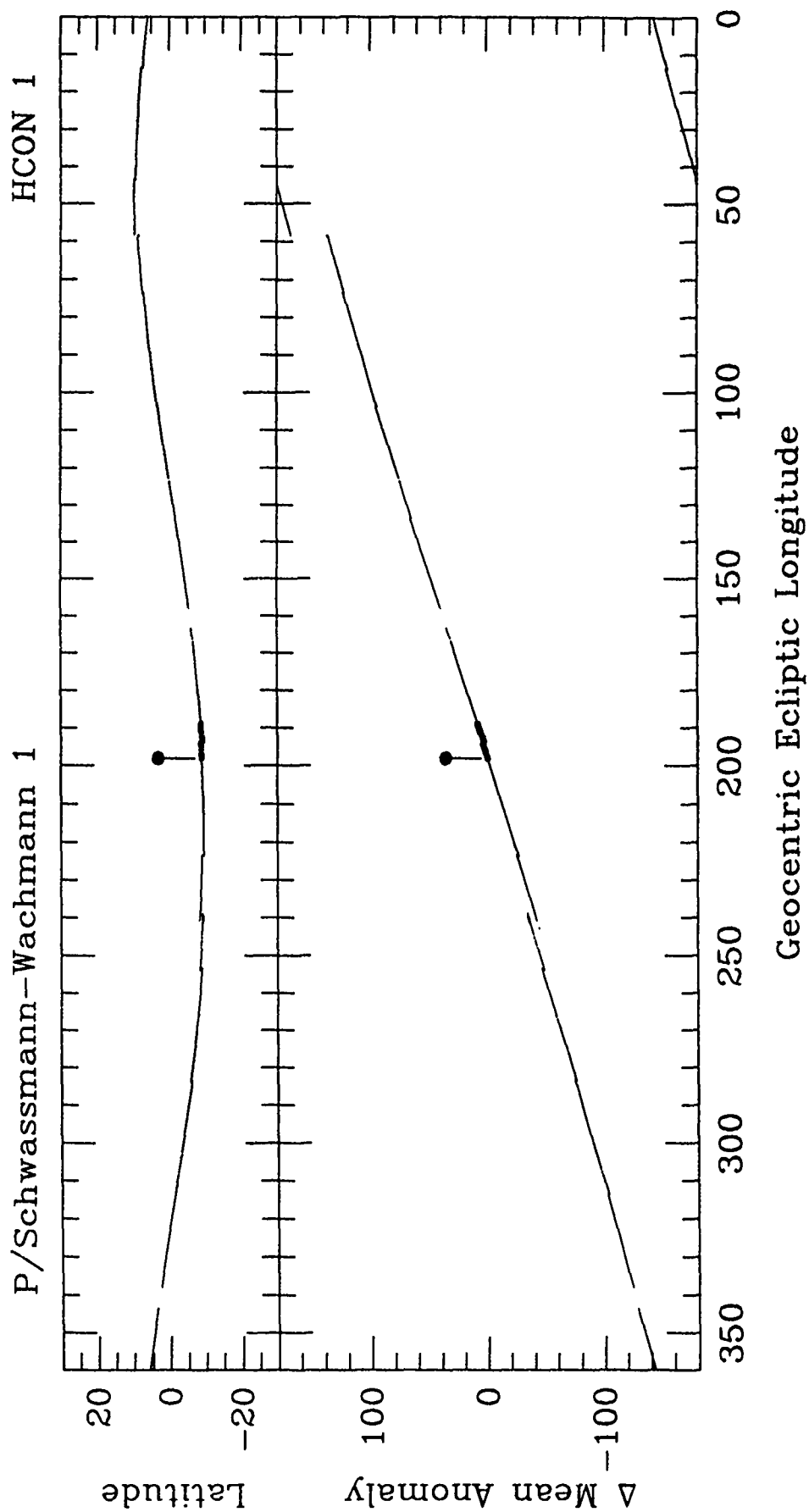


Figure 19. Schwassmann-Wachmann 1, HCON 1. See Fig. 4.

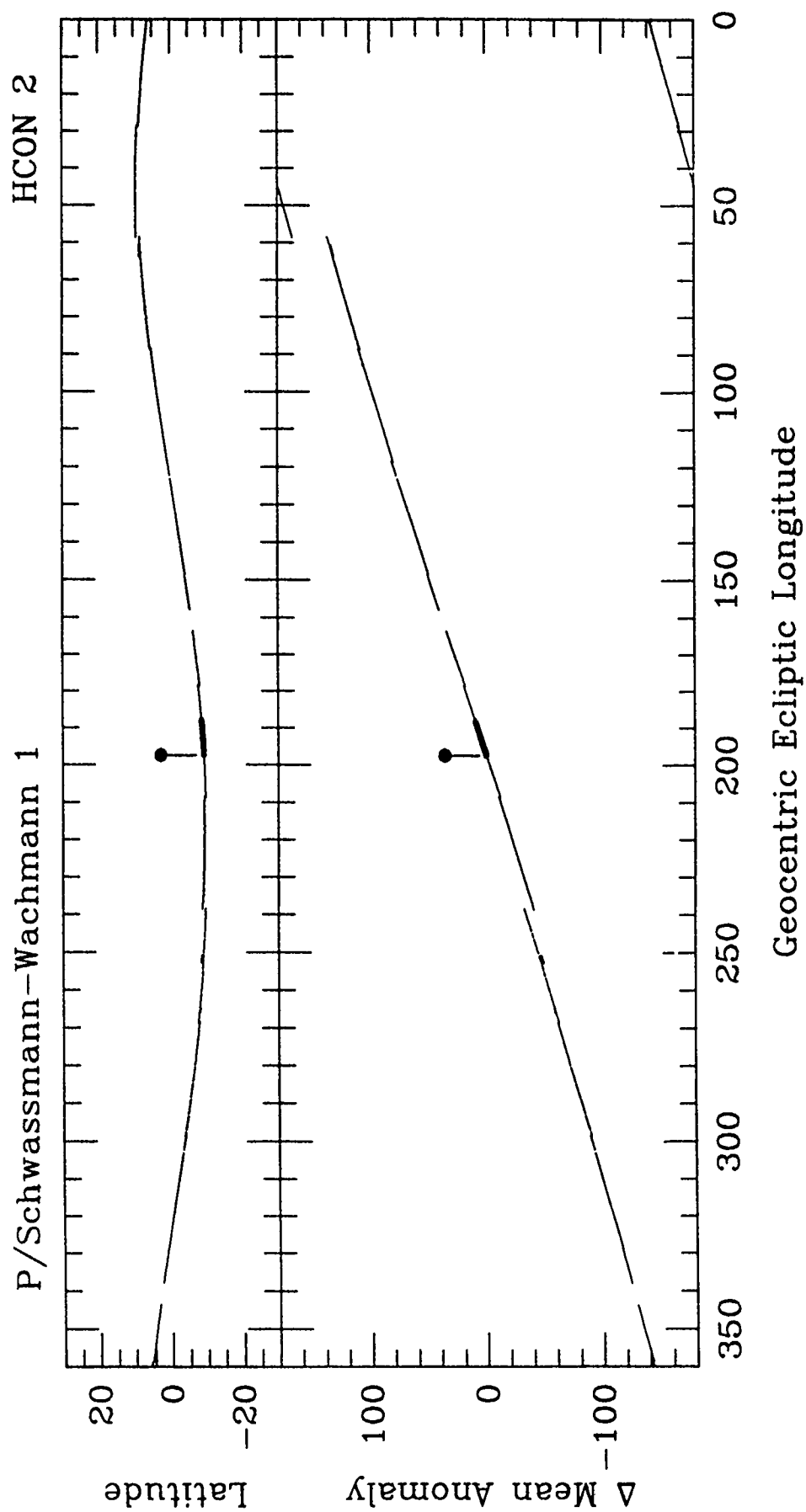


Figure 20. Schwassmann-Wachmann 1, HCON 2. See Fig. 4.

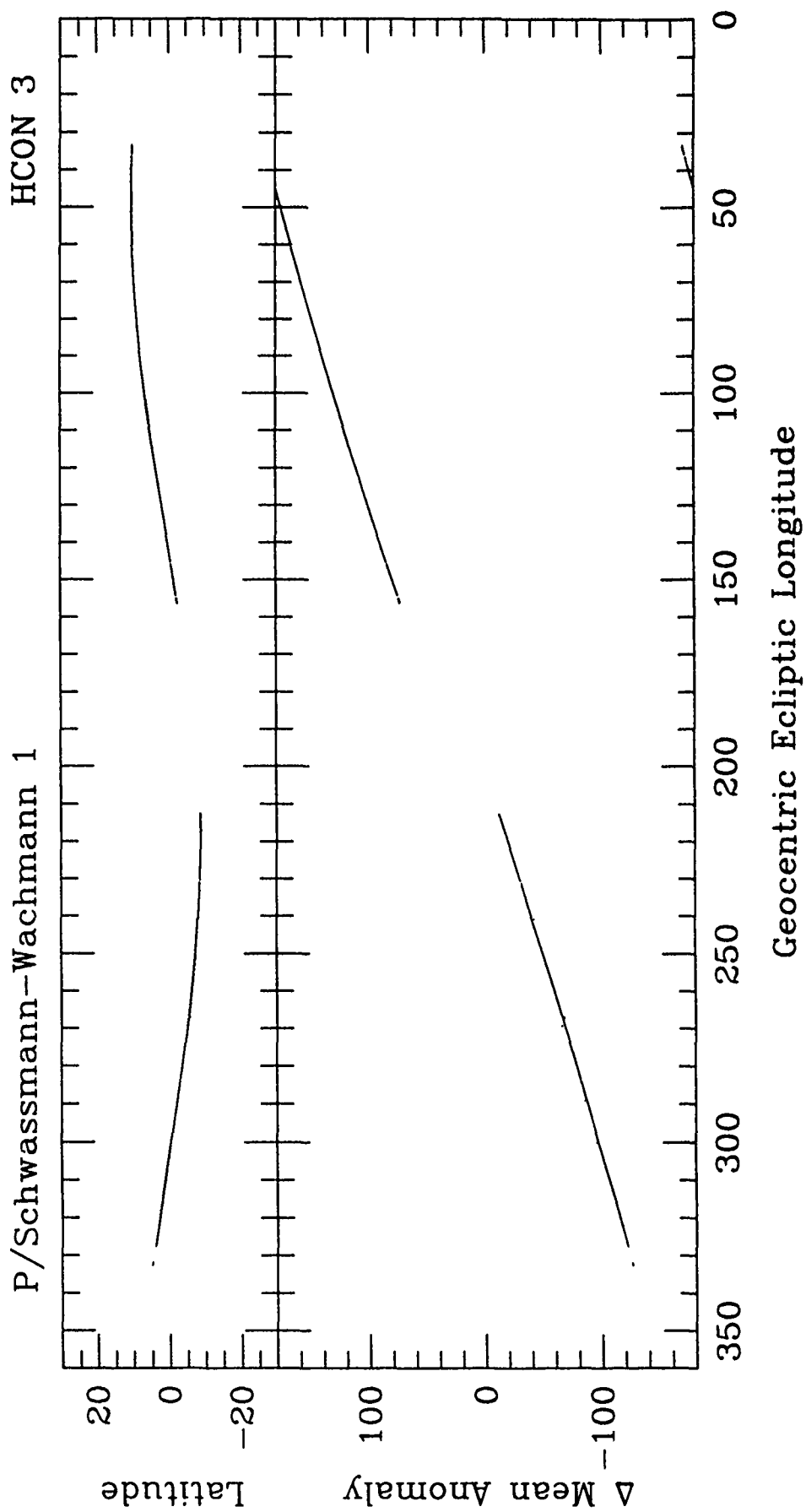


Figure 21. Schwassmann-Wachmann 1, HCON 3. See Fig. 4.

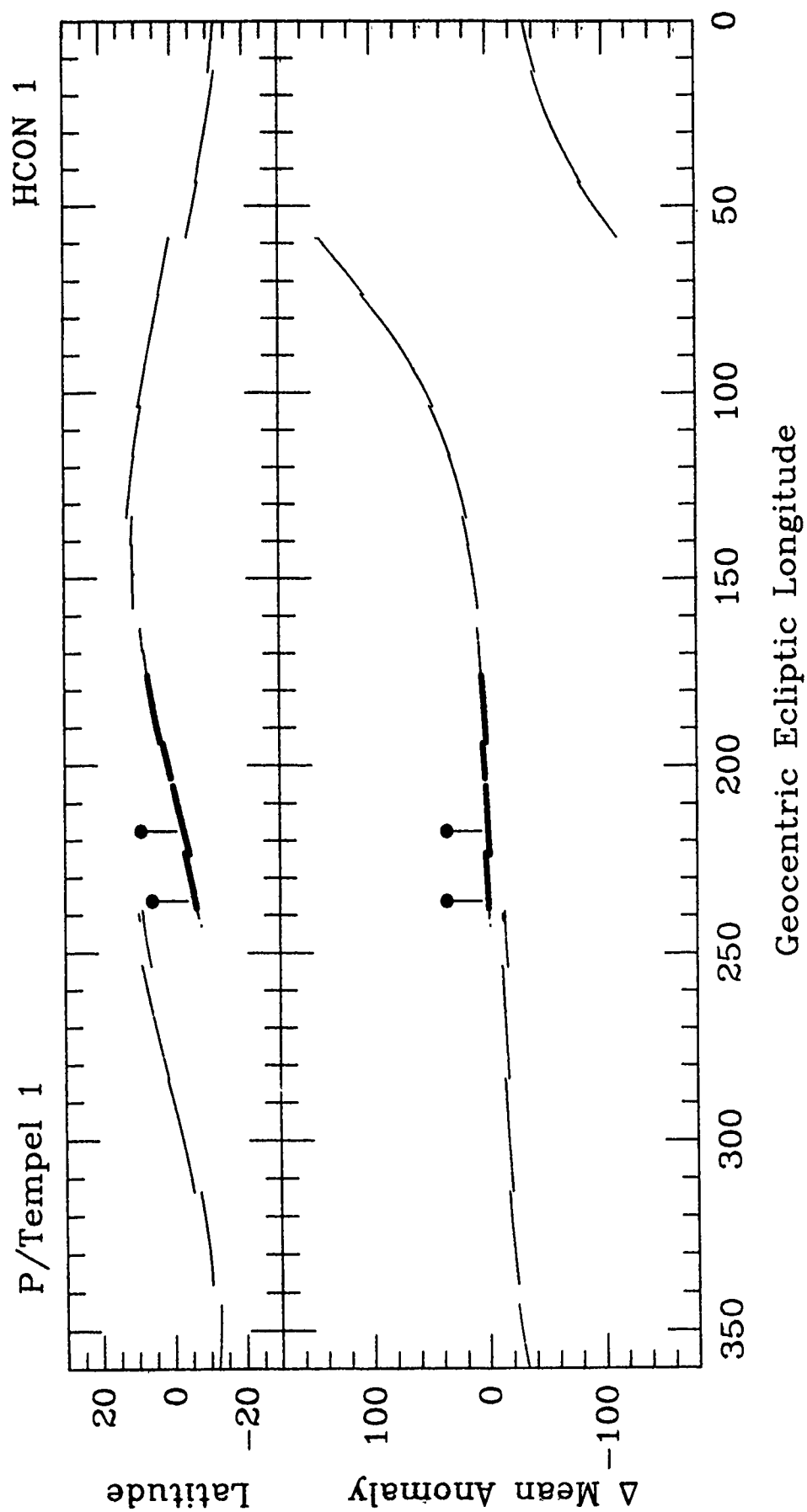


Figure 22. Tempel 1, HCON 1. See Fig. 4.

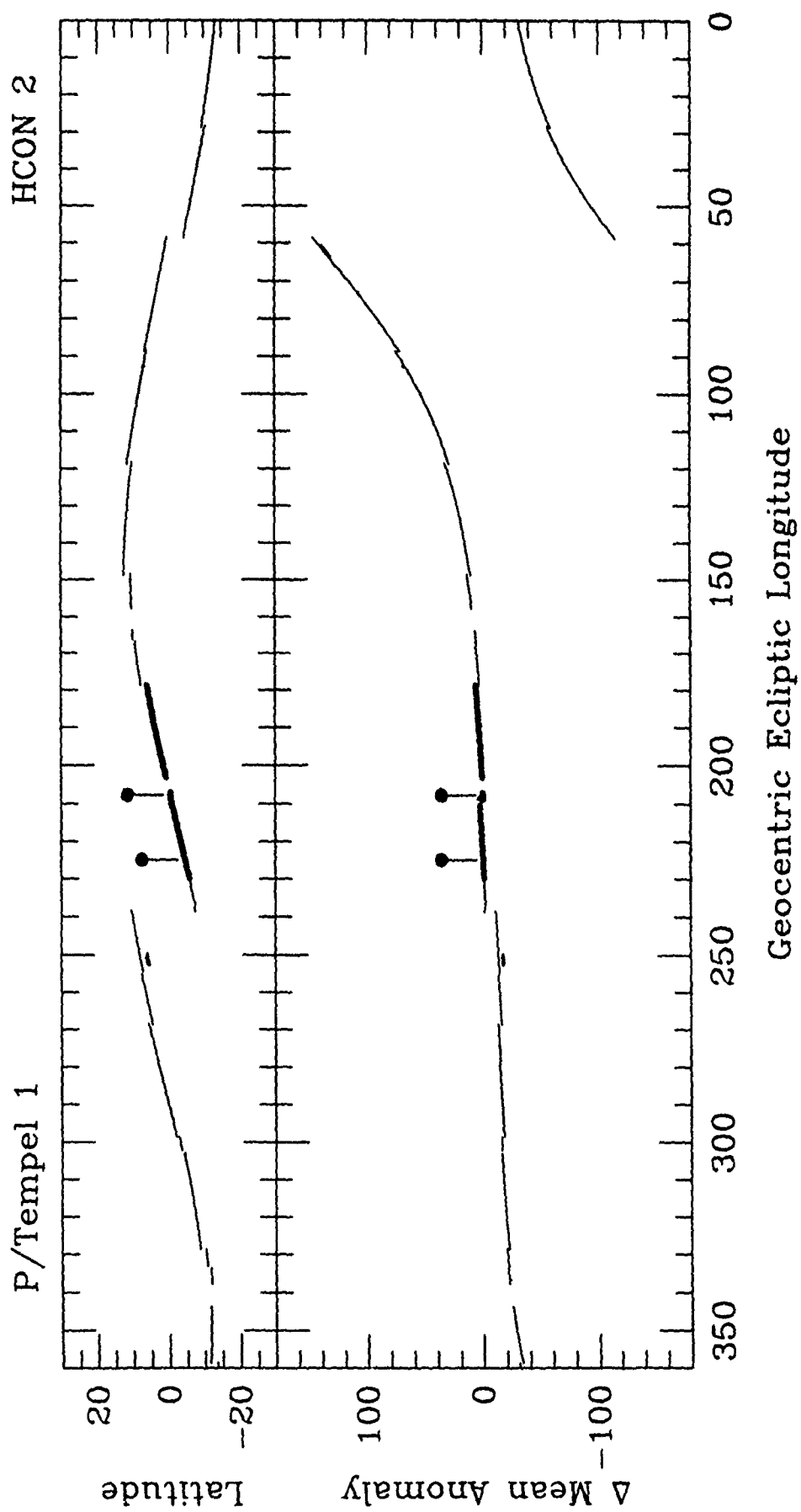


Figure 23. Tempel 1, HCON 2. See Fig. 4.

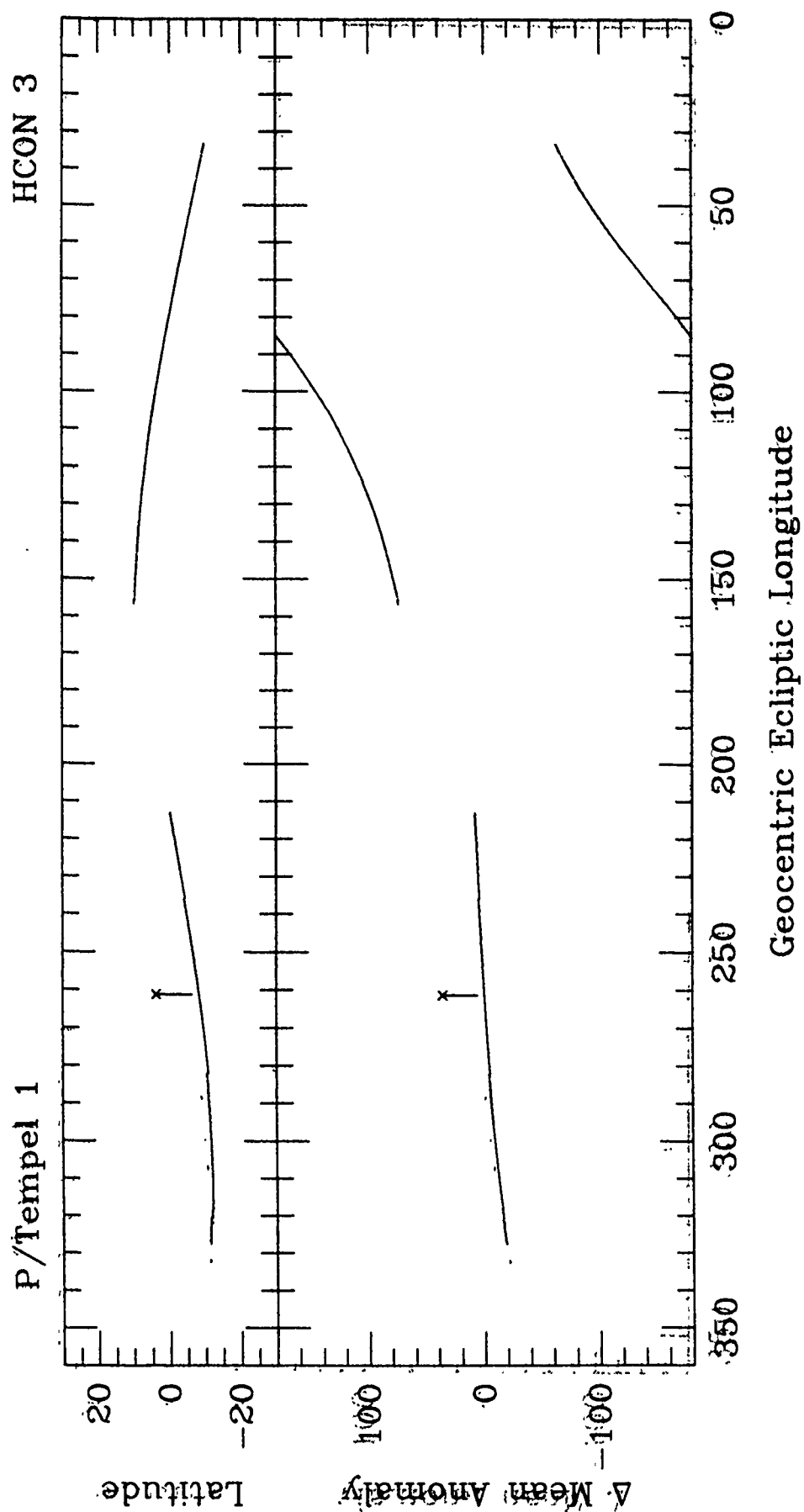


Figure 24. Tempel 1, HCON 3. See Fig. 4.

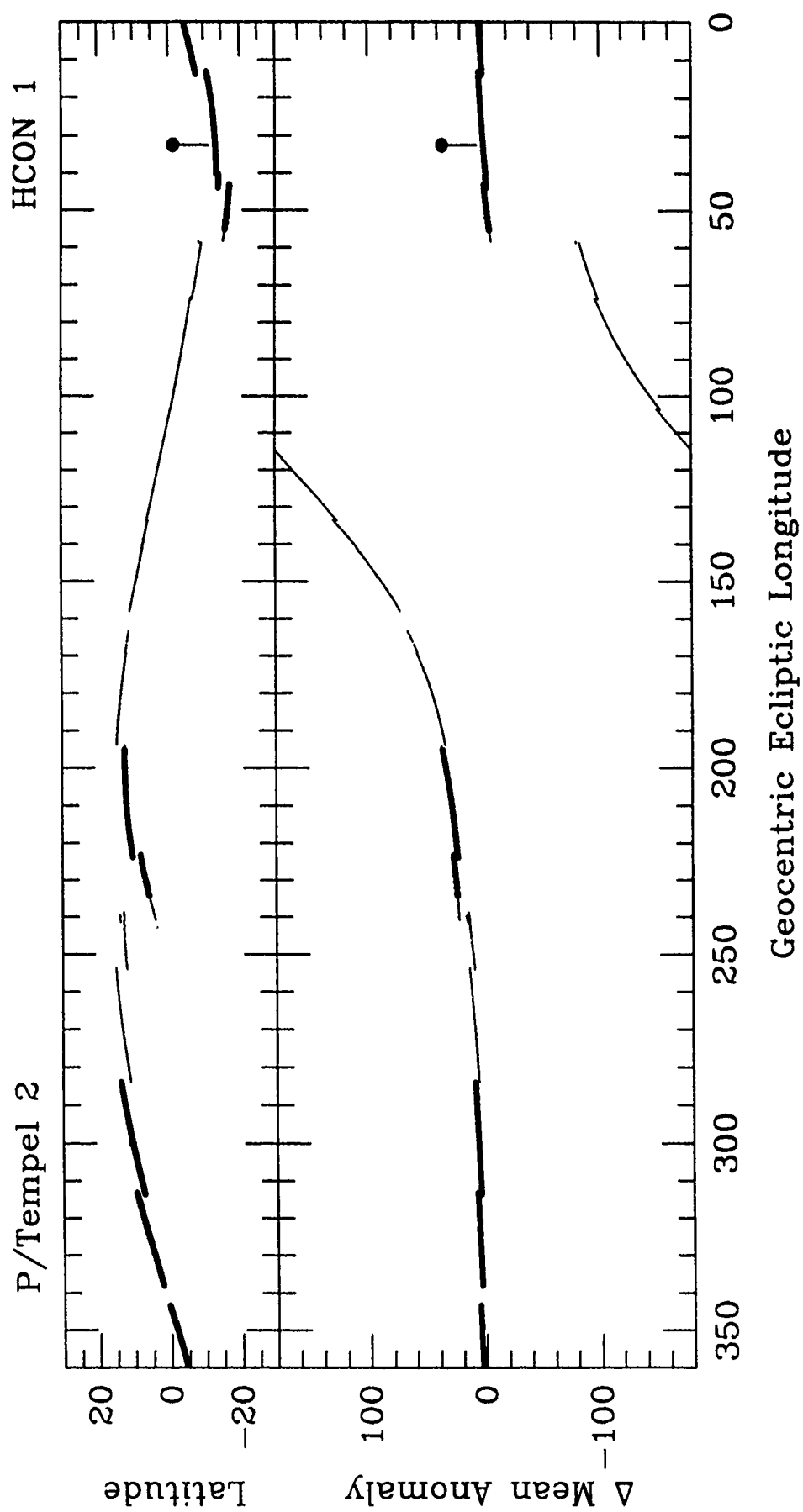


Figure 25. Tempel 2, HCON 1. See Fig. 4.

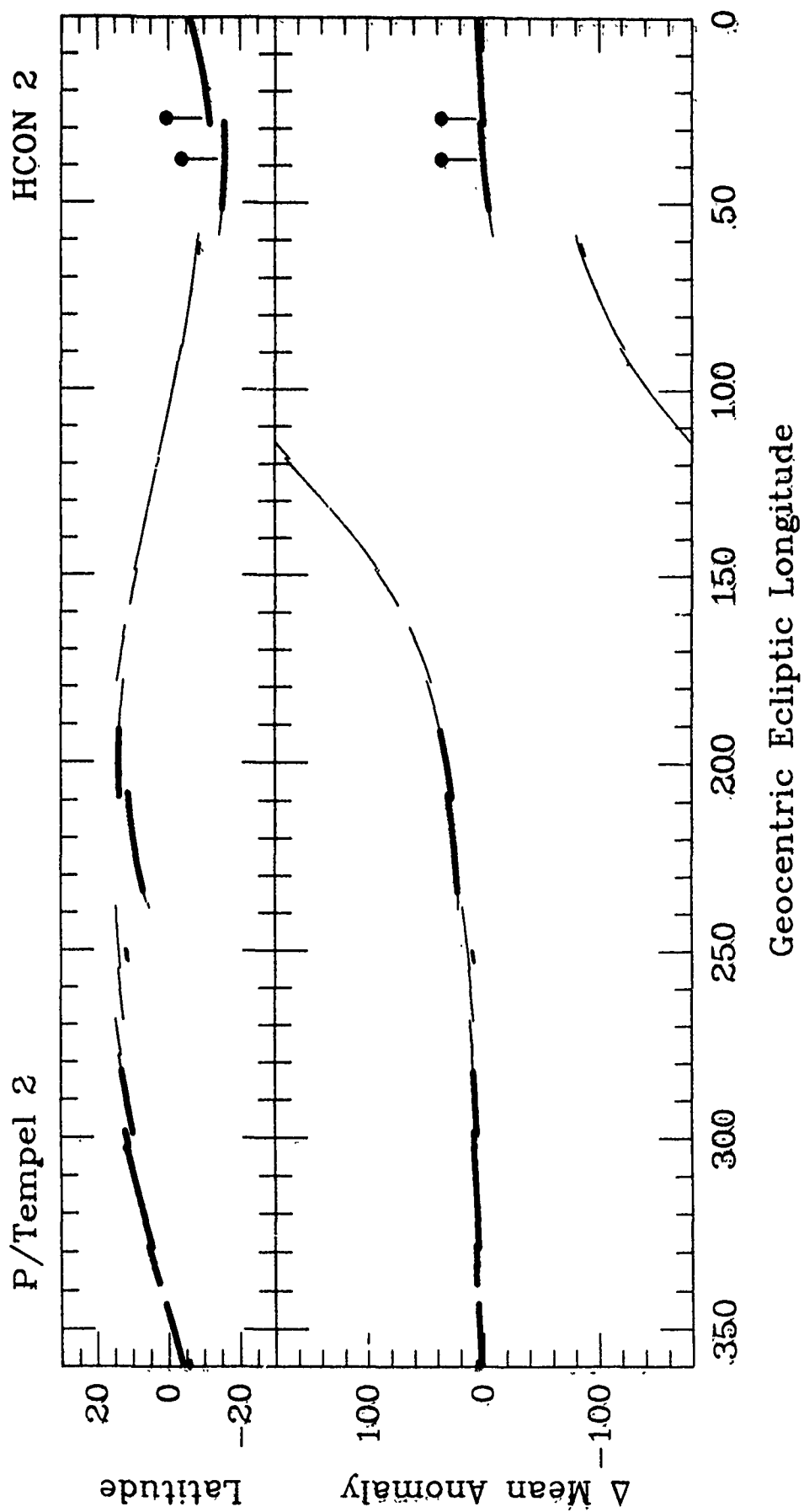


Figure 26. Tempel 2, HCON 2. See Fig. 4.

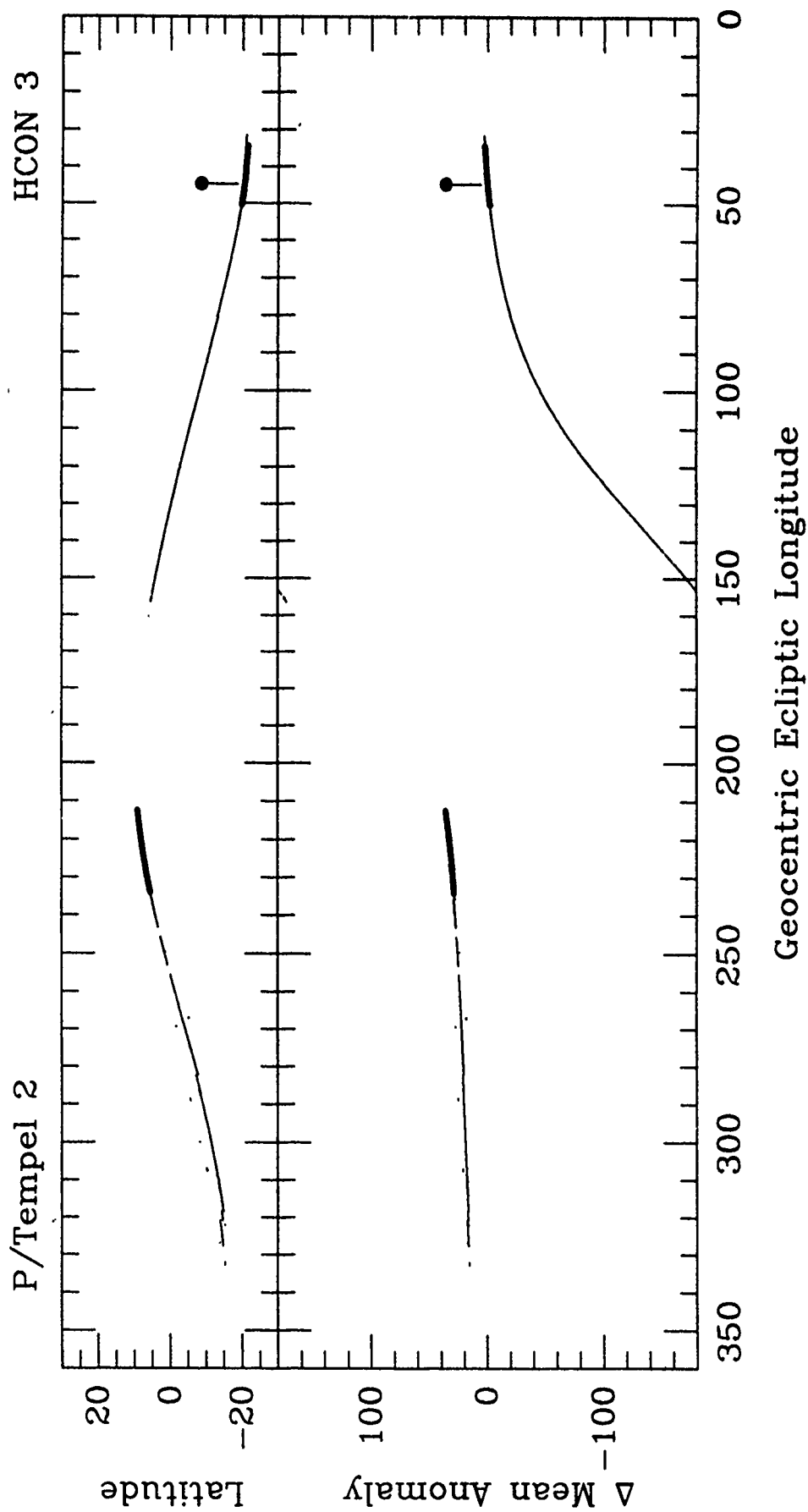


Figure 27. Tempel 2, HCON 3. See Fig. 4.

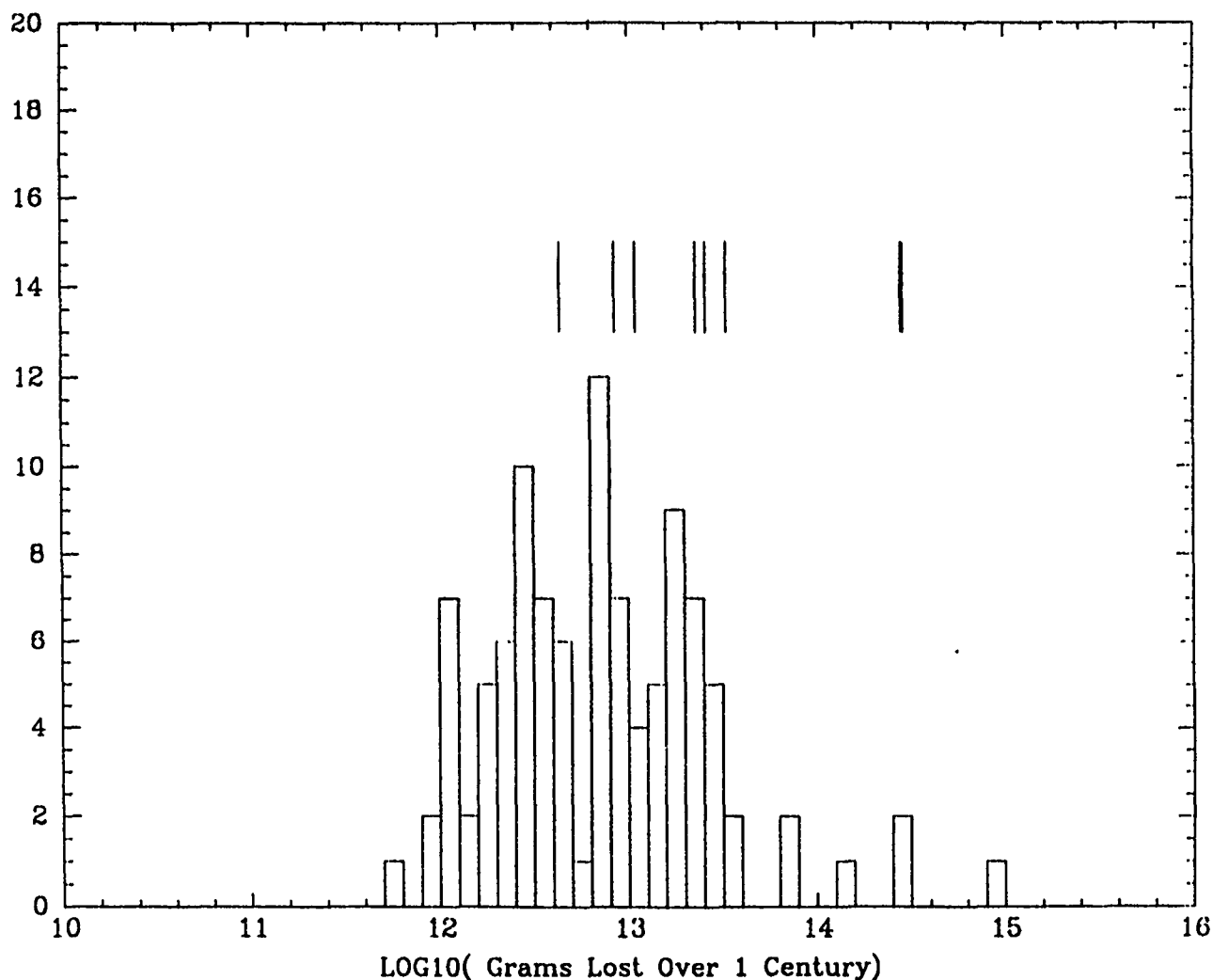


Figure 28. A histogram of cometary dust mass loss over the past century calculated from the results of Kresák and Kresáková (1988). Values for trail comets are shown for (1) Churyumov-Gerasimenko, (2) Pons-Winnecke, (3) Tempel 1, (4) Gunn, (5) Tempel 2, (6) Kopff, (7) Schwassmann-Wachmann 1, and (8) Encke. The most productive comet in the histogram is P/Halley. Overall, trail comets are seen to be somewhat more active members of the short-period comet population.

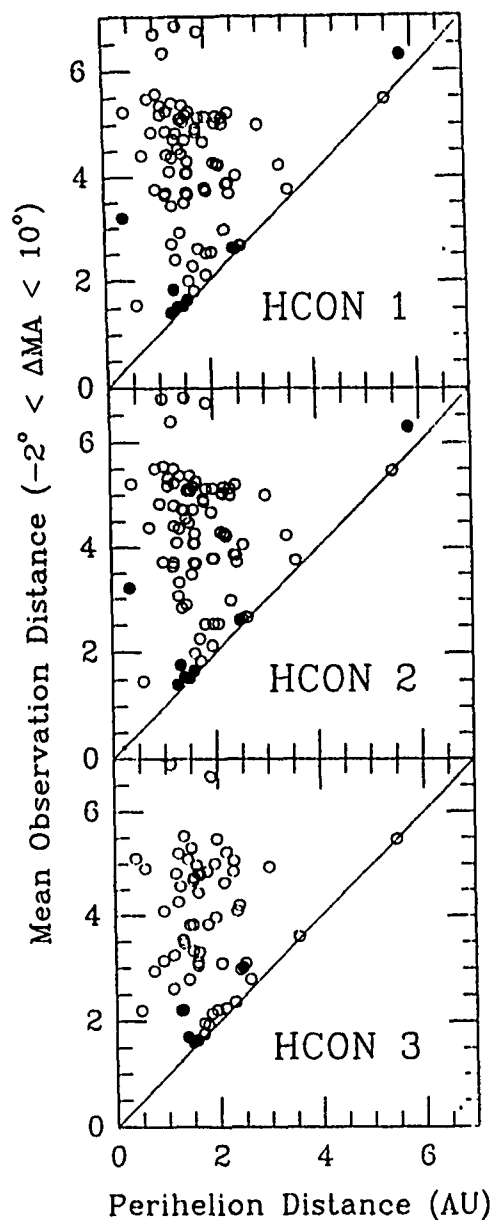


Figure 29. The mean distance in AU that IRAS scanned near the position of one of 122 comets is plotted as a function of the comet perihelion distance. Many comets were actually missed by IRAS, during one or two HCONs, only to be scanned during a different HCON. Filled circles (●) denote comets with detected trails, open circles (○) denote comets with no detected trail. Encke and Schwassmann-Wachmann 1 are seen to the extreme left and right, respectively. The remaining trail comets are seen to have been observed at their perihelion distances. The open circle observed at the lowest heliocentric distance during HCON 1 and 2, corresponds to P/Brorsen, which was last detected in 1890.

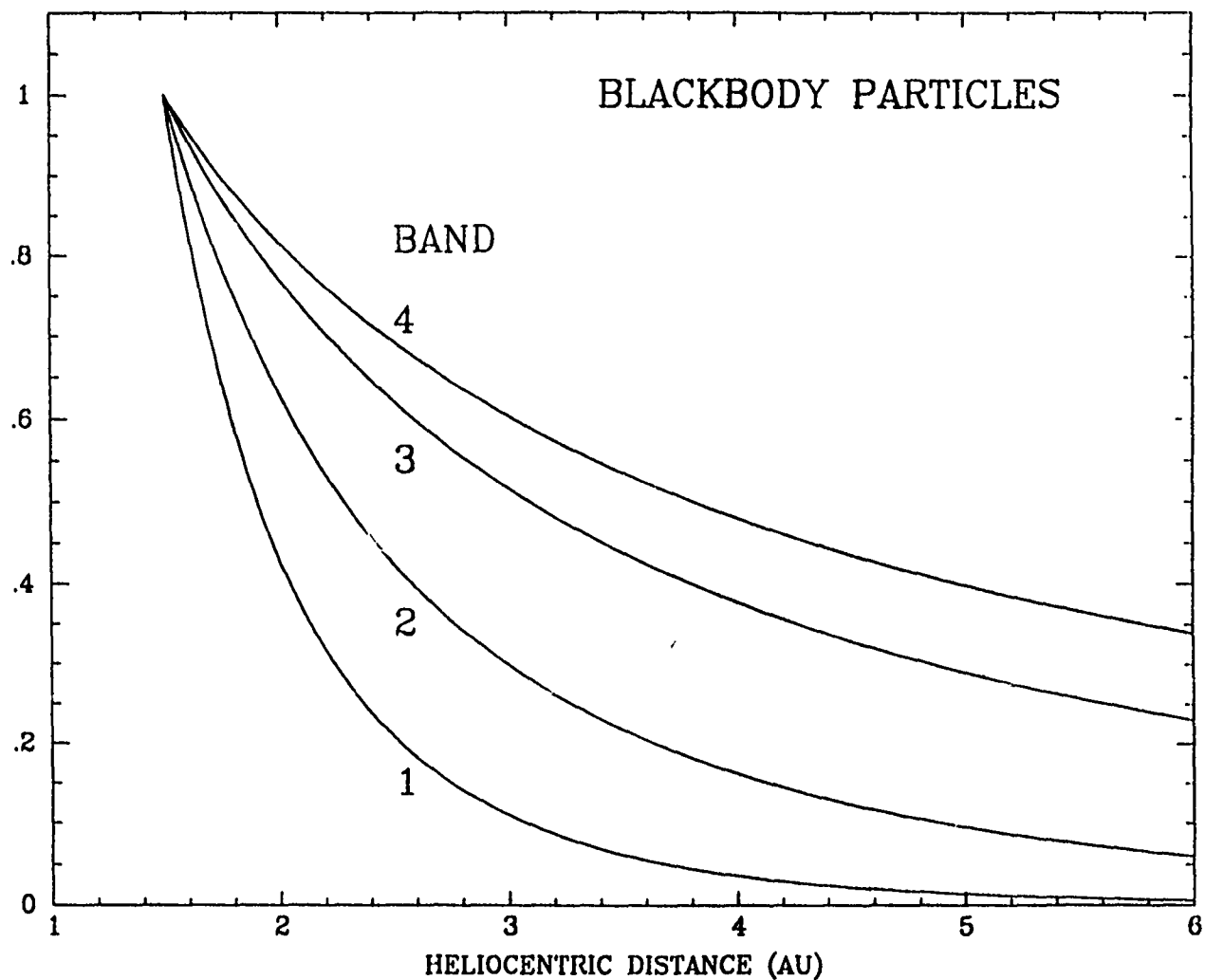


Figure 30. The surface brightness integrated over each of the IRAS passbands of blackbody particles in radiative equilibrium with sunlight as a function of heliocentric distance, ratioed to 1.5 AU.

TABLE 1. POTENTIAL PARENTS

Short-Period Comets

Arend	Finlay	Kowal 2	Shoemaker 2
Arend-Rigaux	Forbes	Kowal-Mrkos	Slaughter-Burnham
Ashbrook-Jackson	Gale	Kowal-Vávrová	Smirnova-Chernykh
Biela	Gehrels 1	Longmore	Stephan-Oterma
Boethin	Gehrels 2	Neujmin 1	Swift-Gehrels
Borrelly	Gehrels 3	Neujmin 2	Takamisawa
Bowell	Giacobini-Zinner	Neujmin 3	Taylor
Bowell-Skiff	Giclas	Olbers	Tempel 1
Bradfield	Grigg-Skjellerup	Oterma	Tempel 2
Brooks 2	Gunn	Perrine-Mrkos	Tempel-Swift
Brorsen	Halley	Peters-Hartley	Tempel-Tuttle
Brorsen-Metcalf	Haneda-Campos	Pons-Brooks	Tritton
Bus	Harrington	Pons-Winnecke	Tsuchinshan 1
Churyumov-Gerasimenko	Harrington-Abel	Reinmuth 1	Tsuchinshan 2
Clark	Hartley-IRAS	Reinmuth 2	Tuttle
Comas-Solá	Herschel-Rigollet	Russell 1	Tuttle-Giacobini-Kresák
Crommelin	Holmes	Russell 2	Van Biesbroek
D'Arrest	Honda-Mrkos-Pajdušáková	Russell 3	Väisälä
Daniel	Howell	Russell 4	West-Kohoutek-Ikamu
De Vico-Swift	IRAS	Sanguin	Westphal
Denning-Fujikawa	Jackson-Neujmin	Schaumasse	Whipple
Du Toit 1	Johnson	Schuster	Wild 1
Du Toit-Hartley	Kearnes-Kwee	Schwassmann-Wachmann 1	Wild 2
Du Toit-Neujmin-Delporte	Klemola	Schwassmann-Wachmann 2	Wild 3
Dubiago	Kohoutek	Schwassmann-Wachmann 3	Wirtanen
Encke	Kojima	Shajn-Schaldach	Wolf
Faye	Kopff	Shoemaker 1	Wolf-Harrington

Long-Period Comets

Austin (1982 VI)	Hartley (1985 XIV)	Machholz (1985 VIII)	Shoemaker (1985 XII)
Austin (1984 XIII)	Hartley-Good (1985 XVII)	Meier (1984 XX)	SOLWIND 2 (1981 I)
Bowell (1982 I)	IRAS (1983 I)	Panther (1981 II)	SOLWIND 3 (1981 XIII)
Bus (1981 XI)	IRAS (1983 VI)	Russell (1981 V)	SOLWIND 4 (1981 XXI)
Černis (1983 XII)	IRAS (1983 XVI)	Shoemaker (1983 XV)	SOLWIND 5 (1984 XII)
Elias (1981 XV)	IRAS-Araki-Alcock (1983 VII)	Shoemaker (1984 XV)	Sugano-Saigusa-Fujikawa (1983 V)
Gonzales (1981 VII)	Levy-Rudenko (1984 XXIII)	Shoemaker (1985 II)	Theile (1985 XIX)

TABLE 1 (CONT.). POTENTIAL PARENTS

Asteroids With Comet-Like Orbits

334 Chicago	2060 Chiron	3752 (1985 PA)	1983 LC
944 Hidalgo	2101 Adonis	4015 (1979 VA)	1983 RB
1256 Normannia	2102 Tantalus	1973 NA	1983 VA
1580 Betulia	2201 Oljato	1974 MA	1983 XF
1863 Antinous	2212 Hephaistos	1982 DB	1984 BC
1866 Sisyphus	2329 Orthos	1982 RA	1984 KB
1921 Pala	3200 Phaethon	1982 TA	1985 TB
1922 Zulu	3552 (1983 SA)	1982 YA	1986 DA
1981 Midas	3671 Dionysius	1983 LB	6344 P-L

Meteor Streams

Andromedids	δ Cancriids	Librids	Northern Piscids
Annual Andromedids	α Capricornids	April Lyrids	Quadrantids
η Aquarids	Corvids	June Lyrids	α Scorpiids
δ Arietids	κ Cygnids	Monocerotids	χ Scorpiids
Northern δ Aquarids	δ Draconids	θ Ophiuchids	Daytime Sextantids
Southern δ Aquarids	October Draconids	Northern χ Orionids	Daytime β Taurids
Northern ι Aquarids	Geminids	Southern χ Orionids	Southern Taurids
Southern ι Aquarids	ϵ Geminids	Orionids	Northern Taurids
κ Aquarids	r Herculids	Pegasids	Ursids
Daytime Arietids	σ Hydrids	Perseids	Virginids
α Boötids	Leo Minorids	Daytime ζ Perseids	μ Virginids
ϕ Boötids	Leonids	December Phoenicids	
June Boötids	δ Leonids	July Phoenicids	
Camelopardalids	σ Leonids	Southern Piscids	

TABLE 2.
TYPE I DUST TRAILS IN THE IRAS SKYFLUX PLATES

PLT/HCON	λ_0 (1950)	β_0 (1950)	λ_1 (1950)	β_1 (1950)	ΔMA_0	ΔMA_1	Comments*
56 1	124.387550	7.906315	128.403364	7.863007	1.13	-0.07	C-G (coma)
1	133.924973	6.943444	135.137955	6.914125	0.36	-0.05	C-G (coma)
72 1	14.213708	5.153361	24.421719	0.503429	10.77	-11.63	Encke
1	9.164062	3.925794	13.431341	4.546709	22.76	8.46	Encke
2	9.671945	4.244484	24.170834	6.177160	23.83	-13.11	Encke
95 1	357.034424	1.865459	9.888929	4.029937	80.22	20.16	Encke
2	359.726532	2.551209	9.889992	4.278696	66.68	22.99	Encke
1	350.418793	-1.067407	6.074000	-6.074819	4.98	2.49	Tempel 2
2	350.607300	-1.393038	358.859222	-3.713891	3.72	2.47	Tempel 2
2	359.891174	-5.926529	5.574126	-7.409752	5.23	4.42	Tempel 2
96 1	5.121358	-5.844675	13.481000	-7.724786	2.69	1.06	Tempel 2
1	14.048326	-10.946827	19.979362	-11.984856	4.04	2.95	Tempel 2
2	4.380317	-7.134231	20.587673	-10.591124	4.58	1.65	Tempel 2
97 1	18.827351	-11.773843	35.877399	-13.423677	3.16	-1.01	Tempel 2 (coma)
2	19.648220	-10.390770	28.721813	-11.630341	1.83	-0.34	Tempel 2 (coma)
2	28.751648	-15.652569	35.026012	-15.827680	2.49	0.95	Tempel 2
98 1	34.650265	-13.432027	39.467449	-13.559826	-0.61	-2.16	Tempel 2
1	41.794926	-14.133006	43.739124	-14.117133	-2.34	-3.04	Tempel 2
1	43.691772	-17.164413	51.287430	-16.448332	-0.78	-3.58	Tempel 2
2	33.841038	-15.779714	51.530251	-15.011994	1.24	-4.86	Tempel 2 (coma)
3	34.479713	-21.480413	50.227848	-19.799938	3.25	-1.83	Tempel 2 (coma)
99 1	50.047771	-16.546680	55.164597	-15.908616	-3.10	-5.37	Tempel 2
107 1	176.058655	6.956966	186.532608	5.016053	5.53	2.92	Tempel 1
2	178.954361	5.990831	186.828445	4.490393	6.19	4.17	Tempel 1
2	178.985260	4.924236	186.557709	5.205716	17.42	13.55	Kopff
108 1	195.193710	12.554204	199.976624	12.513857	36.81	33.77	Tempel 2
1	185.370697	5.270563	193.422974	3.472945	3.16	1.47	Tempel 1
1	195.878586	2.264314	202.303894	0.768320	4.26	2.87	Tempel 1
1	187.513855	5.626348	193.831863	5.774901	11.99	9.66	Kopff
1	195.865234	4.814285	202.985992	4.797383	11.61	9.07	Kopff
2	191.543045	13.666253	199.244110	13.924667	37.03	32.06	Tempel 2
2	185.380035	5.166706	202.743652	5.408048	14.08	7.50	Kopff
2	185.636765	4.739122	202.496796	0.813562	4.42	0.88	Tempel 1
109 1	198.540802	12.546599	216.582169	11.394038	34.63	25.85	Tempel 2
1	201.798843	4.822292	212.507645	4.578817	9.43	6.31	Kopff
2	198.041077	13.904992	208.393890	13.822097	32.73	27.48	Tempel 2
2	208.832260	11.243883	217.019012	10.324701	30.70	27.17	Tempel 2
2	201.566559	5.402317	208.193054	5.338406	7.89	6.00	Kopff
2	208.976532	4.295098	211.366806	4.231767	8.55	7.86	Kopff
3	212.632690	9.037502	217.713852	8.379668	36.17	33.85	Tempel 2
110 1	215.396149	11.520839	223.549469	10.357949	26.34	23.53	Tempel 2
2	215.786194	10.503631	225.365738	8.870387	27.59	24.29	Tempel 2

	3	216.492935	8.558039	221.799957	7.775908	34.37	32.17	Tempel 2
116	1	314.062927	9.411806	322.978821	6.810231	7.37	6.19	Tempel 2
117	1	322.497925	6.959069	337.249176	2.523213	6.27	4.23	Tempel 2
	2	323.204590	6.088303	328.661072	4.500309	4.91	4.51	Tempel 2
	2	328.974579	5.258886	337.291046	2.716496	5.26	5.97	Tempel 2
118	1	336.545135	2.726181	351.577728	-2.059085	4.29	4.85	Tempel 2
	2	336.358246	3.050694	351.798274	-1.723108	6.11	3.57	Tempel 2
120	1	0.226384	-22.056042	7.463731	-22.978146	2.15	0.	P-W (coma)
	2	3.768632	-20.808037	12.681046	-26.610825	2.58	-0.18	P-W (coma)
131	1	188.984299	-8.754807	193.008530	-9.088402	8.29	4.07	S-W 1
	2	188.211716	-8.521176	192.995987	-8.911768	9.56	4.52	S-W 1
132	1	191.096420	-8.938723	193.495087	-9.127597	6.05	3.56	S-W 1
	1	195.083572	-8.776935	198.177383	-8.956430	3.17	0.	S-W 1 (coma)
	1	200.640717	1.184829	204.907516	0.134709	3.20	2.32	Tempel 1
	2	191.096893	-8.761195	197.404358	-9.201373	6.52	0.	S-W 1 (coma)
	2	200.589355	1.304591	205.083603	0.137821	1.22	0.46	Tempel 1
133	1	203.282059	0.548697	222.473938	-4.339222	2.64	-0.84	Tempel 1 (coma)
	1	209.414C41	4.644820	219.148911	4.332558	7.15	4.70	Kopff
	2	203.188553	0.618127	208.188950	-0.088356	0.79	-0.08	Tempel 1 (coma)
	2	209.014923	-0.632426	222.271693	-3.889977	2.98	0.46	Tempel 1
	2	208.974792	4.308023	219.424606	3.873339	8.55	5.86	Kopff
	3	212.973709	3.430291	219.626923	3.142338	12.87	11.03	Kopff
134	1	224.109314	8.067718	234.164856	5.824548	27.05	23.87	Tempel 2
	1	220.107758	-3.710375	223.197968	-4.538164	-0.44	-0.98	Tempel 1
	1	224.208176	-3.526715	231.101059	-5.078986	2.31	0.96	Tempel 1
	1	217.508804	4.379894	223.451324	4.076388	5.11	3.79	Kopff
	1	224.222595	3.230187	234.912903	2.502056	6.61	4.29	Kopff
	2	223.210526	9.307357	233.926758	6.887533	24.96	21.95	Tempel 2
	2	219.914001	-3.280891	229.645157	-5.645858	0.89	0.78	Tempel 1 (coma)
	2	217.764145	3.978576	234.866165	2.900977	6.18	2.63	Kopff
	3	219.654144	8.090461	234.053085	5.381752	33.05	28.37	Tempel 2
	3	217.988266	3.223224	234.124741	2.273944	11.46	7.86	Kopff
135	1	233.236801	2.604616	238.481979	2.209785	4.60	3.56	Kopff
	2	233.210327	3.037457	235.367691	2.851344	2.92	2.53	Kopff
	3	233.434265	2.309254	238.875137	1.951485	8.06	7.62	Kopff
138	1	284.144073	13.877756	293.333008	12.070649	9.33	7.66	Tempel 2
	2	282.416809	13.081878	293.234039	11.025568	8.52	6.41	Tempel 2
139	1	291.904602	12.360771	308.004883	8.773201	7.90	5.20	Tempel 2
	2	291.763245	11.287588	298.723297	9.845864	6.65	5.34	Tempel 2
	2	298.783600	11.957493	301.677429	11.269445	7.94	7.47	Tempel 2
	2	303.298218	11.431726	308.372803	10.130794	7.82	7.06	Tempel 2
140	1	306.546906	9.108483	313.228210	7.438509	5.41	4.30	Tempel 2
	1	314.056885	9.393433	322.723969	6.870560	7.37	6.23	Tempel 2
	2	308.835175	9.978965	322.256378	6.335083	6.98	5.02	Tempel 2
141	1	322.275513	7.017034	332.278351	3.982780	6.30	4.90	Tempel 2
	1	326.495453	-9.739374	332.947083	-10.155661	5.88	2.54	Gunn
	2	321.541931	6.550813	328.217712	4.641628	5.15	4.14	Tempel 2
142	1	330.790802	-10.026687	337.992981	-10.360558	3.69	-0.26	Gunn (coma)
	2	330.288818	-10.337832	331.027100	-10.385097	4.49	4.10	Gunn
	2	333.522858	-10.996874	337.828979	-11.168563	3.47	1.19	Gunn
158	1	228.957077	-4.605928	237.971909	-6.014661	1.37	-0.33	Tempel 1 (coma)
162	3	275.634857	-1.133098	291.783691	-2.371355	1.41	-0.45	Kopff (coma)

Trails Having Unknown Parents (Orphans)

4	3	55.214	98.258	53.442	91.351	(coma?)
54	1	4.163	98.219	4.565	102.900	
107	1	7.231	177.677	6.246	181.563	
110	3	12.287	218.284	12.342	219.798	
119	1	-10.323	4.166	-9.940	359.738	
123	1	-39.830	57.975	-40.745	56.462	
135	1	1.540	240.756	6.912	235.213	(coma?)
171	3	-59.523	48.185	-66.223	39.515	
188	2	-64.234	338.784	-65.355	356.874	

**Notes*

C-G = Churyumov-Gerasimenko

P-W = Pons-Winnecke

S-W 1 = Schwassmann-Wachmann 1

(coma) = The cometary coma is seen within the trail segment.

TABLE 3. OBSERVATIONS AND CHARACTERISTICS FROM INDIVIDUAL SCANS

Trails	$R(AU)$	$\Delta(AU)$	$\phi(^{\circ})$	$\Delta MA(^{\circ})$	$F_p(12\mu m)$	$F_p(25\mu m)$	$F_p(60\mu m)$	$F_p(100\mu m)$	$W(10^3 km)$	$T(K)$	$\tau \times 10^{-9}$	$\epsilon/(1-A)$
Churyumov-Gerasimenko	2.278	2.098	26.2	0.05	0.47 \pm 0.05	0.92 \pm 0.08	0.52 \pm 0.03	***	51 \pm 9	210 \pm 15	4.6 \pm 0.1	0.6 \pm 0.2
Encke	3.926	3.779	14.9	52.8	***	0.07 \pm 0.01	0.06 \pm 0.01	***	680 \pm 71	147 \pm 15	1.3 \pm 0.1	0.8 \pm 0.2
Gunn	2.681	2.473	22.2	0.82	0.22 \pm 0.06	0.97 \pm 0.08	0.55 \pm 0.03	***	111 \pm 25	183 \pm 12	7.1 \pm 0.9	0.8 \pm 0.2
Kopff	1.577	0.953	38.0	0.53	1.04 \pm 0.14	1.19 \pm 0.20	***	***	26 \pm 15	248 \pm 20	4.9 \pm 1.0	0.6 \pm 0.2
Pons-Winnecke	1.531	1.155	41.6	0.94	0.31 \pm 0.06	0.52 \pm 0.06	***	***	40 \pm 14	236 \pm 19	2.2 \pm 0.1	0.6 \pm 0.2
Schwassmann-Wachmann 1	6.287	6.281	9.24	0.96	***	0.11 \pm 0.02	0.15 \pm 0.02	0.10 \pm 0.02	769 \pm 127	108 \pm 18	7.6 \pm 1.2	1.1 \pm 0.9
Tempel 1	1.517	1.149	41.9	0.29	0.36 \pm 0.05	0.59 \pm 0.07	0.31 \pm 0.06	***	68 \pm 10	227 \pm 16	2.6 \pm 0.2	1.0 \pm 0.3
Tempel 2	1.460	1.086	44.1	0.37	2.44 \pm 0.09	3.93 \pm 0.14	1.54 \pm 0.05	***	31 \pm 1	248 \pm 8	11.0 \pm 0.3	0.8 \pm 0.1

TABLE 4. TRAIL EXTENT AND DERIVED CHARACTERISTICS

Trails	ΔMA (-)	ΔMA (+)	v_{peri} (m/s)	v_{ap} (m/s)	Age $(\beta = 10^{-3})$ (Years)	Age $(\beta = \beta_{min})$ (Years)	Period (Years)	M_{resid} Log(g)	dM/dT (IRAS) Log(g/Cent.)	dM/dT (K&K) Log(g/Cent.)	IRAS/K&K
Churyumov-Gerasimenko	0.1	1.1	2.5	0.6	2.6	11.	6.6	12.0	13.6	12.6	10.
Encke	13.	80.	40.	3.3	19.	21.	3.3	14.2	14.9	14.5	2.7
Gunn	0.3	4.5	3.0	1.6	20.	57.	6.8	13.1	13.8	13.4	2.5
Kopff	0.5	17.	1.6	0.5	51.	286.	6.4	12.9	13.2	13.5	0.5
Pons-Winnecke	0.2	2.6	3.0	0.7	5.5	21.	6.4	11.9	13.2	12.9	2.0
Swassmann-Wachmann 1	0.0	9.6	5.2	4.7	114.	148.	15.	14.5	14.5	14.4	1.3
Tempel 1	1.0	6.2	4.5	1.4	14.	38.	5.5	12.5	13.4	13.0	2.5
Tempel 2	5.4	60.	2.2	0.7	140.	665.	5.3	13.8	13.6	13.4	1.6

TABLE 5. ORBIT SHIFTS

Trails	Nr. Years Before 1983	Δq (AU)	ΔQ (AU)	Δe	Δi (°)	$\Delta \omega$ (°)	$\Delta \Omega$ (°)
Churyumov-Gerasimenko	24	-1.5	-0.2	0.27	-16	-21	-1.5
Encke	STABLE*						
Gunn**	18	-0.9	0.0	0.14	-1.0	23	-12
Kopff	29	0.1	0.1	-0.01	-2.5	131	-133
Pons-Winnecke	41	0.1	0.0	-0.03	2.6	0.0	-4
Schwassmann-Wachmann 1	STABLE						
Tempel 1	STABLE						
Tempel 2	STABLE						

* STABLE indicates only small changes in orbital elements over the past 200 years.

** Prior to 1813, the orbit of P/Gunn was completely outside that of Jupiter.

Appendix V.

THERMAL PROPERTIES OF COMETARY DUST

D. Lien

ABSTRACT

The equilibrium grain temperatures (T_{eq}) for heterogeneous grains were calculated using the Maxwell-Garnett and Bruggeman effective dielectric medium theories for admixtures of magnetite, water ice, and a silicate. Admixtures of magnetite and a silicate were analyzed as a function of the total volume fraction occupied by each mineral. The equilibrium grain temperature depends upon the volume fraction and which theory is applied, but is not a volume weighted average of the temperatures of the two homogeneous grains. Spectra of a size distribution of heterogeneous grains show differences which depend on the theory and the relative volume fractions, although these differences may not always be detectable.

The Maxwell-Garnett theory was applied to an admixture of water ice and magnetite or a silicate. The presence of an inclusion raises the equilibrium temperature, but sublimation reduces the magnitude of this increase. The spectrum of dirty ice shows spectral features similar to that of pure ice in the 10 μm region. The grains are never warm enough to excite the O-H vibration modes seen at 3.1 μm . Small ($a < 100 \mu\text{m}$) dirty ice grains have lifetimes less than 15 minutes at 1 AU, although larger or less dirty grains may exist long enough to form an icy grain halo surrounding the nucleus of a comet.

I. INTRODUCTION

The first theoretical study of the thermal properties of dust associated with comets was presented by J.H. Poynting in 1904 (Poynting, 1904) for centimeter-sized dust grains—large enough for scattering effects to be unimportant, but small enough to be isothermal. He calculated what is now referred to as the equilibrium black-body temperature, effectively showing that the grains emit in the infrared (IR). Sixty-one years later, this thermal IR radiation was detected (Becklin and Westphal, 1966).

Thermal emission from cometary dust grains have been observed in a number of comets (cf. review by Ney, 1982; Hanner, 1984). Coupled with theoretical treatments of the thermal properties of small, spherical, homogeneous dust grains, these observations have been used to set limits on the composition and particle size distribution of the dust (Hanner, 1980; Campins and Hanner, 1982; Hanner, 1984).

A potential difficulty with using homogeneous, spherical particles for the theoretical computations is that "real" comet dust is probably neither spherical nor homogeneous (Hanner, 1984; Hanner et al., 1985). For example, laboratory studies of interplanetary dust particles (IDP; Fraundorf et al. 1982; Sandford and Walker, 1985) show that most of the particles are aggregates of smaller particles, often with a variety of compositions.

The purpose of this paper is to analyze the effects of heterogeneity on the equilibrium grain temperature of small grains. In Section II, the basic methods used to determine the equilibrium grain temperature are presented as are results for homogeneous grains composed of magnetite, water, and "astronomical silicate" (Draine and Lee, 1984; Draine, 1985). In Section III, the basic equations used to determine the optical constants of heterogeneous grains are presented for two different approximations: The Bruggeman theory (Bruggeman, 1935) for an aggregate-type grain, and the Maxwell-Garnett theory

(Maxwell-Garnett, 1904) for a grain in which small inclusions are embedded in a homogeneous matrix. In Section IV, these theories are applied to an admixtures of magnetite, astronomical silicate, and water ice. The results are summarized in Section V.

II. EQUILIBRIUM GRAIN TEMPERATURES

A grain of dust in the coma of a comet can absorb energy from a number of sources: radiation from the sun, impacts from solar wind ions, scattered solar radiation and thermal radiation from other grains in the coma as well as collisions and condensation by the outflowing gas, and reflected and thermal radiation from the nucleus. The grain can release energy in the form of thermal radiation or through the sublimation of volatiles. If the energy absorbed is equal to the energy released, the grain is said to be in thermal equilibrium

$$E_{sol} + E_{sw} + E_{coma} = E_{rad} + E_{subl}. \quad (1)$$

The major source of heating is the absorption of solar radiation by a grain of radius a (Lamy, 1974):

$$E_{sol} = \frac{\Omega \pi a^2}{\pi} \int_0^\infty Q_a(a, \lambda) F(\lambda) d\lambda \quad (2)$$

where Ω is the solid angle of the sun, $F(\lambda)$ is the solar flux (Neckel and Labs, 1985; White, 1977), and $Q_a(a, \lambda)$ is the absorption efficiency of the grain (assumed to be spherical).

Heating by the solar wind (E_{sw}) is negligible, although the life time of a grain composed primarily of volatiles can be reduced greatly via sputtering by solar wind ions (Mukai and Schwehm, 1981; Brown, Lanzerotti and Johnson, 1982).

The collisional heating by gases in the coma is negligible due to the small velocity difference between the dust and the gas ($E_{coma}=0$).

In the near-nuclear region where the optical thickness of the dust may be large, radiation from the gas, dust, and nucleus may be very important in the thermal equilibrium of the dust. Because the analysis of the inner coma is very model dependent, these effects will be ignored in this paper ($E_{nuc}=0$).

A dust grain can cool via thermal radiation and sublimation. The thermal radiation term can be expressed as

$$E_{rad} = 4\pi a^2 \int_0^\infty Q_a(a, \lambda) B(T_{eq}, \lambda) d\lambda \quad (3)$$

where $B(T_{eq}, \lambda)$ is the Planck radiation function evaluated at the equilibrium temperature of the grain, T_{eq} . Sublimation removes energy from the grain at a rate

$$E_{subl} = \eta 4\pi a^2 L_s(T_{eq}, \lambda) d\lambda \quad (4)$$

where $L_s(T_{eq})$ is the latent heat of sublimation and dE/dt is the mass sublimation rate, both evaluated at T_{eq} . If the grain is heterogeneous, the area of the surface from which

molecules can sublime is not equal to the total surface area. The fraction of the surface composed of the subliming material is called the covering factor and is parameterized by η .

For the heliocentric distances discussed in this paper, water is the only material for which sublimation is important in determining the equilibrium grain temperature. The mass sublimation rate can be expressed as (Lamy, 1974)

$$\frac{dE}{dt} = 5.83 \times 10^{-2} \alpha p \sqrt{\frac{\mu}{T}} \quad (5)$$

where m is the atomic weight, α is the accommodation coefficient ($=1$ for water ice, Patashnick and Rupprecht, 1977), and p is the vapor pressure in torr. The vapor pressure for water is described in detail by Leger et al. (1983); we use the formula from the International Critical Tables as referenced in Mukai (1986) for crystalline water ice.

The latent heat of sublimation is related to the vapor pressure through the Clausius-Clapyron equation (Rock; 1983, Leger et al. 1983):

$$\ln(p) = \frac{L_s}{RT} + b \quad (6)$$

where R is the gas constant and b is a constant of integration. A plot of $\ln(p)$ versus $1/T$ has a slope of $-L_s/R$. For $T=273$ K, $L_s = 2.83 \times 10^{10}$ erg/gm, compared with an experimental value of 2.84×10^{10} erg/gm (Dwight, 1972). Between 90 K and 300 K, a plot of $1/T$ versus $\ln(p)$ is very linear—the average slope corresponds to a value for the latent heat of sublimation of 2.85×10^{10} erg/gm which we adopt as the value for the latent heat of sublimation. Lamy (1974) and Mukai (1986) quote a value of 2.6×10^{10} erg/gm—this value corresponds to the latent heat of sublimation of 0 K (Leger et al. 1983). The difference between the two values is important in controlling the equilibrium grain temperature only for the smallest grains at the smallest heliocentric distances. For other sizes and heliocentric distances, the difference corresponds to less than 1 K in the equilibrium temperature.

Based on the discussion above, we solve a modified version of Equation (1) for the equilibrium grain temperature:

$$E_{sol} = E_{rad} + E_{subl} \quad (7)$$

with the appropriate substitutions from Equations (2)-(5).

The absorption efficiency, $Q_a(a, \lambda)$, seen in both Equation (2) and Equation (3), is calculated assuming that the particles are spherically symmetric using the code BHMIE (Bohren and Huffman, 1983). Optical constants for H_2O are from the compilation of Warren (1984). Since the equilibrium grain temperature is independent of the choice of IR optical constants (Mukai and Mukai, 1984; Patashnick and Rupprecht (1977) suggest, however, that the IR optical constants are important), we decided not to incorporate the optical constants for amorphous ice (Leger et al. 1983).

The optical constants for magnetite are those of Huffman and Stapp (1973) and Steyer (1974) and were obtained in tabular form from Dr. M. Hanner. We use the optical constants of Draine and Lee (1984—tabulated in Draine, 1985) as a representative silicate.

The absorption efficiency ($Q_a(a, \lambda)$) was calculated at 694 logarithmically spaced wavelengths between 2000 Å and 200 μm. These cutoffs are based on the absence of observed scattered solar radiation shortward of ~ 2800 Å, the rapid decrease in the solar flux below 2000 Å (White, 1977), and the lack of thermal radiation from the coldest dust particles longward of 150 μm. An example of the absorption efficiency as a function of the size parameter is presented in Figure 1 for $(n, k) = (1.5, .5)$. The size parameter is given by $x = \frac{2\pi a}{\lambda}$.

Equation (7) was iteratively solved for the equilibrium grain temperature for 20 equally spaced heliocentric distances between 0.2 AU and 4.0 AU for 17 different grain radii equally spaced in the log of the radius between .001 μm and 100 μm.

The smallest grain has a radius equal to 10 Å. There is a question as to whether particles smaller than 50-100 Å have optical properties similar to the bulk properties of the material (Bohren and Huffman, 1983). The small particles were included in the calculations to determine if there is a way of detecting these very small particles using spectroscopic techniques, providing that the small particles have optical properties similar to the bulk properties of the mineral. Under these assumptions, we find that there is no difference between the thermal properties of a 10 Å grain and a 100 Å grain. However, other factors may be important in determining the equilibrium grain temperature of the smallest grains. Wavelength shortward of 2000 Å, below the short wavelength cutoff used in evaluating the integral in Equation (3), may be important for the smallest grains. Additionally, the absorption of a single UV photon may raise the temperature of a 10 Å grain to over 1000 K (Sellgren, Werner and Dinerstein, 1983). The equilibrium temperature of the smallest grains may be a complicated function of heliocentric distance, grain composition and solar activity. A detailed discussion of these effects will be presented in a future paper.

Figure 2 illustrates the grain temperature at 1 AU plotted as a function of the log of the grain size (in microns) for homogeneous grains consisting of magnetite, "astronomical silicate," and water ice (with and without sublimation). The temperature of a black-body at 1 AU is indicated by the light horizontal line. Also indicated are comparisons with previously published theoretical calculations. The agreement is quite good—differences exist primarily where different optical parameters were used (cf. Section IV for a discussion of the effects of a change in the optical parameters on the equilibrium grain temperature).

The general functional form of the equilibrium grain temperature with radius can be understood using the plot in Figure 1. Let $Q_a(V)$ be the average absorption efficiency in the visible and $Q_a(IR)$ be the corresponding efficiency in the infrared near the peak of the black-body curve. For a given particle size, the size parameter in the visible ($x_V = \frac{2\pi a}{\lambda_V}$) will be different from the size parameter in the IR ($x_{IR} = \frac{2\pi a}{\lambda_{IR}}$). The corresponding optical and IR absorption efficiencies will most likely be different, particularly if they have the identical relationship of $Q_a(a, \lambda)$ with the size parameter (i.e., Figure 1 is the same for both $Q_a(IR)$ and $Q_a(V)$). The ratio $Q_a(V)/Q_a(IR)$ is a measure of the ability of the grain to absorb and reradiate—if $Q_a(V)/Q_a(IR)$ increases, so does the temperature. For very small grains ($x \ll 1$), $Q_a(a, \lambda)$ is proportional to x (Bohren and Huffman, 1983), hence $Q_a(V)/Q_a(IR)$ is a constant and the temperature is independent of the grain radius. As $x_V \rightarrow 1$, $Q_a(V)$ increases more rapidly than $Q_a(IR)$, reaching a maximum near $x_V \sim 2$. This corresponds to the maximum equilibrium grain temperature (Figure 2; note that the

size parameter corresponding to the maximum grain temperature depends on the composition of the grain). As the size of the particle increases further, $Q_a(V)$ begins to decrease, eventually approaching a constant for large x_V . $Q_a(IR)$ is increasing, however, and the ratio $Q_a(V)/Q_a(IR)$ decreases, reaching a minimum at $x_{IR} \sim 2$, which corresponds to the minimum in the equilibrium grain temperature (Figure 2). The temperature increases for larger x_{IR} since $Q_a(V) \sim \text{constant}$ while $Q_a(IR)$ decreases. For large x_{IR} and x_V , $Q_a(V)/Q_a(IR) \sim 1$ and the equilibrium temperature approaches that of a black-body. In general, this behavior is independent of the composition of the grain. Note that this simplistic explanation is not always accurate. $Q_a(V)$ for water ice never approaches 1 for sizes of grains which would be considered isothermal, hence the resultant equilibrium grain temperature for large particles does not approach that of a black-body at 1 AU.

At 1 AU, sublimation cools pure water ice grains for $a < 1 \mu m$. The drop in the temperature for larger grains is due to the increase in the emissivity of the grains in the IR. This drop in the temperature is the cause of the reduction in the sublimation rate and the increase in the lifetime of pure water ice (Patashnick and Rupprecht, 1975).

According to Equation (4), the energy lost due to sublimation is a function only of the temperature. However, both E_{rad} and E_{sub} increase with increasing particle size. Thus as the radius increases, sublimation becomes less important in controlling the equilibrium temperature for pure water ice. The grain size at which sublimation no longer helps mediate the equilibrium temperature depends on the heliocentric distance of the ice grain.

Figures 3, 4 and 5 show the functional dependence of T_{eq} on the grain radius at various heliocentric distances for magnetite, astronomical silicate, and water ice (Figures 3, 4, and 5, respectively).

The curves in Figures 3 and 4 are essentially scaled versions of the curves in Figure 2. For water ice, Figure 5 shows a decrease in the effectiveness of E_{sub} in controlling the temperature at larger heliocentric distances; beyond 2.4 AU, sublimation contributes negligibly to the energy balance of the grain.

Since icy grains lose mass, they exist as solid grains for only a finite length of time. The lifetime of a grain is defined as the time it takes to lose its entire mass via sublimation, or

$$\tau(a) = \frac{\frac{4}{3}\pi a^3 \rho}{4\pi a^2 \frac{dE}{dt}} \quad (8)$$

where ρ is the density of ice (0.917 g cm⁻³) and dE/dt is assumed to be independent of the radius. However, dE/dt depends on the temperature which is a function of the size of the grain. A more appropriate expression for the lifetime is

$$\tau(a) = \int_0^a t(\alpha) d\alpha \quad (9)$$

where $\tau(a)$ is the time it takes the grain to reduce its radius from $a+da$ to a . The lifetimes of pure ice grains for different heliocentric distances are plotted in Figure 6a and includes the effects due to the mass loss from sputtering by the solar wind (Mukai and Schwehm, 1981). Isotemporal curves for pure ice are shown in Figure 6b. Table 1 lists the log of the lifetime, in seconds, of a 100 μm grain for a range of heliocentric distances.

The sharp increase in the lifetime for particles larger than $1\text{ }\mu\text{m}$ is due to the decrease in the temperature, and thus the sublimation rate, of the ice particles.

For $R < 1.5\text{ AU}$, sublimation controls the lifetime for all sizes. As the heliocentric distance increases, the solar wind becomes more important for determining the lifetime. The dotted line in Figure 6a indicates the lifetime of an ice particle at 2 AU without solar wind sputtering. By 4 AU, even the lifetime of the smallest grains are determined by sputtering. If icy grains in the coma of a comet are shielded from the solar wind by the gaseous coma, then the lifetimes which are determined primarily by sputtering are lower limits to the true lifetimes.

III. HETEROGENEOUS GRAINS

Interplanetary dust particles (IDP; Fraundorf et al. 1982; Sandford and Walker, 1985), some of which may be cometary in origin, are neither spherical or homogeneous. Most IDP are aggregates of smaller particles whose compositions are varied (Fraundorf et al. 1982); the thermal behavior of such a grain will not necessarily be equivalent to a volume weighted average of the thermal properties of the individual components (cf. Section IV).

Water ice grains leaving the surface of a comet may not be pure. Small amounts of absorbing material can increase the equilibrium temperature, causing a decrease in the lifetime (Hanner, 1981; Mukai, 1986; Mukai et al., 1986). Additionally, the sublimation of water ice entrained within a non-volatile grain would lower the equilibrium grain temperature.

Recently, much attention has been given to the optical properties of heterogeneous materials (Barker, 1893; Genzel and Martin, 1973; Bohren and Battan, 1980; Stroud and Pan, 1978; Hayashi et al. 1979; Chylek and Srivastava, 1983; Bohren and Wickramasinghe, 1977; Mukai, 1986; Mukai et al. 1986).

There are two conceptual models for which first order approximations exist (Chylek and Srivastava, 1983): the aggregate model, where the composite grain consists of a mixture of small grains randomly packed together; and the separated-grain model, where the composite grain consists of small individual grains embedded in a matrix. The first order approximations are known respectively as the Bruggeman theory (Bruggeman, 1935) and the Maxwell-Garnett (MG) theory (Maxwell-Garnett, 1904). Stroud and Pan (1978) and Chylek and Srivastava (1983; hereafter CS) have extended the first order approximations to include the effects of magnetic dipole interactions (Stroud and Pan, 1978; CS), non-Rayleigh particle sizes (CS), and particle size distribution (CS). Note however that the theory presented by CS may result in unphysical results (Bohren, 1986).

For mixtures of magnetite and astronomical silicate, the MG theory requires that either magnetite or astronomical silicate is the matrix material and has embedded in it small inclusions ($x \ll 1$ for all wavelengths) of the other material. The Bruggeman theory is conceptually similar to the aggregate of particles seen in IDP (Fraundorf et al. 1982).

The MG theory (Maxwell-Garnett, 1904) averages the dielectric constant of a large number of very small particles ($x \ll 1$ for all wavelengths), referred to as inclusions, with the dielectric constant of the material in which the inclusions are embedded (called the matrix). Let ϵ_m be the complex dielectric constant of the matrix, ϵ_i be the complex dielectric constant of the inclusions, and f_i be the volume fraction of the medium occupied

by the inclusion. The average dielectric constant of the medium is (Maxwell-Garnett, 1904)

$$\epsilon_{eff} = \epsilon_m \left[\frac{1 + 3f_i(\epsilon_i - \epsilon_m)(\epsilon_i + 2\epsilon_m)^{-1}}{1 - f_i(\epsilon_i - \epsilon_m)(\epsilon_i + 2\epsilon_m)^{-1}} \right] \quad (10)$$

The effective dielectric constant derived from the Bruggeman theory is the solution to the sum (CS)

$$\sum_j \frac{f_j(\epsilon_j - \epsilon_{eff})}{(\epsilon_j + 2\epsilon_{eff})} = 0 \quad (11)$$

where f_j is the volume fraction the medium occupied by small grains with dielectric constant ϵ_j . For a two component grain, Equation (11) is a simple quadratic.

Both approximations rely on two assumptions. First, that the inclusions are small compared to the wavelength, and second, that a small element of the mixture contains a large number of inclusions such that the concept of an effective dielectric constant exists. The approximations are developed assuming that the forward scattering intensity from each small element of the mixture is identically zero (CS).

The Bruggeman theory is symmetric with respect to interchange of the different grains, whereas the MG theory is not symmetric (Bohren and Battan, 1980). Conceptually, the MG theory differentiates between magnetite conclusions embedded in an ice matrix and ice inclusions in a magnetite matrix (i.e., a fluffy grain whose spaces are filled with ice). This conceptual difference is reflected by a quantitative difference in the effective dielectric constant of the grain when the roles of the matrix and inclusion compositions are reversed (Equation 10).

To understand better the thermal and spectral properties of heterogeneous grains, results are presented based on the first order approximations (Equations 10 and 11). Neglecting the magnetic dipole component of the forward scattering is reasonable for small silicate grains, but may introduce errors into the effective dielectric constant for magnetite. Since the purpose of this paper is to investigate the effects of a heterogeneous composition on the thermal properties of small grains, the addition of a more detailed model is unwarranted at this time.

Figure 7 shows the real and imaginary indices of refraction for magnetite, astronomical silicate, and a 50-50 mix calculated from the dielectric constants obtained with Equations (10) and (11) ($\epsilon_1 = n^2 - k^2$; $\epsilon_2 = 2nk$). Astronomical silicate was used as the matrix material for the curve labeled 50/50 in Figure 7. The complex index of refraction when magnetite is the matrix material is very similar to the curve labeled 50/50. The Bruggeman theory retains the spectral features of all components, even when the fractional abundance of a component is very small. The MG theory tends to show the spectral features of the matrix material over those of the inclusions (cf. Section IV).

Both the MG theory and the Bruggeman theory have successes and failures in predicting the effective dielectric constant of a heterogeneous medium. Bohren and Battan (1980) find that the MG theory is quite accurate in describing the radar backscattering from a water-ice mixture. Shroud and Pan (1977) find that the Bruggeman theory correctly explains the transition from dielectric to metal as the volume fraction of the metal

component increases. Alexander and Bates (1984) used a higher order MG theory analysis (CS) and found that it reproduced well observations of gold inclusions in a quartz matrix.

IV. RESULTS

Figures 8 and 9 show the temperature as a function of grain radius at 1 AU for heterogeneous grains (MG theory) composed of magnetite and astronomical silicate. Figure 8 has astronomical silicate as a matrix, and Figure 9 has magnetite as a matrix. The equilibrium grain temperature for two mixes of astronomical silicate and magnetite using the Bruggeman theory are also shown in both figures. The equilibrium grain temperature for homogeneous grains of magnetite and astronomical silicate are shown for comparison.

As the fraction of the inclusion increases, the equilibrium grain temperature becomes more like that of a homogeneous grain composed of the inclusion material. However, the equilibrium grain temperature is not equal to the volume weighted average of the equilibrium temperatures of the homogeneous grains. For example, the mean temperature of a $0.01\text{ }\mu\text{m}$ homogeneous magnetite and astronomical silicate grain is 415 K. The temperature for a 50% blend of each component is 476 K. The mean temperature is midway between the equilibrium temperature of a 75% astronomical silicate - 25% magnetite blend calculated with the MG theory (420 K) and a 90% astronomical silicate - 10% magnetite blend calculated with the Bruggeman theory (410 K).

The equilibrium temperature based on the MG theory is almost independent of which element is the inclusion and which is the matrix. For example, there is less than 8 K difference between the equilibrium temperatures of the smallest grains composed of 90% astronomical silicate and 10% magnetite when the role of matrix and inclusion is interchanged.

In comparing between the two theories, recall that the Bruggeman theory retains the spectral characteristics of the less abundant aggregate more readily than the MG theory. In Figure 8, this is reflected by the higher temperature of the smaller grains for equivalent fractional abundances because the absorption in the visible is enhanced by the large absorption of the magnetite component.

Conceptually, a matrix of 10% magnetite (or 10% astronomical silicate) by volume envisions the matrix acting as a glue and the inclusions being fewer in number and larger in size. In this case, the first order approximations for the effective dielectric constant (Equations 10 and 11) are no longer valid, and higher order terms must be included (CS). Based on the curves in Figures 8 and 9, any variation in the effective dielectric constant will change the equilibrium temperature of the smallest grains. Grains larger than $\sim 1\text{ }\mu\text{m}$ have very similar temperatures. The equilibrium temperature for the largest grains are almost independent of the composition and are very close to the black-body temperature (cf. Section II).

The spectrum of heterogeneous grains in the thermal IR depends on the radius, the volume fractions of the materials, and the theory used. Figure 10 shows the thermal emission from $1\text{ }\mu\text{m}$ and $10\text{ }\mu\text{m}$ grains at 1 AU for homogeneous grains of magnetite and astronomical silicate and for a 50-50 admixture of these minerals using both the MG theory and the Bruggeman theory.

For the 1 μm grains (Figure 10a and 10b), the spectral features observed are those seen in their respective imaginary index of refraction (Figure 7). Differences in the integrated emissivities are partly due to differences in the equilibrium grain temperature of each grain at 1 AU—ranging from 306 K for magnetite to 340 K for the 50-50 mixture calculated with the Bruggeman theory—and partly due to the total energy absorbed (and hence re-emitted) by the grain. For example, even though magnetite and astronomical silicate have nearly equivalent equilibrium grain temperatures (306 K and 307 K, respectively), astronomical silicate absorbs, and hence re-emits, much less energy than the grain of magnetite. The spectral features of the heterogeneous grains show the effect of the mixing theory used. For the MG theory, the spectral features are due primarily to the matrix material. For the Bruggeman theory, the spectral features of both materials are observed. In Figure 10b, this latter effect is seen as a strong absorption feature at 7.4 μm and a strong emission feature at 10 μm superposed on the near-blackbody spectrum of pure magnetite.

The spectrum of a 10 μm grain is very different than that of a 1 μm grain (Figure 10c and 10d). At 10 μm , the emissivity of the grain is almost constant as a function of wavelength, hence the spectrum is close to that of a blackbody, regardless of the composition. The small differences in the spectra of the 10 μm grains are due to differences in equilibrium grain temperatures and to differences in the composition. For larger grains, this latter effect becomes even less important.

Ground-based observations of comets do not detect single grains; rather, the thermal emission is from a large number of grains with a distribution in sizes. Recent work by Hanner and her co-workers (Hanner, 1980; Campins and Hanner, 1982; Hanner, 1985) report the effects of the particle size distribution on the thermal radiation from comets. The size distribution used is

$$n(a) = \left(1 - \frac{a_0}{a}\right)^M \left(\frac{a_0}{a}\right)^N \quad (12)$$

(Hanner, 1984), which has been shown to give a good fit to the thermal emission spectra of several comets (Hanner, 1983; Hanner et al. 1986) and is based on the size distribution of grains derived from dynamical analysis (Sekanina and Farrell, 1982). To better compare size distribution effects with previously published work, Equation (12) is used with $a_0=0.1$ μm , $M=28$, and $N=4.2$ (Hanner et al. 1986) to calculate the thermal emission from a distribution of particles. All calculations were made using the equilibrium temperature calculated at $R=1$ AU for each grain size.

Figure 11 shows the thermal emission spectrum of a distribution of sizes of homogeneous grains of astronomical silicate and magnetite at 1 AU. The 10 μm silicate feature is clearly seen, as is the 18 μm and 28 μm emission features of magnetite. Only the thermal emission is shown in Figure 11; scattering of solar radiation by the grains becomes the dominant source of radiation at wavelengths shortward of about 4 μm . The exact wavelength where the scattering component is equal to the thermal emission depends on the size distribution, composition, and scattering angle.

A 50% mix of astronomical silicate and magnetite result in the spectra shown in Figure 12. Using the MG theory with magnetite as the matrix results in a spectrum which, although slightly different from a pure magnetite spectrum (Figure 11), probably would not be detectable as such with ground-based observations. The secondary peaks

at about $6.2 \mu\text{m}$ in the spectrum of the grains calculation from the Bruggeman and MG (astronomical silicate as the matrix) theories is due to the smaller particles in the size distribution (Figure 10).

As the fraction of the mixture changes to favor one of the components, the differences between spectra calculated with different methods decrease. Figure 13 shows the spectra of three mixes, all with 90% astronomical silicate and 10% magnetite (by volume). The results for the Bruggeman theory and the MG theory with magnetite as the matrix are very similar.

In Section II, the equilibrium grain temperatures for pure water ice as a function of both heliocentric distance and radius of the particle were presented. However, the ice particles leaving the nucleus of the comet are probably not pure water ice; rather, they are an admixture of water ice, solid grains, and entrained complex molecules. As this "dirty ice" grain sublimates, it releases the solid particles and complex molecules into the coma. Conceptually, there are two type of "dirty ice" grains: one in which small solid particles are embedded in a matrix of ice, and the other is which small inclusions of ice are filling the pores of what is often referred to as a "fluffy" dust grain, in which case the mineral component would be considered as a matrix. Both types of "dirty ice" grains are discussed below.

A zeroth order analysis of the effects of dirt in ice (constant imaginary index of refraction for $\lambda < 1\mu\text{m}$; Hanner, 1981) on the equilibrium grain temperature and lifetime showed that the lifetime of the dirty ice grain decreased substantially for even a small amount of absorbing material.

The observed cometary gas to dust ratio (by mass) varies between 1 and 10 (Ney, 1982). Table 2 shows the gas to dust ratio for various volume fractions of the inclusion for inclusions of either magnetite or astronomical silicate, assuming that the gas originates as water ice. The density of astronomical silicate is assumed to be that of pyroxene (CRC, 1982).

The sublimation from a dirty ice grain cannot occur from the entire surface. The inclusions will be uncovered as the grain sublimates, reducing the surface area available for mass loss. This "covering factor" is quantitatively incorporated into the solution for the equilibrium grain temperature through the parameter η in Equation (4). The fraction of the surface exposed for a given volume fraction of the matrix ($f_m = 1 - f_i$) depends on the size of the inclusions. A first order approximation to the covering factor is $\eta = f_m$. For large bodies, an expression similar to that used by Fanale and Salvail (1984) for their "aereal factor" yields $\eta = \frac{2}{3}f_m$. For $f_m=0.9$ (90% water ice), the maximum temperature difference between the two approximation is 1 K, but reaches 7 K for $f_m=0.5$. All calculations reported here have been done using the simplest form for η ($\eta = f_m$).

Figure 14 shows the equilibrium grain temperature for dirty ice grains at 1 AU calculated from the optical constants derived from the MG theory using water as the matrix. The inclusions in Figure 14 are primarily magnetite, chosen as a "worst case"—a mineral with strong absorption in the visible. Calculations using astronomical silicate as the inclusion are cooler for an equivalent volume fraction. Calculations using magnetite as the matrix and water ice as the inclusion have curves identical to those shown in Figure 14 for equivalent volume fractions of the two elements, consistent with the behavior of a

magnetite-astronomical silicate grain. The results presented here show the same trends as reported by Hanner (1981), and are identical with those of Mukai (1986) for comparable computations.

The most important result from Figure 14 is the effect of sublimation on the equilibrium grain temperature. For example, the equilibrium grain temperature for grain containing 1% magnetite by volume without sublimation is shown for comparison. The equilibrium grain temperatures of this mixture with sublimation is 70-100 K cooler, depending on the radius. This is primarily due to the very strong dependence of the vapor pressure of ice on the temperature (Leger et al. 1983). Sublimation also smooths out the rapid change in the temperature due to the delayed change in the optical and infrared absorption efficiencies (cf. Section II). As the temperature increases for grain sizes around $0.1 \mu m$, the sublimation rate increases, keeping the temperature roughly constant. The temperature drop due to the increase in $Q_a(IR)$ reduces the sublimation rate, and hence the cooling efficiency, decreasing the magnitude of the drop in the grain temperature. The general rise in the temperature as the grain radius increases is due to the increase in E_{sol} and E_{rad} relative to E_{subl} (cf. Section II). Only for a gas to dust ratio of about 100 ($f_i=0.003$) with astronomical silicate as the inclusion does the dirty ice grain begin to mimic the equilibrium grain temperature of pure ice in having a drop in the temperature for $a > 10 \mu m$ grains. The equilibrium grain temperature for inclusions of magnetite with an equivalent volume fraction ($f_i=0.003$) does not show the same effect.

The thermal evolution of a dirty ice grain can proceed along two paths depending on the structure of the grain. Starting with a $100 \mu m$ grain, sublimation of the ice will reduce the radius. If the small inclusions are released simultaneously with the gas such that the volume fraction of the inclusion remains constant, the dirty ice grain will cool down, following a path of constant volume fraction (f_i). If the dirty ice grain breaks up onto smaller pieces as it sublimates, effectively increasing the volume fraction of the inclusion, then the dirty ice grain will heat up as it grows smaller, moving across the lines of constant volume fraction. The temperature of the dirty ice grain will inexorably increase until it reaches the equilibrium grain temperature for the radius of the embedded solid, at which point the ice has sublimated away completely. The evolution of a "real" dirty ice grain is probably a combination of these two evolutionary paths.

To illustrate the behavior of dirty ice at different heliocentric distances, Figure 15 shows the equilibrium grain temperature at five different heliocentric distances for an ice matrix with a volume fraction of 90%. Curves are shown for inclusions of magnetite and astronomical silicate. Small grains containing magnetite are hotter than those containing astronomical silicate. The difference in temperature increases as the heliocentric distance increases. For the largest grains, the temperature difference decreases, eventually disappearing completely. Essentially, this is because for large grains, $Q_a(V) \sim Q_a(IR) \sim 1$ for all wavelengths independent of the composition (cf. Section II). The effects of sublimation also decrease with increasing heliocentric distance. At 1 AU, the largest grains are 100 K cooler than a black-body, whereas at 2 AU the temperature is 17 K cooler. Small magnetite grains are warmer than black-body at 3 and 4 AU and small astronomical silicate grains are cooler. The equilibrium grain temperature of the largest grains approaches that of a black-body at 3 and 4 AU, identical to the way in which admixtures of magnetite and

astronomical silicate behave at 1 AU (cf. Figures 8 and 9). Mukai (1986) also pointed out this phenomena—large grains of dirty ice are slightly cooler than black-body radiators at heliocentric distances greater than ~ 2.5 AU due to a combination of the decrease in the effectiveness of sublimation in controlling the equilibrium grain temperature and the approach of the ratio of $Q_a(V)/Q_a(IR)$ to unity as the radius of the grain increases.

The lifetimes of dirty ice grains are shown in Figure 16 for different mixtures at 1 AU. Except for astronomical silicate inclusions with a volume fraction of $f_i = 0.003$, the maximum lifetime for a $100\ \mu\text{m}$ grain is less than 1 hour. A 50-50 mix with magnetite inclusions has a lifetime of only 5 minutes. The equilibrium grain temperature is approximately constant for the largest grains for most volume fractions (Figure 14). Table 3 gives the log of the lifetime in seconds for $100\ \mu\text{m}$ dirty ice grains of different volume fractions for four separate heliocentric distances. Extrapolation of the lifetime to larger grains assuming the isothermicity of the larger grains ($\tau(a)$ from Equation (8)) will give accurate lifetimes (i.e., equivalent to those calculated from a full treatment) for $f_i > 0.1$ for astronomical silicate and $f_i > 0.01$ for magnetite.

Sublimation controls the lifetime of all dirty ice grains studied in this work out to 4 AU. Sputtering by the solar wind does not contribute significantly to the lifetime of a dirty ice particle. At large heliocentric distances, this will certainly not be the case. However, the effects of the solar wind on the lifetime of the particles will have to be re-evaluated in the presence of a gaseous coma.

The lifetimes of the largest grains suggest that a small ($< 500\ \text{km}$) icy grain halo may exist. If, during the sublimation process (either from the nucleus or from larger grains), smaller ($a > 10\ \mu\text{m}$) icy grains break off with $f_i < 0.001$, their lifetimes would increase dramatically, creating a more extensive icy grain halo.

Figure 17 shows the thermal emission of pure and dirty ice for the particle size distribution given in Equation (12). The peak thermal irradiance for pure ice grains is about 1/100 that of solid grains (Figures 11 and 12). As the volume fraction of the inclusion increases, the total flux increases, and the peak shifts to shorter wavelengths. This is due primarily to the increase of the temperature of the grains. The shape of the spectrum is primarily that of pure water ice. The spectral features characteristic of the inclusions are not readily apparent.

V. SUMMARY AND CONCLUSIONS

The effects of heterogeneity on the equilibrium grain temperature and thermal spectrum has been studied for combinations of magnetite, astronomical silicate (Draine and Lee, 1984), and water ice using two theories describing the effective dielectric constants of a heterogeneous grain in terms of the dielectric constants of the components: the Maxwell-Garnett (MG) theory and the Bruggeman theory.

The equilibrium grain temperature of a heterogeneous grain was found to be intermediate between, but not a simple weighted average of, the temperatures of homogeneous grains of the component parts. Temperatures derived from the MG theory were independent of the choice of matrix for equivalent compositions. The spectra of a distribution of sizes of heterogeneous grains were different for equivalent compositions (and for the composition of the matrix in the MG theory).

The laboratory analysis of interplanetary dust grains suggests that pure silicate grains do not exist. Based on the analysis of heterogeneous grains, the equilibrium temperature of grains similar to collected interplanetary dust grains (Fraundorf et al. 1982) are hotter than a pure silicate grain for small grains ($a < 1\mu m$) and about the same temperature for large ($a > 10\mu m$) grains.

Only the MG theory was applied to the admixture of either magnetite or astronomical silicate embedded in a matrix of ice. The equilibrium grain temperature, however, was found to be symmetric with respect to interchange of the composition of the matrix and the inclusions.

The equilibrium grain temperature for dirty ice grains was found to be quite low at all heliocentric distances studied. The highest grain temperature found was ~ 220 K for a $100\mu m$ grain composed of 50% water ice and 50% magnetite at 0.2 AU. Sublimation is very effective at cooling the dirty ice grain. The resultant lifetime of the grain is greatly reduced over that of pure water. Most grains have lifetimes less than 15 minutes. An extension of the lifetimes to larger grains suggests that a $1\mu m$ dirty ice grain (50% water ice, 50% magnetite) will have a lifetime of about an hour at 1 AU. This suggests that a small (dirty) icy grain halo may exist. The spectrum of a distribution of dirty ice grains has features similar to the spectrum of the same distribution of pure ice grains, except hotter. The dirty ice grains are too cool to show the $3.1\mu m$ emission feature.

At large heliocentric distances sublimation is less important in controlling the equilibrium grain temperature which thus approaches a black-body temperature for large grains. This behavior is identical to that found for large homogeneous and heterogeneous grains (which do not contain a volatile component) at all heliocentric distances.

I wish to thank M. Hanner for supplying me with the optical constants for magnetite in digital form, and would also like to thank the staff of Lowell Observatory for their kindness and warmth shown to me during my brief, but enjoyable stay. This research was partly funded through NSF Grant AST-83717113 and by Air Force Geophysics Lab contract number F19628-87-K-0045.

Table 1
Lifetime of 100 μ m Homogeneous Ice Grains

R (AU)	Log τ (s)	R (AU)	Log (s)
0.2	2.9	1.6	12.7
0.4	3.7	2.0	13.0
0.6	5.2	2.4	13.2
0.8	7.6	2.8	13.3
1.0	9.8	3.0	13.4
1.2	11.5	3.4	13.5
1.4	12.3	4.0	13.6

Table 2
Gas to Dust Ratio for Dirty Ice

Ice Fraction	Inclusion	
	Magnetite	Ast. Silicate
0.997	60	100
0.99	20	30
0.9	2	3
0.75	0.5	0.9
0.5	0.2	0.3
0.1	0.02	0.03

Table 3
Log Lifetime (s) of Dirty Ice

Inclusion ^a	f_i	Heliocentric Distance			
		1 AU	2 AU	3 AU	4 AU
A	0.1	3.2	4.5	7.5	10.3
M	0.01	3.2	4.3	6.6	9.4
M	0.1	3.0	4.1	6.5	9.3
M	0.25	2.8	4.0	6.6	9.4
M	0.5	2.5	3.7	6.6	9.4
A	0.003	6.5	12.3	13.1	13.6
H	0.0	9.8	13.0	13.4	13.6
H ^b	0.0	9.8	>14.0	>14.0	>14.0

^aM = magnetite, A = astronomical silicate, H = pure water ice

^bNo solar wind sputtering.

REFERENCES

- Alexander, N., and Bates, C.W. 1984, *Sol. State Comm.*, 51, 331.
- Barker, A.S. 1973, *Phys. Rev.*, B7, 2507.
- Becklin, E.E., and Westphal, J.A. 1966, *Ap.J.*, 145, 445.
- Bohren, C.F. 1986, *J. Atm. Sci.*, 43, 468.
- Bohren, C.F., and Battan, L.J. 1980, *J. Atm. Sci.*, 37, 1821.
- Bohren, C.F., and Huffman, D.R. 1983, *Absorption and Scattering of Light by Small Particles* (New York: Wiley).
- Bohren, C.F., and Wickramasinghe, N.C. 1977, *Astrophys. Space Sci.*, 50, 461.
- Brown, W.L., Lanzerotti, L.J., and Johnson, R.E. 1982, *Science* 218, 525.
- Bruggeman, D.A.G. 1935, *Ann. Phys. (Leipzig)*, 24, 636.
- Campins, H., and Hanner, M.S. 1982, in *Comets*, ed. L.L. Wilkening (Tucson: University of Arizona Press), p. 341.
- Chylek, P., and Srivastava, V. 1983, *Phys. Rev.* B27, 5098.
- CRC Handbook of Physics and Chemistry*, 1982 62nd ed. B199.
- Draine, B.T. 1985, *Ap.J. Suppl.* 57, 587.
- Draine, B.T. and Lee, H.M. 1984, *Ap.J.*, 285, 89.
- Dwight, E.G. 1972, *American Inst. of Physics Handbook*, 3rd ed. (New York: McGraw-Hill).
- Eaton, N. 1984, *Vistas in Astronomy*, 27, 111.
- Fanale, T., and Savail, P. 1984, *Icarus*, 60, 476.
- Fraundorf, P., Brownlee, D.E., and Walker, R.M. 1982, in *Comets*, ed. L.L. Wilkening (Tucson: University of Arizona Press), p. 383.
- Genzel, L., and Martin, T.P. 1973, *Surf. Sci.*, 34, 33.
- Hanner, M.S. 1980, in *Solid Particles in the Solar System*, ed. I. Halliday and B.A. McIntosh (Dordrecht: Reidel), p. 223.
- Hanner, M.S. 1981, *Icarus* 47, 342.
- Hanner, M.S. 1983, in *Cometary Exploration*, ed. T.I. Gombosi, Vol. II, p. 1.
- Hanner, M.S. 1984, *Adv. Space Res.*, 4, 189.
- Hanner, M.S., Aitken, D.K., Knacke, R., McCorkle, S., Roche, P.F., and Tokunaga, A.T. 1985, *Icarus*, 62, 97.
- Hanner, M.S., and Campins, H. 1986, *Icarus*, 67, 51.
- Hayashi, S., Nakamori, N., and Kanamori, H. 1979, *J. Phys. Soc. Jap.*, 46, 1976.
- Huffman, D.R., and Stapp, J.L. 1973, in *Interstellar Dust and Related Topics*, ed. J.M. Greenburg and H.C. van de Hulst (Reidel; Dordrecht), p. 297.
- Lamy, P.L. 1974, *Astron. Astrophys.*, 35, 197.
- Leger, A., Gauthier, S., Defourneau, D., and Rouan, D. 1983, *Astron. Astrophys.*, 117, 164.
- Lien, D.J. 1985, unpublished results.
- Lien, D.J. 1990, in preparation.
- Maxwell-Garnett, J.C. 1904, *Phil. Trans. R. Soc.*, A203, 385.
- McGregor, W.K. 1978, *J. Quant. Spectrosc. Rad. Transfer*, 19, 659.
- Mukai, T. 1986, *Astron. Astrophys.*, 164, 397.

- Mukai, T., Fechtig, H., Grun, E., Giese, R.H., and Mukai, S. 1986, *Astron. Astrophys.*, 167, 364.
- Mukai, T., and Mukai, S. 1984, *Adv. Space Res.*, 4, 207.
- Neckel, H. and Labs, D. 1985, *Sol. Phys.* 95, 229.
- Ney, E.P. 1982, in *Comets*, ed. L.L. Wilkening (Tucson: University of Arizona Press), p. 323.
- Patashnick, H., and Rupprecht, G. 1975, *Ap.J. (Letters)*, 197, L79.
- Poynting, J.H. 1904, *Phil. Trans. R. Soc.*, A202, 525.
- Rock, P.A. 1983, *Chemical Thermodynamics*, (Mill Valley: University Science Books), p. 280.
- Sandford, S.A., and Walker, R.M. 1985, *Ap.J.*, 291, 838.
- Sekanina, Z., and Farrell, J.A. 1982, *Astron. J.*, 87, 1836.
- Sellgren, K. Werner, M.W. and Dinerstein, H.L. 1983, *Ap.J. (Letters)*, 271, L13.
- Steyer, T.R. 1974, Ph.D. Thesis, University of Arizona.
- Stroud, D., and Pan, F.P. 1978, *Phys. Rev.*, B17, 1602.
- Warren, S.G. 1984, *Appl. Opt.*, 23, 1206.
- Weiss-Wrana, K. 1983, *Astron. Astrophys.*, 126, 240.
- White, O. 1977, *The Solar Output and Its Variation*, (Colo. Univ. Press: Boulder).

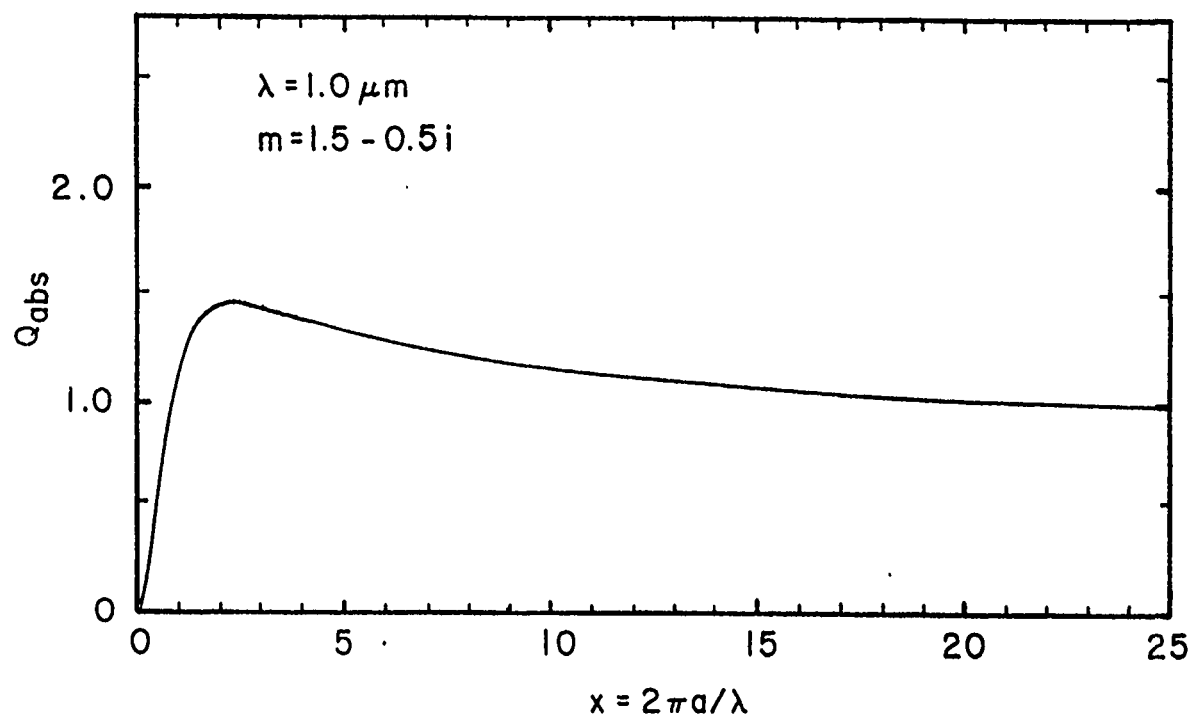


Fig. 1 Absorption efficiency as a function of the size parameter $x (= \frac{2\pi a}{\lambda})$.

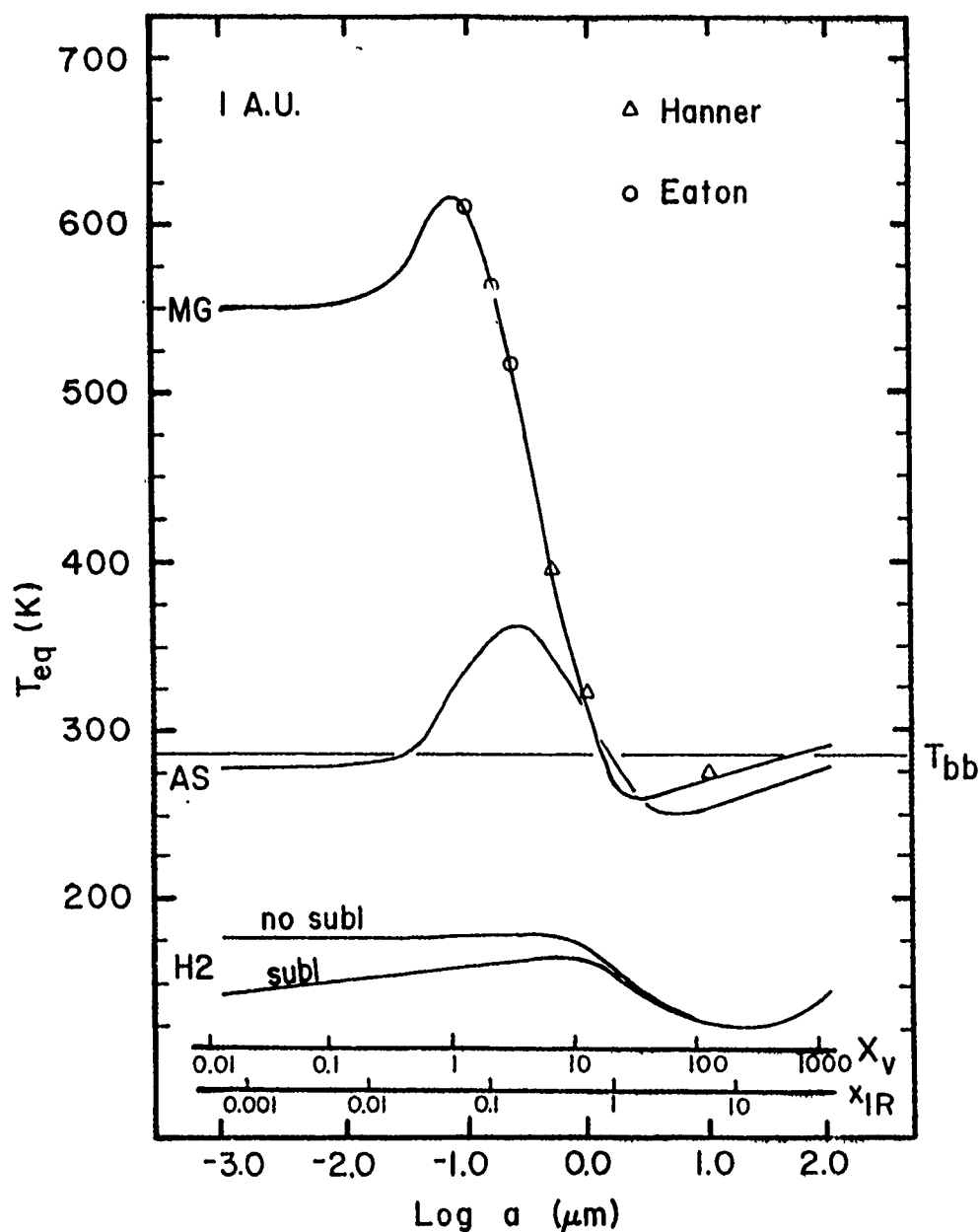


Fig. 2 Equilibrium grain temperature at 1 AU for magnetite (MG), astronomical silicate (AS), and water ice (H2; with and without sublimation) as a function of the log of the particle radius in microns. The dimensionless size parameter, x , is also shown on the abscissa for wavelengths of 0.5 μm and 10 μm . Published equilibrium grain temperatures from Hanner (1981) and Eaton (1984) are shown for comparison. The black-body temperature at 1 AU is indicated by the thin horizontal line.

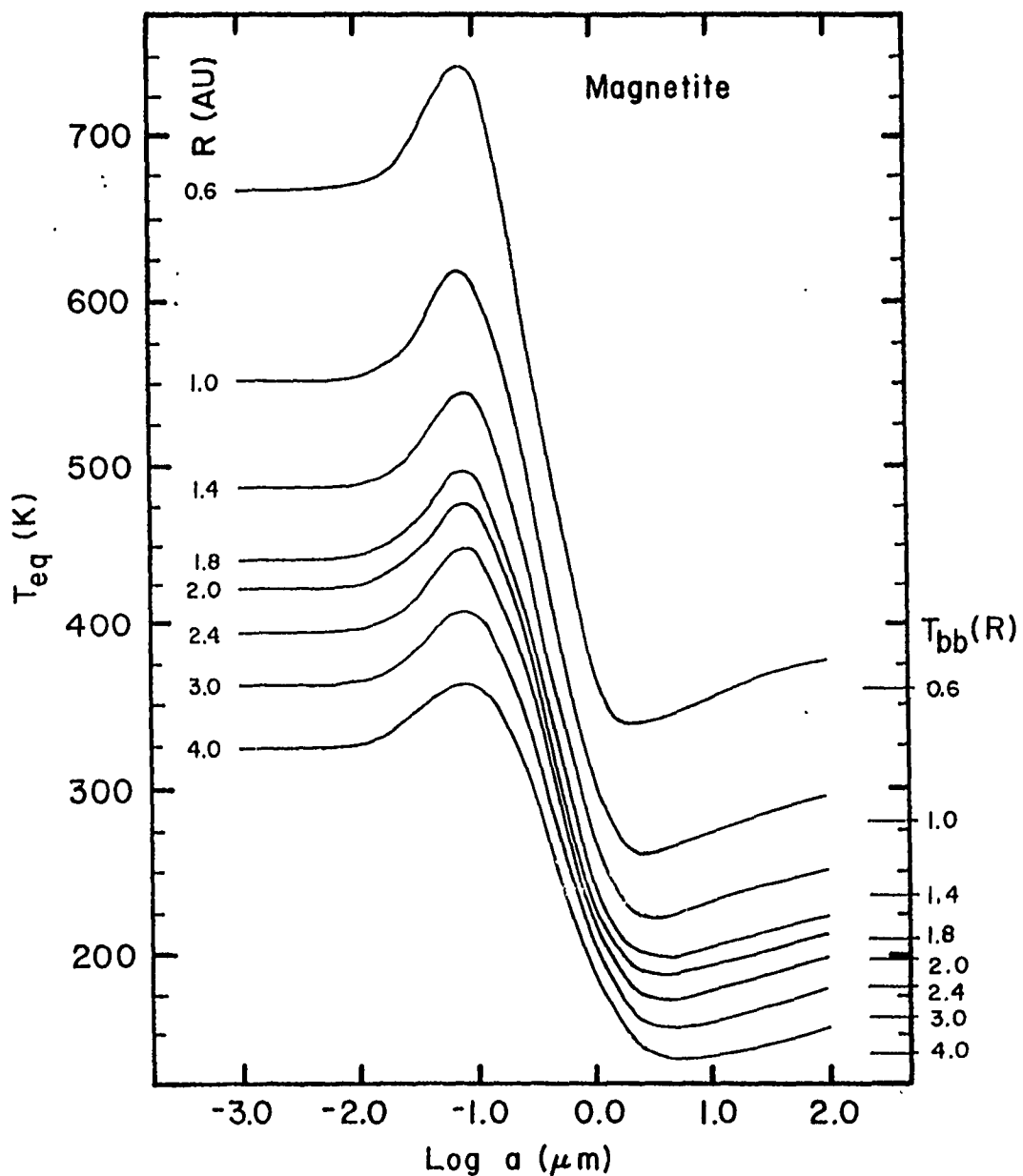


Fig. 3 The equilibrium grain temperature of magnetite as a function of the log of the particle radius at various heliocentric distances. The black-body temperature at each heliocentric distance is indicated.

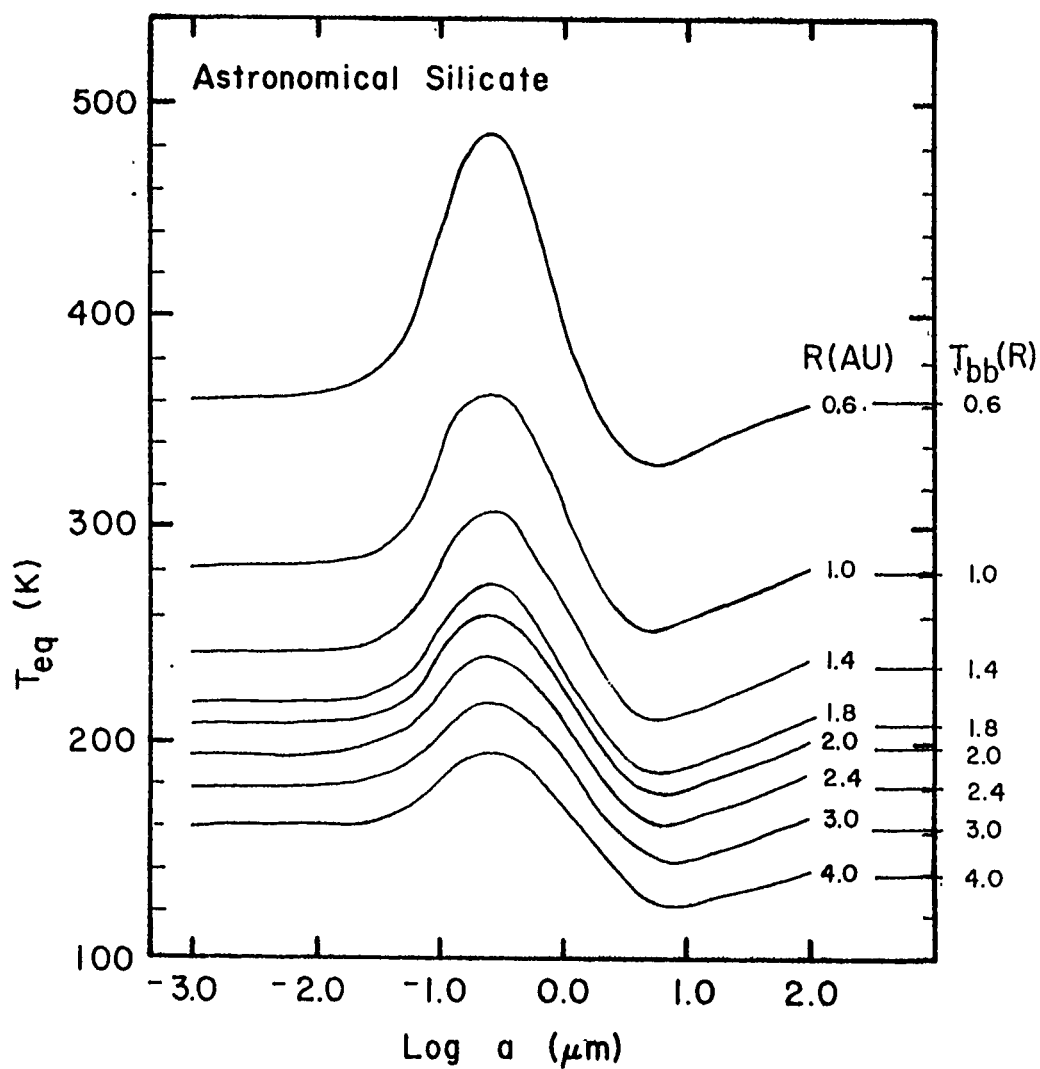


Fig. 4 The same as Figure 3, except for astronomical silicate.

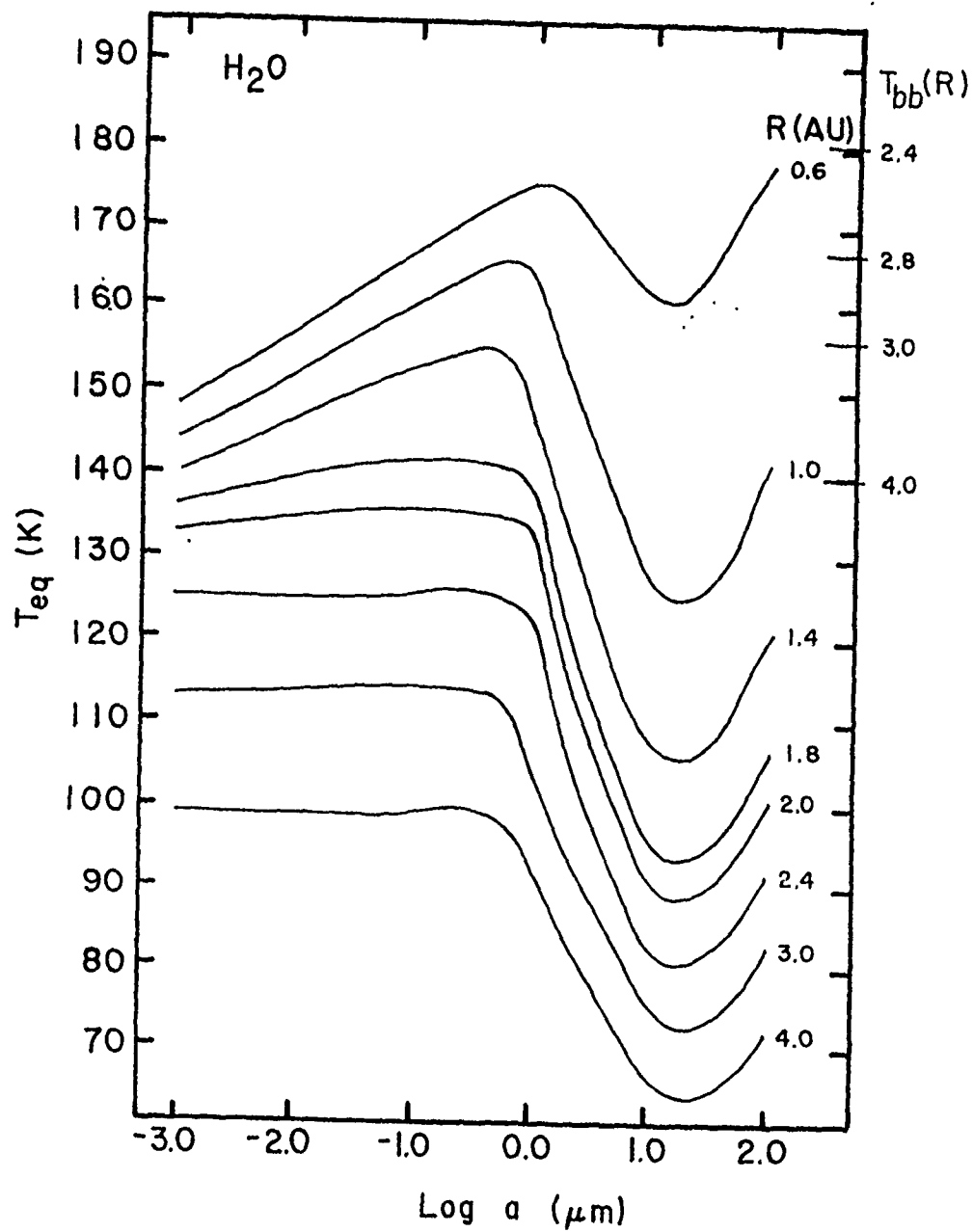


Fig. 5 The same as Figure 3, except for pure water ice.

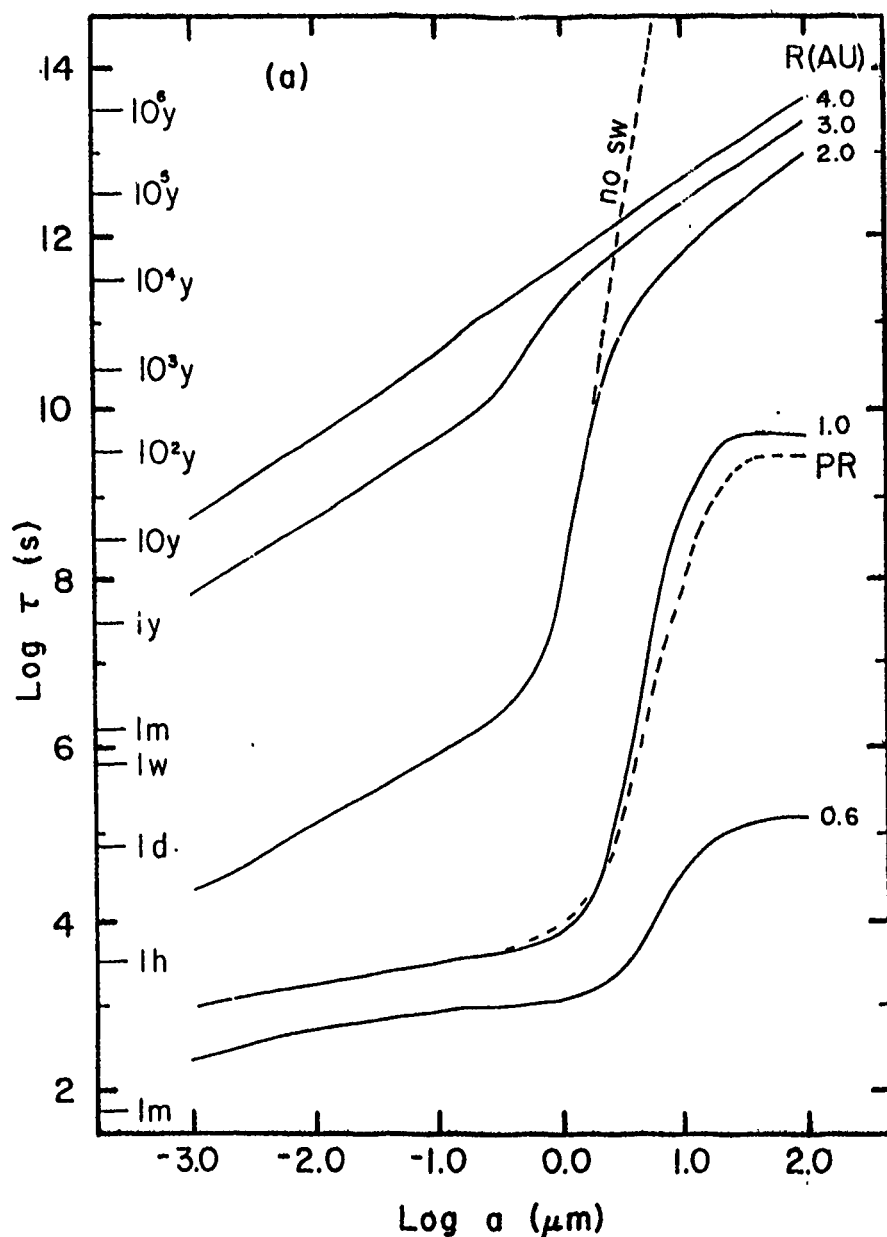


Fig. 6 a) the log of the lifetime of a pure water ice grain in seconds as a function of the log of the particle radius for five different heliocentric distances. The corresponding data from Patashnick and Rupprecht (PR) are shown at 1 AU for comparison. The lifetime of at 2 AU without the inclusion of mass loss due to sputtering from the solar wind is also shown. b) Isotemporal curves of the log of the lifetime for pure water ice for a range of particle size.

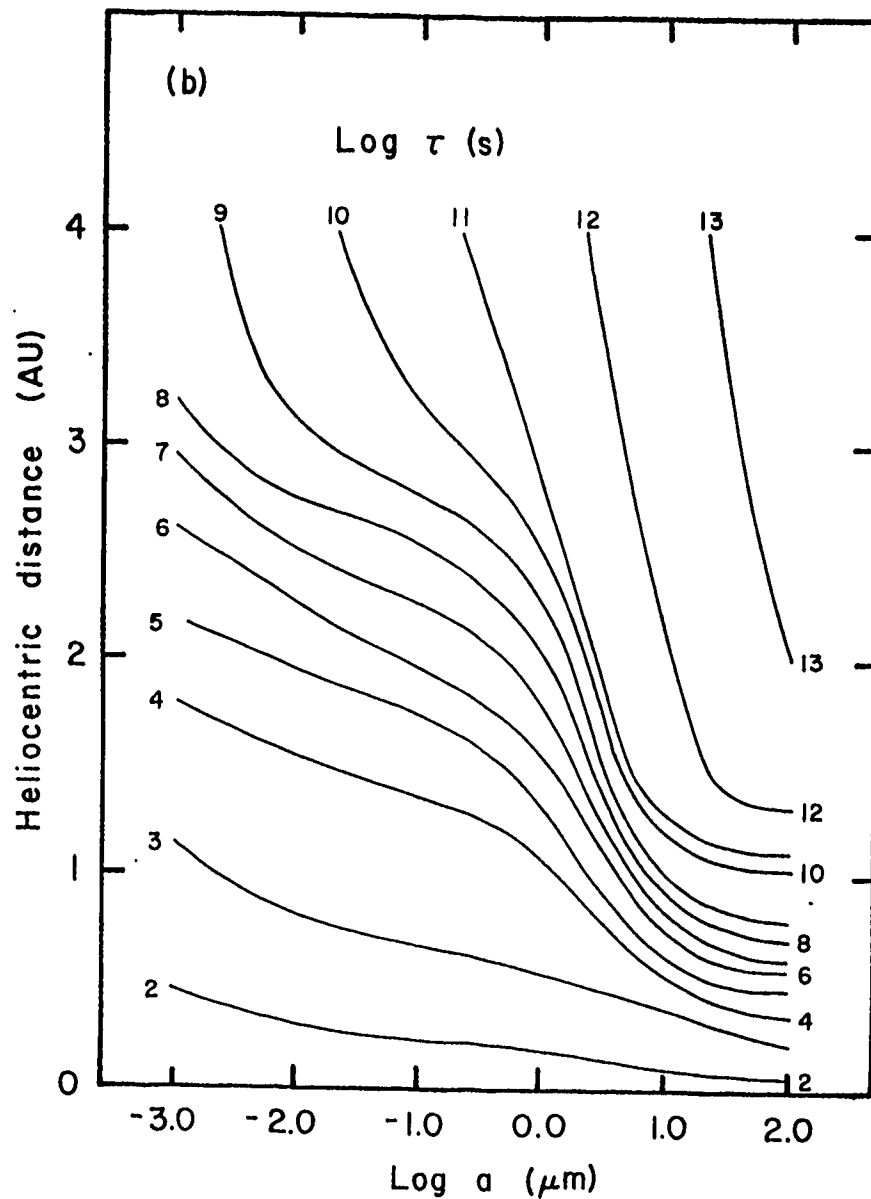


Fig. 6 a) the log of the lifetime of a pure water ice grain in seconds as a function of the log of the particle radius for five different heliocentric distances. The corresponding data from Patashnick and Rupprecht (PR) are shown at 1 AU for comparison. The lifetime of at 2 AU without the inclusion of mass loss due to sputtering from the solar wind is also shown. b) Isothermal curves of the log of the lifetime for pure water ice for a range of particle size.

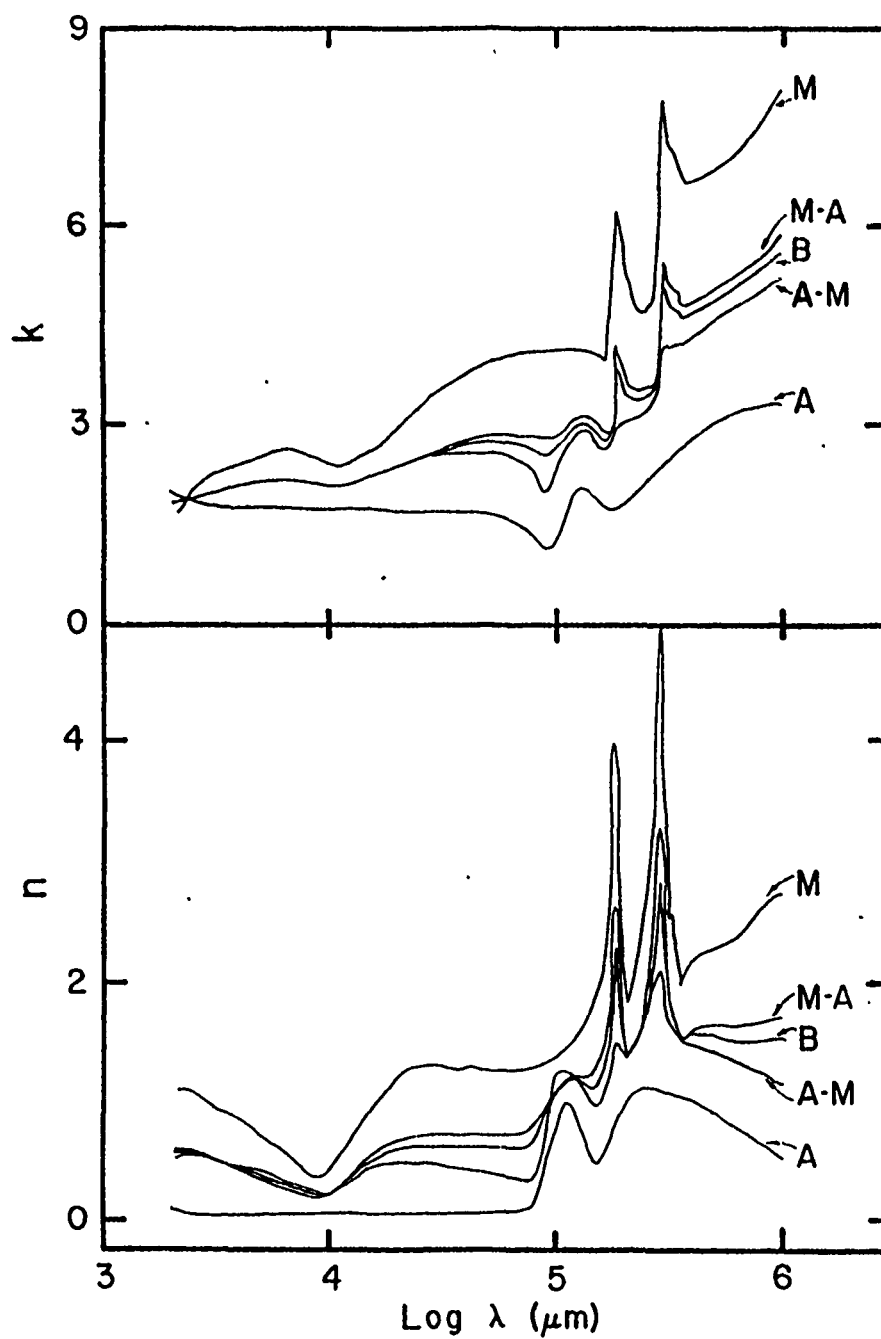


Fig. 7 Real (n) and imaginary (k) index of refraction for magnetite (M), astronomical silicate (A), and 50-50 blends using the Bruggeman theory (B) and the Maxwell-Garnett theory (astronomical silicate with inclusions of magnetite).

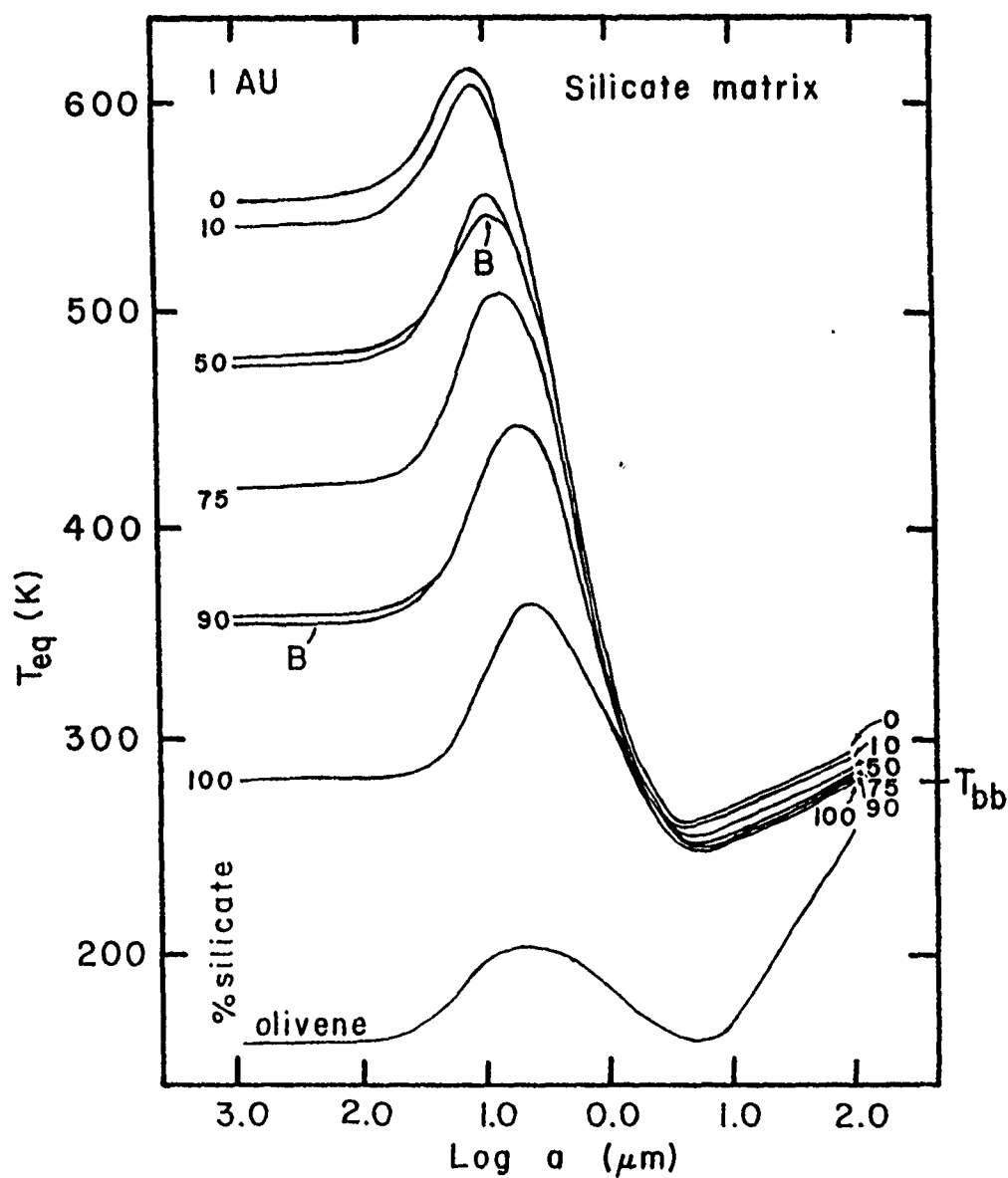


Fig. 8 Equilibrium grain temperature at 1 AU as a function of the log of the particle radius for heterogeneous blends of astronomical silicate (matrix) and magnetite (inclusions) based on the Maxwell-Garnett theory. Also shown are results from blends calculated with the Bruggeman theory (B). Equilibrium temperatures of magnetite, astronomical silicate, and olivene are included for comparison.

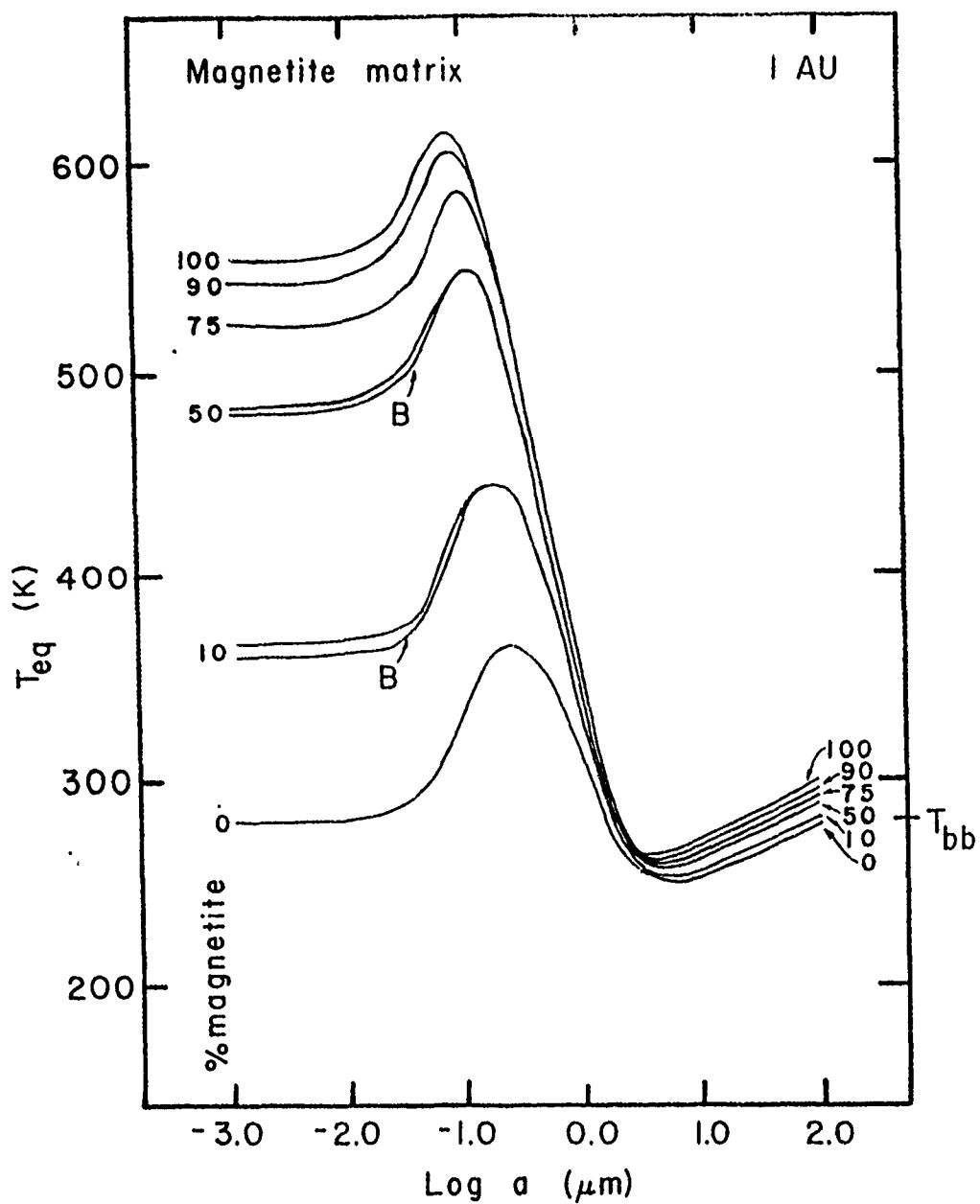


Fig. 9 The same as Figure 8, but with magnetite as the matrix material and astronomical silicate as the inclusion.

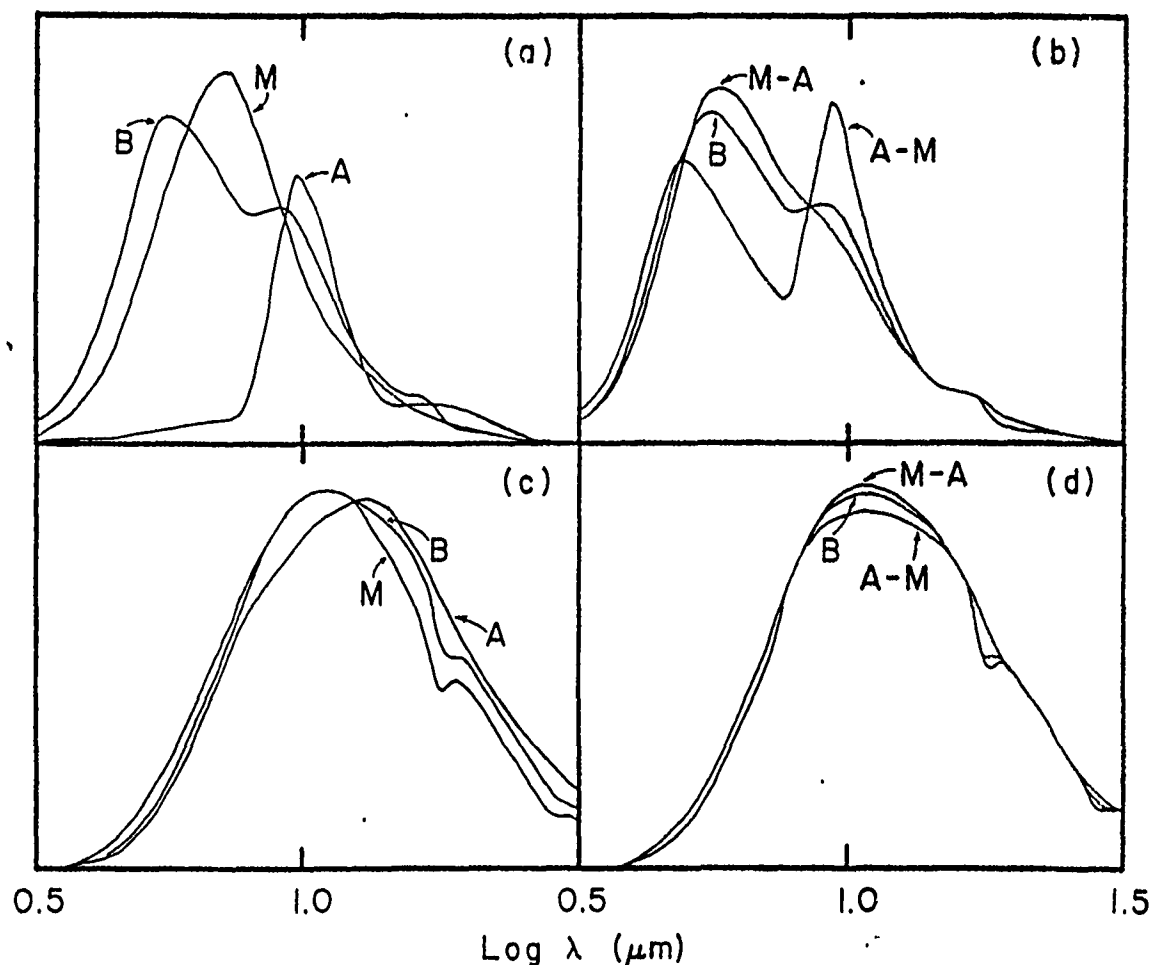


Fig. 10 The thermal spectrum of a $1\ \mu\text{m}$ and $10\ \mu\text{m}$ grain at 1 AU: a) $1\ \mu\text{m}$ grains of magnetite (M), astronomical silicate (A), and a 50-50 blend calculated with the Bruggeman theory (B); b) $1\ \mu\text{m}$ grains of 50-50 blends calculated with the Maxwell-Garnett theory: magnetite as the matrix (M-A) and astronomical silicate as the matrix (A-M). Also shown for comparison is the blend from the Bruggeman theory; c) the same as (a), but for $10\ \mu\text{m}$ grains; d) the same as (b), but for $10\ \mu\text{m}$ grains.

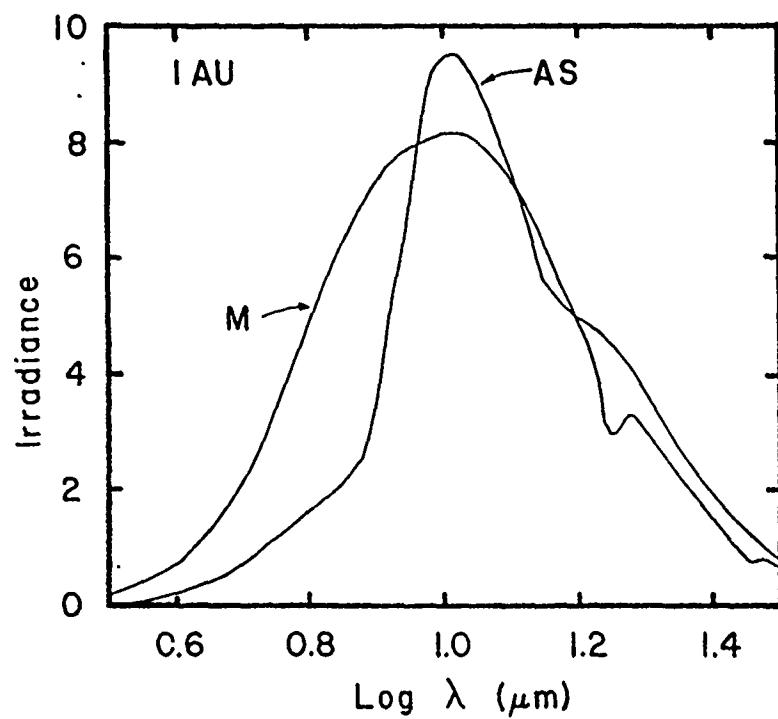


Fig. 11 The thermal spectrum of a size distribution of grains at 1 AU (Equation 12 in text) for astronomical silicate (A) and magnetite (M).

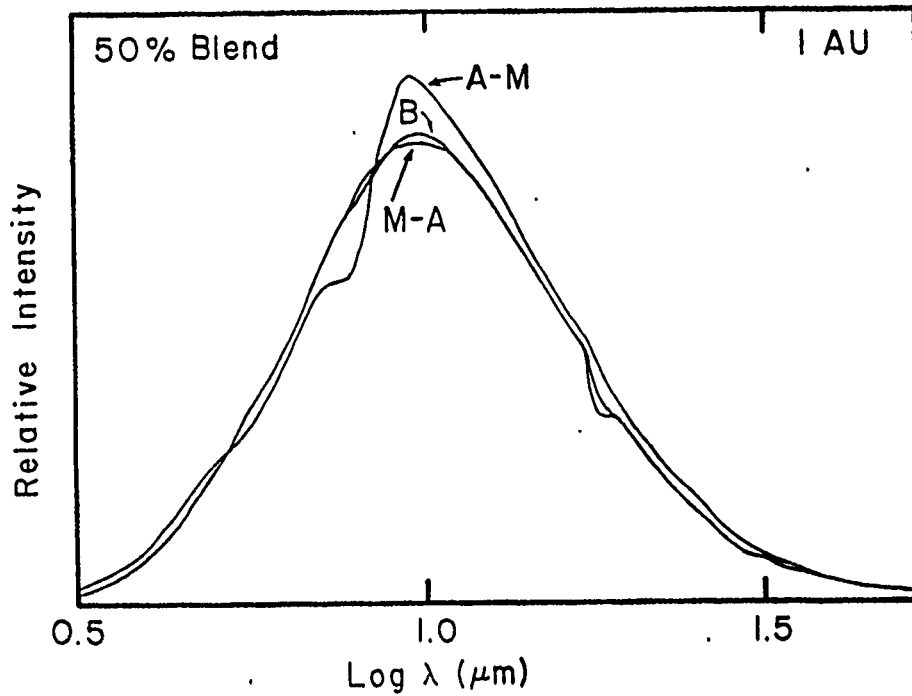


Fig. 12 The same as Figure 11 for 50-50 blends of astronomical silicate and magnetite using the Bruggeman theory (B) or the Maxwell- Garnett theory: magnetite as the matrix (M-A) and astronomical silicate as the matrix (A-M).

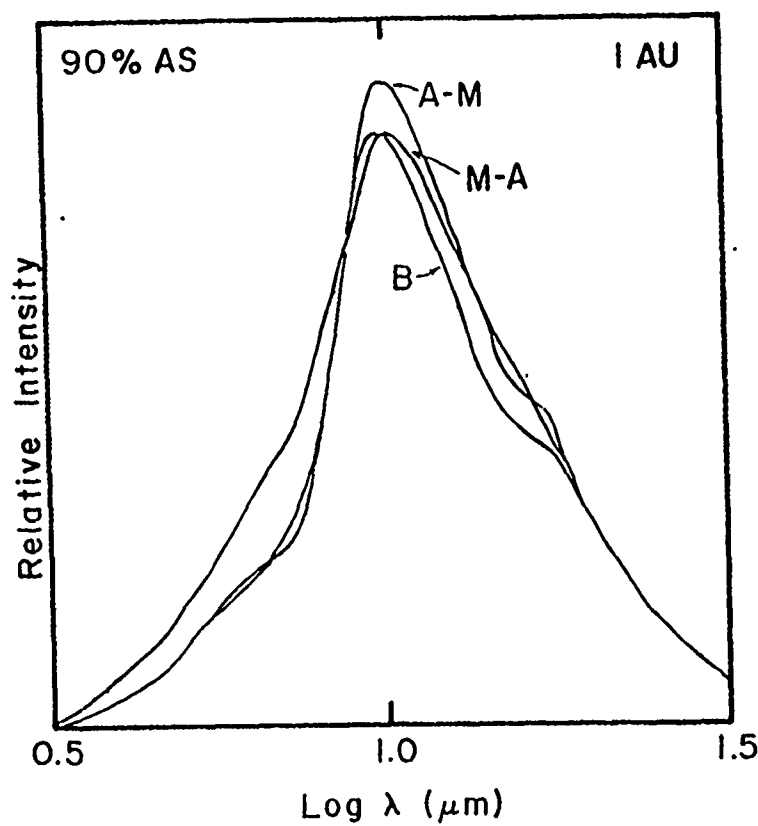


Fig. 13 The same as Figure 12 except for a 90% astronomical silicate- 10% magnetite blend.

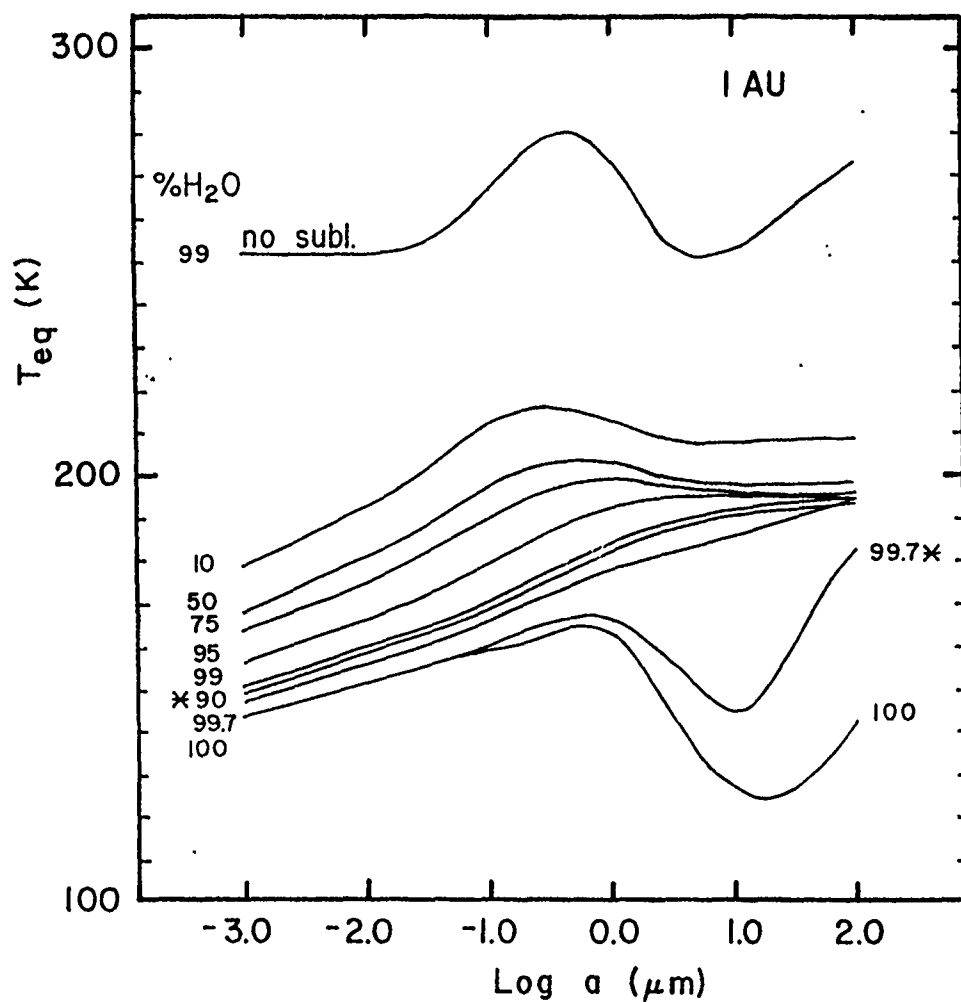


Fig. 14 The equilibrium grain temperature of a matrix of water ice at 1 AU with either magnetite (M) or astronomical silicate (A) as the inclusion. The fraction of the inclusion is indicated in the left column. Blends with astronomical silicate are indicated with an asterisk (*). Also shown is T_{eq} for pure water ice and T_{eq} for a grain composed of 99% water ice and 1% magnetite when sublimation is not included as a cooling mechanism.

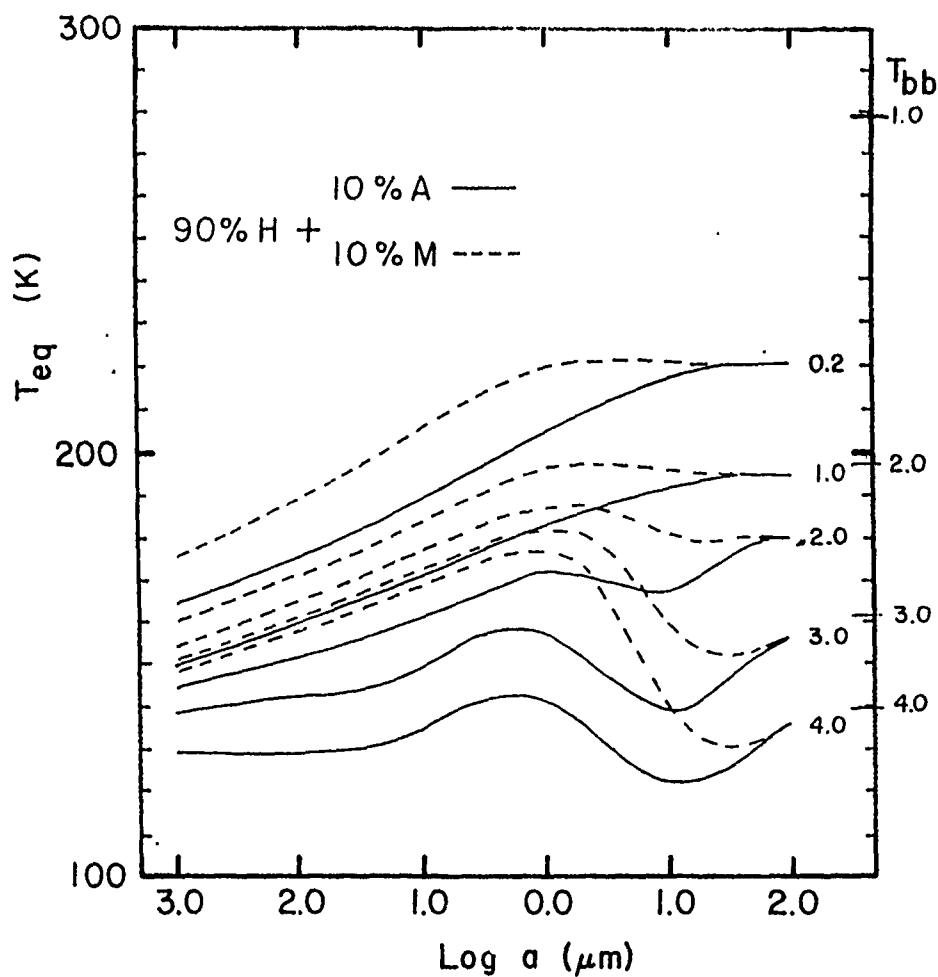


Fig. 15 The equilibrium grain temperature of dirty ice (90% water, 10% either magnetite [M; dashed line] or astronomical silicate [A; solid line]) as a function of the log of the radius for five different heliocentric distances. Black-body temperatures at these distances are indicated.

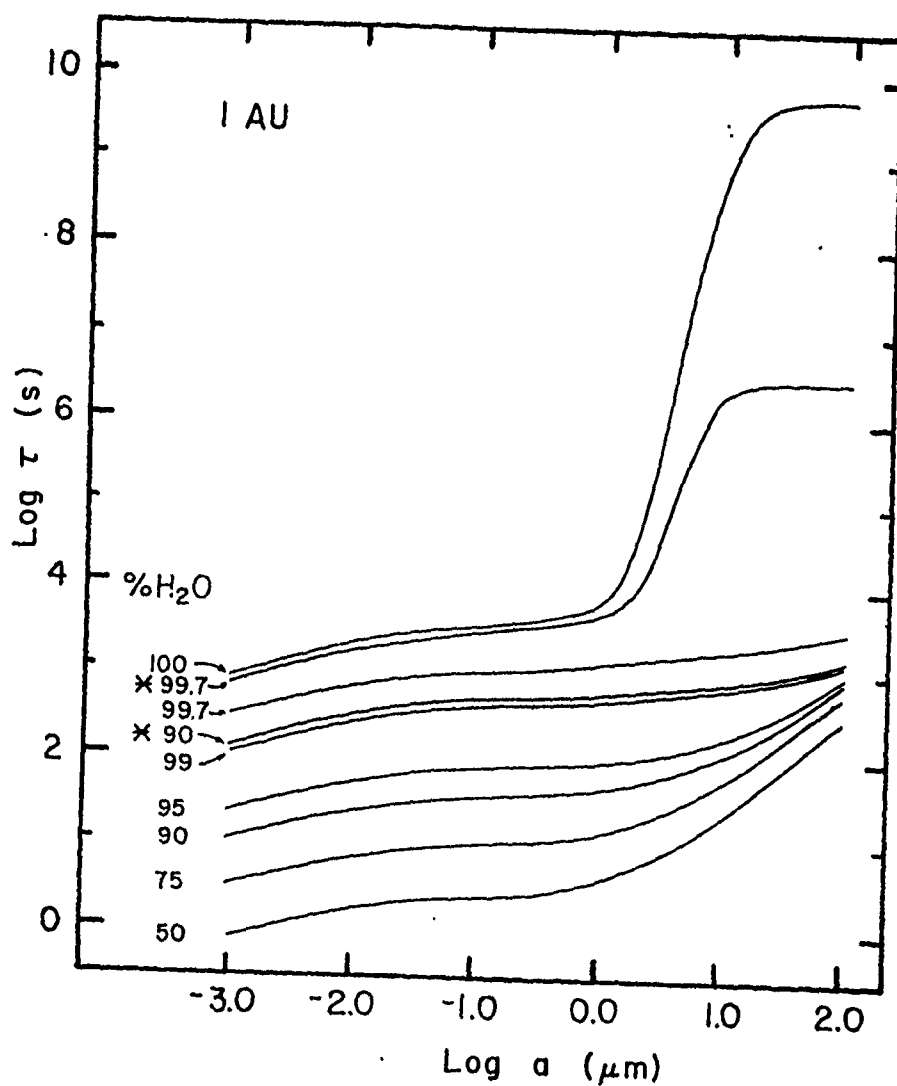


Fig. 16 The log of the lifetime of dirty ice grains at 1 AU for different volume fractions of the inclusion (magnetite (M) or astronomical silicate (A)) as a function of the log of the particle radius. Blends with astronomical silicate are indicated with an asterisk (*). Also shown for comparison is the lifetime of a homogeneous grain of water ice.

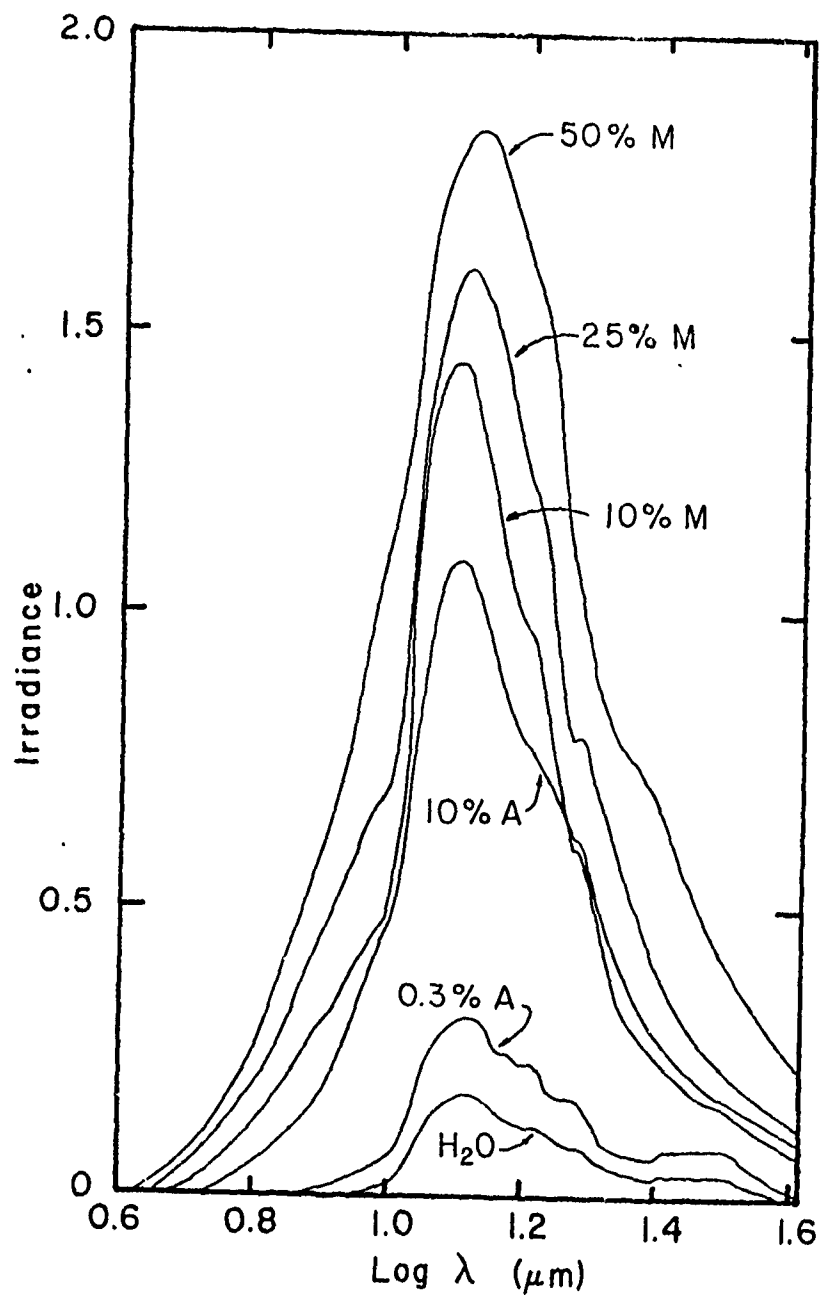


Fig. 17 The thermal spectrum of a size distribution of dirty ice grains at 1 AU for different volume fractions (f_i) of the inclusion (magnetite (M) or astronomical silicate (A)). Also shown for comparison is the thermal spectrum of a size distribution of homogeneous water ice grains.